APPLIED COMPUTATIONAL ELECTROMAGNETICS SOCIETY JOURNAL

February 2015
Vol. 30 No. 2
ISSN 1054-4887

The ACES Journal is abstracted in INSPEC, in Engineering Index, DTIC, Science Citation Index Expanded, the Research Alert, and to Current Contents/Engineering, Computing & Technology.

The illustrations on the front cover have been obtained from the research groups at the Department of Electrical Engineering, The University of Mississippi.

EMERITUS EDITORIAL ASSISTANTS

FEBRUARY 2015 REVIEWERS

THE APPLIED COMPUTATIONAL ELECTROMAGNETICS SOCIETY

JOURNAL

Vol. 30 No. 2 February 2015

TABLE OF CONTENTS

Comparison of Calculation Methods of Braided Shield Cable Transfer Impedance Using FSV Method

Jinjun Bai [1], Gang Zhang [1], Lixin Wang [1], Alistair Duffy [2], Chao Liu [1], and Tianyu Shao [1]

[1] School of Electrical Engineering and Automation
Harbin Institute of Technology, Harbin 150001, China
hitbaijinjun@163.com, zhang_hit@hit.edu.cn, wlx@hit.edu.cn, lcathit@163.com, shty.hit@gmail.com

[2] School of Engineering
De Montfort University, Leicester LE1 9BH, UK
apd@dmu.ac.uk

Abstract ─ This paper presents the results of recent work based on finite element numerical modeling in Ansoft HFSS to predict the surface transfer impedance of braided coaxial cables. Two approaches to the cable 3D modeling are investigated: (1) a simplified structural model, and (2) a rigorous structural model of braided shielded cable which is designed in Pro/Engineer software. The proposed approach provides a robust method that can overcome the challenges in the existing theoretical analysis. Factors influencing the cable transfer impedance are analyzed in detail. The validity of this simulation method is verified by comparison with a new measurement method based on time-domain response of two cable samples. The reliability of these two sets of data is analyzed by use of the feature selective validation method.

Index Terms ─ Braided shield cable, feature selective validation method, finite element method, transfer impedance.

I. INTRODUCTION

The structure of a cable shielded layer, especially for braided cables, is complex compared with other forms of shielding. These complexities can arise through design approaches such as the use of copper-clad-aluminum, non-copper braids, hybrid shields, where braided wires form part of a more complex shield, or where spindles are loaded with different diameter braid wires. Also, there are many rhombic apertures in the shielded layer, and the weaving of the braid makes the equivalent thickness of the shielded layer change. The basic modeling tools of existing EM simulation software cannot easily model complex braid structures because of the high level of complexity and fine detail required. Consequently, the calculation of the braided shield cable transfer impedance [1] which is an indicator of the quality of cable shield, relies on analytical methods in most cases.

Several theoretical models of the transfer impedance have been discussed in the literature. These include the models described by Tyni, Vance, Sali, Kley, Demoulin, etc. [2]-[6]. The predictions of these approaches are excellent at low frequencies (under 10 MHz), but become larger than the measurement results at high frequencies. This difference may be attributed to non-inclusion eddy currents caused by magnetic field between the two layers of the braid, which will produce unpredictable attenuation values for the transfer impedance [7]. So an improved model for the calculation of transfer impedance was proposed in [7] and provided better prediction results. However, the analytical method is, itself, empirical and therefore not suited without additional rigorous analysis to analyze novel structures, materials or non-uniform structures.

At present, common numerical analysis methods for solving the problem of field-line coupling are the MoM method, the FDTD method and the FEM method. Reference [8] used the MoM method to analyze the electromagnetic radiation effect of the aperture on a coaxial cable, providing a reference for the numerical computation of the

Submitted On: August 14, 2013
Accepted On: October 11, 2014

shielded cable transfer impedance. Reference [9] uses the Z transform and FDTD method for solving the radiation leakage of coaxial cable in free space. However, both methods have a common drawback: for the spindly structures, the diameter is relatively large compared with the size of the smallest elements, thus placing heavy computational demands making it difficult to get an accurate figure for the transfer impedance of shielded cable. Reference [10] first proposed using the finite element method to calculate the transfer impedance matrix of multi-core shielded cable. And more subtle FEM models of braided shield cable were discussed in [11].

This paper studies the braided shield cable structure, and then constructs two FEM models based on the work in [12]. In addition, factors influencing the cable transfer impedance are analyzed in detail using the proposed models. The performance of the proposed models is validated by use of the Feature Selective Validation (FSV) method [13] through comparing the simulated and measured results.

The FSV method is a kind of numerical calculation of the validation rating recommended in IEEE Standard 1597.1, which can give qualitative and quantitative results with regard to the agreement between data sets. The results of the FSV methods are given in different layers. In this paper, the single value and qualitative histogram results of the Global Difference Measure (GDM) results, GDMtot and GDMc are used to show the agreement between results given by different methods. More details of this method can be found in [13].

The transfer impedance definition and its calculation are briefly summarized in Section II along with mathematical modeling using FEM in Section III. Section IV describes the construction of simplified and rigorous models of braided shield cable. The results given by different methods are compared and discussed in Section V. Further, factors influencing the transfer impedance are analyzed in Section VI. Section VII gives a summary and some concluding remarks.

II. TRANSFER IMPEDANCE DEFINITION AND ITS CALCULATION

Transfer impedance is defined as:

$$Z_{\mathrm{T}} = \frac{1}{I_0}\frac{\partial V}{\partial z}\Big|_{I=0}, \tag{1}$$

where $\partial V/\partial z$ is the RMS voltage per unit length of the uniform transmission line created by the inner surface of the shielding layer and the cable core. I_0 is the induced current flowing through the outer surface of the shielded layer. I is the current flowing through the core wire.

Generally, the theoretical expression [7] for the transfer impedance is given by:

$$Z_{\mathrm{T}} = Z_{\mathrm{d}} + j\omega(M_{\mathrm{h}} \pm M_{\mathrm{b}}) + Z_{\mathrm{e}}, \tag{2}$$

where Z_{d} is diffusion impedance due to the diffusion of the current induced in the shield. It describes the linkage between the fields inside and those outside at low frequencies. Its value decreases as the frequency increases. M_{h} is hole inductance caused by the direct leakage of the magnetic field through the rhombic holes of the shield. M_{b} is the braid inductance caused by the magnetic flux linkage between the inner and outer braided layers. Z_{e} is the extra inductance indicating the influence of eddy current caused by electromagnetic field between the inner and outer braid layers. The detail of these parameters can be found in [7].

III. MATHEMATICAL MODELING

Broadly speaking, three-dimensional Maxwell equations are the governing equations of electromagnetic field problems. However, under normal circumstances, in order to facilitate the modeling and obtaining a solution, the two Maxwell curl equations are used to obtain the Vector Helmholtz equation as the key equation [14]:

$$\nabla\times(\frac{1}{\mu_r}\nabla\times\boldsymbol{E}) - k_0^2\varepsilon_r\boldsymbol{E} = 0, \tag{3}$$

where μ_{r} is the relative magnetic permeability, k_0 is the wave number of the free space, $\boldsymbol{E}(x,y,z)$ is the corresponding vector of time-harmonic field, $\boldsymbol{E}(x,y,z,t) = R\left\{\boldsymbol{E}(x,y,z)e^{j\omega t}\right\}$, ε_{r} is the relative dielectric constant.

The function of equation (3) can be derived from variation principle:

$$F(\boldsymbol{E}) = \iiint_{\Omega} \left\{ \frac{1}{\mu_r} (\nabla \times \boldsymbol{E})(\nabla \times \boldsymbol{E}) - k_0^2 \varepsilon_r \boldsymbol{E}\boldsymbol{E} \right\} d\Omega = 0. \quad (4)$$

The boundary condition of the configuration illustrated in Fig. 1 shows the braided cable simulation model diagram, from outside to inside consisting of air, braided layer, the inner insulating layer, and the core wire. On the radiation surface, the boundary condition is:

$$(\nabla \times \boldsymbol{E})_{\tan} = jk_0 \boldsymbol{E}_{tan} - \frac{j}{k_0} \nabla_{\tan} \times (\nabla_{\tan} \times \boldsymbol{E}_{tan}) + \frac{j}{k_0} \nabla_{\tan} (\nabla_{\tan} \boldsymbol{E}_{tan}), \quad (5)$$

where $\boldsymbol{E}_{tan}$ is the tangential component of the surface electric field.

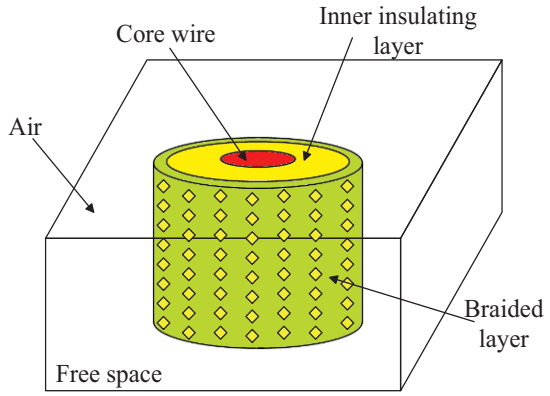

Fig. 1. Diagram of braided cable simulation model.

The two terminal cross sections of the shielded cable were set to PEC (Perfect Electrical Conductor, or Perfect E Condition) to stop the fields entering the cable through the ends. PEC can be described as:

$$\nabla(\varepsilon \boldsymbol{E}) = 0, \quad \hat{n} \times \boldsymbol{E} = 0. \quad (6)$$

A plane wave was chosen to be the excitation source. The plane wave can be described as:

$$E_{\text{inc}} = E_0 e^{-jk_0(\boldsymbol{kr})}, \quad (7)$$

where E_{inc} is the incident wave, E_0 is electric polarization vector, k_0 is wave number of free space, $\boldsymbol{k}$ is unit propagation vector, $\boldsymbol{r}$ is a position vector, $\boldsymbol{r} = x\hat{\boldsymbol{x}} + y\hat{\boldsymbol{y}} + z\hat{\boldsymbol{z}}$.

After $\boldsymbol{E}(x, y, z)$ is obtained, formula (1) can be redefined as:

$$\frac{\partial V}{\partial z} = \frac{1}{A_e} \iint_{S_e} \boldsymbol{E}_z d\boldsymbol{S}_e, \quad (8)$$

$$I_0 = \iint_{S_i} \sigma \boldsymbol{E} d\boldsymbol{S}_i, \quad (9)$$

where E_z is the longitudinal electric field component. $\boldsymbol{S}_e$ is the inner surface of the cable shield, $\boldsymbol{S}_i$ is its transversal surface as shown in Fig. 2. A_e is the area of $\boldsymbol{S}_e$. σ is the electrical conductivity of shield.

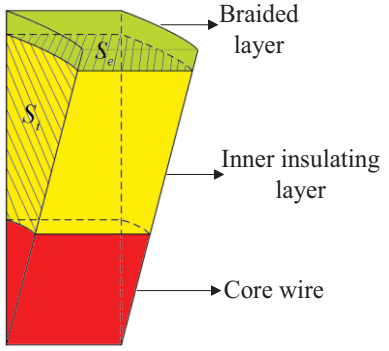

Fig. 2. Integral surfaces.

IV. MODEL DESCRIPTION

A. The simplified structural model

In order to decrease the complexity of the model and increase the simulation speed, the change of the equivalent thickness of the shielded layer caused by the braiding has been ignored in order to focus on the numerous rhombic holes on the shielded layer. Figure 3 shows the basic unit of braided shield. The key to create a simplified numerical structural model is to determine the side length of every rhombic hole, l_{rh}, and the horizontal and vertical distance of two adjacent holes, l_1, l_2, according to the known data of the cable. Figure 4 shows the simplified structural model. Once we know the structure parameter of the shielded layer, the parameters l_{rh}, l_1, l_2, can be described as in (10) to (13):

$$l_{rh} = \frac{W - Nd}{\sin(2\alpha)}, \quad (10)$$

$$l_1 = \frac{2\pi D_m}{C}, \quad (11)$$

$$l_2 = \frac{l_1}{\tan\alpha}, \tag{12}$$

$$W = \frac{2\pi D_m}{C}\cos\alpha, \tag{13}$$

where N is number of woven wires in a bundle. d is the diameter of the braided wire. C is the number of beams of the braid knitting. α is braiding angle. D_m is the diameter of the shield.

As the braiding effect is ignored, the effective thickness of shielded layer becomes a constant, so the thickness of shielded layer $T=2d$ when we use the simplified structure model:

$$D_m = D_0 + 4d, \tag{14}$$

where D_0 is the diameter of the insulating materials (inner diameter of shield).

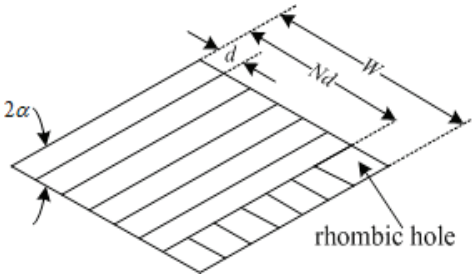

Fig. 3. Basic unit of braided layer.

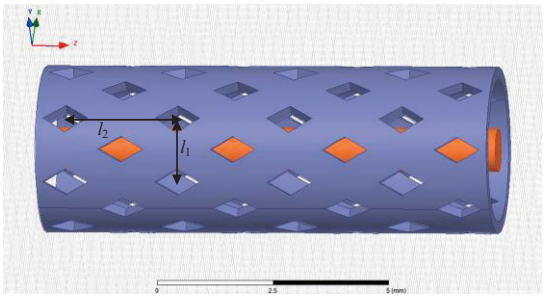

Fig. 4. The simplified structure model.

B. The rigorous structural model

Conversely, the rigorous structure model considered the change of the equivalent thickness of the shielded layer caused by braiding in and out of the weaving beams, as shown in Fig. 5. The cylindrical tube represents the shielded layer. The groove running on the tube represents the area that the weaving beam is not overlapping. The thickness is T=1.5*d*. The length of the long diagonal of the rhombic holes:

$$l_d = \frac{W - Nd}{\sin\alpha}. \tag{15}$$

The width of each knitting beam:

$$l_b = Nd. \tag{16}$$

The rest of the area of the tube represents the weaving beam overlapping, where the thickness of shielded layer T=2.5*d*.

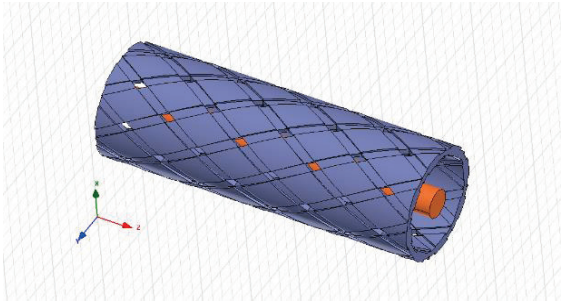

Fig. 5. The rigorous structure model.

V. RESULTS AND THE ANALYSIS OF FSV

In order to verify the aforementioned analytical or numerical methods, the models of TV cables SYV50-3 and SYV75-2-1 are established. Transfer impedance measurements of these two cables are performed using the method mentioned in reference [15]. The theoretical result is calculated according to formula (2) which comes from [7]. The simplified structure model and the rigorous structure model are shown in Figs. 4 and 5, respectively. Both of the models are calculated using the Ansoft HFSS software.

Parameters of SYV50-3 and SYV75-2-1 are shown in Table 1. D is the diameter of the core wire, D_0 is the diameter of the insulating materials (inner diameter of shield), C is the number of beams of the braid knitting, d is the diameter of the braided wire, N is number of woven wires in a bundle, p is the woven pitch, ε_r is the relative magnetic permeability, σ is electrical conductivity. Both the cable's core wire material is copper, the insulating layer is solid polyethylene, and the shielded layer material is copper.

For a more intuitive comparison, the results of measurement, theoretical calculation and simulation results of SYV50-3 and SYV75-2-1 are shown in Figs. 6 and 7, respectively. It can be seen from the figures that both the analytical and numerical methods can give generally reasonable

results, and the difference between them and measurement results is difficult to be identified by visual assessment. So the FSV method is introduced to compare the simulated or analytical results with measurement result to show the advantage or disadvantage of these methods. In addition to the quantitative assessment of data agreement, the FSV method can give the qualitative assessment described by natural language which cannot be shown by root-mean-square error or residual.

Table 1: Parameters of SYV50-3 and SYV75-2-1

Parameters	SYV50-3	SYV75-2
D (mm)	0.9	0.4
D_0 (mm)	2.95	2.3
C	16	16
d (mm)	0.12	0.11
N	6	6
p (mm)	18.8	23
ε_r	2.029	2.25
σ (S/m)	5.8e^7	5.8e^7

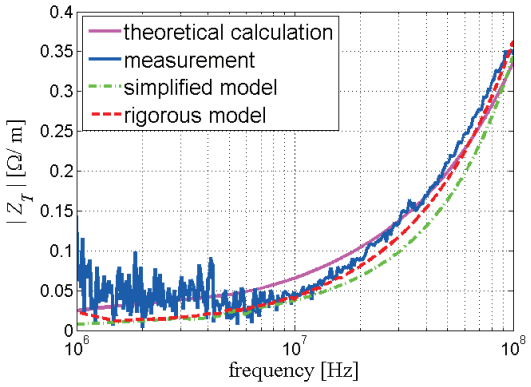

Fig. 6. Results for SYV50-3.

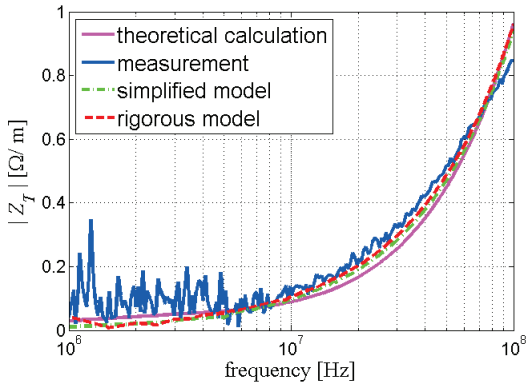

Fig. 7. Results for SYV75-2-1.

Figures 8 and 9 outline the GDMc results. Specifically, GDMc results can mirror the distribution of survey results given by a group of experts who are asked to describe the agreement between data sets using natural language (Excellent, Very Good, Good, etc.). Table 2 shows the GDMtot results which are the quantitative measure of global difference between predicted results and measurement result. The smaller GDMtot value the better accuracy of method.

It is demonstrated by the FSV results that the FEM models can give more accurate predictions than the analytical method for both of the cables. And the results of the rigorous structure are more accurate than the simplified one for the SYV50-3. But for the SYV75-2-1, there is no obvious difference between the two FEM models. Generally, the simplified structure model is a good compromise between the modeling complexity and accuracy as indicated in Table 2. It should be noted that even the analytical result can show "Good" agreement with measurement results.

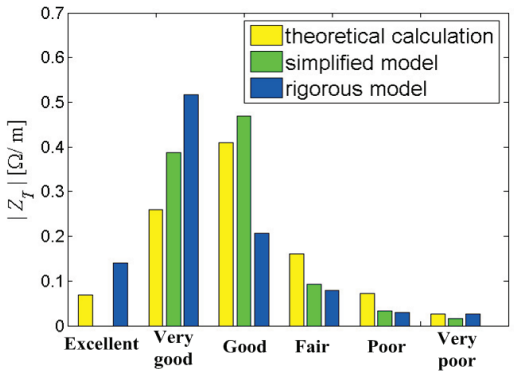

Fig. 8. Comparison of GDMc results for SYV50-3.

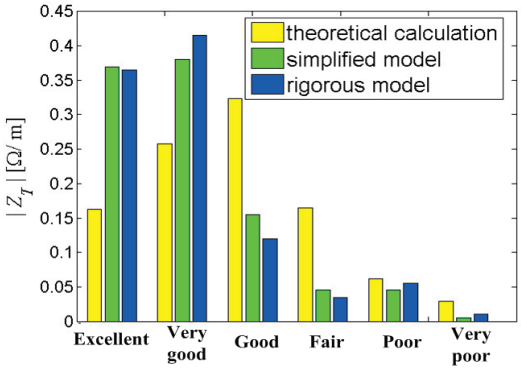

Fig. 9. Comparison of GDMc results for SYV75-2-1.

Table 2: GMDtot results of the three models

GDMtot	Theoretical Calculation	Simplified Model	Rigorous Model
SYV50-3	0.40	0.31	0.28
SYV75-2-1	0.37	0.20	0.21

VI. INFLUENCING FACTORS OF TRANSFER IMPEDANCE

In order to analyze the influencing factors of braided shielded cable transfer impedance, four important parameters including simulation length of the cable, shielding material, inner diameter of the shield and diameter of the braided wire are discussed.

A. Simulation length of cable

Theoretically, the simulation length of the cable has no effect on the simulation results. We chose the former mentioned rigorous structure model of cable SYV50-3 as an example. Different lengths (10 mm, 15 mm and 20 mm) were simulated. Figure 10 (a) shows the results. These results are consistent in the whole frequency range, noting the observation made later in this section. This indicates that the length of the cable in the simulation does not affect the simulation results when the cable is electrically short. However, the computer performance limits the length of the cable which can be simulated in a reasonable period of time. The simulation times of these three models are 10 hours, 12.5 hours and 38 hours respectively. It has the exponential growth trend. The CPU is Pentium (R) Dual-Core E5300 @ 2.6 GHz with 2 GB memory. The program was set parallelized.

B. Shielding material

In this section, the influence of shielding layer materials is analyzed. We chose the former mentioned rigorous structure model of cable SYV75-2-1 as an example. Three different materials: copper, tin and steel were simulated. As shown in Fig. 10 (b), at low frequency, the shielding effectiveness of copper is better than the other two materials. As the frequency went up to 30 MHz, the copper shielding becomes worse. So when the cable is used in low frequency range (less than 30 MHz), cables with copper shielding are recommended, and when the cable is used in the higher frequency range (more than 30 MHz), tin or steel may make more efficient shields for this geometry.

C. Inner diameter of the shield

The influence of inner diameter of shield (D_0 mentioned in Table 1) on the transfer impedance is observed based on the rigorous structure model of cable SYV50-3. The impedance for different D_0 (2.91 mm, 2.93 mm, 2.95 mm, 2.97 mm and 2.99 mm) are shown in Fig. 10 (c). It can be seen that the increase of D_0 leads to the reduction of the transfer impedance. For this reason, the shielding effectiveness will improve, but the cost will increase.

D. Diameter of the braided wire

In this section, the former mentioned rigorous structure model of cable SYV50-3 is also used to analyze the influence of braided wire diameter (d mentioned in Table 1). Figure 10 (d) shows the change of the transfer impedance for different d (0.115 mm, 0.118 mm, 0.12 mm, 0.122 mm and 0.125 mm). It is shown that with the increase of d, the transfer impedance may decrease. As a result, the shielding effectiveness can be improved. Accordingly, the costs of cable production will increase.

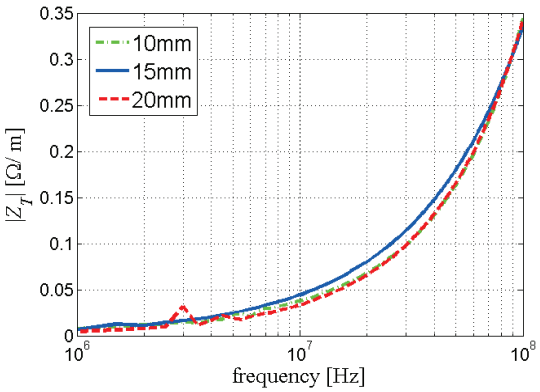

(a) Simulation length

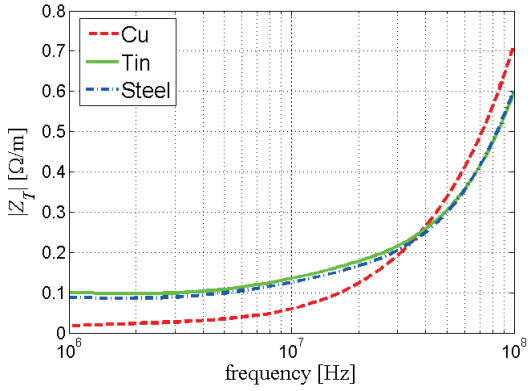

(b) Shielding material

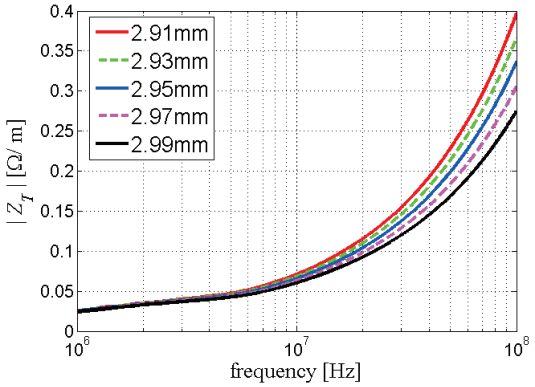

(c) Diameter of the insulating materials

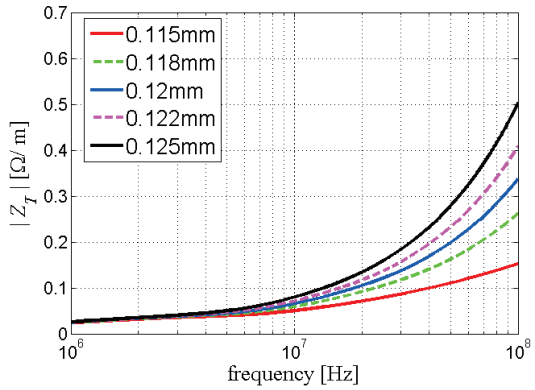

(d) Diameter of the braided wire

Fig. 10. Influence of different parameters.

VII. CONCLUSION

Several methods for transfer impedance calculation of braided shielded cable have been discussed. Two 3D models: the simplified structure model and the rigorous structure model have been modeled using Ansoft HFSS. The results of both models are verified by measurement results and compared with theoretical calculation using the FSV method. From the FSV analysis, we can see that the simplified structure model provides a reasonable approximation to the measurement results. The results of the rigorous structure are more accurate than the simplified one; however, one goal of analyses such as these is to investigate the question "how efficient can the simulation be made?" This paper has suggested that a reasonable level of simplification can lead to reasonable computational demands with only a small reduction in the accuracy of the results obtained.

Finally, factors influencing the transfer impedance, including simulation length of cable, material of the shielding layer, inner diameter of the shield and diameter of the braided wire, were investigated as examples of the application of the approach proposed in this paper.

REFERENCES

[1] S. A. Schelkunoff, "The electromagnetic theory of coaxial transmission lines and cylindrical shields," *Bell Syst. Tech. J.*, vol. 13, no. 4, pp. 532-579, 1934.

[2] M. Tyni, "The transfer impedance of coaxial cables with braided outer conductor," *Digest of the 10th International Wroclaw Symposium on EMC*, pp. 410-419, 1976.

[3] E. F. Vance, "Shielding effectiveness of braided-wire shields," *IEEE Trans. Electromagnetic Compatibility*, vol. EMC-17, no. 2, pp. 71-77, 1975.

[4] S. Sali, "An improved model for the transfer impedance calculations of braided coaxial cables," *IEEE Trans. Electromagnetic Compatibility*, vol. 33, no. 2, pp. 139-143, 1991.

[5] T. Kley, "Optimized single-braided cable shields," *IEEE Trans. Electromagnetic Compatibility*, vol. 35, no.1, pp. 1-9, 1993.

[6] B. Demoulin and P. Degauque, "Shielding effectiveness of braids with high optical coverage," *Proceedings of the International Symposium on EMC*, Zurich, pp. 491-495, 1981.

[7] W. Xiaoling, et al., "An improved model for the transfer impedance calculations of braided coaxial cables," *IEEE 7th International Power Electronics and Motion Control Conference (IPEMC)*, vol. 2, 2012.

[8] T. Liu and L. Zhang, "Electromagnetic radiation effect of the aperture on a coaxial cable," *Electronic Components & Device Applications*, vol. 12, no. 5, pp. 90-94, 2010.

[9] F. Linlin, "Leakage radiation analysis of coaxial cable based on FDTD," *Harbin Engineering University*, Harbin, 2010.

[10] M. Feliziani and F. Maradei, "A FEM approach to calculate the impedances of shielded multiconductor cables," *IEEE Trans. Magnetics*, vol. 2, no. 2, pp. 1020-1025, 2002.

[11] R. Otin, J. Verpoorte, and H. Schippers, "Finite element model for the computation of the transfer impedance of cable shields," *IEEE Trans. Electromagnetic Compatibility*, vol. 53, no. 4, pp. 950-958, 2011.

[12] C. Liu, A. Duffy, and L. Wang, "Calculation of braided shielded cable transfer impedance based on FEM method," *The 29th International Review of Progress in Applied Computational Electromagnetics*, Monterey, CA, 2013.

[13] "IEEE standard for validation of computational electromagnetics computer modeling and simulations," *IEEE STD 1597.1-2008*, pp. 1-41,

2008.
[14] J. Jin, "The finite element method in electromagnetics," 2nd ed., *Hoboken, NJ: Wiley*, 2002.
[15] B. Vanlandschoot and L. Martens, "New method for measuring transfer impedance and transfer admittance of shields using a triaxial cell," *IEEE Trans. Electromagnetic Compatibility*, vol. 39, no. 2, pp. 180-185, 1997.

Jinjun Bai was born in Jilin, China, on January 21, 1991. He received the B.Eng. degree in Electrical Engineering and Automation from the Harbin Institute of Technology, Harbin, China, in 2013. He is currently working towards the Ph.D. degree in Electrical Engineering at the Harbin Institute of Technology, Harbin, China. His research interests include computational electromagnetics and electromagnetic compatibility of indoor power line communication systems.

Gang Zhang received the B.Sc. in Electrical Engineering from China University of Petroleum, Dongying, China, in 2007, and the M.Sc. and Ph.D. degrees in Electrical Engineering from Harbin Institute of Technology (HIT), Harbin, China, in 2009 and 2014, respectively.

He is now with the Faults Online Monitoring and Diagnosis Laboratory at Harbin Institute of Technology. His research interests include analysis of electromagnetic compatibility, electromagnetic simulation, and the validation of CEM.

Lixin Wang received the B.S. degree in Electrical Engineering from Nankai University, Tianjin, China, in 1988, and the M.S. and D.Sc. degrees in Electrical Engineering from Harbin Institute of Technology (HIT), Harbin, China, in 1991 and 1999, respectively.

He is currently a Professor of Power Electronic and Electric Drives at HIT. He conducts research with Faults Online Monitoring and Diagnosis Laboratory, HIT, on a wide variety of topics including electromagnetic compatibility at the electronic system level, aircraft electromechanical fault diagnosis expert system and Prediction and Health Management (PHM) of Li-ion battery.

Alistair Duffy was born in Ripon, U.K., in 1966. He received the B.Eng. (Hons.) degree in Electrical and Electronic Engineering and the M.Eng. degree from the University College, Cardiff, U.K., in 1988 and 1989, respectively. He received the Ph.D. degree from Nottingham University, Nottingham, U.K., in 1993 for his work on experimental validation of numerical modeling and the MBA from the Open University in 2003.

He is currently a Reader in electromagnetics at De Montfort University, Leicester, U.K. He is the author of over 150 articles published in journals and presented at international symposia. His research interests include CEM validation, communications cabling, and technology management.

Duffy is a Fellow of the Institution of Engineering and Technology (IET) and a Member of the International Compumag Society and the Applied Computational Electromagnetics Society. He is a Member of the IEEE EMC Society Board of Directors and is the Chair of the IEEE EMC Society Standards Development and Education Committee.

Chao Liu received the B.Sc. and M.Sc. degrees in Electrical Engineering from Harbin Institute of Technology (HIT), Harbin, China, in 2005 and 2007, respectively. He is currently working towards the Ph.D. degree at HIT and involved in the research of electromagnetic compatibility of test system and electromagnetic simulation of cables.

Tianyu Shao received the B.Sc. in Electrical Engineering from Harbin Institute of Technology (HIT), Harbin, China, in 2012. He is currently working towards the M.Sc. degree at HIT and involved in the research of electromagnetic compatibility of indoor power line communication systems.

Hybrid IE-DDM-MLFMA with Gauss-Seidel Iterative Technique for Scattering from Conducting Body of Translation

Ming Jiang, Jun Hu, Ran Zhao, Xiang Wei, and Zai-ping Nie

School of Electronic Engineering
University of Electronic Science and Technology of China, Chengdu 611731, People's Republic of China
hujun@uestc.edu.cn

Abstract ─ In this paper, a hybrid Integral Equation-Domain Decomposition Method-Multilevel Fast Multipole Algorithm (IE-DDM-MLFMA) with Gauss-Seidel iterative technique is proposed to calculate the scattering from perfectly electric conducting Body of Translation (BoT). The BoT can be partitioned into translational non-overlapping sub-domains. A hybrid local/global MLFMA framework is adopted to realize efficient matrix-vector multiplication in sub-domains and between sub-domains by utilizing the feature of translational invariance of BoT. To reduce the number of interactions between sub-domains, Gaussian-Seidel iterative technique is applied. Numerical examples are presented to demonstrate the efficiency of the present method.

Index Terms ─ Body of translation, Gauss-Seidel iteration, multilevel fast multipole algorithm, non-overlapping domain decomposition method.

I. INTRODUCTION

In practical electronic information area, some important conducting objects have gained intensive interests and attention of researchers in electromagnetic community, which are Bodies of Translation (BoT). In practice, high speed trains, aircraft wings and fuselages can often be approximated as bodies of translation. Some numerical methods including the method of moment have been developed to solve the BoT. Medgyesi-Mitschg and Putnam developed a general systematic approach based on the method of moment for BoT in 1983. The functional variation of the surface currents along the axis of translation of the BoT is represented by a total-domain Fourier expansion and a piecewise continuous function along the generating curve [1].

To solve electromagnetic problems for large BoT, Davis used the rectangular basis functions to segment the body of translation into a set of identical cells along the translation of the body. The impedance matrix can be evaluated efficiently by converting all surface integrals over the basis functions into line integrals [2]. Medgyesi-Mitschg and Putnam also expand the method of moment for analysis of wire antenna attached on the BoT by incorporating a special junction basis function set for the antenna attachment points [3]. Although the above methods can accurately solve the BoT problems, they can be only applicable for moderate problems due to large computational complexity of method of moment. As a well-known fast algorithm used for integral equation, Multilevel Fast Multipole Algorithm (MLFMA) [4] has only computational complexity of O(NlogN). Although MLFMA is a general fast algorithm for accelerating matrix vector multiplication in iterative solution of matrix equation for objects with arbitrary geometry, for very large BoT problems, the MLFMA is still time consuming and requires large memory storage. Thus, it is still necessary to seek novel numerical methods to solve larger BoT problems more efficiently.

In order to realize efficient solution of conducting structures with large sizes, the Multi-Region Iterative Multilevel Fast Multipole Algorithm (MRI-MLFMA) combined the Generalized Forward/Backward (GFB) technique was developed by us [5]. Although it has better performance than traditional MLFMA, the buffer zones are required to ensure the continuity of current across the interfaces between multi-regions, and the property of matrix can't be improved in

Submitted On: September 1, 2013
Accepted On: September 26, 2014

essence. Recently, a novel Integral Equation based non-overlapped Domain Decomposition Method (IE-DDM) [6] is introduced by Peng, et al. In this paper, in order to realize efficient solution of scattering from the Perfect Electric Conductor (PEC) BoT with large electric size, a hybrid scheme named IE-DDM-MLFMA with Gaussian-Seidel iterative technique is developed. The computational BoT is partitioned into several same closed sub-domains, so Combined Field Integral Equation (CFIE) can be used in each sub-domain. In addition, Gauss-Seidel iterative technique is used to update the unknown current in each sub-domain in real time. A hybrid local/global MLFMA framework is adopted to realize efficient matrix-vector multiplication in sub-domains and between sub-domains by utilizing translation invariant feature of BoT.

The rest of paper includes the following parts. Section II gives a brief introduction on integral equation based domain decomposition method, followed by Section III for the extension of IE-DDM for the BoT. Section IV presents some typical numerical results, and finally, the conclusions are given in Section V.

II. INTEGRAL EQUATION BASED DOMAIN DECOMPOSITION METHOD

A. Equation formatting boundary value statement

Considering electromagnetic scattering by a PEC target occupying a finite domain illustrated in Fig. 1. The scattered electric and magnetic fields in free space can be obtained from the Stratton-Chu representation formula [7,8] as:

$$\boldsymbol{E}^s(\boldsymbol{J};\partial\Omega)(\boldsymbol{r}) = \eta_0 \boldsymbol{L}_{k_0}(\boldsymbol{J};\partial\Omega)(\boldsymbol{r}) \quad \boldsymbol{r}\in\Omega_{ext}, \tag{1}$$

$$\boldsymbol{H}^s(\boldsymbol{J};\partial\Omega)(\boldsymbol{r}) = K_{k_0}(\boldsymbol{J};\partial\Omega)(\boldsymbol{r}) \quad \boldsymbol{r}\in\Omega_{ext}, \tag{2}$$

where η_0 is the free space intrinsic impedance and k_0 is the free space wave number. $\boldsymbol{J}$ is electric current on the surface $\partial\Omega$. The Electric Field Integral Operator (EFIO) and Magnetic Field Integral Operator (MFIO) are denoted by L and K as follows:

$$\begin{aligned} L_{k_0}\left(\boldsymbol{X}(\boldsymbol{r}');\partial\Omega\right)(r) &= ik_0\int_{\partial\Omega}\boldsymbol{X}(\boldsymbol{r}')G(\boldsymbol{r},\boldsymbol{r}';k_0)d\boldsymbol{r}' \\ &\quad + \frac{i}{k_0}\int_{\partial\Omega}\left(\nabla'\bullet\boldsymbol{X}(\boldsymbol{r}')\right)\nabla G(\boldsymbol{r},\boldsymbol{r}';k_0)d\boldsymbol{r}' \\ K_{k_0}\left(\boldsymbol{X}(\boldsymbol{r}');\partial\Omega\right)(r) &= \int_{\partial\Omega}\nabla G(\boldsymbol{r},\boldsymbol{r}';k_0)\times\boldsymbol{X}(\boldsymbol{r}')d\boldsymbol{r}', \end{aligned} \tag{3}$$

$G(\boldsymbol{r},\boldsymbol{r}';k_0) = \dfrac{\exp(ik_0|\boldsymbol{r}-\boldsymbol{r}'|)}{4\pi|\boldsymbol{r}-\boldsymbol{r}'|}$ is the Green's function in free space.

Here, the following tangential trace and twisted tangential trace operators will be used [9,10]:

$$\pi_\tau(v_m) := \hat{\boldsymbol{n}}_m\times\left(\boldsymbol{v}_m\times\hat{\boldsymbol{n}}_m\right)\big|_{\partial\Omega_m} \quad \gamma_\tau(v_m) := \hat{\boldsymbol{n}}_m\times\boldsymbol{v}_m\big|_{\partial\Omega_m}. \tag{4}$$

So Eq. (1), (2) can be rewritten:

$$\boldsymbol{e}^s(\boldsymbol{j};\partial\Omega)(\boldsymbol{r}) = \pi_\tau\boldsymbol{L}_{k_0}(\boldsymbol{j};\partial\Omega)(\boldsymbol{r}) \quad \boldsymbol{r}\in\partial\Omega, \tag{5}$$

$$\boldsymbol{j}^s(\boldsymbol{j};\partial\Omega)(\boldsymbol{r}) = \frac{1}{2}\boldsymbol{j} + \gamma_\tau\bar{K}_{k_0}(\boldsymbol{j};\partial\Omega)(\boldsymbol{r}) \quad \boldsymbol{r}\in\partial\Omega, \tag{6}$$

where $\bar{K}$ stands for the principle value of K.

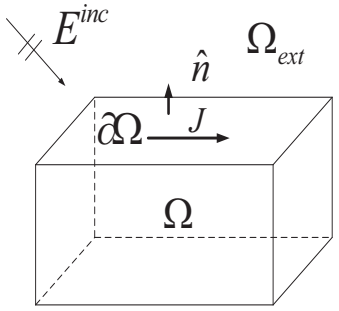

Fig. 1. EM wave scatting by PEC.

B. Decomposed combined field integral equations

The current integral equation based on domain decomposition method begins by partitioning the original problem domain into N non-overlapping sub-domains:

$$\Omega = \bigcup_{i=1,N}\Omega_i,\ \Omega_i\bigcap\Omega_j = \varnothing,\ \ 1\le i\ne j\le N. \tag{7}$$

Denote the boundary of Ω_i as $\partial\Omega_i$, the touching face Γ_{ij} is defined as $\Gamma_{ij} = \partial\Omega_i\bigcap\partial\Omega_j$. Obviously, $\Gamma_{ij} = \Gamma_{ji}$; however, here we still make an artificial distinction in order to the possibility of differing triangulations on either side of the touching face. Γ_{ij} is used when Ω_i is the "master" sub-domain and Γ_{ji} if the converse is true. Moreover, the boundary $\partial\Omega_i$ contains two parts $\partial\Omega_i = \partial\widehat{\Omega}_i\bigcup\Gamma_{ij}, \partial\widehat{\Omega}_i = \partial\Omega_i/\Gamma_{ij}$. The reason we do so is due to the fact that the touching face meshes on Γ_{ij} and Γ_{ji} are allowed to be non-matching grids (non-conformal). For the sake of simplicity and without loss of generality, here we consider

only the case of $N=2$, as shown in Fig. 2. Subsequently, the well-known Combined Field Integral Equation (CFIE) governing the electric and magnetic fields on the PEC surface $\partial\Omega_1$ and $\partial\Omega_2$, is written as follows, respectively:

$$(1-\alpha)\boldsymbol{j}_i(\boldsymbol{r})-\alpha\boldsymbol{e}_i^s(\boldsymbol{r})-(1-\alpha)\boldsymbol{j}_i^s(\boldsymbol{r}) = \alpha\boldsymbol{e}_i^{INC}(\boldsymbol{r})+(1-\alpha)\boldsymbol{j}_i^{INC}(\boldsymbol{r}) \quad (i=1,2), \tag{8}$$

where $\boldsymbol{j}_i^{INC}(\boldsymbol{r})=\eta_0\gamma_\tau\left(H_i^{INC}(\bar{r})\right), \boldsymbol{e}_i^{INC}(\boldsymbol{r})=\pi_\tau\left(E_i^{INC}(\bar{r})\right)$ and α is the factor of CFIE.

Taking the sub-domain Ω_1 for example, note that the incident field on the $\partial\Omega_1$ can be written as follows:

$$\boldsymbol{e}_1^{INC}(\boldsymbol{r})=\boldsymbol{e}_1^{inc}(\boldsymbol{r})+\boldsymbol{e}_2^s(\boldsymbol{r}) \qquad \boldsymbol{r}\in\partial\Omega_1, \tag{9}$$

$$\boldsymbol{j}_1^{INC}(\boldsymbol{r})=\boldsymbol{j}_1^{inc}(\boldsymbol{r})+\boldsymbol{j}_2^s(\boldsymbol{r}) \qquad \boldsymbol{r}\in\partial\Omega_1. \tag{10}$$

The first term in Eq. (9-10) stands for the primary incident field, the second term stands for the scattering field excited by the sources on the $\partial\Omega_2$. Straightforwardly, the combining of (8), (9) and (10) results in the CFIE solver for the decomposed problem.

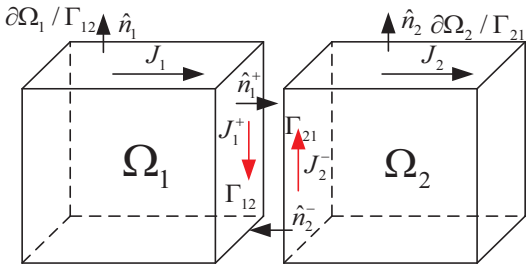

Fig. 2. Non-overlapping IE-DDM scheme: 2 sub-domains.

C. Transmission conditions

The decomposed problem will not be equivalent to the original entire domain problem unless proper transmission conditions are observed for every sub-domain touching face Γ_{ij}. Obviously, the transmission condition $\boldsymbol{J}_1^+=-\boldsymbol{J}_2^-$ should be satisfied on the touching faces. So the following Robin transmission condition on Γ_{12}, Γ_{21} are used [10]:

$$\alpha\boldsymbol{e}_1^{INC}(\boldsymbol{r})\big|_{\Gamma_{12}}+(1-\alpha)\boldsymbol{j}_1^{INC}(\boldsymbol{r})\big|_{\Gamma_{12}} = -\alpha\boldsymbol{e}_1^s(\boldsymbol{r})\big|_{\Gamma_{12}}-(1-\alpha)\boldsymbol{j}_2^-(\boldsymbol{r})\big|_{\Gamma_{21}}-(1-\alpha)\boldsymbol{j}_1^s(\boldsymbol{r})\big|_{\Gamma_{12}}, \tag{11}$$

$$\alpha\boldsymbol{e}_2^{INC}(\boldsymbol{r})\big|_{\Gamma_{21}}+(1-\alpha)\boldsymbol{j}_2^{INC}(\boldsymbol{r})\big|_{\Gamma_{21}} = -\alpha\boldsymbol{e}_2^s(\boldsymbol{r})\big|_{\Gamma_{21}}-(1-\alpha)\boldsymbol{j}_1^+(\boldsymbol{r})\big|_{\Gamma_{12}}-(1-\alpha)\boldsymbol{j}_2^s(\boldsymbol{r})\big|_{\Gamma_{21}}. \tag{12}$$

To expand the surface current in each sub-domain, traditional RWG basis function [11] is used. To assure the current continuity across corner edges, a corner edge based RWG basis function is defined for corner edge current. It not only avoids the introducing of half RWG basis function, but keeps exactly the same formulation of the CFIE matrix with the one of single sub-domain. A demonstrative figure is shown in Fig. 3.

Considering the coefficient vector $\boldsymbol{x}_i=\left[\boldsymbol{x}_i^e \quad \boldsymbol{x}_i^c \quad \boldsymbol{x}_i^t\right]^T$, stands for the coefficients of the RWG basis function for current on exterior surface, on the corner edge and on the touching face respectively.

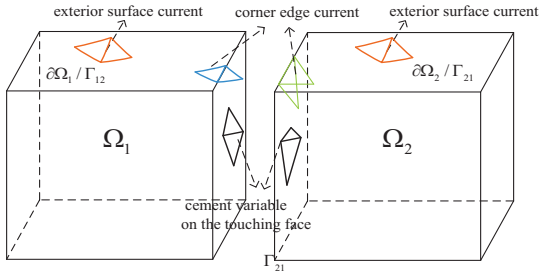

Fig. 3. Three kinds of RWG basis functions for expanding the current on exterior surface, on the corner edge and on the touching face in the IE-DDM.

Based on Galerkin testing, we yield the matrix equation of IE-DDM as follows:

$$\begin{bmatrix}\boldsymbol{A}_1 & 0\\ 0 & \boldsymbol{A}_2\end{bmatrix}\begin{bmatrix}\boldsymbol{x}_1\\ \boldsymbol{x}_2\end{bmatrix}=\begin{bmatrix}\boldsymbol{b}_1\\ \boldsymbol{b}_2\end{bmatrix} + \begin{bmatrix}\boldsymbol{B}_1 & \boldsymbol{C}_{12}\\ \boldsymbol{C}_{21} & \boldsymbol{B}_2\end{bmatrix}\begin{bmatrix}\boldsymbol{x}_1\\ \boldsymbol{x}_2\end{bmatrix}+\begin{bmatrix}0 & \boldsymbol{D}_{12}\\ \boldsymbol{D}_{21} & 0\end{bmatrix}\begin{bmatrix}\boldsymbol{x}_1\\ \boldsymbol{x}_2\end{bmatrix}, \tag{13}$$

where

$$\boldsymbol{A}_i=\begin{bmatrix}\boldsymbol{A}_i^{ee} & \boldsymbol{A}_i^{ec} & \boldsymbol{A}_i^{et}\\ \boldsymbol{A}_i^{ce} & \boldsymbol{A}_i^{cc} & \boldsymbol{A}_i^{ct}\\ \boldsymbol{A}_i^{te} & \boldsymbol{A}_i^{tc} & \boldsymbol{A}_i^{tt}\end{bmatrix}, \boldsymbol{B}_i=\begin{bmatrix}0 & 0 & 0\\ \boldsymbol{B}_i^{ce} & \boldsymbol{B}_i^{cc} & \boldsymbol{B}_i^{ct}\\ \boldsymbol{B}_i^{te} & \boldsymbol{B}_i^{tc} & \boldsymbol{B}_i^{tt}\end{bmatrix},$$

$$\boldsymbol{C}_{ij}=\begin{bmatrix}\boldsymbol{C}_{ij}^{ee} & \boldsymbol{C}_{ij}^{ec} & \boldsymbol{C}_{ij}^{et}\\ \boldsymbol{C}_{ij}^{ce} & \boldsymbol{C}_{ij}^{cc} & \boldsymbol{C}_{ij}^{ct}\\ 0 & 0 & 0\end{bmatrix}, \boldsymbol{D}_{ij}=\begin{bmatrix}0 & 0 & 0\\ 0 & 0 & 0\\ 0 & \boldsymbol{D}_{ij}^{tc} & \boldsymbol{D}_{ij}^{tt}\end{bmatrix}, \text{ and}$$

$1\le i\ne j\le 2$.

It is worth to note that two triangles of RWG basis function related to corner edges locate on different surfaces; i.e., exterior surface and touching face. So, different boundary conditions are used in corresponding triangle for this special RWG basis function. The matrix blocks $\boldsymbol{A}_i$ forms the usual Combined Field Integral Equation (CFIE) matrix for sub-domain Ω_i. The sub-matrix $\boldsymbol{B}_i$ denotes the self-impedance matrix of each sub-domain, the sub-matrix $\boldsymbol{C}_{ij}$ denotes mutual impedance matrix between two sub-domains, while the sub-matrix $\boldsymbol{D}_{ij}$ is sparse motar matrix.

III. GAUSS-SEIDEL ITERATION TECHNIQUE

For solution of Eq. (13), two iterative processes are needed: the inner iterative process and the outer iterative process. For the inner iterative process, GMRES iterative technique is used. For the outer iterative process, Gauss-Seidel iterative technique is used instead of Jacobi iteration technique in this paper; which updates the currents on each sub-domain in real time. The Gauss-Seidel iteration procedure is given as follows:

Step 1: Initialization

The currents in all N sub-domains are initialized to 0, starting the outer iteration, $k=1$.

Step 2: Iterative solution of sub-domains

For $i=1,2,...,N$ (N is the number of sub-domains):

a) The Eq. (13) is solved via GMRES iterative solver in each sub-domain;
b) Updating the current in sub-domain in real time once it has been solved.

Step 3: Error computation and convergence evaluation

Computing the maximal relative residual error, $\text{error\_max}(k)$, for N sub-domains. If the error achieves the desired threshold, the outer iteration process is over. Otherwise, $k=k+1$; return to Step 2, continue the iteration process.

The maximal relative residual error of current at the k-th outer iteration is defined as:

$$\text{error\_max}(k)=\max_i \frac{\left\|\boldsymbol{I}_i^k-\boldsymbol{I}_i^{k-1}\right\|}{\left\|\boldsymbol{I}_i^k\right\|}. \qquad (14)$$

$\boldsymbol{I}_i^k$ denotes the currents on the i-th sub-domain at the k-th outer iteration. $\|\ \|$ denotes the 2-norm of the complex vector.

IV. HYBRID LOCAL/GLOBAL MLFMA FRAMEWORK

For the problem of BoT, the computational original domain can be partitioned into several same sub-domains, as shown in Fig. 4. Because for each sub-domain, the self-coupling is the same, the self-impedance matrix in each sub-domain can be implemented only once. Here, hybrid local/global MLFMA framework is developed: local MLFMA is used to reduce the time of matrix filling and matrix-vector multiplication in each sub-domain, global MLFMA is used to accelerate the computation of coupling between sub-domains.

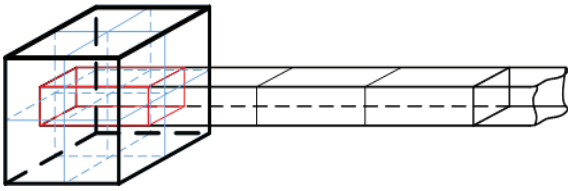

Fig. 4. Hybrid local/global MLFMA framework for BoT: each sub-domain is same.

From Eq. (13), we can see that there are three kinds of matrix blocks $\boldsymbol{A}$, $\boldsymbol{B}$, $\boldsymbol{C}$. For matrix $\boldsymbol{A}$, we can implement the matrix-vector multiplication of $\boldsymbol{A}\bullet x$; by local MLFMA, it is the same with traditional MLFMA because matrix $\boldsymbol{A}$ is exactly the same with traditional impedance matrix of sub-domain divided. For matrix $\boldsymbol{B}$, $\boldsymbol{C}$ are for specific sources and observation points, different from traditional case in which the sources distribution is identical with the observation points distribution.

To implement the MLFMA, the object is enclosed by a large cube which is partitioned into eight children cubes, every sub-cube is then recursively subdivided into smaller cubes until the edge length of the finest cube is about 0.3 wavelength. Further non-empty cubes are recorded using tree-structured data at all levels.

The representation of matrix-vector multiplication using MLFMA is often written as:

$$A\bullet x=A_{near}\bullet x+U^t\bullet T\bullet V\bullet x. \qquad (15)$$

The matrix A_{near} represents the interaction matrix from nearby region which is computed by

the MoM. V,T,U^t is aggregation, translation, disaggregation matrix respectively; they represent three processes of interaction between non-nearby regions. The details can be referred to references [4,12].

V. NUMERICAL RESULTS

This section validates the accuracy and demonstrates the efficiency through some numerical examples. To validate the accuracy of IE-DDM code developed here, two examples A1-A2 are given first. The examples B1-B3 are used to show the ability of the present method for the BoT.

A1. EM scattering from a PEC sphere

Bistatic RCS of a PEC sphere of radius R=3 m excited by a θ polarized plane wave incident from -z direction is computed. The frequency is f=300 MHz. The sphere is partitioned into two closed hemispheres. The conventional MLFMA and MIE method are used for comparisons. The number of unknowns by the MLFMA and IE-DDM-MLFMA is 49,531 and 55,401 respectively.

The RCS results by the MIE method and IE-DDM-MLFMA are shown in Fig. 5. A good agreement between the result by the IE-DDM-MLFMA and the one by MIE method is confirmed. Figure 6 shows the current distribution using the conventional MLFMA and IE-DDM-MLFMA respectively. They agree well with each other. In addition, the electric currents across the touching face between two neighbouring sub-domains are normal continuous.

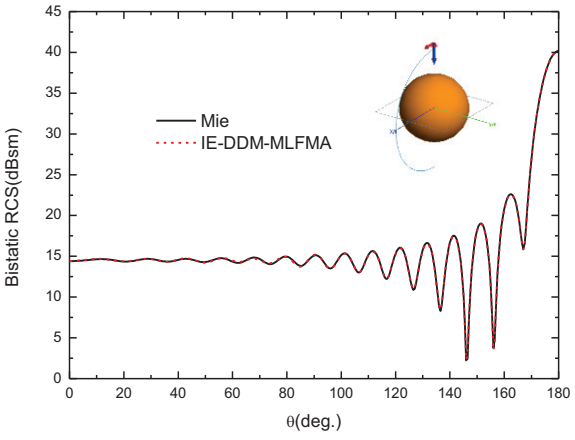

Fig. 5. Bistatic RCS of PEC sphere.

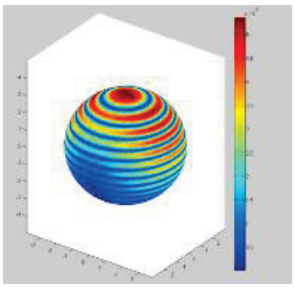

(a)

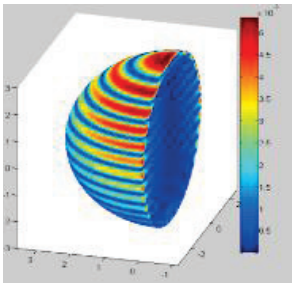

(b)

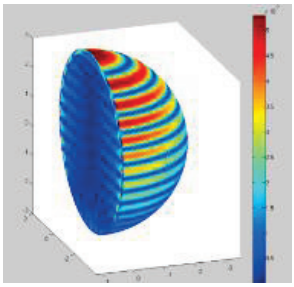

(c)

Fig. 6. (a) Current distribution of PEC sphere using conventional MLFMA, and (b), (c) current distribution of 2 sub-domains using IE-DDM-MLFMA.

A2. Simplified helicopter model

The second example we consider is a simplified helicopter model with length of 4.5 m. The entire model is divided into 8 closed-surface regions and different color denotes different regions, as depicted in Fig. 7. The frequency of the incident plane wave $(\theta_i = 90°, \varphi_i = 0°)$ is 3.0 GHz. Each region is meshed independently according to its geometry complexity. Due to the non-conformal feature of the IE-DDM, each sub-region can be meshed with good quality, which results in 461,667 totally. The bistatic RCS results with horizontal polarization in the $z-x$ plane are plotted in Fig. 8 (a), together with the MLFMA solutions. It is found that good agreements are obtained. In addition, IE-DDM converges to relative residual error of 10^{-2} with 7 outer iterations.

The bistatic RCS results by the MLFMA and the IE-DDM-MLFMA are shown in Fig. 8 (a), a very good agreement is achieved. The current distribution of Helicopter is also given in Fig. 8 (b).

The above two examples have validated the ability of the IE-DDM-MLFMA. In the following

parts, the examples B1-B3 are used to demonstrate the performance of the present method for BoT.

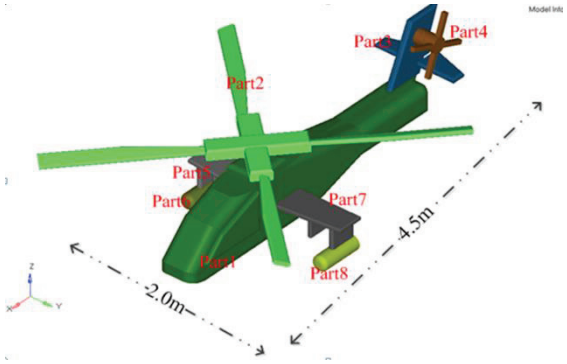

Fig. 7. Geometry model of simplified helicopter: 8 sub-domains.

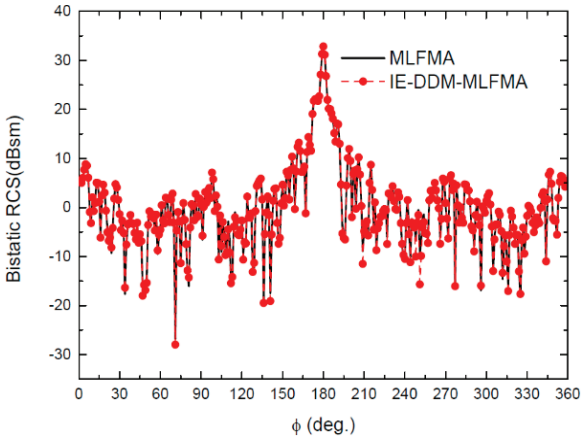

(a)

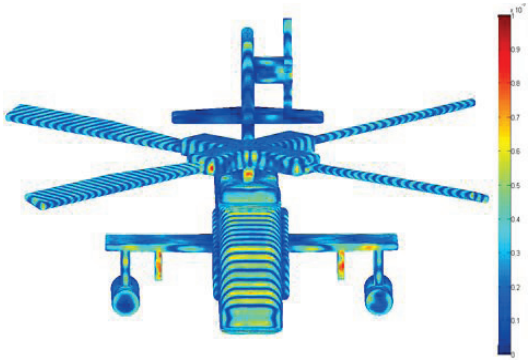

(b)

Fig. 8. (a) RCS of the helicopter model, and (b) current distribution of helicopter at 3 GHz.

B1. EM scattering from a PEC cylinder

A PEC cylinder of radius R=0.5 m and height H=1 m is excited by a plane wave incident from -z direction. The frequency is f=0.3 GHz. The cylinder is partitioned into two closed same sub-domains. The number of unknowns by the CFIE and IE-DDM is 1,928 and 2,352 respectively. A comparison of bistatic RCS computed using the IE-DDM solver and conventional CFIE is shown in Fig. 9 (a), a very good agreement is observed. A comparison of convergence using IE-DDM with Jacobi iteration and with Gauss-Seidel iteration is also shown in Fig. 9 (b). Obviously, Gauss-Seidel iteration has better convergence than Jacobi iteration due to it updating the currents in each sub-domain in real time.

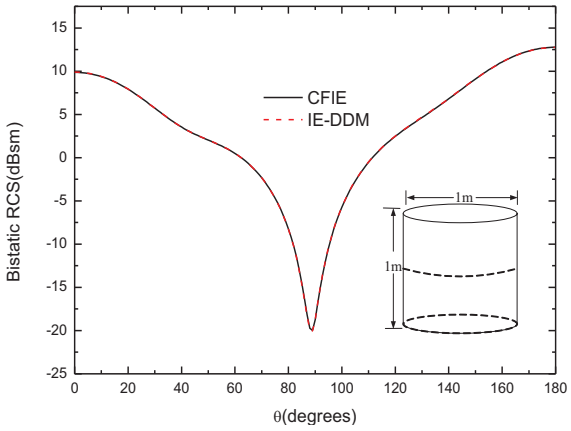

(a)

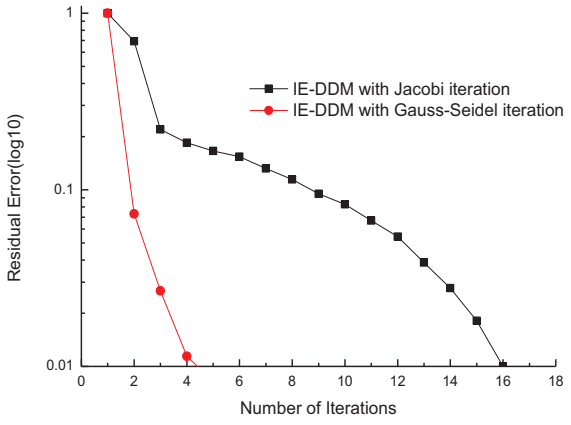

(b)

Fig. 9. (a) Bistatic RCS for PEC cylinder, and (b) the convergence history with Jacobi iteration and Gauss-Seidel iteration.

B2. Large PEC square cylinder

The scattering of a large PEC square cylinder is investigated. The frequency is 300 MHz. It is divided into 4 same sub-domains along long axial

direction. The number of unknowns by the MLFMA and IE-DDM-MLFMA is 386,400, 393,600 respectively. The incident wave, is polarized in the θ direction, with the incident angles $\theta^i = 90^\circ$ and $\varphi^i = 0^\circ$. The bistatic RCS at $\theta^s = [0^\circ, 180^\circ]$ and $\varphi^s = 0^\circ$ is shown in Fig. 10. In addition, the computational statistics on the MLFMA and IE-DDM-MLFMA is also listed in Table 1. The filling time for impedance matrix by the MLFMA and IE-DDM-BoT is 4,669, 1,290 seconds respectively. For this large PEC square cylinder, only 5 outer iterations are required to achieve the convergence threshold of 0.01. The total solution time by the MLFMA is 10,127 seconds, but the one by IE-DDM-BoT is only 5,941 seconds.

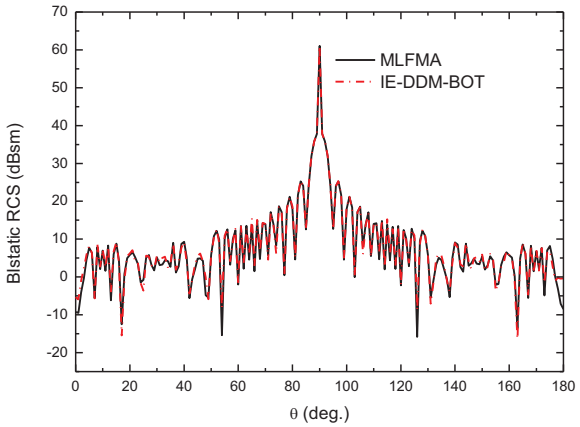

Fig. 10. Bistatic RCS for PEC square cylinder: four same sub-domains divided.

Table 1: The computational statistics using IE-DDM-MLFMA and MLFMA for large PEC square cylinder

Methods	Unknowns	Time For Filling Zmn(near) (s)	Total Solution Time (s)	Memory (MB)	Niter
MLFMA	386,400	4,669	10,127	2,032	29
IE-DDM-BoT	393,600	1,290	5,941	1,130	5

Although the IE-DDM-BoT requires more unknowns compared with the MLFMA, it reduces total CPU time and storage requirement greatly, as shown in Table 1. This is because only a few outer iterations are required by the IE-DDM-BoT, and hybrid local/global MLFMA framework can attain efficient matrix-vector multiplication in sub-domains and between sub-domains based on the feature of translational invariance of BoT.

B3. Stability investigation of IE-DDM in case of many sub-domains

Here, we use IE-DDM-MLFMA with 10, 20, 30 same sub-domains to solve three PEC circular cylinders with length of 10 m, 20 m, 30 m respectively, in order to investigate the stability of the IE-DDM-MLFMA when dividing many sub-domains. The size of sub-domain is fixed as length of 1.0 m, radius of 1.0 m. The frequency is 300 MHz. The number of unknowns by the IE-DDM-MLFMA with 10, 20, 30 sub-domains is 40,122, 83,664, and 119,814 respectively. Bistatic RCS in horizontal polarization is computed. The convergence history of IE-DDM-MLFMA for cylinders with 10, 20, 30 sub-domains is shown in Fig. 11. From Fig. 11, it is shown that the IE-DDM-MLFMA has a good convergence even for the case of 30 sub-domains.

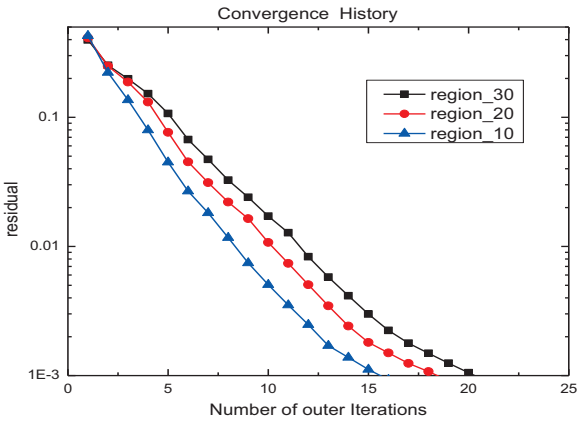

Fig. 11. The convergence history of IE-DDM-MLFMA for PEC cylinders, 10, 20, 30 same sub-domains divided.

The result of PEC cylinder with length of 20 m and radius of 1 m when dividing 20 sub-domains is shown in Fig. 12. Bistatic RCS in horizontal polarization is computed. A good agreement

between the results by the IE-DDM-MLFMA and the one by the MLFMA is also achieved, from Fig. 12. This example shows the present method using many sub-domains can still attain stable and accurate solution of large BoT.

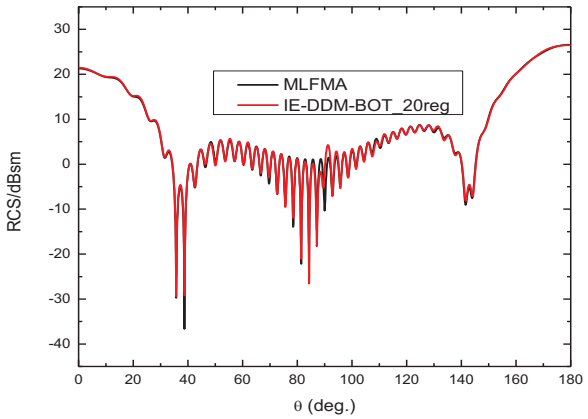

Fig. 12. Bistatic RCS for cylinder by IE-DDM-MLFMA, 20 same sub-domains divided.

VI. CONCLUSIONS

In this paper, hybrid IE-DDM-MLFMA with Gaussian-Seidel iterative technique is proposed for fast solution of PEC BoT. By updating the current in sub-domains in real time, fast convergence of outer iterations is realized.

A hybrid local/global MLFMA framework is developed for efficient implementation of fast matrix-vector multiplication in and between sub-domains. By utilizing the feature of translational invariance of BoT, the self-impedance matrix in each sub-domain is calculated only once. Compared with the traditional MLFMA, the main advantage of the present method is a reduction in storage requirements and solving time. Numerical results prove the present method is very efficient for scattering from PEC BoT.

ACKNOWLEDGMENT

Thanks to National Excellent Youth Foundation (NSFC No. 6142500243) and NSFC under Grant 61271033, the Programme of Introducing Talents of Discipline to Universities under Grant b07046.

REFERENCES

[1] L. N. Medgyesi-Mitschang and J. M. Putnam, "Scattering from finite bodies of translation: plates, curved surfaces, and noncircular cylinders," *IEEE Tran. Antennas Propagat*., vol. AP-31, no. 6, pp. 847-852, November 1983.

[2] G. Davis, "Electromagnetic calculations for large bodies of translation," *IEEE International Symposium on Antennas and Propagation*, June 18-23, 1995.

[3] L. N. Medgyesi-Mitschg and J. M. Putnam, "Formulation for wire radiators on bodies of translation with and without end caps," *IEEE Trans, Antennas Propagat*., vol. AP-31, no. 6, pp. 853-862, November 1983.

[4] J. M. Song, C. C. Lu, and W. C. Chew, "Multilevel fast multipole algorithm for electromagnetic scattering by large complex objects," *IEEE Trans. Antennas Propagat*., vol. 45, no. 10, pp. 1488-1493, October 1997.

[5] R. Xi, H. Jun, and N. Z. Ping, "Solving scattering from multiple conducting objects by hybrid multi-level fast multipole algorithm with generalized forward-and-backward method," *Electromagnetics*, 28:572-581, 2008.

[6] Z. Peng, X. C. Wang, and J. F. Lee, "Integral equation based domain decomposition method for solving electromagnetic wave scattering from non-penetrable objects," *IEEE Trans. Antenna Propagat*., vol. 59, no. 9, pp. 3328 -3338, September 2011.

[7] L. N. Medgyesi-Mitschang, J. M. Putnam, and M. B. Gedera, "Generalized method of moments for three-dimensional penetrable scatterers," *J. Opt. Soc. Am. A*, vol. 11, 1383-1398, April 1994.

[8] B. M. Kolundzija, "Electromagnetic modelling of composite metallic and dielectric structures," *IEEE Trans. on Microwave Theory and Techniques*, vol. 47, no. 7, 1021-1032, July 1999.

[9] X. Claeys and R. Hiptmair, ''Electromagnetic scattering at composite objects: a novel multi-trace boundary integral formulation,'' *ETH Zurich*, *Tech. Rep. 2011/58, Seminar for Applied Mathematics*, Zurich, Switzerland, 2011.

[10] Z. Peng, K. H. Lee, and J. F. Lee, ''Computations of electromagnetic wave scattering from penetrable composite targets using a surface integral equation method with multiple traces,'' *IEEE Trans. Antennas Propag*., vol. 61, no. 1, pp. 256-169, January 2013.

[11] S. M. Rao, D. R. Wilton, and A. W. Glisson, "Electromagnetic scattering by surfaces of arbitrary shape," *IEEE Trans. Antennas Propag*., vol. AP-30, pp. 409-418, May 1982.

[12] H. Jun, N. Zai-ping, et al., "Multilevel fast multipole algorithm for solving scattering from 3-D electrically large object," *Chinese Journal of Radio Science*, pp. 509-514, May 2004.

Jiang Ming was born in Anhui, China, in 1985. He received the B.S. degree in Electronic and Information Engineering from Anhui University in 2009. He is presently working on his Ph.D. degree in Electromagnetic Field and Microwave Technique with the Department of Microwave Engineering, at the University of Electronic Science and Technology of China (UESTC). His research interests include numerical methods in computational electromagnetic, electromagnetic scattering and radiation.

Jun Hu received the B.S., M.S., and Ph.D. degrees in Electromagnetic Feld and Microwave Technique from the University of Electronic Science and Technology of China (UESTC), Chengdu, in 1995, 1998, and 2000, respectively.

During 2001, he was with the Center of Wireless Communication in the City University of Hong Kong, Kowloon, as a Research Assistant. During March to August in 2010, he was Visiting Scholar in the ElectroScience Laboratory of Department of ECE of the Ohio State University. He was Visiting Professor of City University of Hong Kong during February to March in 2011. He is currently Full Professor with the School of Electronic Engineering of UESTC, IEEE Senior Member, and Member of Applied Computational Electromagnetics Society. He also serves as Chairman of Student Activities Committee in IEEE Cheng du Section, Vice Chairman of IEEE Chengdu AP/EMC Joint Chapter. He is the author or co-author of over 200 technical papers, received 2004 Best Young Scholar Paper prize of Chinese Radio Propagation Society. His doctoral students were awarded Best Student Paper prizes in 2010 IEEE Chengdu Section, at 2011 National Conference on Antenna, at 2011 National Conference on Microwave, at 2012 IEEE International Workshop on Electromagnetics: Applications and Students' Innovation Competition in Chengdu.

His current research interests include integral equation methods in computational electromagnetics, electromagnetic scattering and radiation.

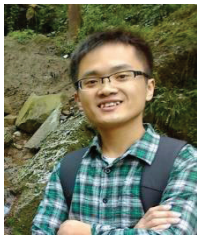

Zhao Ran received the B.S. degree in Electronic and Information Engineering from Anhui University in 2011. Since September 2011, he studied in electromagnetic field and microwave technique with the Department of Microwave Engineering, at the University of Electronic Science and Technology of China (UESTC), Chengdu, China. He is presently working on his Ph.D. degree in the same department.

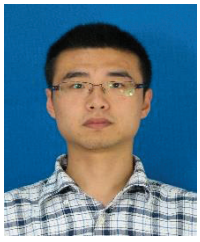

Wei Xiang received the B.E. degree in Biomedical Engineering from the University of Electronic Science and Technology of China (UESTC), Chengdu in 2011. Since September 2011, he studied in electromagnetic field and microwave technique with the Department of Microwave Engineering at UESTC. His research interests include integral equation methods in computational electromagnetics, electromagnetic scattering and radiation.

Zaiping Nie was born in Xi'an, China, in 1946. He received the B.S. degree in Radio Engineering and the M.S. degree in Electromagnetic Field and Microwave Technology from the Chengdu Institute of Radio Engineering (now UESTC: University of Electronic Science and Technology of China), Chengdu, China, in 1968 and 1981, respectively. From 1987 to 1989, he was a Visiting Scholar with the Electromagnetics Laboratory, University of Illinois, Urbana. Currently, he is a Professor with the Department of Microwave Engineering, University of Electronic Science and Technology of China, Chengdu, also IEEE Fellow. He has published more than 300 journal papers. His research interests include antenna theory and techniques, fields and waves in inhomogeneous media, computational electromagnetics, electromagnetic scattering and inverse scattering, new techniques for antenna in mobile communications, transient electromagnetic theory and applications.

An Improved MLPG Method and Application in the Calculation of Electro-Thermal Field of Transmission Line

Bing Gao [1], Fan Yang [1], Minyou Chen [1], Pan Duan [2], Qing-jun Peng [3], and Yongming Yang [1]

[1] State Key Laboratory of Power Transmission Equipment & System Security and New Technology
School of Electrical Engineering, Chongqing University, Chongqing, 400044, China
gaobing.cqu@gmail.com, yangfancqu@gmail.com, mchencqu@126.com

[2] Chongqing Power Company
South Bank Bureau, Chongqing, 404100, China

[3] Postdoctoral Workstation of Yunnan Power Grid Corporation
Kunming, 650217, China

Abstract ― An improved local Petrov-Galerkin method (MLPG) is proposed to solve the general electro-thermal problems in the paper, in which the method to determine the support domain is improved. Two electro-thermal problems are analyzed and solved with the method in the paper, the results indicate that the precision of the final solution is increased. In addition, the electro-thermal field and ampacity of ±800kV ultra high voltage direct current (UHVDC) transmission line are calculated, great accuracy of the solution to the electro-thermal coupling problem is obtained. Results indicate that the maximum and minimum value of surface electric field intensity on each sub-conductor lies on the inner and outer surface, the ampacity of transmission line varies almost linearly with environment temperature inversely.

Index Terms ― Ampacity, bundled conductors, electro-thermal coupling, meshfree method, the local Petrov-Galerkin method, UHVDC.

I. INTRODUCTION

The meshfree method does not require the generation of a mesh for the solution domain, only nodes scattered in the solution domain as well as sets of nodes scattered on the boundaries. It not only overcomes the error caused by interpolation, but also in electromagnetic field, electric parameters can be derived from shape function directly. Owing to these advantages, it has received more and more attention in recent years [1-7,22].

In many fields, such as electric engineering and chemical engineering [8-11], especially for microelectronic device and electrolysis industrial materials often suffer impacts of electro-thermal coupling field. In addition, in power system, electro-thermal characteristic parameter can be an efficient method to design and dialogue [12-13].

The characteristic of device or material strongly depends on temperature which is also affected by electric parameter; in power system, a portion of device breakdown owes to overheat caused by current. Therefore, analysis of the characteristic of device under electro-thermal coupling field is particularly important.

For devices of complex physical model, if finite element method (FEM) is adopted, huge computer cost will be required for accuracy. Due to the superiority of meshfree method, in this paper, an improved MLPG method is adopted to deal with the electro-thermal coupling problems, a generalized support domain method is proposed to get higher accuracy. Then two rectangle domain problems are analyzed to verify the accuracy of this proposed MLPG method. Combing with the harsh climate of western of China, the ampacity of ultra high voltage direct current (UHVDC) transmission line is analyzed, and influence of environment temperature on ampacity is also discussed.

This paper is organized as follows, in Section II, the basic principle of MLPG is briefly

Submitted On: September 4, 2013
Accepted On: October 4, 2014

introduced. The mechanism of generalized support domain is discussed in Section III. The electro-thermal model is proposed in Section IV. In Section V, two numerical experiments are discussed firstly in order to confirm the accuracy of this improved method, then an engineering problem about the ampacity of UHVDC transmission line under extremely climate is analyzed, and Section VI concludes the study.

II. MATHEMATICAL MODEL OF MLPG

A. The MLS approximation scheme

The widely used method for construction of the meshfree shape function of MLS is adopted in this paper. Consider *u(x)* to be function of the field variable defined in the problem domain Ω. The approximation of u(x) is denoted $u^h(\mathrm{x})$:

$$u^h(\mathrm{x}) = \sum_j^m p_j(\mathrm{x}) a_j(\mathrm{x}) \equiv \mathbf{p}^{\mathrm{T}}(\mathbf{x})\mathbf{a}(\mathbf{x}), \tag{1}$$

where *m* is the number of terms of monomials, and **a(x)** is a vector of coefficients given by:

$$\mathbf{a}^{\mathrm{T}}(x) = \{a_0(x)\ a_1(x)\ \cdots\ a_m(x)\}, \tag{2}$$

which are functions of *x*.

In this paper, the square function basis is used for 2D:

$$\mathbf{p}^{\mathrm{T}}(\mathbf{x}) = [1\ x\ y\ x^2\ xy\ y^2]. \tag{3}$$

The basis assures the MLS approximation can reproduce any smooth function and its first derivative with arbitrary accuracy, the coefficient $a_j(\boldsymbol{x})$ can be obtained at the point ***x*** by minimizing a weighted discrete L_2 norm as follows:

$$J = \sum_{I=1}^n w(\mathbf{x}-\mathbf{x}_I)[\mathbf{p}^T(\mathbf{x}_I)\mathbf{a}(\mathbf{x}) - u_I]^2, \tag{4}$$

where *n* is the number of nodes in the neighborhood of ***x*** which weight function $w(\mathbf{x}-\mathbf{x}^I) \geq 0$. The u_I is the value of *u* at $\boldsymbol{x}=\boldsymbol{x}_I$. The neighborhood of ***x*** size is called the domain of influence of ***x***. By applying the difference method, the coefficient of ***a(x)*** we obtain:

$$\mathbf{a}(\mathbf{x}) = \mathbf{A}^{-1}(\mathbf{x})\mathbf{B}(\mathbf{x})\mathbf{U}_s, \tag{5}$$

where the matrices **A(x)**, **B(x)** and $\mathbf{U}_s$ are defined by:

$$\mathbf{A}(\mathbf{x}) = \sum_I^n w(\mathbf{x}-\mathbf{x}_I)\mathbf{p}^T(\mathbf{x}_I)\mathbf{p}(\mathbf{x}_I), \tag{6}$$

$$\mathbf{B}(\mathbf{x}) = [w_1(\mathbf{x}-\mathbf{x}_1)\mathbf{p}(\mathbf{x}_1),\ w_2(\mathbf{x}-\mathbf{x}_2)\mathbf{p}(\mathbf{x}_2), \ldots, w_n(\mathbf{x}-\mathbf{x}_n)\mathbf{p}(\mathbf{x}_n)], \tag{7}$$

$$\mathbf{U}_s = [U_1,\ U_2, \ldots, U_n]. \tag{8}$$

Hence, we have:

$$\begin{aligned} u^h(\mathbf{x}) &= \sum_I^n \sum_j^m p_j(\mathbf{x})(\mathbf{A}^{-1}(\mathbf{x})\mathbf{B}(\mathbf{x}))_{jI} u_I \\ &\equiv \sum_I^n N_I(\mathbf{x}) u_I, \end{aligned} \tag{9}$$

where the shape function is defined by:

$$N_I(\mathbf{x}) = \sum_j^m p_j(\mathbf{x})(\mathbf{A}^{-1}(\mathbf{x})\mathbf{B}(\mathbf{x}))_{jI}. \tag{10}$$

The following weight function is adopted in this paper [2]:

$$w(\mathbf{x}-\mathbf{x}_I) \equiv w(r) = \begin{cases} \frac{2}{3} - 4r^2 + 4r^3 & for\ r \leq \frac{1}{2} \\ \frac{4}{3} - 4r + 4r^2 - \frac{4}{3}r^3 & for\ \frac{1}{2} < r \leq 1 \\ 0 & for\ r > 1 \end{cases}, \tag{11}$$

where $r = d_I / d_{mI}$, $d_I = \|\mathbf{x}-\mathbf{x}_I\|$ and d_{mI} is the size of the domain of influence of the I^{th} node.

B. The MLPG formulation

In this section, the strong form of the steady-state heat conduction equation for two dimensional problem can be described as [8-9]:

$$\lambda \frac{\partial^2 T}{\partial x^2} + \lambda \frac{\partial^2 T}{\partial y^2} = -q_v. \tag{12}$$

The essential and the natural boundary conditions are given by the following equations, respectively:

$$T = \bar{T} \quad \text{on} \quad \Gamma_u, \tag{13a}$$

$$-\frac{\partial T}{\partial \mathbf{n}} = h(T - T_f) \quad \text{on} \quad \Gamma_q, \tag{13b}$$

where the domain is enclosed by $\partial\Omega = \Gamma_u \cup \Gamma_q$; and **n** is the outward normal direction to the boundary.

Instead of writing the global weak form for the above equilibrium equations, the MLPG methods construct the weak-form over local sub-domains such as Ω_S, which is a small region taken for each node inside the global domain. A local weak form of the governing equation (12) and the boundary conditions (13) can be written as:

$$\int_{\Omega_S}(\lambda\frac{\partial^2 T}{\partial x^2}+\lambda\frac{\partial^2 T}{\partial y^2}+q_v)w_I d\Omega$$
$$-\alpha\int_{\Gamma_{su}}(T-T_0)w_I d\Gamma=0. \quad (14)$$

Applying the divergence theorem and boundary on (14) yields:

$$\int_{\Omega_S}(\lambda\frac{\partial w_I}{\partial x}\frac{\partial T}{\partial x}+\lambda\frac{\partial w_I}{\partial y}\frac{\partial T}{\partial y}-q_v w_I)d\Omega+\int_{\Gamma_s}w_I q_n d\Gamma$$
$$=\int_{\Gamma_{sq}}-w_I h(T-T_f)d\Gamma-\alpha\int_{\Gamma su}(T-T_0)w_I d\Gamma, \quad (15)$$

where Γ_{sq} and Γ_{su} are the intersection between local sub-domain with natural boundary and essential boundary, respectively. If a sub-domain is totally inside the global domain and has no intersection between Ω_S, the $\Gamma_s=\partial\Omega_s$.

The weight function w_I used in the MLS approximation is chosen as the test function in the MLPG method. So the test function will vanish on the boundary of the local domain Ω_S and the boundary Γ_s, the equation can be rewritten as:

$$\int_{\Omega_S}(\lambda\frac{\partial w_I}{\partial x}\frac{\partial T}{\partial x}+\lambda\frac{\partial w_I}{\partial y}\frac{\partial T}{\partial y}-q_v w_I)d\Omega=$$
$$\int_{\Gamma_{sq}}-w_I h(T-T_f)d\Gamma-\alpha\int_{\Gamma su}(T-T_0)w_I. \quad (16)$$

By applying the above theory, the value of T can written as:

$$T=\sum_{i=1}^{n}N_i T_i, \quad (17)$$

where N_i represents the shape function, T is node value, and more detailed information can be seen in reference [2].

Thus, the equation (17) can be rewritten as:

$$\mathbf{KT}=\mathbf{F}, \quad (18)$$

where:

$$K_{IJ}=\int_{\Omega_s}\lambda(\frac{\partial w_I}{\partial x}\frac{\partial N_J}{\partial x}+\frac{\partial w_I}{\partial y}\frac{\partial N_J}{\partial y})d\Omega$$
$$+h\int_{\Gamma_{sq}}w_I N_J d\Gamma+a\int_{\Gamma_{su}}w_I N_J d\Gamma \quad (19)$$
$$F_I=\int_{\Gamma_{sq}}w_I h T_f d\Gamma+\int_{\Omega_s}q_v w_I d\Omega+a\int_{\Gamma_{su}}w_I\bar{T}d\Gamma.$$

III. THE PRINCIPLE OF GENERALIZED SUPPORT DOMAIN

The accuracy of MLPG method mainly relies on the shape function which is closely related to supporting domain. The common way to confirm its size is node distance multiplies by a constant, which can be described as [2]:

$$d_s=a_s d_c, \quad (20)$$

where a_s=2.0~3.0.

For regular domain, d_c is the distance between two neighborhood nodes; for irregular domain, d_c is assumed to be average distance and mainly selected by experienced equation and can be solved by:

$$d_c=\frac{\sqrt{A_s}}{\sqrt{n_{As}}-1}, \quad (21)$$

where A_s is the predefined size of supporting domain which needn't to be accurate, nA_s is the included number of nodes in A_s.

However, for inhomogeneous nodes distribution, this method may cause large error, in extremely condition (for 2D problem), when nodes in support domain all lie in x direction or y direction, the basis function can't be calculated [7].

The meshfree method can get high accuracy, if the number of nodes used for interpolation is appropriate, which mainly is about 12~28. Thus, a method to confirm the size of support domain is proposed in this paper, the size of domain can be confirmed by calculating the distance between calculated node and the other nodes. In 2D condition, the principle is as shown in Fig. 1; for particular node, searching about k nodes around it and the size of support domain is the biggest value among distances between these numbered k nodes and the calculated node multiplies a coefficient, which is 1.2~2 and k is 10~18 in this paper. As explained in Fig. 1, the total nodes in support domain and the size are labeled in color.

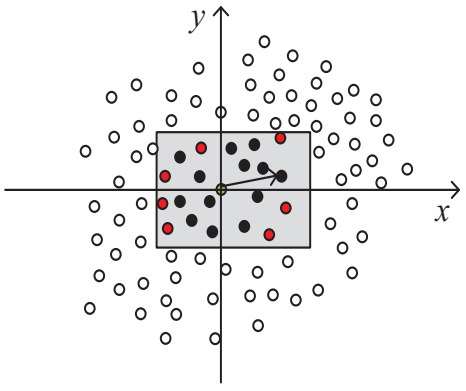

Fig. 1. The schematic diagram of the generalized support domain meshfree method.

IV. ELETRO-THERMAL FIELD MODEL

In power system, the characteristic of device is often affected by more than one field, and these fields also have interaction with each other. The typical one is electro-thermal coupling. The temperature of electric device depends on the losses which can be calculated by solving the following equation [8-9]:

$$-\nabla(\sigma(T)\nabla u) = Q_j, \tag{22}$$

where $\sigma(T)$ is the electrical conductivity, u is the electrostatic potential, Q_j is the current source.

By applying the same theory analysis just shown in the above part, equation (23) can be got:

$$\begin{aligned}&\int_{\Omega_s}(w_i\nabla(\sigma\nabla u)-w_iQ_j)d\Omega\\&=\int_{\Omega_s}w_i\left(\nabla\sigma\nabla u+\rho\nabla^2u\right)d\Omega-\int_{\Omega_s}w_iQ_j)d\Omega\\&=\int_{\Omega_s}w_i\nabla\sigma\nabla u d\Omega+\int_{\Omega_s}w_i\sigma\nabla^2u d\Omega-\int_{\Omega_s}w_iQ_j d\Omega.\end{aligned} \tag{23}$$

The second part equals with:

$$\begin{aligned}&\int_{\Omega_s}w_i\sigma\nabla^2u d\Omega\\&=\int_{\Omega_s}\nabla\left(w_i\sigma\nabla u\right)d\Omega-\int_{\Omega_s}\nabla w_i\left(\sigma\nabla u\right)d\Omega-\int_{\Omega_s}w_i\nabla\sigma\nabla u d\Omega\\&=\int_{\Gamma_i}\left(w_i\sigma\nabla u\right)\mathbf{n}d\Gamma_i-\int_{\Omega_s}\nabla w_i\left(\sigma\nabla u\right)d\Omega-\int_{\Omega_s}w_i\nabla\sigma\nabla u d\Omega.\end{aligned} \tag{24}$$

The local weak form can be written as:

$$\begin{aligned}&\int_{\Omega_s}(w_i\nabla(\sigma\nabla u)-w_iQ_j)d\Omega\\&=\int_{\Gamma_i}\left(w_i\sigma\nabla u\right)\mathbf{n}d\Gamma_i-\int_{\Omega_s}\nabla w_i\left(\sigma\nabla u\right)d\Omega-\int_{\Omega_s}w_iQ_j d\Omega.\end{aligned} \tag{25}$$

If a sub-domain is totally inside the globe domain and has no intersection between Ω_i, the first part is zero; otherwise, using the essential and natural boundary condition and trail functions whose forms are similar with equation (14), just after the same theoretical analysis in Section II, we can obtain:

$$\mathbf{Ku}=\mathbf{f}, \tag{26}$$

where

$$K_{ij}=\int_{\Omega_s}\nabla w_i(\sigma\nabla N_j)d\Omega+\alpha\int_{\Gamma_{su}}w_iN_j d\Gamma, \tag{27a}$$

and

$$f_i=\int_{\Gamma_{sq}}\sigma w_i\bar{q}d\Gamma+\alpha\int_{\Gamma_{su}}w_iu_0 d\Gamma-\int_{\Omega_s}w_iQ_j d\Omega, \tag{27b}$$

where u_0 and $\bar{q}$ are electric parameters for essential and the natural boundary.

Then the Joule heat per unit length in the conductor can be calculated as follows [8-9]:

$$q=\int\frac{JJ^*}{\sigma}dS, \tag{28}$$

where J is the current density.

The losses in a model are dependent on the temperature. The temperature distribution can be obtained by solving the nonlinear electro-thermal coupling model. Solution of this dynamic procedure can be obtained by applying the Newton-Raphson iteration method as shown in Fig. 2 [14].

In order to investigate the accuracy of the improved MLPG method, a relative error is calculated as follows [21]:

$$error=\sqrt{\frac{\sum_{i=1}^{N}(u_i^{fem}-u_i^{num})^2}{\sum_{i=1}^{N}(u_i^{fem})^2}}, \tag{29}$$

where u_i^{num} denotes the numerical solution of the i_{th} node and the u_i^{fem} denotes the FEM solution of the i_{th} node.

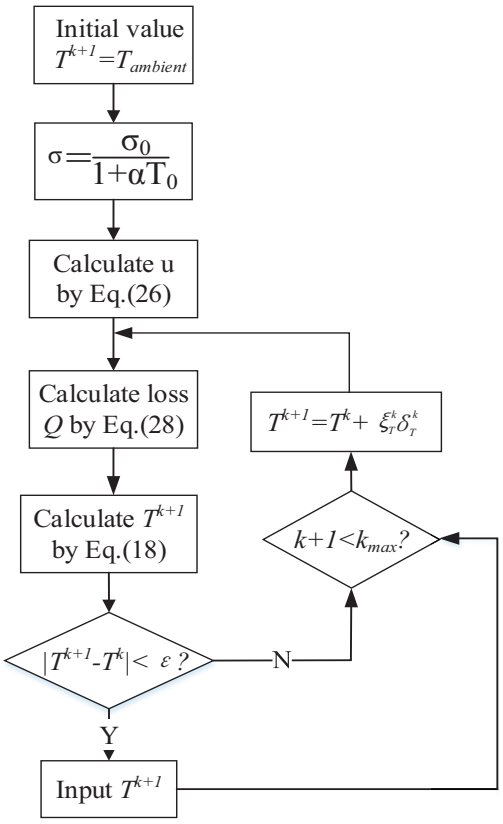

Fig. 2. The flowchart of solving the electro-thermal coupling model.

V. NUMERICAL EXPERIMENTS

In some conditions, such as the breakdown process of cable, the temperature rising is a transient process. Thus, transient electro-thermal coupling case is analyzed.

For this condition, the equation (12) can be written as [8-9]:

$$\rho c \frac{\partial T}{\partial t} = \lambda \frac{\partial^2 T}{\partial x^2} + \lambda \frac{\partial^2 T}{\partial y^2} + q_v, \tag{30}$$

where ρ is the material density; c is the specific heat capacity.

According to the derivation principle as described in Section II, the final equation is written as follows:

$$\mathbf{C}\dot{\mathbf{T}} + \mathbf{K}\mathbf{T} = \mathbf{F}, \tag{31}$$

$$\{[K] + \frac{[C]}{\Delta t}\}\{T\}_t = \{f\}_t + \frac{[C]}{\Delta t}\{T\}_{t-\Delta t}, \tag{32}$$

where $C_{ij} = \int_{\Omega_s} w(x, x_i)\rho c N_j(x) d\Omega$.

A problem domain as shown in Fig. 3 is illustrated.

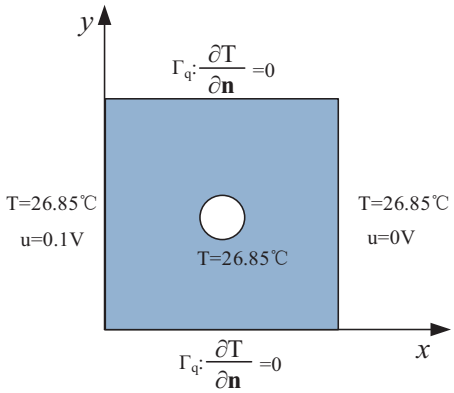

Fig. 3. The transient analysis model.

The parameter of k is set as 12, and the local quadrature domain with four subdivision cells and 4×4 integration points in each cell. The time step is set 0.05s. Both temperature distribution at t=1s and y=0.5 are analyzed, just as shown in Figs. 4 and 5.

The relative error is 0.203%, which is less than 1%, and results from Fig. 4 to Fig. 5 show very good accuracy between the improved MLPG method and FEM method; it indicates that this improved method can deal with complex problem domain well.

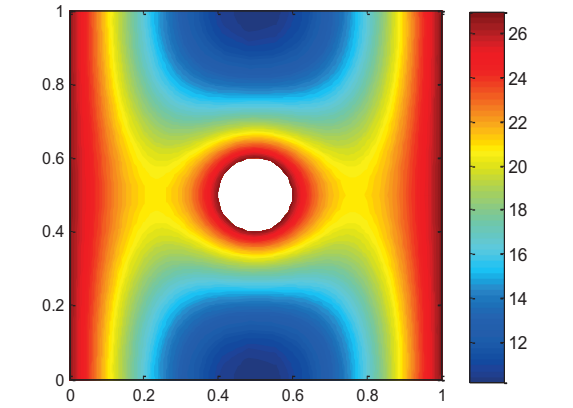

(a) Temperature distribution at t=1 of MPLG method

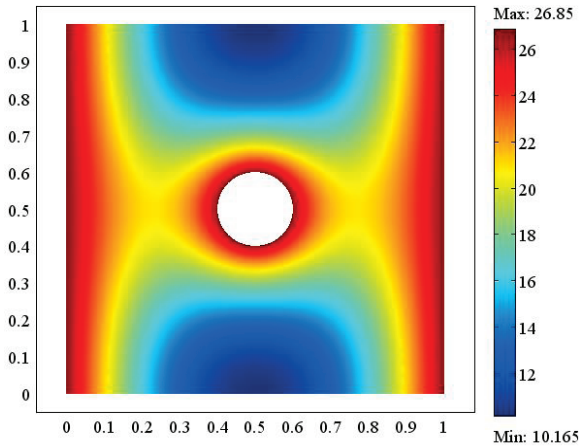

(b) Temperature distribution at t=1 of FEM method

Fig. 4. Comparisons between: (a) improved MLPG method results, and (b) FEM results.

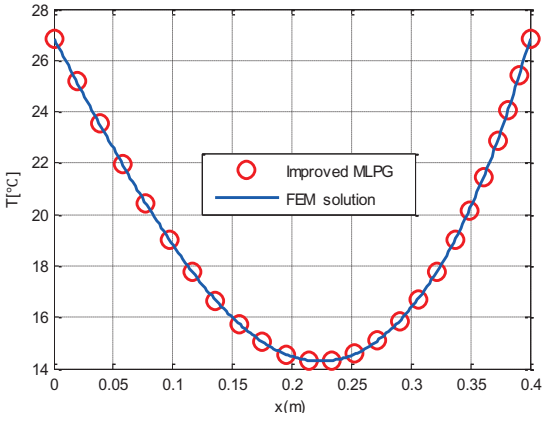

Fig. 5. Comparison between improved MLPG and FEM method along y=0.5 at t=0.5s.

In this section, a steady rectangle domain as described in Fig. 6, was first discussed.

The parameter of k is set as 12, and the local quadrature domain with four subdivision cells and 4×4 integration points in each cell. The comparison between improved MLPG method results and finite element method (FEM) results is shown in Fig. 7.

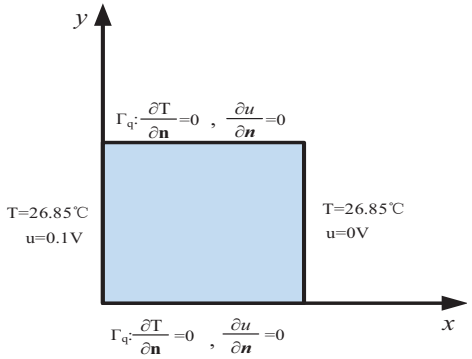

Fig. 6. The rectangle problem domain.

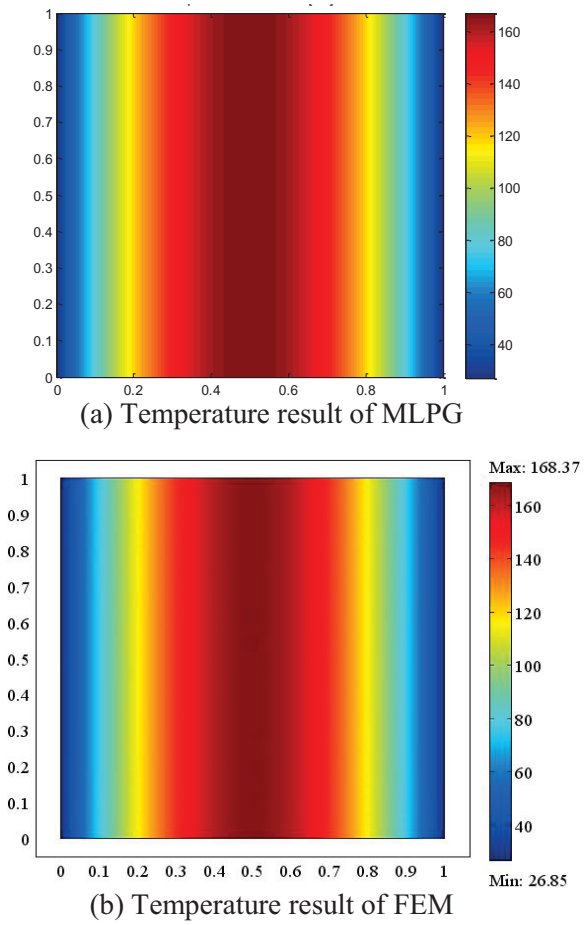

(a) Temperature result of MLPG

(b) Temperature result of FEM

Fig. 7. Comparisons between: (a) improved MLPG method results, and (b) FEM results.

The relative error between improved MLPG and FEM method is about 0.117%. We can observe good agreement between the improved MLPG results and FEM results both for electric and temperature distribution from Figs. 8 and 9. And, we can conclude that the improved MLPG method has a great accuracy. In addition, this method can be more accurate if more nodes are used in the calculation.

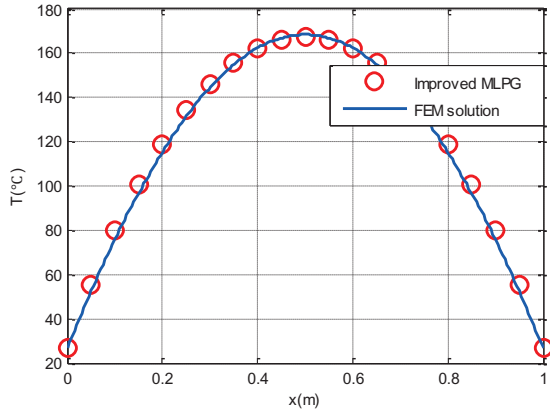

Fig. 8. Comparison between improved MLPG and FEM method along y=0.5.

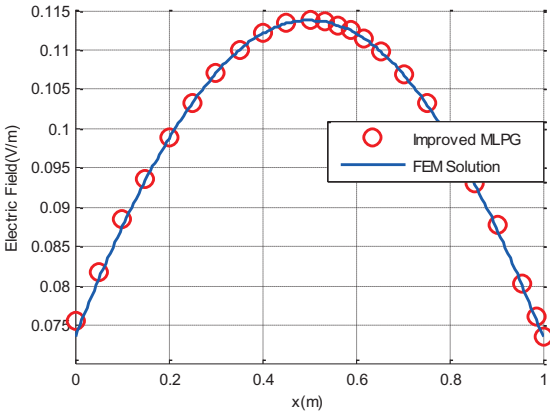

Fig. 9. Comparison along y=0.5 of the electric field.

Based on the analysis discussed in this section, a conclusion can be made that the improved MLPG method can deal with electro-thermal coupling problems well. Then, an engineering problem about the ampacity of ultra high voltage direct current (UHVDC) transmission line which will be built in the western of China where it suffers harsh climate is analyzed; then influence of environment temperature on its ampacity is also discussed.

According to the standard of China,

temperature of aluminium cable steel reinforced cannot exceed 70℃ [15-19]. However, the climate of western of China is harsh, especially for Chongqing city where the outer environment temperature can be over 40℃ in summer; in addition, with highly electrical consumption at the same time, causing serous heating. Therefore, we should make the most use of the capacity of transmission line under safety permission. Effect of wind is not taken into account because of low wind speed in this city. As the length in the axis direction is much longer than that of radial direction, in addition, the impact of sag is ignored, then the line can be regarded as limitless long. Therefore, the electro-thermal distribution can be presented by 2D situation.

As shown in Fig. 10, the main line used is 6 split conductor. Impact of sunshine is assumed as a heat flux into the domain. In order to get higher accuracy, nodes around the sub-conductors is intensive, while in other parts is coarse.

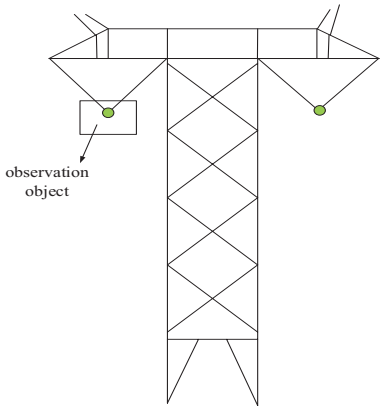

(a) Width of right way

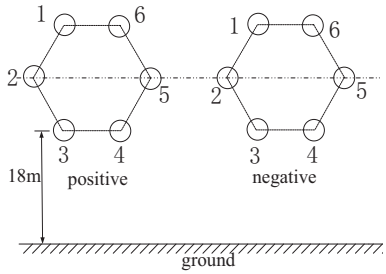

(b) Detailed explanation of observation object in (a)

Fig. 10. Schematic diagram of UHVDC transmission lines.

Because the transmission line is two-orders lower than that of the total domain, thus, an observation plane is chosen to analyze the electric and thermal characteristics. The temperature and electric field intensity distribution are shown in Fig. 11 and Fig. 12, respectively.

It can be seen that the highest temperature lies on the transmission line, because the lines are heat source. The temperature of the space surrounded by sub-conductors is higher than that of outer space, this is mainly because the inner space is nearest to all heat source. Temperature and electric field intensity distribution of the space surrounded by sub-conductors are non-uniform. Moreover, temperature in the right side of space surrounded by positive sub-conductors is higher than that of the left side. However, this situation is opposite for negative sub-conductors. This owes to the electric field intensity in space between positive pole and negative pole, which is higher than that of other space.

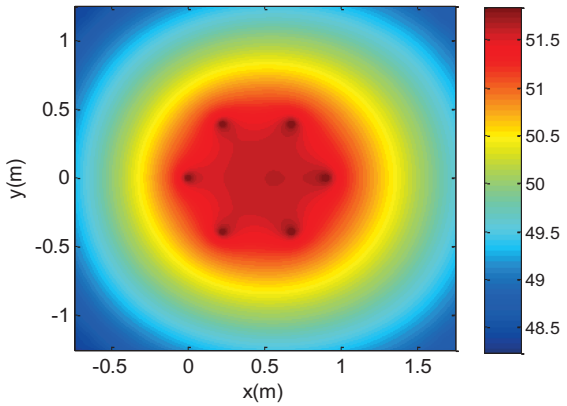

(a) The temperature distribution of space surrounded by positive sub-conductors

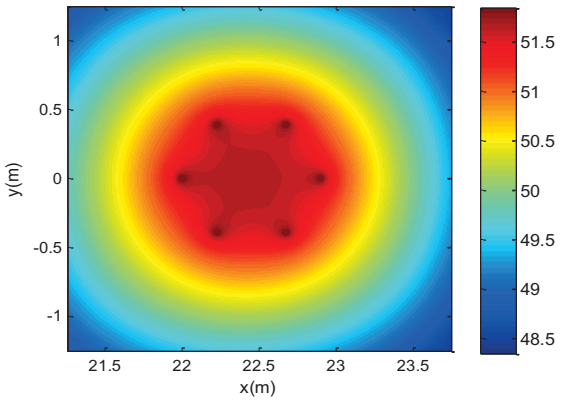

(b) The temperature distribution of space surrounded by negative sub-conductors

Fig. 11. The temperature distribution of UHDC transmission line.

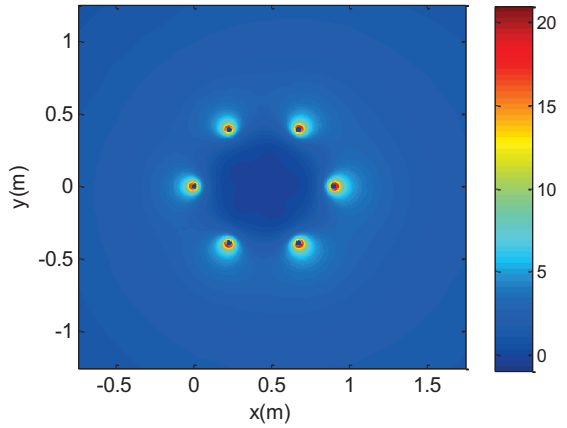

(a) The electric field intensity in space surrounded by positive sub-conductors

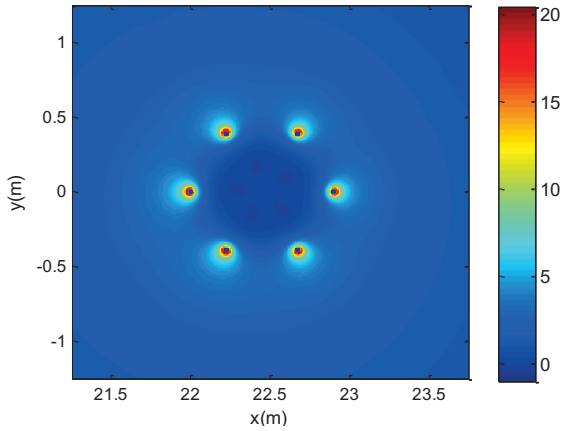

(b) The electric field intensity of space surrounded by negative sub-conductors

Fig. 12. Electric field distribution in sub-conductors.

It can be seen in Fig. 12, the electric field intensity in space between positive polar and negative polar is higher than that of other pace, the main reason is that the grounded capacitance and capacitor among sub-conductor are different due to the spacing positions and relative positions of sub-conductors [20].

At the same time, we can conclude from Fig. 12, that the maximum and minimum value of surface electric field intensity on each sub-conductor lies on the inner and outer surface, which is in the direction of the center connection line of each sub-conductor and polar conductor, respectively. And the relative location is illustrated in Fig. 13 as colored in black spots.

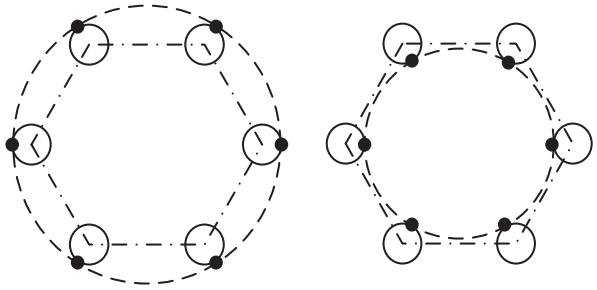

(a) Maximum electric field (b) Minimum electric field

Fig. 13. The maximum and minimum electric field intensity positions of the positive and negative sub-conductors.

Because the environment temperature has a great impact on transmission capacity, influence of it should be considered seriously for the design and operation of ultra-high-voltage transmission lines [16]. Here in this paper, the city of Chongqing is taken as an example to analyze the influence of environment temperature on the capacity of transmission line. According to the history data, the range of environment temperature of Chongqing city is 28~42℃. Variation of the ampacity with environment temperature is shown in Fig. 14.

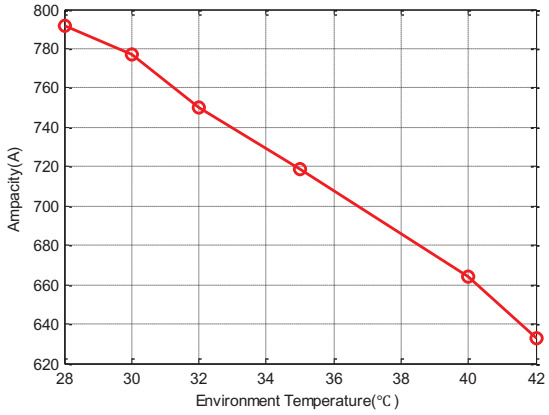

Fig. 14. The ampacity variation with environment temperature.

Results in Fig. 14 indicate that the ampacity decreases almost linearly with the increasing of environment temperature, when the temperature increases to 42℃, the ampactiy drops to 633.1A and achieves 20.02%.

VI. CONCLUSIONS

An improved MLPG method is proposed where the nodes required to construct shape function can be got directly. Then, two rectangle domain problems and ampacity of UHVDC transmission line are analyzed. The calculated results presented in this paper lead to the following conclusions:

1) The generalized support domain has a good accuracy with FEM method.
2) The improved MLPG method can deal with the electro-thermal coupling problem well.
3) Temperature of the place surrounded by of transmission lines is non-uniform; the face-to-face side is higher than the back-to-back side in the sub-conductors, the maximum and minimum value of surface electric field intensity on each sub-conductor lies on the inner and outer surface, which is in the direction of the center connection line of each sub-conductor and polar conductor
4) Ampacity of transmission line decreases almost linearly with environment temperature inversely; what's more, when the temperature increases to 42℃, the ampactiy drops to 633.1A and achieves 20.02%.

ACKNOWLEDGMENT

This work is supported by the Fundamental Research Funds for the Central Universities (No. CDJZR13150051), the Scientific Research Foundation of State Key Lab. of Power Transmission Equipment and System Security (Project No. 2007DA10512711203), and the National Natural Science Foundation of China (No. 51477013).

REFERENCES

[1] G. R. Liu, *Meshfree Methods: Moving Beyond the Finite Element Method*, Boca Raton,CRC, 2009.

[2] G. R. Liu, *An Introduction to Meshfree Methods and Their Programming*, ShanDong Univerisity Press, 2007.

[3] L. N. Williams and R. C. Mesquita, "The meshless local Petrov-Galerkin method in two-dimensional electromagnetic wave analysis," *IEEE Transactions on Antennas and Propagation*, vol. 60, no. 4, pp. 1957-1968, April 2012.

[4] M. Y. Chen, Z. Peng, and P. Hui, "Ampacity calculation for power cables using element free Galerkin method," *Proceedings of the CSEE*, vol. 30, no. 22, pp. 85-91, August 2010.

[5] P. H. Ni and S. Y. Yang, "The element free Galerkin method and its application in numerical computations of electromagnetic fields," *Electric Machines and Control*, vol. 7, no. 1, pp. 26-29, March 2003.

[6] M. L. Zhao, Y. F. Nie, and C. W. Zuo, "Local Petrov-Galerkin method for electro-magnetic field computation," *Electric Machines and Control*, vol. 9, no. 4, pp. 397-400, July 2005.

[7] Fonseca and R. Alexandre, "Improving the mixed formulation for meshless local Petrov-Galerkin method," *IEEE Transactions on Magnetics*, vol. 46, no. 8, pp. 2907-2910, August 2010.

[8] Y. C. Li, "Steady-state thermal analysis of power cable systems in ducts using streamline-upwind/Petrov-Galerkin finite element method," *IEEE Transactions on Dielectrics and Electrical Insulation*, vol. 19, no. 1, pp. 283-290, February 2012.

[9] G. Jin, "Simulation of electric field and temperature field in 30 kV DC XLPE cable," *Electric Wire & Cable*, vol. 6, no. 6, pp. 9-12, December 2009.

[10] L. Miao and R. D. Zhou, "A simulation and study of electro-thermal coupling effects in CMOSIC's," *Microelectronics*, vol. 31, no. 1, pp. 10-12, February 2001.

[11] M. Celuch, M. Soltysiak, and U. Erle, "Computer simulations of microwave heating with coupled electromagnetic, thermal, and kinetic phenomena," *Applied Computational Electromagnetics Society (ACES) Journal*, vol. 26, no. 4, pp. 275-283, April 2011.

[12] X. F. Cui, *The Multi-Physical Field Modeling and Construction Optimization of 20kA Grade Inert Electrode Aluminum Reduction Cell*, Metallurgical Science and Engineering College, Central South University, MS, Spring 2011.

[13] D. Min, L. Qi, and S. W. Wang, "Study of the coupled multidiscipline problem of electronic equipment," *Journal of Guilin University of Electronic Technology*, vol. 30, no. 4, pp. 338-342, August 2010.

[14] S. Qing, X. C. Li, and J. F. Mao, "Electrothermal coupling model based on newton-raphson iteration," *National Conference Proceedings Microwave and Millimeter Wave*, Qingdao, China, pp. 1817-1820, June 2011.

[15] L. J. Ren, G. H. Sheng, and Z. Yi, "A conductor temperature model based on dynamic line rating technology," *Automation of Electric Power Systems*, Qingdao, China, pp. 40-44, June 2009.

[16] Y. Z. Lin, "The calculation of current carrying capacity and temperature of high voltage overhead lines," *Southern Power System Technology*, vol. 6, no. 4, pp. 23-27, June 2012.

[17] G. T. Yin, *Study on Improving Transmission Line Current Capacity Based on Line Temperature Monitoring*, Department of Electrical and Eengineering, Chongqing University, MS, Spring 2011.
[18] T. O. SEPPA, "Increasing transmission capacity by real time monitoring," *Proceedings of the IEEE Power Engineering Society Winter Meeting*, New York, USA, pp. 1208-1211, August 2002.
[19] Y. Yang and D. Divan, "MLPN based parameter estimation to evaluate overhead power line dynamic thermal rating," *15th International Conference on Intelligent System Applications to Power Systems*, Curitiba, Brazil, pp. 8-12, November 2009.
[20] Z. Yu and Z. Wei, "Numerical calculation of electric field intensity on the surface of bundle conductors of overhead transmission lines," *High Voltage Engineering*, vol. 31, no. 1, pp. 23-24+27, January 2005.
[21] Q. Li, S. Shen, and S. N. Atluri, "Application of meshless local Petrov-Galerkin (MLPG) to problems with singularities, and material discontinuities, in 3-D elasticity," *Computer Modeling in Engineering & Sciences*, vol. 4, no. 5, pp. 571-585, March 2003.
[22] W. He, Z. H. Liu, and R. K. Gordon, "A comparison of the element free Galerkin method and the meshless local Petrov-Galerkin method for solving electromagnetic problems," *Applied Computational Electromagnetics Society (ACES) Journal*, vol. 27, no. 8, pp. 620-629, August 2012.

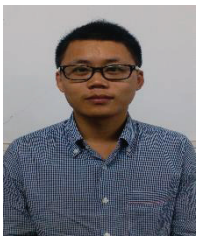

Bing Gao was born in 1987, Hunan Province, China. He received his B.E. degree in Electrical Engineering at Chongqing University in 2011. Now he is a Ph.D. candidate with the School of Electrical Engineering, Chongqing University, China. His research activities mainly include: multi-fields of power converter and meshless methods for solving electrothermal problems.

Fan Yang was born in ShanDong Province, China. He received his Ph.D. degree from the School of Electrical Engineering, Chongqing University, China and now he is a Ph.D. Supervisor in Electrical Engineering of Chongqing University. His research interests includes high voltage electrical apparatus, electromagnetic devices and sensors, electromagnetic environment of power system.

Minyou Chen was born in Chongqing, Province. He received the Ph.D. degree in Control Engineering from the University of Sheffield, Sheffield, U.K., in 1988. Now he is a Professor at the School of Electrical Engineering, Chongqing University, China. His current research interests are control, state monitoring and algorithms of new energy power system.

Truncation Error Analysis of a Pre-Asymptotic Higher-Order Finite Difference Scheme for Maxwell's Equations

Yu Shao and Shumin Wang

Department of Electrical and Computer Engineering
Auburn University, Auburn, AL 36830, USA
yzs0016@auburn.edu, james.wang@ieee.org

Abstract ─ Pre-asymptotic higher-order methods are useful to the mitigation of numerical dispersion error in large-scale Finite-Difference Time-Domain (FDTD) simulations. Its truncation error is shown in this study to be $\mathcal{O}(\Delta t^2)+\mathcal{O}(\Delta s^2)$ in general. In the limiting case where the Courant-Friedrichs-Levy number approaches to zero, it becomes $\mathcal{O}(\Delta t^2)+\mathcal{O}(\Delta s^4)$.

Index Terms ─ FDTD, higher-order, pre-asymptotic, truncation error.

I. INTRODUCTION

Numerical dispersion error is a major concern in large-scale finite-difference simulations of wave propagation and scattering problems [1]. For its mitigation, various techniques based on higher-order finite-difference schemes and non-canonical grids have been proposed in past decades [2]-[6]. However, the inherent frequency dependency and angle dependency (anisotropy) of their dispersion properties may not be desired in practical applications, such as those involving high-permittivity biological bodies at high frequency. For instance, their dispersion errors decrease at lower frequency, where the electrical size of certain geometry is smaller and the significance of dispersion error diminishes. It is preferred to have less dispersion error at higher frequency rather than lower frequency.

Pre-asymptotic higher-order methods were devised to solve the above problems by "engineering" the dispersion properties of finite-difference schemes for certain applications [7]-[11]. They start from defining an error functional related to the dispersion property of a given stencil; e.g., the conventional (2,4) stencil [2]. The coefficients of the underlining finite-different scheme are then determined by minimizing this error functional. The criteria can be either minimum dispersion error in a certain angular span or in a certain frequency range. In the former case, one obtains angularly optimized finite-difference schemes [7]-[9]. In the latter case, one obtains so-called Dispersion-Relation-Preserving (DRP) schemes [10]-[11].

An important question arising from the development of pre-asymptotic methods is their truncation error properties. Although they are based on a stencil which is supposed to have a higher-order truncation error, the finite-difference coefficients have been modified for desired numerical dispersion properties. Thus, it is unclear whether the original truncation error properties can be retained.

In order to answer the above question, the truncation error of the Three-Dimensional (3D) DRP scheme, which is based on the (2,4) stencil, is analyzed in this study [11]. This analysis can be adapted to other pre-asymptotic schemes.

II. 3D DRP EQUATIONS

Details of the DRP method can be found in [11]. It is briefly repeated here for convenience. The FDTD discretization of 3D Maxwell's equations in a Cartesian grid by using a (2,4) stencil can be written as:

$$\vec{E}^{i+1}=\vec{E}^{i}+\frac{\Delta t}{\varepsilon}\vec{S}\times\vec{H}^{i+\frac{1}{2}}, \tag{1}$$

$$\vec{H}^{i+\frac{1}{2}}=\vec{H}^{i-\frac{1}{2}}-\frac{\Delta t}{\mu}\vec{S}\times\vec{E}^{i}, \tag{2}$$

Submitted On: October 23, 2013
Accepted On: September 8, 2014

where superscripts indicate time steps. The finite-difference operator $\vec{S}$ is defined as:

$$\vec{S}=\frac{1}{\Delta x}(C_{1x}S_x^{+}+C_{2x}S_x^{++})\hat{x}+\frac{1}{\Delta y}(C_{1y}S_y^{+}+C_{2y}S_y^{++})\hat{y}+\frac{1}{\Delta z}(C_{1z}S_z^{+}+C_{2z}S_z^{++})\hat{z}, \quad (3)$$

where C_{1s} and C_{2s}, s = x, y, z are coefficients to be determined, and S_s^{+} and S_s^{++} are "grid displacement" operators [6] defined by:

$$S_x^{+}E^i_{y_{(l+\frac{1}{2},m+\frac{1}{2},n)}}=E^i_{y_{(l+1,m+\frac{1}{2},n)}}-E^i_{y_{(l,m+\frac{1}{2},n)}}, \quad (4)$$

$$S_x^{++}E^i_{y_{(l+\frac{1}{2},m+\frac{1}{2},n)}}=E^i_{y_{(l+1,m+\frac{1}{2},n)}}-E^i_{y_{(l,m+\frac{1}{2},n)}}, \quad (5)$$

and similarly for the other components. In the above, subscripts indicate spatial locations. By applying standard Fourier analysis, we obtain:

$$\vec{\mathcal{E}}\sin(\frac{\omega\Delta t}{2})=-\frac{\Delta t}{\varepsilon}\vec{F}\times\vec{\mathcal{H}}, \quad (6)$$

$$\vec{\mathcal{H}}\sin(\frac{\omega\Delta t}{2})=\frac{\Delta t}{\mu}\vec{F}\times\vec{\mathcal{E}}, \quad (7)$$

with

$$\vec{F}=F_x\hat{x}+F_y\hat{y}+F_z\hat{z},$$

$$F_x=\frac{1}{\Delta x}[C_{1x}\sin(\frac{k_x\Delta x}{2})+C_{2x}\sin(\frac{3k_x\Delta x}{2})],$$

$$F_y=\frac{1}{\Delta y}[C_{1y}\sin(\frac{k_y\Delta y}{2})+C_{2y}\sin(\frac{3k_y\Delta y}{2})],$$

$$F_z=\frac{1}{\Delta z}[C_{1z}\sin(\frac{k_z\Delta z}{2})+C_{2z}\sin(\frac{3k_z\Delta z}{2})].$$

Considering the H update for the TE^z wave propagating along the (θ, ϕ) direction, its wavenumber components read $k_x = k\sin\theta\cos\phi$, $k_y = k\sin\theta\sin\phi$, $k_z = k\cos\theta$. We have:

$$\mathcal{E}_x=-\mathcal{E}\sin\phi,\ \mathcal{E}_y=\mathcal{E}\cos\phi,\ \mathcal{E}_z=0, \quad (8)$$

$$\mathcal{H}_x=-\mathcal{H}\cos\theta\cos\phi,\ \mathcal{H}_y=-\mathcal{H}\cos\theta\sin\phi,\ \mathcal{H}_z=\mathcal{H}\sin\theta. \quad (9)$$

The following two independent equations can be obtained by substituting (8) and (9) into (7):

$$\mathcal{H}\cos\theta\sin(\frac{\omega\Delta y}{2})=\frac{\Delta t}{\mu\Delta z}[C_{1z}\sin(\frac{k_z\Delta z}{2})+C_{2z}\sin(\frac{3k_z\Delta z}{2})]\mathcal{E}, \quad (10)$$

$$\mathcal{H}\sin\theta\sin(\frac{\omega\Delta y}{2})=\frac{\Delta t}{\mu}\{\frac{1}{\Delta x}\cos\phi[C_{1x}\sin(\frac{k_x\Delta x}{2})+C_{2x}\sin(\frac{3k_x\Delta x}{2})]+\frac{1}{\Delta y}\sin\phi[C_{1y}\sin(\frac{k_y\Delta y}{2})+C_{2y}\sin(\frac{3k_y\Delta y}{2})]\}\mathcal{E}. \quad (11)$$

The other polarization gives similar equations for the E-field update.

C_{1z} and C_{2z} can be determined from Eqs. (10) and (11). In a regular Cartesian grid, the remaining coefficients can be likewise determined because they obey identical equations with respect to the elevation angles of the associated axes. By enforcing $E=\eta H$, and denoting the Courant-Friedrichs-Levy (CFL) [1] number as $\chi_s=\sqrt{3}v_p\Delta t/\Delta s$, Eq. (10) can be written as:

$$\frac{\sqrt{3}}{\chi_s}\sin(\frac{\pi q_s\chi_s}{\sqrt{3}})\cos\theta=C_{1s}\sin(\pi q_s\cos\theta)+C_{2s}\sin(3\pi q_s\cos\theta), \quad (12)$$

where $q_s=\Delta s/\lambda$ denotes the wavelength to grid-cell size ratio, and Δs stands for either Δx, Δy, or Δz.

An error functional can be defined as the difference between the left- and the right-hand sides of Eq. (12). Expanding it in a series of spherical harmonics $Y_{lm}(\theta,\phi)$ yields:

$$\delta(C_{1s},C_{2s},\theta,\phi)=\sum_{l=0}^{\infty}\sqrt{\pi(4l+3)}[C_{1s}I_{2l+1}(\pi q_s)+C_{2s}I_{2l+1}(3\pi q_s)]\,Y_{2l+1,0}(\theta,\phi)+\frac{2\sqrt{\pi}}{\chi_s}\sin(\frac{\pi q_s\chi_s}{\sqrt{3}})Y_{1,0}(\theta,\phi), \quad (13)$$

where $I_l(\alpha)=0$ for l even. For odd l, $I_l(\alpha)$ can be obtained via integration by parts as:

$$I_l(\alpha)=[\frac{2(2l-3)}{2l-5}-\frac{(2l-1)(2l-3)}{\alpha^2}]I_{l-2}(\alpha)-\frac{2l-1}{2l-5}I_{l-4}(\alpha). \quad (14)$$

The first two terms are given by:

$$I_1(\alpha)=\frac{2(\sin\alpha-\alpha\cos\alpha)}{\alpha^2},$$

$$I_3(\alpha)=\frac{6(2\alpha^2-5)\sin\alpha-2\alpha(\alpha^2-15)\cos\alpha}{\alpha^4}.$$

By enforcing the two leading terms in Eq. (12) to be zero and solving for C_{1s} and C_{2s}, one obtains:

$$C_{1s}=C_{1s}^{(\infty)}\equiv\frac{\pi^2q_s^2[3\pi q_s(5-3\pi^2q_s^2)\cos(3\pi q_s)+(18\pi^2q_s^2-5)\sin(3\pi q_s)]\sin(\frac{\pi q_s\chi_s}{\sqrt{3}})}{\Xi}, \quad (15)$$

$$C_{2s}=C_{2s}^{(\infty)}\equiv\frac{27\pi^2q_s^2[\pi q_s(\pi^2q_s^2-15)\cos(\pi q_s)+3(5-2\pi^2q_s^2)\sin(\pi q_s)]\sin(\frac{\pi q_s\chi_s}{\sqrt{3}})}{\Xi}, \quad (16)$$

where the denominator in Eqs. (15) and (16) writes as:

$$\Xi=20\sqrt{3}\chi_s\{(1+3\pi^2q_s^2)\cos(2\pi q_s)-\cos(4\pi q_s)+\pi q_s\{3\pi q_s[\cos(4\pi q_s)-2\pi q_s\cos(\pi q_s)\sin(\pi q_s)^3]+2[\sin(2\pi q_s)-2\sin(4\pi q_s)]\}\}.$$

In order to implement these coefficients in time domain, C_{1s}^{∞} and C_{2s}^{∞} can be expanded in a Taylor series around $q_s = 0$. By retaining the lowest order terms and substituting the second order time derivative by the spatial derivative operator $v_p^2\nabla^2$ (from Helmholtz's equation in the continuum), one obtains:

$$C_{1s}^{(2)}=\frac{9}{8}+\frac{1}{64}(\chi_s^2-1)\Delta s^2\nabla^2\equiv C_{11s}^{(2)}-C_{12s}^{(2)}\Delta s^2\nabla^2, \quad (17)$$

$$C_{1s}^{(2)} = -\frac{1}{24} - \frac{1}{1728}(\chi_s^2 - 9)\Delta s^2\nabla^2 \equiv C_{21s}^{(2)} - C_{22s}^{(2)}\Delta s^2\nabla^2 . \quad (18)$$

The final finite-difference scheme is obtained by substituting these coefficients in Eq. (2).

III. TRUNCTION ERROR

Let us consider the H_z update of the DRP scheme in a uniform grid, which is written as:

$$H^{i+\frac{1}{2}}_{z(l+\frac{1}{2},m+\frac{1}{2},n)} = H^{i-\frac{1}{2}}_{z(l+\frac{1}{2},m+\frac{1}{2},n)} + \frac{\Delta t}{\mu}\{\frac{1}{\Delta y}[C_{1y}(E^i_{x(l+\frac{1}{2},m+1,n)} - E^i_{x(l+\frac{1}{2},m,n)}) + C_{2y}(E^i_{x(l+\frac{1}{2},m+2,n)} - E^i_{x(l+\frac{1}{2},m-1,n)})] - \frac{1}{\Delta x}[C_{1x}(E^i_{y(l+1,m+\frac{1}{2},n)} - E^i_{y(l,m+\frac{1}{2},n)}) + C_{2x}(E^i_{y(l+2,m+\frac{1}{2},n)} - E^i_{y(l-1,m+\frac{1}{2},n)})]\}. \quad (19)$$

Plugging Eqs. (17) and (18) into Eq. (19), one obtains:

$$H^{i+\frac{1}{2}}_{z(l+\frac{1}{2},m+\frac{1}{2},n)} = H^{i-\frac{1}{2}}_{z(l+\frac{1}{2},m+\frac{1}{2},n)} + \frac{\Delta t}{\mu}\{\frac{1}{\Delta s}[(\frac{9}{8} + \frac{1}{64}(\chi_s^2 - 1)\Delta s^2\nabla^2)(E^i_{x(l+\frac{1}{2},m+1,n)} - E^i_{x(l+\frac{1}{2},m,n)}) + (-\frac{1}{24} - \frac{1}{1728}(\chi_s^2 - 9)\Delta s^2\nabla^2)(E^i_{x(l+\frac{1}{2},m+2,n)} - E^i_{x(l+\frac{1}{2},m-1,n)})] - \frac{1}{\Delta s}[(\frac{9}{8} + \frac{1}{64}(\chi_s^2 - 1)\Delta s^2\nabla^2)(E^i_{y(l+1,m+\frac{1}{2},n)} - E^i_{y(l,m+\frac{1}{2},n)}) + (-\frac{1}{24} - \frac{1}{1728}(\chi_s^2 - 9)\Delta s^2\nabla^2)(E^i_{y(l+2,m+\frac{1}{2},n)} - E^i_{y(l-1,m+\frac{1}{2},n)})]\}. \quad (20)$$

Note that, the difference between the above update and a conventional (2,4) scheme involves the spatial derivative terms. The time derivative is treated similarly in both approaches, which results in a temporal truncation error of $\mathcal{O}(\Delta t^2)$. So the spatial truncation error will be focused in the following.

Let us consider the spatial derivative term involving E_x only because the E_y term is treated the same as E_x in Eq. (20). One has:

$$\frac{1}{\Delta s}[[\frac{9}{8} + \frac{1}{64}(\chi_s^2 - 1)\Delta s^2\nabla^2](E^i_{x(l+\frac{1}{2},m+1,n)} - E^i_{x(l+\frac{1}{2},m,n)}) + [-\frac{1}{24} - \frac{1}{1728}(\chi_s^2 - 9)\Delta s^2\nabla^2](E^i_{x(l+\frac{1}{2},m+2,n)} - E^i_{x(l+\frac{1}{2},m-1,n)})]. \quad (21)$$

By expanding $E^i_{x(l+\frac{1}{2},m+1,n)}$ in Taylor series as:

$$E^i_{x(l+\frac{1}{2},m+1,n)} = [1 + (\frac{\Delta s}{2})\frac{\partial}{\partial y} + (\frac{\Delta s}{2})^2\frac{1}{2!}\frac{\partial^2}{\partial^2 y} + (\frac{\Delta s}{2})^3\frac{1}{3!}\frac{\partial^3}{\partial^3 y} + (\frac{\Delta s}{2})^4\frac{1}{4!}\frac{\partial^4}{\partial^4 y} + (\frac{\Delta s}{2})^5\frac{1}{5!}\frac{\partial^5}{\partial^5 y}]E^i_{x(l+\frac{1}{2},m+\frac{1}{2},n)} + \mathcal{O}(\Delta s^6), \quad (22)$$

and the other terms similarly, it was found that:

$$\frac{1}{\Delta s}[\frac{9}{8}(E^i_{x(l+\frac{1}{2},m+1,n)} - E^i_{x(l+\frac{1}{2},m,n)}) - \frac{1}{24}(E^i_{x(l+\frac{1}{2},m+2,n)} - E^i_{x(l+\frac{1}{2},m-1,n)})] = \frac{\partial}{\partial y}E^i_{x(l+\frac{1}{2},m+\frac{1}{2},n)} + \mathcal{O}(\Delta s^4). \quad (23)$$

The remaining term in (21) that needs to be considered is:

$$\frac{1}{\Delta s}[\frac{1}{64}(\chi_s^2 - 1)\Delta s^2\nabla^2(E^i_{x(l+\frac{1}{2},m+1,n)} - E^i_{x(l+\frac{1}{2},m,n)}) - \frac{1}{1728}(\chi_s^2 - 9)\Delta s^2\nabla^2(E^i_{x(l+\frac{1}{2},m+2,n)} - E^i_{x(l+\frac{1}{2},m-1,n)})]. \quad (24)$$

The ∇^2 operators in Eq. (24) are approximated by centered difference; i.e.,

$$\nabla^2 E^i_{x(l+\frac{1}{2},m+1,n)} \approx \frac{1}{\Delta s^2}[E^i_{x(l-\frac{1}{2},m+1,n)} - 2E^i_{x(l+\frac{1}{2},m+1,n)} + E^i_{x(l+\frac{3}{2},m+1,n)}] + \frac{1}{\Delta s^2}[E^i_{x(l+\frac{1}{2},m,n)} - 2E^i_{x(l+\frac{1}{2},m+1,n)} + E^i_{x(l+\frac{1}{2},m+2,n)}] + \frac{1}{\Delta s^2}[E^i_{x(l+\frac{1}{2},m+1,n-1)} - 2E^i_{x(l+\frac{1}{2},m+1,n)} + E^i_{x(l+\frac{1}{2},m+1,n+1)}]. \quad (25)$$

By using Taylor expansion, it is found that:

$$\nabla^2 E^i_{x(l+\frac{1}{2},m+1,n)} = [\frac{\partial^2}{\partial^2 x} + (\Delta s^2)\frac{1}{12}\frac{\partial^4}{\partial^4 x} + \frac{\partial^2}{\partial^2 y} + (\Delta s^2)\frac{1}{12}\frac{\partial^4}{\partial^4 y} + \frac{\partial^2}{\partial^2 z} + (\Delta s^2)\frac{1}{12}\frac{\partial^4}{\partial^4 z}]E^i_{x(l+\frac{1}{2},m+1,n)} + \mathcal{O}(\Delta s^4). \quad (26)$$

By using the following expressions:

$$\frac{\partial^2}{\partial^2 x}E^i_{x(l+\frac{1}{2},m+1,n)} = [\frac{\partial^2}{\partial^2 x} + (\frac{\Delta s}{2})\frac{\partial^3}{\partial^2 x\partial y} + (\frac{\Delta s}{2})^2\frac{\partial^4}{\partial^2 x\partial^2 y} + (\frac{\Delta s}{2})^3\frac{\partial^5}{\partial^2 x\partial^3 y} + (\frac{\Delta s}{2})^4\frac{\partial^6}{\partial^2 x\partial^4 y}]E^i_{x(l+\frac{1}{2},m+\frac{1}{2},n)} + \mathcal{O}(\Delta s^5), \quad (27)$$

$$\frac{\partial^4}{\partial^4 x}E^i_{x(l+\frac{1}{2},m+1,n)} = [\frac{\partial^4}{\partial^4 x} + \left(\frac{\Delta s}{2}\right)\frac{\partial^5}{\partial^4 x\partial y} + \left(\frac{\Delta s}{2}\right)^2\frac{\partial^6}{\partial^4 x\partial^2 y} + \left(\frac{\Delta s}{2}\right)^3\frac{\partial^7}{\partial^4 x\partial^3 y} + \left(\frac{\Delta s}{2}\right)^4\frac{\partial^8}{\partial^4 x\partial^4 y}]E^i_{x(l+\frac{1}{2},m+\frac{1}{2},n)} + \mathcal{O}(\Delta s^5), \quad (28)$$

one can obtain:

$$\frac{1}{64}(\chi_s^2 - 1)\Delta s^2\nabla^2(E^i_{x(l+\frac{1}{2},m+1,n)} - E^i_{x(l+\frac{1}{2},m,n)}) = \frac{1}{64}(\chi_s^2 - 1)\Delta s^2[(\Delta s)\frac{\partial^3}{\partial^2 x\partial y} + 2\left(\frac{\Delta s}{2}\right)^3\frac{\partial^5}{\partial^2 x\partial^3 y} + (\Delta s)\frac{\partial^3}{\partial^3 y} + 2\left(\frac{\Delta s}{2}\right)^3\frac{\partial^5}{\partial^5 y} + (\Delta s)\frac{\partial^3}{\partial^2 z\partial y} + 2\left(\frac{\Delta s}{2}\right)^3\frac{\partial^5}{\partial^2 z\partial^3 y}]E^i_{x(l+\frac{1}{2},m+\frac{1}{2},n)} + \mathcal{O}(\Delta s^5), \quad (29)$$

$$-\frac{1}{1728}(\chi_s^2-9)\Delta s^2\nabla^2(E^i_{x(l+\frac{1}{2},m+2,n)}-E^i_{x(l+\frac{1}{2},m-1,n)})$$
$$=-\frac{1}{1728}(\chi_s^2-9)\Delta s^2[(3\Delta s)\frac{\partial^3}{\partial^2 x\partial y}+2\left(\frac{3\Delta s}{2}\right)^3\frac{\partial^5}{\partial^2 x\partial^3 y}+(3\Delta s)\frac{\partial^3}{\partial^3 y}+$$
$$2\left(\frac{3\Delta s}{2}\right)^3\frac{\partial^5}{\partial^5 y}+(3\Delta s)\frac{\partial^3}{\partial^2 z\partial y}+2\left(\frac{3\Delta s}{2}\right)^3\frac{\partial^5}{\partial^2 z\partial^3 y}]E^i_{x(l+\frac{1}{2},m+\frac{1}{2},n)}+\mathcal{O}(\Delta s^5). \quad (30)$$

Thus, (24) becomes:

$$\frac{\chi_s^2}{72}\Delta s^2[\frac{\partial^3}{\partial^2 x\partial y}+\frac{\partial^3}{\partial^3 y}+\frac{\partial^3}{\partial^2 z\partial y}]E^i_{x(l+\frac{1}{2},m+\frac{1}{2},n)}+\mathcal{O}(\Delta s^4). \quad (31)$$

Together with Eq. (23), Eq. (21) is written as:

$$\frac{1}{\Delta s}[[\frac{9}{8}+\frac{1}{64}(\chi_s^2-1)\Delta s^2\nabla^2](E^i_{x(l+\frac{1}{2},m+1,n)}-E^i_{x(l+\frac{1}{2},m,n)})+$$
$$[-\frac{1}{24}-\frac{1}{1728}(\chi_s^2-9)\Delta s^2\nabla^2]E^i_{x(l+\frac{1}{2},m+2,n)}-E^i_{x(l+\frac{1}{2},m-1,n)}]$$
$$=\frac{\partial}{\partial y}E^i_{x(l+\frac{1}{2},m+\frac{1}{2},n)}+\frac{\chi_s^2}{72}\Delta s^2[\frac{\partial^3}{\partial^2 x\partial y}+\frac{\partial^3}{\partial^3 y}+\frac{\partial^3}{\partial^2 z\partial y}]E^i_{x(l+\frac{1}{2},m+\frac{1}{2},n)}+\mathcal{O}(\Delta s^4). \quad (32)$$

Therefore, the truncation error of the DRP scheme is generally $\mathcal{O}(\Delta t^2)+\mathcal{O}(\Delta s^2)$. In the limiting case where the CFL number χ_s goes to zero, the truncation error recovers to $\mathcal{O}(\Delta t^2)+\mathcal{O}(\Delta s^4)$ (from Eq. (32)).

IV. CONCLUSIONS

The truncation error of the DRP scheme was investigated in this study. It serves to reinforce the basic trade-off of pre-asymptotic higher-order finite-difference schemes, which trade low numerical dispersion error at a pre-assigned frequency window or angular range for larger numerical dispersion errors outside the range of interest; in particular, at sufficiently low frequencies where the cumulative numerical dispersion error decreases due to the smaller electrical size. Although higher-order truncation error is not preserved in general, this approach is more relevant to improving the accuracy of practical large-scale simulations of hyperbolic problems, in which the frequency is often limited in a prescribed band.

REFERENCES

[1] A. Taflove, "Advances in computational electrodynamics: the finite-difference time-domain method," *Boston: Artech*, 1998.

[2] J. Fang, "Time domain computation for Maxwell's equations," *Ph.D. dissertation, Univ. California at Berkeley*, 1989.

[3] C. K. W. Tam and J. C. Webb, "Dispersion-relation-preserving finite difference schemes for computational acoustics," *J. Comp. Phys*., vol. 107, pp. 262-281, 1993.

[4] M. F. Hadi and M. Piket-May, "A modified FDTD (2,4) scheme for modeling electrically large structures with high-phase accuracy," *IEEE Trans. Antennas Propagat*., vol. 45, no. 2, pp. 254-264, 1997.

[5] J. B. Cole, "A high accuracy FDTD algorithm to solve microwave propagation and scattering problems on a coarse grid," *IEEE Trans. Microwave Theory Tech*., vol. 43, no. 9, pp. 2053-2058, 1995.

[6] E. A. Forgy and W. C. Chew, "A new FDTD formulation with reduced dispersion for the simulation of wave propagation through inhomogeneous media," *IEEE AP-S Int. Symp. Proc*., vol. 2, pp. 1316-1319, 1999.

[7] S. Wang and F. L. Teixeira, "A finite-difference time-domain algorithm optimized for arbitrary propagation angles," *IEEE Trans. Antennas Propagat*., vol. 51, no. 9, pp. 2456-2463, September 2003.

[8] S. Wang and F. L. Teixeira, "A three-dimensional angle-optimized FDTD algorithm," *IEEE Trans. Microwave Theory & Tech*., vol. 51, no. 3, pp. 811-817, March 2003.

[9] S. Wang and F. L. Teixeira, "Grid-dispersion error reduction for broadband electromagnetic simulations," *IEEE Trans. Magnetics*, vol. 40, no. 2, pp. 1440-1443, March 2004.

[10] S. Wang and F. L. Teixeira, "Lattice models for large-scale simulations of coherent wave scattering," *Physical Review: E*, vol. 69, 016701, January 2004.

[11] S. Wang and F. L. Teixeira, "Dispersion-relation-preserving FDTD algorithms for large scale three-dimensional problems," *IEEE Trans. Antennas Propagat*., vol. 51, no. 8, pp. 1818-1828, August 2003.

Development of Diplexers Based on Dual-Mode Substrate Integrated Waveguide Cavities

Hui Chu [1], Rong Mao [2], and Jian-Xin Chen [1]

[1] School of Electronics and Information
Nantong University, Nantong, 226019, China
jjxchen@hotmail.com

[2] North Information Control Group Co. Ltd.
Nanjing, 211153, China

Abstract ─ Diplexers based on dual-mode Substrate Integrated Waveguide (SIW) cavities are proposed and implemented. The dual-mode cavities not only act as a resonator for both Rx and Tx channels, but also as the interconnect between these two channels which help to realize the isolation. The dual-mode cavities resonating at TE_{201} and TE_{103} modes in our design show several advantages than those dual-mode cavities operating at TE_{201} and TE_{301} modes. Single-mode cavities are cascaded with the dual-mode cavity to realize the two-order filters for Rx and Tx channels. Two design examples are presented with a normal printed circuit board process and verified by experiments.

Index Terms ─ Diplexer, dual-mode cavity, filter, Substrate Integrated Waveguide (SIW).

I. INTRODUCTION

A T-junction, which connects the two filters and the common input port reserved for an antenna, is widely used in conventional diplexer designs [1-4] composed of waveguide or transmission lines. For recently developed diplexers based on Substrate Integrated Waveguide (SIW) [5-6], a T-junction is also in critical need. The lengths of the transmission lines/waveguides connecting the T-junction to the Rx and Tx filters are the most important design parameters to achieve a good isolation between two channels. In our previous work [7], a novel 40/50 GHz diplexer is proposed using two dual-mode (operating at TE_{102} and TE_{103} modes) cavities. The isolation of this 40/50 GHz diplexer between two channels is realized by properly choosing the geometric shape of the dual-mode cavities and positions of feeding probes instead of using T-junction. Anyhow, due to both of the resonators in the diplexer are of dual-mode cavities, the size of the diplexer is extremely large. Meanwhile, in our previous design, we have to use closely spaced microstrip lines to couple those two cavities which will result in a strong coupling between the microstrip lines and as a result, leading to a poor isolation performance.

In this letter, we propose two diplexers based on dual-mode SIW cavities working at TE_{201} and TE_{103} modes, instead of previous TE_{201} and TE_{301} modes. Same as the diplexer design in [7], the dual-mode cavities involved not only act as a resonator for both Rx and Tx channels, but also the interconnect between these two channels which help to realize the isolation. Anyhow, only one dual-mode cavity is used in each diplexer design in this letter, while two single-mode cavities resonating at TE_{101} mode are placed at different sides of the dual-mode one and cascaded with it. Obviously, the total size of the diplexer will be much smaller than previous design with two dual-mode cavities. Moreover, compared with the dual-mode cavity of TE_{201} & TE_{301} modes, the dual-mode cavity of TE_{201} & TE_{103} modes can be implemented in more cases and has a smaller size for some specific cases, which are explained in detail in Section II. Two design examples of 10/18 GHz and 10/10.5 GHz diplexers are given and verified by

Submitted On: February 17, 2014
Accepted On: October 25, 2014

experiments, separately.

II. ANALYSIS OF PROPOSED DUAL-MODE CAVITY RESONATOR

Figure 1 shows the configuration of a rectangular cavity resonator, where L, W and h are the cavity's length, width and height, respectively. The resonant frequency of the TE_{mnl} or TM_{mnl} mode is decided by where μ_r and ε_r are the relative permeability and relative permittivity of the cavity substrate, c is the speed of light in free space and m, n, l are mode numbers of the resonator. Since the substrate is very thin, only TE mode need be considered in most applications. As a result, the wavenumber n is zero, and m and l are natural integers;

$$f_{mnl} = \frac{c}{2\pi\sqrt{\mu_r\varepsilon_r}}\sqrt{\left(\frac{m\pi}{L}\right)^2+\left(\frac{n\pi}{h}\right)^2+\left(\frac{l\pi}{W}\right)^2}. \quad (1)$$

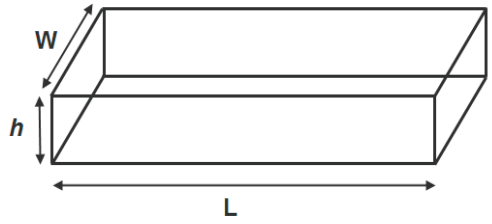

Fig. 1. Geometry of a rectangular resonator.

In [7], resonant modes TE_{201} and TE_{301} are selected and can be controlled to resonant at desired frequency f_0 for Rx channel and f_1 for Tx channel with length L_1 and width W_1, by solving the two equations below:

$$f_0 = \frac{c}{2\pi\sqrt{\mu_r\varepsilon_r}}\sqrt{\left(\frac{2\pi}{L_1}\right)^2+\left(\frac{\pi}{W_1}\right)^2}, \quad (2)$$

$$f_1 = \frac{c}{2\pi\sqrt{\mu_r\varepsilon_r}}\sqrt{\left(\frac{3\pi}{L_1}\right)^2+\left(\frac{\pi}{W_1}\right)^2}. \quad (3)$$

However, the equations (2) and (3) can only be resolved when $f_0/f_1 > 2/3$. As a result, this kind of diplexer design using a dual-mode resonator of TE_{201} and TE_{301} mode is not suitable for applications such as Wireless Local Area Networks (WLAN) whose operating frequency bands are centered at 2.45 GHz and 5.2 GHz, separately.

If we choose TE_{201} and TE_{103} as the resonant modes of the dual-mode cavity instead, the length L_2 and width W_2 of the cavity can be obtained by solving:

$$f_0 = \frac{c}{2\pi\sqrt{\mu_r\varepsilon_r}}\sqrt{\left(\frac{2\pi}{L_2}\right)^2+\left(\frac{\pi}{W_2}\right)^2}, \quad (4)$$

$$f_1 = \frac{c}{2\pi\sqrt{\mu_r\varepsilon_r}}\sqrt{\left(\frac{\pi}{L_2}\right)^2+\left(\frac{3\pi}{W_2}\right)^2}. \quad (5)$$

The equations (4) and (5) will have a solution when $f_0/f_1 > 1/3$, which means this kind of dual-mode cavity can be implemented in more cases of applications. Meanwhile, based on the equations (2), (3), (4) and (5), the cavity's size W_2L_2 will be smaller than W_1L_1 when $f_0/f_1 > 2\sqrt{2}/3$ when these two diplexers operate at the same frequencies for both Rx and Tx channels.

III. DIPLEXER DESIGN EXAMPLES

We present two examples here to show the ability and advantages of using TE_{201}- and TE_{103}-mode cavity for the design of diplexers without a T-junction. Rogers 5880 substrate with relative permittivity of 2.2 and loss tangent of 0.0009 has been used for design. The dielectric thickness is 20 mil. 50-Ω microstrip lines with coupling slots are used for the input/output of cavities and the coupling is controlled by changing the length of the coupling slot with a fixed width. The internal coupling between resonant cavities is obtained by one magnetic post-wall coupling slot on the common wall and controlled by the slot's width.

The first example is a diplexer whose two channels are centered very far at f_0=10 GHz and f_1=18 GHz, respectively. The ratio f_0/f_1 equals 5/9 which is larger than 1/3. The center frequencies of the two channels for the second example are centered extremely closely at f_0=10 GHz and f_1=10.5 GHz, separately. The ratio of f_0/f_1 is 20/21 which is larger than $2\sqrt{2}/3$.

A. 10/18 GHz diplexer

The configuration of a 10/18 GHz diplexer is shown in Fig. 2. The diplexer consists of two two-order filters with fractional bandwidth of 1.0% for the 10 GHz filter and 1.4% for the 18 GHz filter. Cavity 1 is the dual-mode cavity resonating at 10 GHz for TE_{201} mode and 18 GHz for TE_{103} mode. Cavity 2 and cavity 3 are single-mode cavities whose resonant frequency is 10 GHz and 18 GHz,

separately. The coupling slot between cavity 1 and 2 is centered at one-third of the shorter side-wall *aa'* of cavity 1, while the coupling slot between cavity 1 and 3 are placed at the center of the longer side-wall *aa''* of cavity 1. We also plot the electric field distributions of the diplexer at 10 GHz and 18 GHz in Fig. 3 in order to understand its working mechanism. As can be seen in Fig. 3, for the dual-mode cavity, the electric field in region A is strong at 18 GHz for TE_{103} mode but weak at 10 GHz for TE_{201} mode, while region B is strong at 10 GHz but weak at 18 GHz. Therefore, when a coupling slot is opened in region A, it causes a strong coupling at the TE_{103} mode and weak even null coupling at the TE_{201} mode. On the contrary, when a coupling slot is opened in region B, only TE_{201} mode will be excited. As a result, when slot in region B is used to couple a cavity resonated at 10 GHz and slot in region A is coupled to a cavity resonated at 18 GHz, isolation between 10 GHz and 18 GHz can be achieved. The electric field distributions of cavity 3 and cavity 2 shown in Fig. 3 are almost null at 10 GHz and 18 GHz, respectively, which also verify our analysis mentioned above. In order to excite the dual-mode cavity at both of 10 GHz and 18 GHz for the design of the common port of the diplexer, the feeding position of the input port P1 should be chosen at the places where the electric field of the two frequencies overlapped; e.g., at region C in Fig. 3.

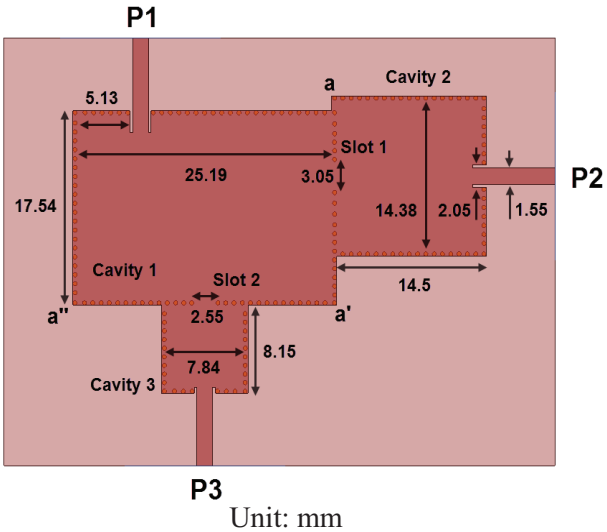

Fig. 2. Geometry of proposed 10/18 GHz diplexer.

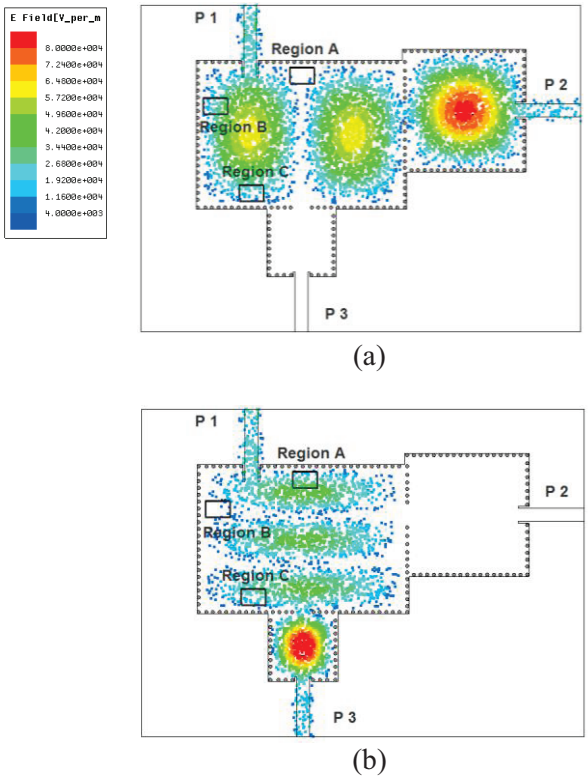

Fig. 3. Electric field distributions of the diplexer at: (a) 10 GHz, and (b) 18 GHz.

Using the equations (4)-(5) and a tuning analysis of the HFSS full-wave simulator, the cavity sizes are determined to be 25.19×17.54×0.508 mm^3 for cavity 1, 14.5×14.38×0.508 mm^3 for cavity 2 and 8.15×7.84×0.508 mm^3 for cavity 3.

The coupling matrix synthesized for 10 GHz filter is:

$$M = \begin{bmatrix} 0 & 0.0122 & 0 & 0 \\ 0.0122 & 0 & 0.0166 & 0 \\ 0 & 0.0166 & 0 & 0.0122 \\ 0 & 0 & 0.0122 & 0 \end{bmatrix}.$$

The coupling matrix synthesized for 18 GHz filter is:

$$M = \begin{bmatrix} 0 & 0.0171 & 0 & 0 \\ 0.0171 & 0 & 0.0232 & 0 \\ 0 & 0.0232 & 0 & 0.0171 \\ 0 & 0 & 0.0171 & 0 \end{bmatrix}.$$

Then, the external quality factor and the inter-resonator coupling coefficients for the two filters of

the diplexer will be obtained by de-normalizing the above generalized coupling matrixes:

$$k_{ij}=FBW\times M_{ij} \quad Q_e=\frac{1}{FBW\times M_{1S}^2} \quad FBW=\frac{BW}{f_0}, \quad (6)$$

where FBW is the frantional bandwidth, BW is the absolute bandwidth and f_0 is the center frequency of the passband. The final parameters of the diplexer are then optimized to meet those external quality factor/coupling coefficients given above [8]. It is also noted that, the external quality factors required by these two filters of the two passband are different for the common cavity (cavity 1), which works as a resonator in both filters. Therefore, the final dimension of the external coupling slot for cavity is chosen to find the balance of meeting the calculated external quality factors for both filters [9]. The detailed dimensions of the diplexer are shown in Fig. 2.

The photograph of the fabricated diplexer is shown in Fig. 4. The S-parameter results of the diplexer were measured using a 2.92 mm southwest super SMA connector. The simulated and measured results for the diplexer are shown in Fig. 5 and Fig. 6. A good agreement between simulations and measurements has been achieved. The measured central frequencies are 10 GHz and 17.9 GHz, and minimum insertion losses are 2 dB at both channels, which are about 0.5 dB larger than simulation predicts. The errors are conjecturally caused by the SMA connectors and manufacturing tolerances. The group delays for both channels are smaller than 0.6 ns in the measurement. The isolation is better than 42 dB for both channels.

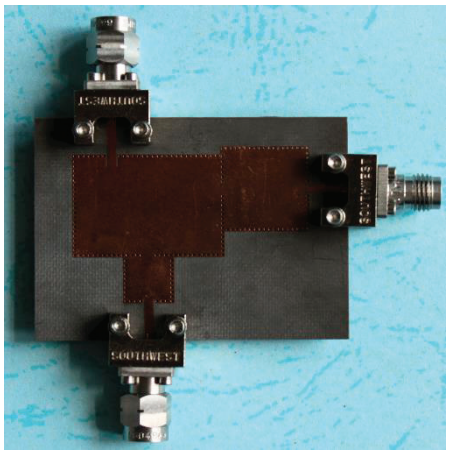

Fig. 4. Photograph of the fabricated diplexer operating at 10 GHz and 18 GHz.

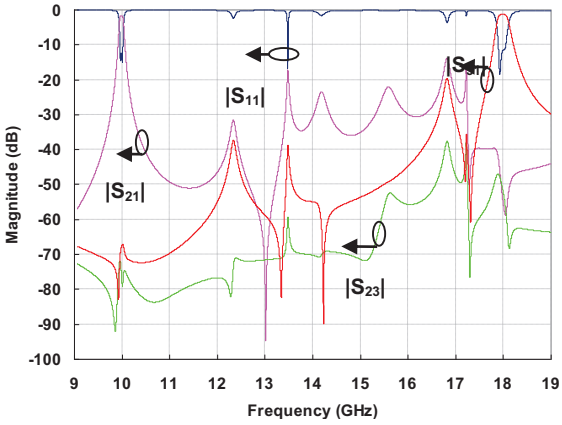

Fig. 5. Simulated S-parameter results of the diplexer.

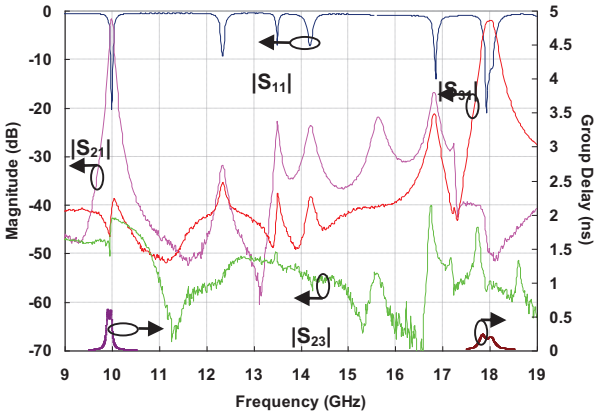

Fig. 6. Measured S-parameter and group delay results of the diplexer.

B. 10/10.5 GHz diplexer

The configuration of the 10/10.5 GHz diplexer is shown in Fig. 7. A fractional bandwidth of 0.5% is required for the 10 GHz filter while it is of 0.8% for the 10.5 GHz filter. The basic configuration and working mechanism of the diplexer is almost the same as the 10/18 GHz one. Cavity 1 is the dual-mode cavity resonating at 10 GHz for TE_{201} mode and 10.5 GHz for TE_{103} mode. Cavity 2 and cavity 3 are single-mode cavities whose resonant frequency is 10 GHz and 10.5 GHz, separately. The coupling slot between cavity 1 and 2 are centered at one-third of the longer side-wall bb' of cavity 1. The coupling slot between cavity 1 and 3 are placed at the center of the shorter side-wall bb'' of cavity 1. The electric field distributions of the diplexer at 10 GHz and 10.5 GHz are plotted in Fig. 8 (a) and (b), respectively.

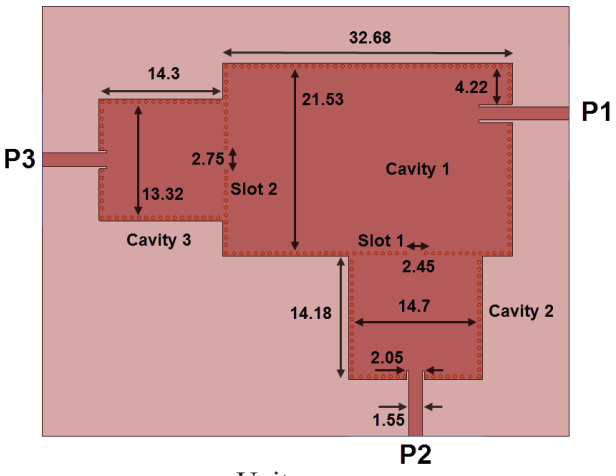

Unit: mm

Fig. 7. Geometry of proposed 10/10.5 GHz diplexer.

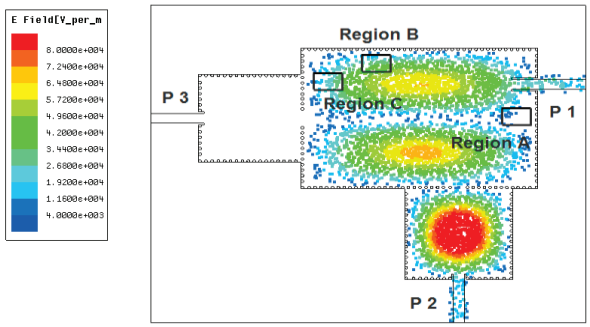

(a)

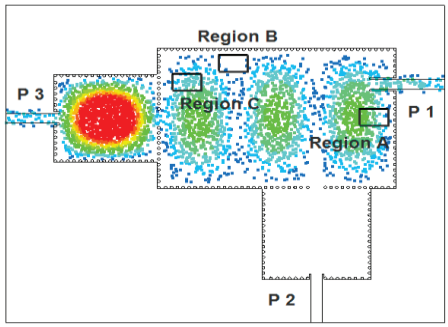

(b)

Fig. 8. Electric field distributions of the diplexer at: (a) 10 GHz, and (b) 10.5 GHz.

Based on the equations (4)-(5), the cavity sizes are optimized to be 32.68×21.53×0.508 mm^3 for cavity 1, 14.7×14.18×0.508 mm^3 for cavity 2 and 14.3×13.32×0.508 mm^3 for cavity 3. As a contrast, if we use a dual-mode cavity of TE_{201} and TE_{301} modes to design this kind of a diplexer, the size of cavity 1 will be 70.8×10.6×0.508 mm^3 and larger than the one of TE_{201} and TE_{103} modes, obviously. The detailed design procedure of this diplexer has been described in Section III.A and is omitted here for brevity.

The photograph of the fabricated diplexer is shown in Fig. 9. The simulated and measured results for the diplexer are shown in Fig. 10 and Fig. 11, respectively. Good agreement between simulations and measurements can also be observed. The insertion losses are both 2.1 dB at the two channels, which are about 0.6 dB larger than those predicted by simulation. The errors are also conjecturally caused by the SMA connectors and manufacturing tolerances. The group delays for both channels are smaller than 1 ns in the measurement. The isolation is better than 49 dB for both channels.

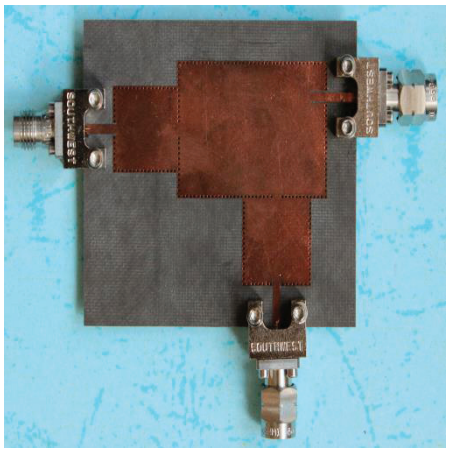

Fig. 9. Photograph of the fabricated diplexer operating at 10 GHz and 10.5 GHz.

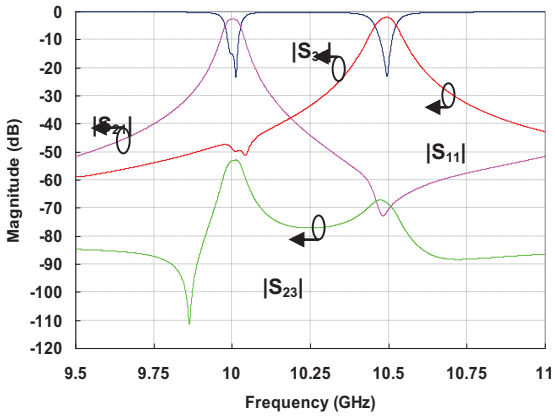

Fig. 10. Simulated S-parameter results of the diplexer.

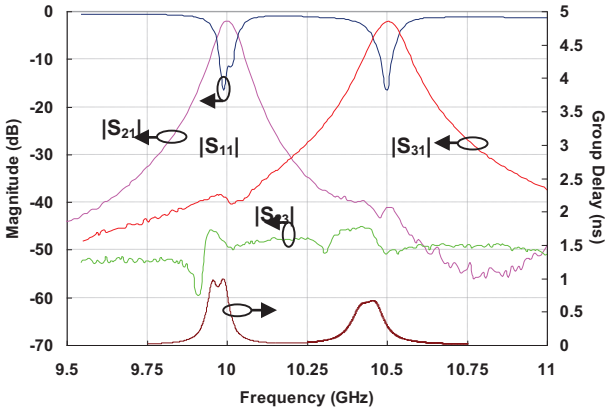

Fig. 11. Measured S-parameter and group delay results of the diplexer.

IV. CONCLUSION

Compared with the design method in our previous work, the diplexer's design method proposed in this paper, using dual-mode SIW cavities resonating at TE_{201} and TE_{103} modes, exhibits advantages of smaller size occupation, better isolation performance and more applicable cases. Two examples of diplexers are designed and implemented. The operating frequencies for the two channels of the two examples are centered either very far or very close for the verification of our design method. Meanwhile, it is easy to construct a higher order diplexer by simply connecting more resonators to those single-mode cavities [e.g., cavity 2 and cavity 3] for a better performance of selectivity. The proposed designs of diplexers are very suitable for different kinds of wireless communication applications.

ACKNOWLEDGMENT

This work is supported by the National Natural Science Foundation of China under Grants 61301044 and 61271136, by the Program for New Century Excellent Talents in University (NCET-11-0993), and by Six Types of Talents Project of Jiangsu Province (2011-DZXX-014).

REFERENCES

[1] T. Yang, P. L. Chi, and T. Itoh, "High isolation and compact diplexer using the hybrid resonators," *IEEE Microw. Wireless Compon. Lett*., vol. 20, no. 10, pp. 551-553, October 2010.

[2] F. Cheng, X. Q. Lin, Z. B. Zhu, L. Y. Wang, and Y. Fan, "High isolation diplexer using quarter-wavelength resonator filter," *Electron. Lett*., vol. 48, no. 6, pp. 330-331, March 2012.

[3] F. M. Vanin, D. Schmitt, and R. Levy, "Dimensional synthesis for wide-band waveguide filters and diplexers," *IEEE Trans. Microw. Theory Tech*., vol. 52, no. 11, pp. 2488-2495, November 2004.

[4] H. W. Deng, Y. J. Zhao, F. Fu, X. J. Zhou, and Y. Y. Liu, "Compact and high isolation microstrip diplexer for GPS and UWB application," *Electron. Lett*., vol. 49, no. 10, pp. 659-661, May 2013.

[5] H. J. Tang, W. Hong, J. X. Chen, G. Q. Luo, and K. Wu, "Development of millimeter wave planar diplexers based on complementary characters of dual-mode substrate integrated waveguide filters with circular and elliptic cavities," *IEEE Trans. Microw. Theory Tech*., vol. 55, no. 4, pp. 776-782, April 2007.

[6] J. H. Lee, N. Kidera, G. Dejean, S. Pinel, J. Laskar, and M. M. Tentzeris, "A V-band front-end with 3-D integrated cavity filters/duplexers and antennas in LTCC technologies," *IEEE Trans. Microw. Theory Tech*., vol. 54, no. 7, pp. 2925-2936, July 2006.

[7] H. Chu, Y. X. Guo, Y. L. Song, and Z. L. Wang, "40/50 GHz diplexer design in LTCC technology," *Electron. Lett*., vol. 47, no. 4, pp. 260-262, February 2011.

[8] J. S. Hong and M. J. Lancaster, "Microstrip filters for RF/microwave applications," *New York: Wiley*, 2001.

[9] H. Chu, L. Bian, and J. X. Chen, "A novel 3D cavity diplexer with compact size using LTCC technologies for V-band wireless communication systems," *To Be Published In Int. J. RF Microwave Comput. Aided Eng.*

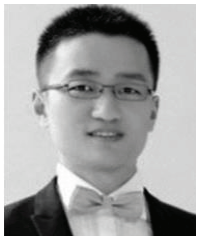

Hui Chu received the M.S. degree from NJUST, Nanjing, China, in 2009, and the Ph.D. degree from NJUST, Nanjing, China, in 2012. He is currently a Lecturer with Nantong University, Jiangsu Province, China. His research interests include antenna/antenna array and passive circuit designs.

Rong Mao was born in Suqian, Jiangsu, China in 1983. She received the M.S. degree from Nanjing University of Science & Technology (NUST), Nanjing, China, in 2006. From 2006 to 2013, she has been with the 14th Institute of China Electronics Technology Group Corporation (CETC 14), where she was an Engineer. Since 2013, she has been with North

Information Control Group Co., Ltd., where she is also an Engineer. Her research interests include electronic circuit designs, embedded software design and the control model simulation.

Jian-Xin Chen was born in Nantong, Jiangsu Province, China, in 1979. He received the B.S. degree from Huai Yin Teachers College, Huai'an City, Jiangsu Province, China, in 2001, the M.S. degree from the University of Electronic Science and Technology of China (UESTC), Chengdu, China, in 2004, and the Ph.D. degree from the City University of Hong Kong, Kowloon, Hong Kong, in 2008. Since 2009, he has been with Nantong University, Jiangsu Province, China, where he is currently a Professor. He has authored or coauthored more than 80 internationally referred journal and conference papers. He holds two Chinese patents and two U.S. patents. His research interests include microwave active/passive circuits and antennas, LTCC-based millimeter-wave circuits and antennas.

Chen was the recipient of the Best Paper Award presented at the Chinese National Microwave and Millimeter-Wave Symposium, Ningbo, China, in 2007. He was Supervisor of 2014 iWEM Student Innovation Competition Winner in Sapporo, Japan.

UWB Monopole Antenna with Dual Band-Notched Function

Y. Ojaroudi [1], S. Ojaroudi [1], and N. Ojaroudi [2]

[1] Young Researchers and Elite Club, Germi Branch
Islamic Azad University, Germi, Iran

[2] Young Researchers and Elite Club, Ardabil Branch
Islamic Azad University, Ardabil, Iran
n.ojaroudi@yahoo.com

Abstract ─ In this letter, an Ultra-Wideband (UWB) monopole antenna with dual frequency band-stop performance is designed and manufactured. In the proposed structure, by inserting an S-shaped parasitic structure inside a square slot in the ground plane a new resonance at higher frequencies can be achieved, which provides a wide usable fractional bandwidth of more than 125%. In order to generate dual band-notched function, we use four L-shaped strips protruded inside square ring. The measured results reveal that the antenna offers a very wide bandwidth from 2.63 to 14.2 GHz with two notched bands covering all the 5.2/5.8 GHz WLAN, 3.5/5.5 GHz WiMAX and 4 GHz C bands. Good VSWR and radiation pattern characteristics are obtained in the frequency band of interest.

Index Terms ─ Dual band-notched function, microstrip-fed antenna, protruded L-shaped strip, ultra-wideband communications.

I. INTRODUCTION

There has been more and more attention in Ultra-Wideband (UWB) antennas ever since the Federal Communications Commission (FCC)'s allocation of the frequency band 3.1-10.6 GHz for commercial use [1]. Designing an antenna to operate in the UWB band is quite a challenge because it has to satisfy the requirements such as ultra wide impedance bandwidth, omni-directional radiation pattern, constant gain, constant group delay, low profile, easy manufacturing, etc. [2-4]. In UWB communication systems, one of key issues is the design of a compact antenna while providing wideband characteristic over the whole operating band. Consequently, a number of microstrip antennas with different geometries have been experimentally characterized [5-8].

There are many narrowband communication systems which severely interfere with the UWB communication system, such as the Worldwide Interoperability Microwave Access (WiMAX) operating at 3.3-3.7 GHz and 5.35-5.65 GHz, Wireless Local Area Network (WLAN) operating at 5.15-5.35 and 5.725-5.825 GHz, etc. Therefore, UWB antennas with band-notched characteristics to filter the potential interference are desirable. Nowadays, to mitigate this effect many UWB antennas with various band-notched properties have developed [9-10]. Many techniques are used to introduce notch band for rejecting the interference in the UWB antennas. It is done either by inserting protruded parasitic structures inside slots [11-12], using slots at radiating stub [13], or with reconfigurable split ring resonator [14].

All of the above methods are used for rejecting a single band of frequencies. However, to effectively utilize the UWB spectrum and to improve the performance of the UWB system, it is desirable to design the UWB antenna with dual band rejection. It will help to minimize the interference between the narrow band systems with the UWB system. Some methods are used to obtain the dual band rejection in the literature [15-18].

In this paper, a new and compact microstrip-fed monopole antenna with enhanced bandwidth and dual band-notched characteristics for UWB

Submitted On: August 16, 2013
Accepted On: September 28, 2014

applications has been designed and manufactured. The proposed antenna has a small size of 12×18 mm^2, or about 0.15λ×0.25λ at 4.2 GHz (first resonance frequency), which has a size reduction of 28% with respect to the previous similar antenna [4-6].

II. ANTENNA DESIGN

The presented small square monopole antenna fed by a microstrip line is shown in Fig. 1 and printed on an FR4 substrate of thickness 0.8 mm, permittivity 4.4, and loss tangent 0.018. The basic monopole antenna structure consists of a square radiating patch, a feed line, and a ground plane. The proposed antenna is connected to a 50-Ω SMA connector for signal transmission.

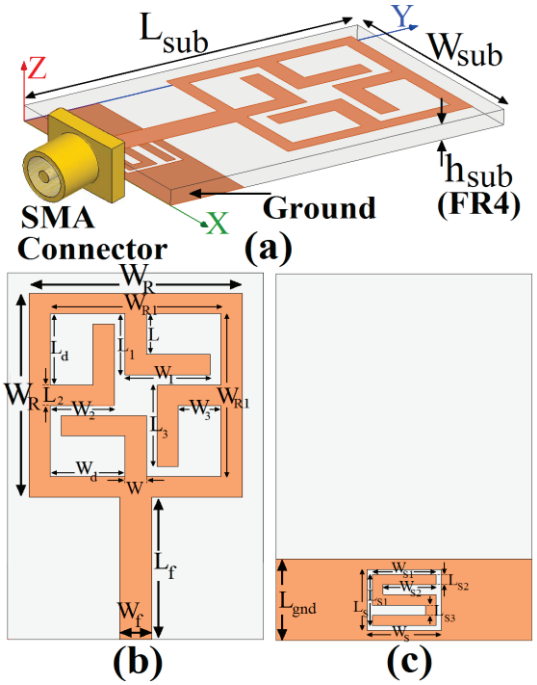

Fig. 1. Geometry of the proposed antenna :(a) side view, (b) top layer, and (c) bottom layer.

In this work, we start by choosing the dimensions of the designed antenna. These parameters including the substrate is $W_{sub}\times L_{sub}=12\times18$ mm^2 or about 0.15λ×0.25λ at 4.4 GHz (the first resonance frequency of the ordinary monopole antenna). We have a lot of flexibility in choosing the width of the radiating patch. This parameter mostly affects the antenna bandwidth. As W_R decreases, so does the antenna bandwidth, and vice versa. Next step, we have to determine the length of the radiating patch. This parameter is approximately $\lambda_{lower}/4$, where λ_{lower} is the lower bandwidth frequency wavelength. λ_{lower} depends on a number of parameters such as the monopole width as well as the thickness and dielectric constant of the substrate on which the antenna is fabricated.

The last and final step in the design is to choose the length of the resonator and the band-stop filter elements. In this design, the optimized length $L_{resonance}$ is set to resonate at $0.25\lambda_{resonance}$, where $L_{resonance}=W_{S2}+L_{S2}+0.5W_{S2}$. Also, the optimized length L_{notch} is set to band-stop resonate at $0.5\lambda_{notch}$, where $L_{notch1}=L_2+W_2+L_3+L_d$, and $L_{notch2}=L_1+W_1+2W$. λ_{notch1} and λ_{notch2} corresponds to first band-notch frequency (3.9 GHz) and second band-notch frequency (5.5 GHz), respectively.

In this study, the square slot with S-shaped parasitic structure inside slot in the ground plane is used to perturb an additional resonance at higher frequencies [19], and the L-shaped strips protruded inside square-ring radiating patch are used to give a dual frequency band-notch operation.

III. RESULTS AND DISCUSSIONS

The planar monopole antenna with various design parameters was constructed, and the numerical and experimental results of the input impedance and radiation characteristics are presented and discussed. The analysis and performance of the proposed antenna is explored by using Ansoft simulation software High-Frequency Structure Simulator (HFSS) [20], for better impedance matching. The final dimensions of the antenna parameters are specified in Table 1.

Table 1: Final dimensions of proposed antenna

Parameter	W_{sub}	L_{sub}	h_{sub}	W_R	L_{gnd}
Value (mm)	12	18	1.6	10	4
Parameter	W_{R1}	L_f	W_f	W	L
Value (mm)	8	7	1.5	0.5	2.5
Parameter	W_1	L_1	W_2	L_2	W_3
Value (mm)	4	3	3	0.5	0.5
Parameter	L_3	W_S	L_S	W_{S1}	L_{S1}
Value (mm)	4	3	3	2.5	2.5
Parameter	W_{S2}	L_{S2}	L_{S3}	L_d	W_d
Value (mm)	2	0.5	0.5	3.75	3.75

Geometry for the ordinary square monopole antenna [Fig. 2 (a)], with S-shaped parasitic structure inside square slot in the ground plane [Fig. 2 (b)], with S-shaped parasitic structure inside square slot in the ground plane and square ring radiating patch with a pair of L-shaped strips protruded inside square ring [Fig. 2 (c)], and the proposed antenna structure [Fig. 2 (d)] are shown in Fig. 2.

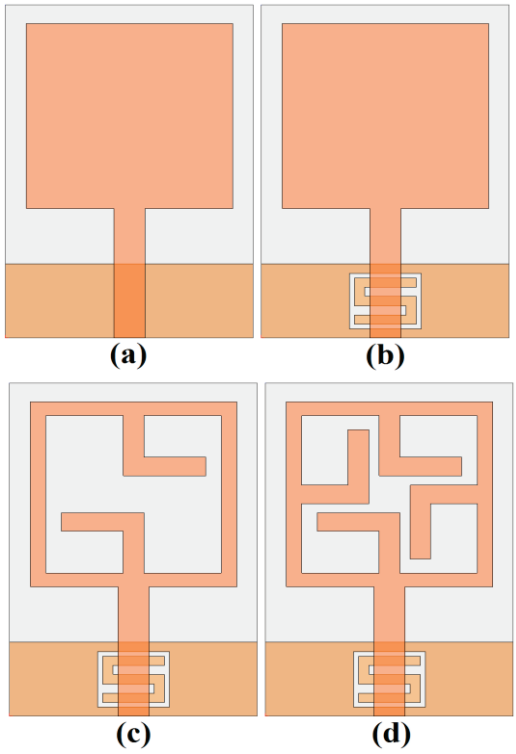

Fig. 2. Various structures for the proposed antenna: (a) ordinary square antenna, (b) with S-shaped parasitic structure inside square slot in the ground plane, (c) with S-shaped parasitic structure inside square slot and square ring radiating patch with a pair of L-shaped strips protruded inside the square ring, and (d) the proposed antenna.

VSWR characteristics for the structures that were shown in Fig. 2 are compared in Fig. 3. As shown in Fig. 3, it is observed by inserting an S-shaped parasitic structure inside the square slot in the ground plane the impedance bandwidth is effectively improved at the upper frequency; also, by creating a square-ring radiating patch with four L-shaped strips protruded inside ring, dual band-notch characteristic is generated.

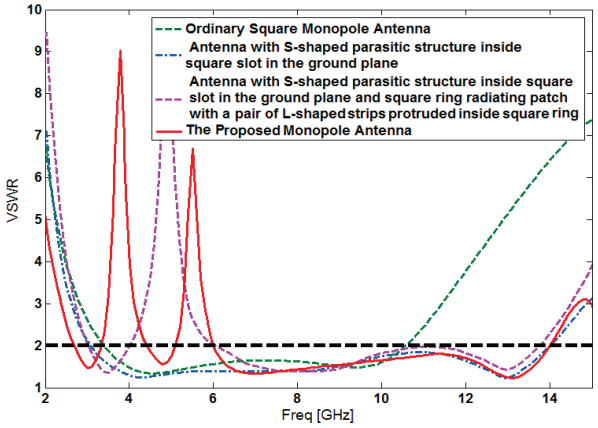

Fig. 3. Simulated VSWR characteristics for the various antennas shown in Fig. 2.

To understand the phenomenon behind this additional resonance performance, simulated current distributions in the ground plane for the proposed antenna at 13.1 GHz are presented in Fig. 4 (a). It is found that by using an S-shaped parasitic structure inside the square slot, third resonance at 13.1 GHz can be achieved. Another important parameter of this structure is the square-ring radiating patch with four L-shaped strips protruded inside the ring. Figures 4 (b) and (c) present the simulated current distributions on this radiating patch at the notched frequencies (3.8 & 5.5 GHz). As shown in Figs. 4 (b) and (c), at the notched frequencies the current flows are more dominant on the L-shaped strips inside the square-ring radiating patch [21-25].

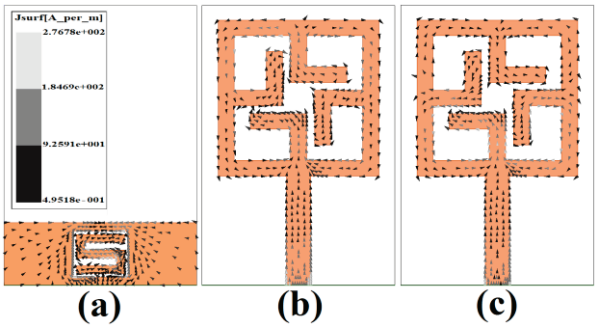

Fig. 4. Simulated surface current distributions on radiating patch for the proposed antenna: (a) in the ground plane at 10.95 GHz (new resonance frequency), (b) at radiating patch at 3.8 GHz (first notched frequency), and (c) at 5.5 GHz (second notched frequency).

The proposed microstrip monopole antenna with final design as shown in Fig. 5 was built and tested, and the VSWR characteristic was measured using a network analyzer in an anechoic chamber. The radiation patterns have been measured inside an anechoic chamber using a double-ridged horn antenna as a reference antenna placed at a distance of 2 m. Also, a two-antenna technique using a spectrum analyzer and a double-ridged horn antenna as a reference antenna placed at a distance of 2 m, is used to measure the radiation gain in the z axis direction (x-z plane).

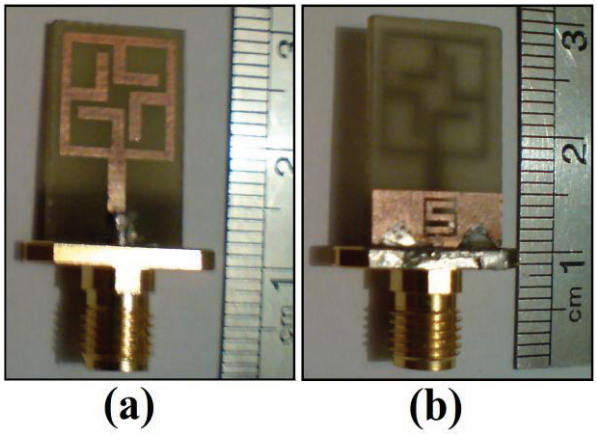

Fig. 5. Photograph of the realized printed monopole antenna: (a) top view, and (b) bottom view.

Figure 6 shows the measured and simulated VSWR characteristics of the proposed antenna. As shown, the fabricated antenna has the frequency band of 2.63 to 14.20 GHz with two rejection bands around 3.32-4.23 and 5.08-5.94 GHz. Figure 7 illustrates the measured radiation patterns, including the co-polarization, in H-plane (E_φ in x-y) and E-plane (E_θ in y-z). It can be seen that quasi-omnidirectional radiation pattern can be observed on x-z plane over the whole UWB frequency range for the three frequencies [26-27].

The radiation patterns on the y-z plane displays a typical figure-of-eight, similar to that of a conventional dipole antenna. It should be noticed that the radiation patterns in E-plane become imbalanced as frequency increases, because of the increasing effects of the cross-polarization. The patterns indicate at higher frequencies, more ripples can be observed in both E- and H-planes, owing to the generation of higher-order modes.

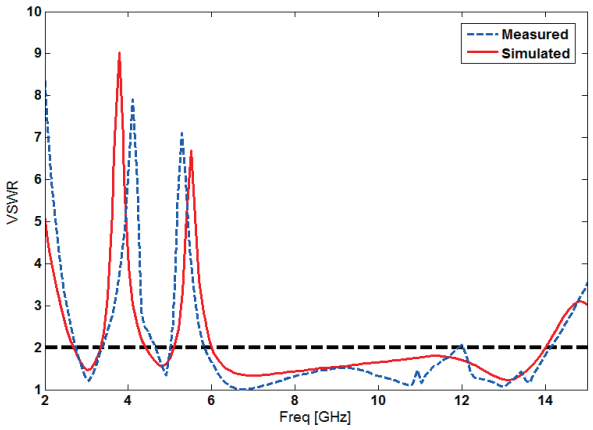

Fig. 6. Measured and simulated VSWR characteristics for the proposed antenna.

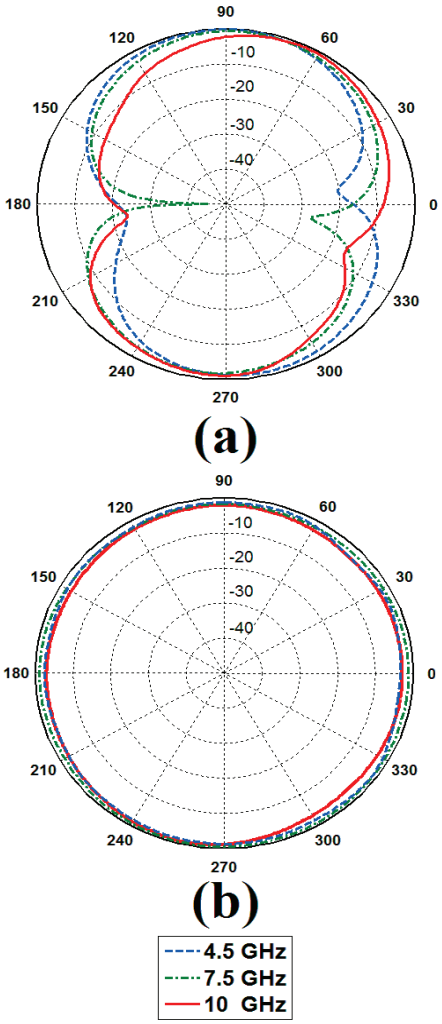

Fig. 7. Measured radiation patterns of the proposed antenna: (a) E_θ in *y-z* plane, and (b) E_φ in *x-y* plane.

Figure 8 shows the measured maximum gain for the proposed monopole antenna. Two sharp decreases of maximum gain in the notched frequencies band at 4 and 5.5 GHz are noticed [28-30].

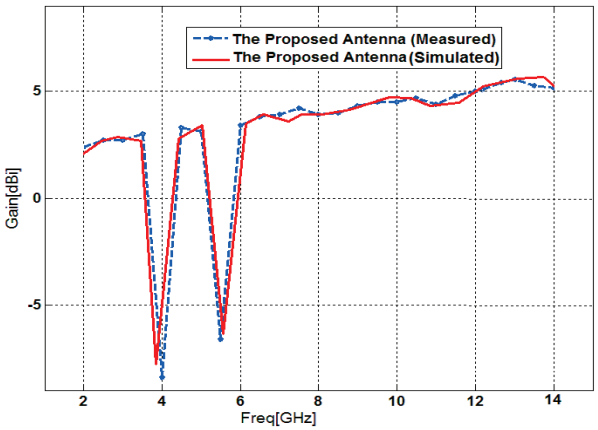

Fig. 8. Measured and simulated maximum gain for the proposed monopole antenna.

IV. CONCLUSION

In this paper, a novel small square monopole antenna with single and dual band-notched characteristics and wide bandwidth capability for UWB applications is analyzed. Proposed dual band-notched antenna can operate from 2.63 to 14.20 GHz with two rejection bands around 3.32-4.23 and 5.08-5.94 GHz. The designed antenna has small size. Good VSWR and radiation pattern characteristics are obtained in the frequency band of interest.

ACKNOWLEDGMENT

The authors are thankful to Microwave Technology (MWT) Company staff for their beneficial and professional help (www.microwave-technology.com).

REFERENCES

[1] D. Cheng, "Compact ultra wideband microstrip resonating antenna," *US Patent 7872606*, January 2011.

[2] Z. N. Chen, "Impedance characteristics of planar bow-tie-like monopole antennas," *Electronics Letters*, vol. 36 (13), pp. 1100-1101, June 2000.

[3] N. Ojaroudi, "Design of ultra-wideband monopole antenna with enhanced bandwidth," *21st Telecommunications Forum, TELFOR 2013*, Belgrade, Serbia, pp. 1043-1046, November 27-28, 2013.

[4] N. Ojaroudi, "A new design of koch fractal slot antenna for ultra-wideband applications," *21st Telecommunications Forum, TELFOR 2013*, Belgrade, Serbia, pp. 1051-1054, November 27-28, 2013.

[5] N. Ojaroudi, "Compact UWB monopole antenna with enhanced bandwidth using rotated L-shaped slots and parasitic structures," *Microw. Opt. Technol. Lett.*, vol. 56, pp. 175-178, 2014.

[6] N. Ojaroudi, M. Ojaroudi, and N. Ghadimi, "UWB omnidirectional square monopole antenna for use in circular cylindrical microwave imaging systems," *IEEE Antennas Wireless Propag. Lett.*, vol. 11, pp. 1350-1353, 2012.

[7] N. Ojaroudi, "Bandwidth improvement of monopole antenna using π-shaped slot and conductor-backed plane," *International Journal of Wireless Communications, Networking and Mobile Computing*, vol. 1, no. 2, pp. 14-19, 2014.

[8] N. Ojaroudi, S. Amiri, and F. Geran, "A novel design of reconfigurable monopole antenna for UWB applications," *Applied Computational Electromagnetics Society (ACES) Journal*, vol. 28, no. 6, pp. 633-639, July 2013.

[9] T. Dissanayake and K. P. Esselle, "Prediction of the notch frequency of slot loaded printed UWB antennas," *IEEE Trans. Antennas and Propag.*, vol. 55, no. 11, pp. 3320-3325, 2007.

[10] N. Ojaroudi, "Design of small reconfigurable microstrip antenna for UWB-CR applications," *19th International Symposium on Antenna and Propagation, ISAP2014*, Kaohsiung, Taiwan, December 2-5, 2012.

[11] N. Ojaroudi, "Application of protruded strip resonators to design an UWB slot antenna with WLAN band-notched characteristic," *Progress In Electromagnetics Research C*, vol. 47, pp. 111-117, 2014.

[12] N. Ojaroudi, "A modified compact microstrip-fed slot antenna with desired WLAN band-notched characteristic," *American Journal of Computation, Communication and Control*, vol. 1, no. 3, pp. 56-60, 2014.

[13] T. G. Ma and S. J. Wu, "Ultrawideband band-notched folded strip monopole antenna," *IEEE Trans. Antennas Propag.*, vol. 55, no. 9, pp. 2473-2479, 2007.

[14] N. Ojaroudi, S. Amiri, and F. Geran, "Reconfigurable monopole antenna with controllable band-notched performance for UWB communications," *20th Telecommunications Forum, TELFOR 2012*, Belgrade, Serbia, November 20-22, 2012.

[15] J. William and R. Nakkeeran, "A new UWB slot antenna with rejection of WiMax and WLAN

bands," *Applied Computational Electromagnetic Society (ACES) Journal*, vol. 25, no. 9, pp. 787-793, September 2010.

[16] N. Ojaroudi, "Microstrip monopole antenna with dual band-stop function for UWB applications," *Microw. Opt. Technol. Lett*., vol. 56, pp. 562-564, 2014.

[17] N. Ojaroudi, "Circular microstrip antenna with dual band-stop performance for ultra-wideband systems," *Microw. Opt. Technol. Lett*., vol. 56, pp. 2095-2098, 2014.

[18] M. C. Tang, S. Xiao, T. Deng, D. Wang, J. Guan, B. Wang, and G. D. Ge, "Compact UWB antenna with multiple band-notches for WiMAX and WLAN," *IEEE Trans. Antennas and Propag.*, vol. 59, no. 4, pp. 1372-1376, 2011.

[19] N. Ojaroudi, "An UWB microstrip antenna with dual band-stop performance using a meander-line resonator," *In Proceedings of the 22nd International Conference on Software, Telecommunications and Computer Networks (SoftCOM)*, Split, Croatia, September 17-19, 2014.

[20] "Ansoft high frequency structure simulator (HFSS)," ver. 13, *Ansoft Corporation*, Pittsburgh, PA, 2010.

[21] N. Ojaroudi, "Design of microstrip antenna for 2.4/5.8 GHz RFID applications," *German Microwave Conference, GeMic 2014*, RWTH Aachen University, Germany, March 10-12, 2014.

[22] N. Ojaroudi, H. Ojaroudi, and Y. Ojaroudi, "Very low profile ultra-wideband microstrip band-stop filter," *Microw. Opt. Technol. Lett*., vol. 56, pp. 709-711, 2014.

[23] N. Ojaroudi and N. Ghadimi, "Design of CPW-fed slot antenna for MIMO system applications," *Microw. Opt. Technol. Lett*., vol. 56, pp. 1278-1281, 2014.

[24] N. Ojaroudi, "New design of multi-band PIFA for wireless communication systems," *19th International Symposium on Antenna and Propagation, ISAP2014*, Kaohsiung, Taiwan, December 2-5, 2012.

[25] N. Ojaroudi, "Reconfigurable microstrip-fed monopole antenna for multimode application," *In Proceedings of the Loughborough Antennas and Propagation Conference (LAPC '14)*, Loughborough, UK, November 10-11, 2014.

[26] N. Ojaroudi, "Microstrip monopole antenna with dual band-stop function for ultra-wideband applications," *Microw. Opt. Technol. Lett*., vol. 56, pp. 818-822, 2014.

[27] N. Ojaroudi, "Small microstrip-fed slot antenna with frequency band-stop function," *21st Telecommunications Forum, TELFOR 2013*, Belgrade, Serbia, pp. 1047-1050, November 27-28, 2013.

[28] N. Ojaroudi, H. Ojaroudi, and N. Ghadimi, "Quad-band planar inverted-f antenna (pifa) for wireless communication systems," *Progress In Electromagnetics Research Letters*, vol. 45, 51-56, 2014.

[29] N. Ojaroudi, "Design of UWB monopole antenna with dual band-stop characteristic," *In Proceedings of the Loughborough Antennas and Propagation Conference (LAPC '14)*, Loughborough, UK, November 10-11, 2014.

[30] N. Ojaroudi, "Application of protruded Γ-shaped strips at the feed-line of UWB microstrip antenna to create dual notched bands," *International Journal of Wireless Communications, Networking and Mobile Computing*, vol. 1, no. 1, pp. 8-13, 2014.

UWB-MIMO Quadruple with FSS-Inspired Decoupling Structures and Defected Grounds

Tayyab Shabbir [1], Rashid Saleem [1], Adeel Akram [1], and Farhan Shafique [2]

[1] Department of Telecommunication Engineering
University of Engineering and Technology, Taxila, 47050, Pakistan
Rashid.Saleem@uettaxila.edu.pk

[2] Centre for Advance Studies in Telecommunication
COMSATS Institute of Information Technology, Park Road, Chak Shahzad, Islamabad, 44000, Pakistan
Farhan.Shafique@comsats.edu.pk

Abstract ─ In this paper, a quad element Ultra Wideband Multiple-Input Multiple-Output (UWB-MIMO) antenna system is presented. The proposed design is compact as it has four semi-elliptical shaped antennas along with the decoupling structures, fabricated on a compact substrate. The substrate employed is a low cost FR-4 laminate. The antenna elements are decoupled by employing Defected Ground Structures (DGS) and structures inspired from Frequency Selective Surfaces. An enhanced impedance match over lower to medium band is achieved by introducing dipole-like parasitic stubs on rear sides of the antennas. Measured results show that the isolation achieved by the proposed design is more than 20 dB over desired frequency band.

Index Terms ─ Frequency Selective Surface (FSS), Multiple Input Multiple Output (MIMO), Ultra Wideband (UWB).

I. INTRODUCTION

A radio system that has a bandwidth more than 25 percent of its center frequency or a bandwidth more than 500 MHz may be defined as UWB. The UWB technology has drawn significant research attention due to low cost, high data rates and low power requirements [1]. The Federal Communication Commission (FCC) has allocated a frequency band of 3.1-10.6 GHz for the UWB technology [2].

A MIMO system needs a number of transmitters and receivers which operate concurrently to achieve system diversity gain [3-5]. However, placing multiple antennas in the limited space of a transceiver poses a significant challenge in the incorporation of MIMO technique. The individual antennas not only have to be impedance matched but also effectively isolated/decoupled from the neighboring MIMO antennas. The more the antennas in the MIMO transceiver, greater is the design challenge. As far as decoupling is concerned, one of the methods is to place antennas far apart. However, this method is not efficient as it is wasteful of space. Therefore, an efficiently designed decoupling/ isolation structure isolates all the antenna elements while not compromising space [6]. Compact MIMO systems for two elements has been proposed in [4,5] to cover the UWB frequency spectra with maximum isolation of 20 dB. The MIMO systems reported in [7,8] are designed to cover the lower and upper band of LTE with isolation of 15 dB and 20 dB, respectively. In [9], four element MIMO array with isolation of 15 dB was designed for the WLAN application. A four element MIMO system is reported in [3] to cover a band of 1.63 to 2.05 GHz.

Here in this work, a UWB-MIMO antenna quadruple is presented. Finite Element Method (FEM) based simulations in Ansys High Frequency Structure Simulator (HFSS) are employed for the proposed design. The fabricated UWB-MIMO quadruple is shown in Figs. 1 (a)

Submitted On: May 5, 2014
Accepted On: October 9, 2014

and 1(b).

As shown in Figs. 1 (a) and 2 (a), the quad antenna elements are semi-elliptical in shape. Each antenna has four rectangular structures placed on the top edge. These rectangular structures act as parasitic patches and provide better resonances, and in turn, an overall enhanced impedance match. Defected Ground Structures (DGS) are present on the rear side of antenna along with semi-circular arcs and vertical stub sections. The DGS provides enhanced impedance match, especially on the middle operating frequencies. Moreover, to further improve impedance match on the middle frequencies, miniature dipole-like parasitic structures [10] are placed on middle of the rear sides of antenna.

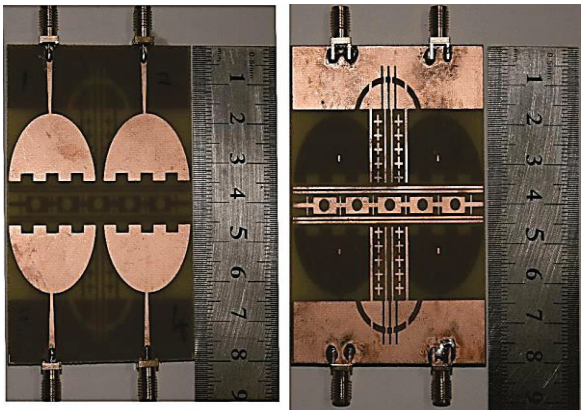

(a) Front view (b) Back view

Fig. 1. Fabricated antenna.

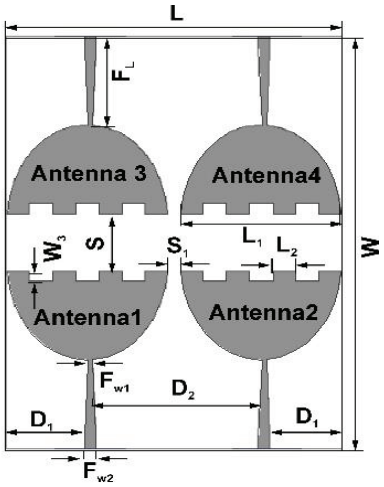

(a) Front view

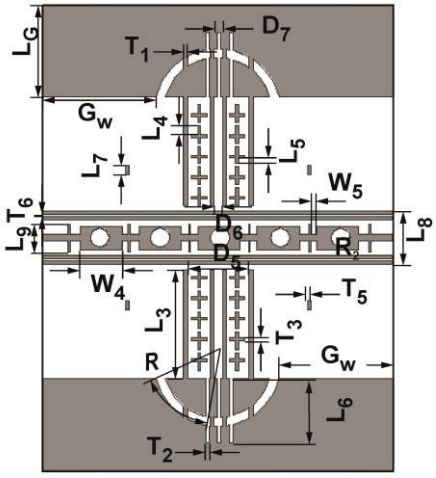

(b) Back view

Fig. 2. UWB-MIMO simulated design.

The decoupled UWB-MIMO quadruple is presented with novel isolation/decoupling structures. As the quadruple is designed for MIMO communication, there are two main challenges in the design. First challenge, is to keep the impedance match of the individual antennas while maintaining a considerable level of decoupling among all of the antenna elements [8]. Second challenge, is to manage overall compactness of the UWB-MIMO array while adjusting four antenna elements and the decoupling structures on the substrate. The antennas placed side-by-side are decoupled by cross-shaped structures placed between pairs of narrow vertical strips attached to the DGS. The cross-shaped structures are similar to those employed in the design of FSSs [11]. Over most of the frequency band, an isolation of 20 dB between the antennas placed side-by-side is achieved by this linear arrangement of cross-shaped structures. The antenna pairs placed across each other are again decoupled by an FSS-inspired structure. This chain-like structure is an alternating combination of crosses and rectangular patches which have miniature circular slots. In general, in most of the frequency band, an isolation of 20 dB is achieved between antennas placed across or diagonally across each other.

The layout of the rest of this paper is as follows: in Section II a discussion of the antenna

elements is given, the FSS-inspired decoupling structures are discussed in Section III, simulated and measured results are discussed in Section IV, and finally in Section V the paper is concluded.

II. ANTENNA ELEMENT DESIGN

The geometry and design of proposed UWB-MIMO system is shown in Figs. 1 and 2. The system is fabricated on an FR-4 substrate of thickness of 1 mm. The proposed MIMO system is compact with dimensions of L=58 mm × W=79 mm. The top layer comprises of quadruple antenna elements; whereas, the ground planes are etched on substrate flip side. The proposed design consists of quadruple semi-elliptical radiating elements. The radiators are independently impedance matched to a 50-Ω tapered feed line of length F_L=17 mm. The taper of this feed line is created by straight lines. The feed line has width of F_{W2}=2 mm at the SMA pcb-type connector and gradually reduces to F_{W1}=0.67 mm at the antenna. The feed lines are separated by a distance D_2=28 mm and located at a distance D_1=13 mm from substrate edges. The antennas are semi-elliptical in order to provide an enhanced impedance bandwidth. The semi-elliptical elements have major axis radii of 18 mm and axial ratios of 0.77. The antenna top end width is kept at L_1=27 mm. The antenna placed side-by-side are separated by a distance of S_1=4 mm at the top ends. However, the antennas placed across each other are separated by a distance of only S=11 mm, so an overall compact size is maintained. Each radiating element has four parasitic structures placed on the top edge. These parasitic structures provide more resonances, or in other words, an enhanced impedance match. Each of these rectangles have dimensions of L_2=4 mm × W_3=2 mm. In the proposed design, a single DGS is shared by antennas placed beside each other. This DGS has dimensions of W=58 mm × L_G=16 mm.

III. DESIGN OF DECOUPLING STRUCTURES

The geometry and design of proposed decoupled UWB-MIMO quadruple is shown in Figs. 1 and 2. The proposed quadruple is mutually decoupled by employing a total of four different arrangements of decoupling structures etched on flip side of the substrate.

A. Decoupling structure for side-by-side antennas

The antennas placed side-by-side are decoupled by multiple structures. First of these multiple structures are cross-shaped. As may be observed, these crosses are placed between narrow vertical strips attached to the DGS. The outer vertical strips are separated by a distance of D_5=15 mm and have dimensions of L_3=10 mm × T_3=1 mm. The inner vertical strips are detached by a distance of D_6=5 mm and have dimensions of L_3=10 mm × T_2=0.5 mm. The crosses each have dimensions of L_4=2 mm × T_3=0.5 mm; L_5=2.5 mm × T_3=0.5 mm.

Second of these decoupling structures are the DGS. A semi-circular slot of radius R=10 mm and width 1 mm is etched in the shared ground plane. Moreover, four vertical stubs are introduced in the circular slot to provide impedance match over the middle frequency band [12]. These slots have dimensions of L_6=2.5 mm × T_2=0.5 mm and a separation of D_7=3 mm. Overall, the proposed circular shaped DGS serves dual purpose of a high order matching network as well as an effective decoupling structure by suppressing the undesired induced currents.

Third of these multiple decoupling structures are four miniature dipole stubs. These stubs are placed behind each radiation element. Dimensions of each stub are L_7=1.5 mm × T_5=0.5 mm. These stubs serve dual purpose of improving the isolation on the lower frequency band and enhancing the impedance bandwidth.

B. Decoupling structures for antennas placed across each other

The antenna pairs placed across each other are separated by a distance of only L_8=11 mm. Therefore, an effective decoupling/isolating structure has to be employed to provide isolation between antennas placed across and diagonally across each other. This decoupling is achieved by the fourth decoupling arrangement. As shown in Figs. 1 (b) and 2 (b), antennas placed across are decoupled by a chain-like arrangement of crosses and rectangular patches. This chain-like structure

is enclosed by double strips on either side. The cross-shaped structures have dimensions of L_9=5 mm × T_5=1 mm; whereas, the rectangular patches have dimensions of W_4=10 mm × L_9=5 mm. The circular slots introduced in each rectangular patch have radii of R_2=2 mm.

IV. SIMULATION AND MEARUREMENTS

A. Decoupling performance

To demonstrate the isolation/decoupling performance, the proposed UWB-MIMO quadruple is simulated, with and without the decoupling arrangement. The simulated and measured insertion loss plots are shown in Fig. 3. As shown in Fig. 3 (a), the isolation between antennas placed side-by-side is not effective without a decoupling structure. However, introduction of the decoupling structure achieves an isolation of more than 20 dB over most of the frequency band. The simulation results for antennas placed across are presented in Fig. 3 (b). It may be observed that, for antennas placed across, without parallel strips enclosed chain structure, considerable isolation cannot be achieved. However, introduction of the chain-like structure achieves an isolation of more than 20 dB over most of the frequency band. The simulation results for antennas placed diagonally across are presented in Fig. 3 (c). For antennas placed diagonally across each other, the decoupling is better when the chain-like decoupling structure is introduced. With the decoupling structure, an isolation of over 25 dB is achieved. Simulated and measured results are shown in Table 1.

Table 1: Comparison of measured isolation; with and without decoupling structure

Frequency (GHz)	Side-by-Side with/without Decoupling Structure (dB)	Placed Across with/without Decoupling Structure (dB)	Diagonally Across with/without Decoupling Structure (dB)
3	-17.5/-8	-15/-18	-34/-20
7	-34/-11.5	-35/-11.3	-38/-16
9	-16/-13	-29/-15	-37/-20

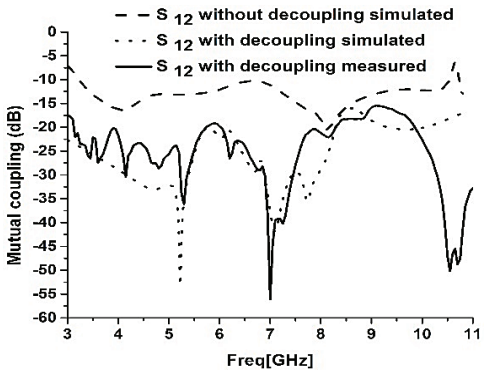

(a) Side-by-side antennas: 1 and 2

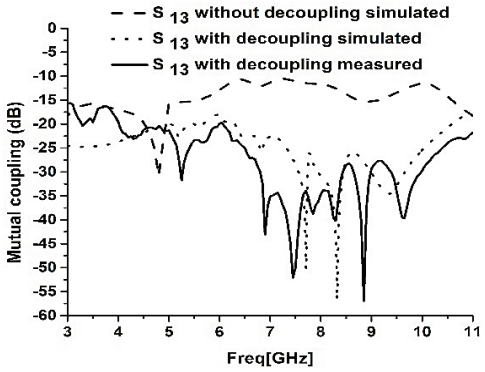

(b) Antenna placed across: 1 and 3

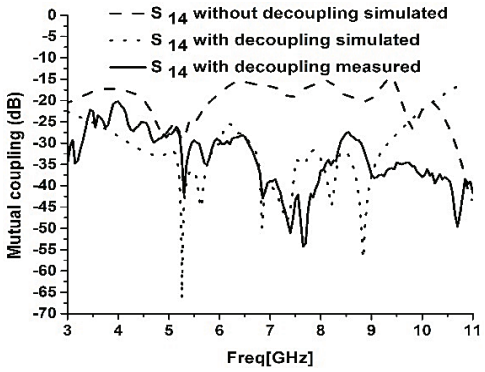

(c) Antenna placed diagonally across: 1 and 4

Fig. 3. Decoupling/isolation between antennas.

B. Higher band impedance enhancement

A comparison of return loss performance of the proposed UWB-MIMO quadruple is presented in this section. Simulated vs. measured results are plotted in Fig. 4. It may be observed that, in the absence of the decoupling structures, there is mismatch at the higher frequency band; i.e., 8-10 GHz. However, when the isolation/decoupling structures are placed, a match on this frequency band is achieved.

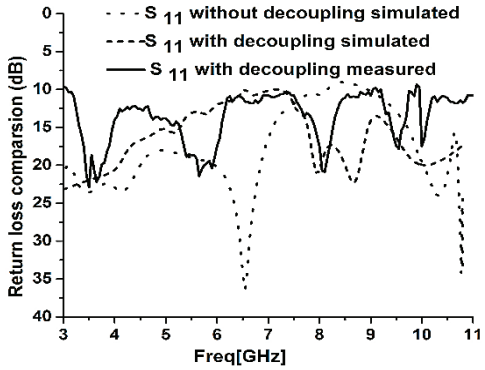

(a) Antenna 1

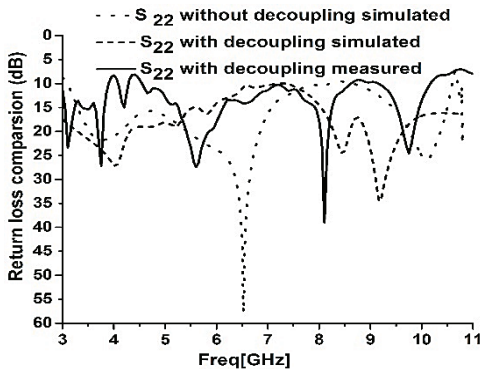

(b) Antenna 2

Fig. 4. Decoupling/isolation between antennas.

C. Total active reflection coefficient

The Total Active Reflection Coefficient, TARC, is defined as the square root of the ratio of reflected power to the incident power. It may be viewed as return loss of the overall MIMO system [13]. The value of TARC for the proposed quadruple is plotted in Fig. 5 (a).

D. Channel capacity loss

Channel capacity of a MIMO systems increases with increase in number of antennas. However, mutual coupling causes a capacity loss in MIMO systems. The acceptable value of channel capacity loss for MIMO system is reported as less than 0.4 bit/sec/Hz [7]. The measured and simulated channel capacity loss plots are shown in Fig. 5 (b). The plots indicate that proposed MIMO system has a capacity loss value below 0.4 bits/sec/Hz.

E. Radiation characteristics

The radiation characteristics of the proposed antenna quadruple is investigated at frequencies 4 and 8 GHz. Simulated radiation patterns for E-field and H-field are shown in Fig. 5 (c). The radiation pattern is found to be nearly omni-directional at 4 GHz. The radiation pattern at 8 GHz depicts distortion within the tolerable limit.

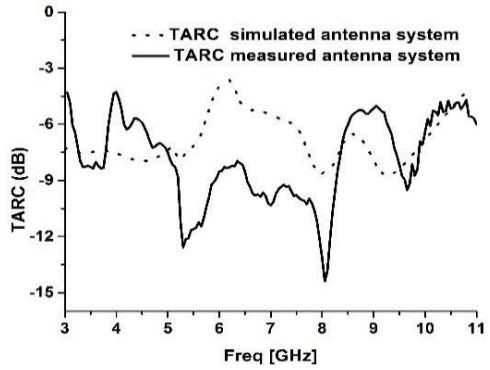

(a) Total active reflection coefficient, TARC

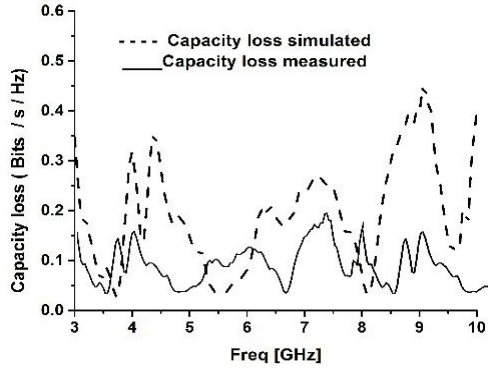

(b) Channel capacity loss, CCL

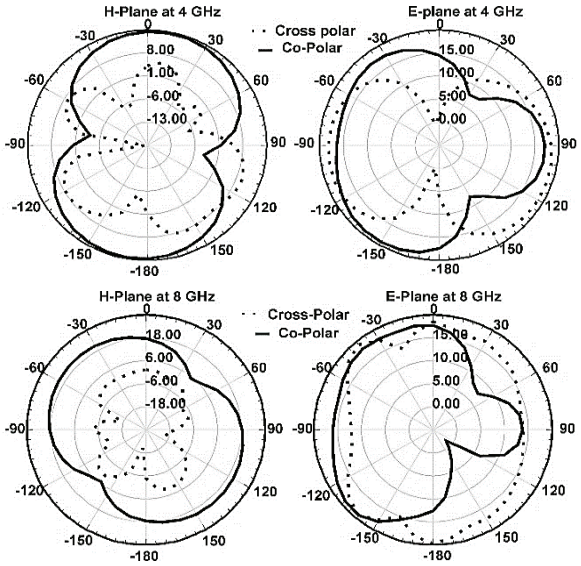

(c) E- and H-plane radiation at 4 and 8 GHz

Fig. 5. TARC, CCL and radiation patterns.

V. CONCLUSION

This paper proposes a quad element UWB-MIMO antenna system. Four mutually decoupled antenna elements are fabricated on a 1 mm thick FR-4 substrate. To achieve enhanced isolation/ decoupling among the antenna elements, DGS and FSS-inspired decoupling structures are employed. The design exhibits impedance match as well as isolation over the entire UWB frequency band. The isolation among antennas, whether placed side-by-side, across or diagonally across is at least 20 dB. More importantly, the proposed design does not compromise compactness while achieving impedance match and isolation.

ACKNOWLEDGMENT

Authors like to thank the National ICT R&D fund for their financial support under Grant No. ICTRDF/HRD/2011/31.

REFERENCES

[1] N. Gogosh, M. F. Shafique, R. Saleem, I. Usman, and A. M. Faiz, "An UWB diversity antenna array with a novel H-type decoupling structure," *Microwave and Optical Technology Letters*, vol. 55, no. 11, pp. 2715-2720, 2013.

[2] S. Mohammad, A. Nezhad, H. R. Hassani, and A. Foudazi, "A dual-band WLAN/UWB printed wide slot antenna for MIMO/diversity applications," *Microwave and Optical Technology Letters*, vol. 55, no. 3, pp. 461-465, 2013.

[3] S. Zhang, P. Zetterberg, and S. He, "Printed MIMO antenna system of four closely-spaced elements with large bandwidth and high isolation," *Electronics Letters*, vol. 46, no. 15, pp. 1052-1053, 2010.

[4] S. Zhang, B. K. Lau, A. Sunesson, and S. He, "Closely packed UWB MIMO/diversity antenna with different patterns and polarizations for USB dongle applications," *IEEE Transactions on Antennas and Propagation*, vol. 60, no. 9, pp. 4372-4380, 2012.

[5] L. Liu, S. Cheung, and T. Yuk, "Compact MIMO antenna for portable devices in UWB applications," *IEEE Transactions on Antennas and Propagation*, vol. 61, no. 8, pp. 4257-4264, 2013.

[6] S. Park and C. Jung, "Compact MIMO antenna with high isolation performance," *Electronics Letters*, vol. 46, no. 6, pp. 390-391, 2010.

[7] X. Zhou, X. Quan, and R. Li, "A dual-broadband MIMO antenna system for GSM/UMTS/LTE and WLAN handsets," *IEEE Antennas and Wireless Propagation Letters*, vol. 11, pp. 551-554, 2012.

[8] M. Sharawi, A. Numan, M. Khan, and D. Aloi, "A dual element dual-band MIMO antenna system with enhanced isolation for mobile terminals," *IEEE Antennas and Wireless Propagation Letters*, vol. 11, pp. 1006-1009, 2012.

[9] J. Kim, J. Ju, S. Eom, M. Song, and N. Kim, "Four channel MIMO antenna for WLAN using hybrid structure," *Electronics Letters*, vol. 49, no. 14, pp. 877-858, 2013.

[10] Z. Li, Z. Du, M. Takahashi, K. Saito, and K. Ito, "Reducing mutual coupling of MIMO antennas with parasitic elements for mobile terminals," *IEEE Transactions on Antennas and Propagation*, vol. 60, no. 2, pp. 473-481, 2012.

[11] M. Li and N. Behdad, "Frequency selective surfaces for pulsed high-power microwave applications," *IEEE Transactions on Antennas and Propagation*, vol. 61, no. 2, pp. 677-687, 2013.

[12] F. Deng, X. Yi, and W. Wu, "Design and performance of a double-layer miniaturized-element frequency selective surface," *IEEE Antennas and Wireless Propagation Letters*, vol. 12, pp. 721-724, 2013.

[13] S. H. Chae, S. K. Oh, and S. O. Park, "Analysis of mutual coupling, correlations, and TARC in wibro MIMO array antenna," *IEEE Antennas and Wireless Propagation Letters*, vol. 6, pp. 122-125, 2007.

Tayyab Shabbir received his B.Sc. degree in Electrical Engineering in 2011 from COMSATS Institute of Information Technology, Islamabad, Pakistan and Masters in Telecommunication Engineering in 2014 from the University of Engineering and Technology (UET) Taxila, Pakistan. Recently he was awarded a funded Ph.D. studentship by UET Taxila. His main research interests are in UWB-MIMO systems, Frequency Selective Surfaces and reflectarrays.

Rashid Saleem received his B.S. degree in Electronic Engineering from Ghulam Ishaq Khan Institute of Engineering Sciences and Technology, Pakistan, in 1999. He pursued a career in the Telecommunication industry for several years while continuing his

education. He received his Ph.D. degree from The University of Manchester, United Kingdom in 2011. He worked on antennas, channel modeling and interference aspects of Ultra Wideband systems during his Ph.D., and was also member of a team designing arrays for the SKA project. His research interests include antennas, angle-of-arrival based channel modeling, FSSs and reflectarrays. Currently, he is working as Assistant Professor at the University of Engineering and Technology (UET), Taxila, Pakistan where he is heading the MAP (Microwave, Antennas and Propagation) research group.

Adeel Akram received his B.S. degree in Electrical Engineering from the University of Engineering and Technology, Lahore, Pakistan in 1995. He received his M.S. degree in Computer Engineering from the National University of Sciences and Technology (NUST), Pakistan and his Ph.D. in Electrical Engineering from the University of Engineering and Technology (UET) Taxila, Pakistan, in 2000 and 2007 respectively. He is the Dean of Faculty of Telecommunication and Information Engineering at UET Taxila. His research interests include microwave and communication systems.

Muhammad Farhan Shafique received his B.Eng. degree from Hamdard University, Karachi, Pakistan, in 2003, his M.S. degree from the University of Paris East Marne-La-Valle, Paris, France, in 2005 and his Ph.D. from the University of Leeds, Leeds, United Kingdom in 2010. His research interests involve multilayer microwave device fabrication on LTCC and thick-film technology, electromagnetic modeling of microwave structures, RF antenna design and microfluidic device fabrication. From 2007 to 2010, he was involved in establishing the LTCC fabrication facility with the Institute of Microwave and Photonics, The University of Leeds, UK. He has extensive experience of laser micromachining and multilayer LTCC device modeling and fabrication. He is working as Assistant Professor at COMSATS Institute of Information Technology, Islamabad, Pakistan where he established the MCAR (Microwave Circuits and Antennas) research group.

A Novel U-Shaped Parasitic Asymmetric Microstrip Cap Loaded Compact Patch Antenna

M. R. Zaman [1], M. T. Islam [2], and Salehin Kibria [1]

[1] Centre for Space Science (ANGKASA)
[2] Dept. of Electrical, Electronic and Systems Engineering, Faculty of Engineering and Built Environment
Universiti Kebangsaan Malaysia, UKM Bangi, 43600, Malaysia
robelhk@yahoo.com, titareq@yahoo.com, sakib2005@yahoo.com

Abstract ─ A novel electromagnetically short antenna with parasitic microstrip cap shape is shown in this paper. The antenna is composed of a U-shaped parasitic microstrip line (cap) excited by coupling with the feed line at patch. The antenna is fabricated in FR4 substrate with dielectric constant, Ɛr=4.55 and thickness of 1.6 mm. Optimization of the proposed antenna is done using modified Particle Swarm Optimization (PSO) algorithm in ZELAND IE3D software environment. That gives resonance at selected frequencies and increased gain than the initial design. By using circular slot at the ground plane with miniaturized structure, dual-band covering 5.29 GHz to 5.89 GHz (C-band) and 7.93 GHz to 8.86 GHz (X-band) is achieved. A fractional bandwidth of 10.74% at C-band and 11.08% at X-band is achieved. A measured gain of 5.65 dBi and 6.61 dBi is achieved at C-band and X-band respectively, with a circular polarization. Gain improvement is achieved compared to the initial design by more than 2 dBi (average) in the selected frequency for the given resonance using modified PSO optimization.

Index Terms ─ C-band, coupled line, optimization, PSO, U-shape, X-band.

I. INTRODUCTION

Modern multiband antenna designs are getting more into different microstrip structures [1-10] due to multiple applications using different frequencies are put together in one system nowadays. To improve the size compatibility with the mobile device, antenna structures are miniaturizing gradually with extensive research. Different types of antennae such as helical, monopole, loop antennae are designed to achieve multiband response in miniaturized volume [1-4]. Due to the size limitation inside the body of mobile devices, the antenna structure becomes more complex. Moreover, the antenna structure tends to be more close to the other parts of the mobile which leads to low resistance and high reactance at the input impedance behaving like an ILA (Inverted L shaped antenna) [5].

In [6], a printed planar antenna for wideband application is shown the antenna is composed of a square patch. However, there is a notch from 4.7 GHz to 5.8 GHz where the antenna is not applicable. In [7], a multiband fractal Sierpinski Gasket antennas' behavior is explained using iterative method. In that research, a basic structure, equilateral triangle is used as sample model. A multiband antenna with resonance response for different application is shown in [8]. The antenna maintains Chebyshev distribution method for slot arrays combined with a triangle shaped patch. The antenna has a relatively large size. To use the same antenna in different applications, switches are installed in a pentagon shaped patch antenna in [9]. In the design, while all the switches are turned on, the resonance shifts a little. A patch antenna with a shape of triangle is explained in [10]. A slot of rectangular shape is cut in the ground plane which can be changed to have different gap size between the two resonant frequencies of the dual-band antenna. To design this triangle shaped patch antenna, a substrate is used with dielectric constant of 1.38 which is not available and not chip compared to FR4 (Fibre-Reinforced plastic) substrates. Planar UWB antenna with Multi-Slotted ground plane is shown in [11]. With a size of 30*22

Submitted On: June 21, 2013
Accepted On: September 26, 2014

mm^2, the antenna bandwidth ranges from 2.57 GHz till 16.72 GHz. However, the gain is very limited within the operating frequency. A metallized dielectric loading technique is shown to achieve multiband behavior in [12]. In this antenna design while the dielectric material is used at the top, the peak gain intends to decrease more than 1.2 dB at the achieved resonance frequencies. Another antenna for L-band application is designed and fabricated using high dielectric constant substrate (ε_r=10.02) to have reasonable axial ratio bandwidth at 1.575 GHz [13]. The simulation results of the antenna indicated that, with the change of the size of the ground plane, the impedance bandwidth of the antenna will significantly change. A triangular patch Yagi antenna is shown in [25] to have reconfigurable characteristics. Two parasitic patches are used to direct the beam of the antenna by using switches on top of them. Another multiband/UWB antenna is shown in [26]. The antenna is composed of two radiating patch along with a 'T' and butterfly shaped stub in the middle of the ground plane. The stub is introduced to have notch in the UWB characteristics. Inductive loading technique is shown in [27] to convert a dual-band antenna into wideband antenna. The bandwidth is enhanced by loading inductive stub component at the ring of the proposed antenna. The measurement result of the antenna shows wider performance than the simulation result. Two L-shaped ground planes are introduced in [28] to have triple band operation in a coplanar waveguide feed antenna. They have also introduced L-shaped and I-shaped slots at the ground plane and radiating patch respectively. However, the peak gain of the antenna is below 2 dBi at most of the operating bands. A circular ring antenna for UWB application is shown in [30] with a compact size of 26*28 mm^2. The antenna has a bandwidth of 14 GHz. However, the antenna gain is minimal at the operating frequency. A coplanar antenna working at 3.53 GHz to 9.5 GHz is shown in [31]. The maximum gain of the antenna is 3.5 dBi with a stable radiation pattern. For antenna performance enhancement, a split ring slotted EBG structure is shown in [32]. By using such design structure as another version of modified ground plane, antenna performance can be enhanced.

Particle Swarm Optimization (PSO) technique is being used widely day by day in designing Electromagnetic structures [14]. PSO is a strong and evolutionary computation technique based on the intelligent swarms' movement. Dual-band/multiband patch antennae, periodic structures, correlator antenna arrays, aperiodic antenna arrays are designed in [15] using PSO. The designs achieved using PSO are fabricated and the measured results tend to agree with the simulated result using the software UCLA antenna lab. A Yagi-Uda antenna design is optimized using BBO and PSO algorithm combined [16]. The paper is more devoted into comparison between two optimization process rather than discussing about the antenna characteristics. A combination of Genetic Algorithm (GA) and PSO is shown in [17]. It shows the optimization of feed-point of microstrip antenna.

In this paper, a dual-band antenna is designed and fabricated with resonance response at the frequencies 6.18 GHz and 8.52 GHz in FR4 substrate. Coupled line cap (CLC) is used to surround the active rectangular patch. By changing the dimension of the cap, the impedance is matched for higher bandwidth. The antenna ground plane is modified using a circular slot centered at the middle with a rectangle shape microstrip line at the center of the slot. The lower resonance frequency shown in the current distribution graph is found by the separated rectangle in the ground plane [18]. Another antenna is designed and fabricated using modified Particle Swarm Optimization (PSO) algorithm which gives the antenna a changed shape with long hands at one side of the CLC and another side is minimized. The PSO algorithm shows similarity with the existing design. By using PSO, increased bandwidth is achieved with almost the same structure at the patch of the antenna without changing the outer dimension (20 mm×20 mm) of the antenna using FR4 substrate with a thickness of 1.6 mm. The proposed patch antenna is designed in FR4 substrate with a compact size lengthening 0.41λ and a width of 0.41λ.

II. ANTENNA DESIGN

Figure 1 shows the structure of the antenna with the parameters tabulated in Table 1.

The boundary conditions for the fields of the dielectric-conductor and conductor-air can be found using Maxwell's equations [19]:

$$\oint_s D.dS = Q_{fce}\,, \tag{1}$$

$$\oint_s E.dl = 0\,, \tag{2}$$

where, Q_{fce} is the free surface charge. The conductor used in the antenna is copper "Cu" which is high in terms of electrical and thermal conductivity, resulting to have $\rho_c \rightarrow 0$ and $\sigma \rightarrow \infty$ which tends to a perfect conductor. The conductor and dielectric substrates interface of the antenna is shown in Fig. 1. The electric field, E=0 at the inside of the conductor. There is an electric field, normal to the conductor throughout the interface of the conductor-dielectric and conductor-air (in the case of air the dielectric constant is '1', so the calculation for electric field is the same as for other dielectric substrates with different dielectric constants) and is external to the conductor.

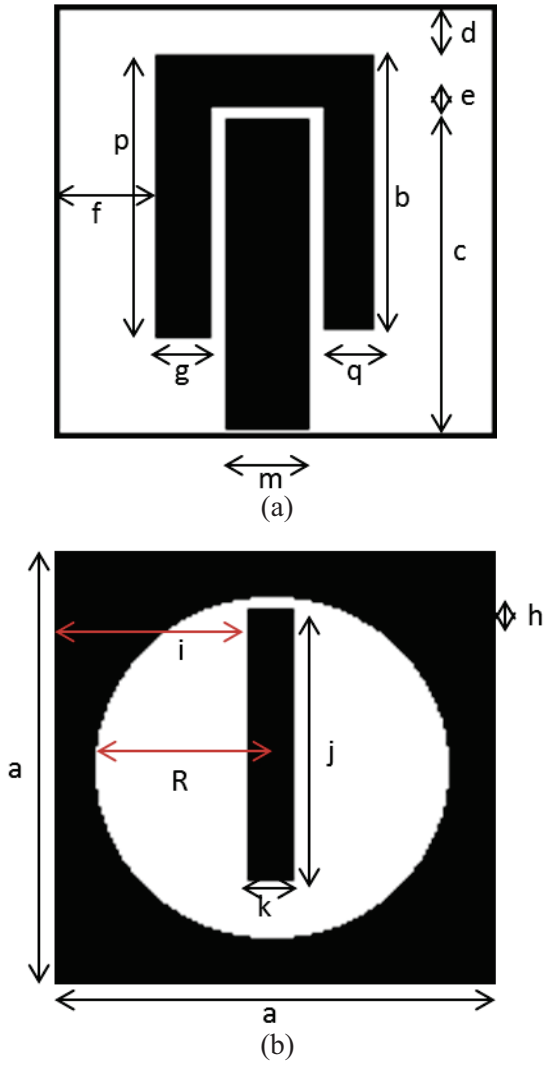

Fig. 1. (a) Patch of the proposed antenna, and (b) ground plane of the proposed antenna.

In Fig. 2, the coupling element that is not connected with the primary patch, electrically partially screens the primary patch. A slit is cut between one microstrip tree and leaf. The characteristics of coupled lines can be applied for the coupling element surrounding the primary patch. From the current distribution of the patch at the later part of this paper, the occurrence of coupling of the primary and coupling element can be observed.

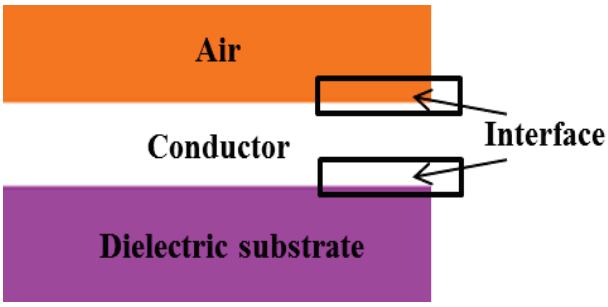

Fig. 2. Antenna material lairs distribution.

The coupling depends on the even and odd mode characteristic impedances of the coupled microstrip lines and vice versa. There are no precise analytic formula which can be applied to the structure shown, whereas approximated formulas can be used to characterize using characteristic impedance (Z_0), even mode impedance (Z_{0e}) and odd mode impedance (Z_{0o}). For the coupled lines with two modes of current flow (electromagnetic consideration), which are due to the ground plane conductor and the displacement of the current coupling between two conductors are specified as differential mode current which is related to Z_{0o}. The energy between the coupled lines flows from the source structure (primary patch) to the matched load structure (coupling element). Due to the thickness of the coupling conductors (minor capacitance), mutual capacitance and ground plane to coupling lines capacitance and distortion due to coupling of each other, the 4 capacitance values for the odd mode is resulting. By considering the magnetic fields, the inductance values can be said to follow the argument. For a non-dissipative system the following equation can be applied:

$$Z_0 = \sqrt{\frac{L(\text{inductance per meter})}{C(\text{capacitance per meter})}}. \qquad (3)$$

For the quarter wavelength matched line, the even and odd mode impedances can be formulated as:

$$Z_{0e} = Z_0\sqrt{\frac{1+k}{1-k}}, \tag{4}$$

$$Z_{0o} = Z_0\sqrt{\frac{1-k}{1+k}}, \tag{5}$$

where, k=10-0.05C, C=coupling between two microstrip lines in dB. From (4) and (5),

$$Z_0 = \sqrt{\frac{Z_{0o}}{Z_{0e}}}. \tag{6}$$

Tracking back, the values of 'L' and 'C' can be found. The coupled structures even (Z_{oe}) and odd (Z_{oo}) mode impedance can be evaluated by using coupled line microstrip structure impedance formulation technique described in [24]:

$$(Z_{0e})_{n-1,n} = \frac{1}{y_0}\left[1+\frac{J_{n-1,n}}{Y_0}+\left(\frac{J_{n-1,n}}{Y_0}\right)^2\right], \tag{7}$$

$$(Z_{0o})_{n-1,n} = \frac{1}{y_0}\left[1-\frac{J_{n-1,n}}{Y_0}+\left(\frac{J_{n-1,n}}{Y_0}\right)^2\right]. \tag{8}$$

With the gap becoming narrower (as small as 0.5 mm for this design), it is more likely for the Z0e to increase due to increment in inductance and decrement in capacitance. As the gap between coupled lines becomes smaller, the field between the common ground of the coupled lines becomes narrower which can be seen in Fig. 3. The eddy current effect can be seen for the electric currents induced within the coupling conductors creating the magnetic field in the middle. The equivalent circuit of a microstrip coupled line gap discontinuity is shown in Fig. 4 [20]. The values for the circuit elements can be calculated using the equations stated below:

$$C_{11} * \frac{25Z_0}{h} = \left[1.125\tanh\left(1.358\frac{W}{h}\right)-0.315\right] \tanh\left[\left(0.0262+0.184\frac{h}{W}\right)+\left(0.217+0.0619\ln\frac{W}{h}\right)\frac{S}{h}\right], \tag{9}$$

$$C_{12} * \frac{25Z_0}{h} = \left[6.832\tanh\left(0.0109\frac{W}{h}\right)+0.910\right] \tanh\left[\left(1.411+0.314\frac{h}{W}\right)+\left(\frac{S}{h}\right)^{1.248+0.360\tan^{-1}\frac{W}{h}}\right], \tag{10}$$

$$L_{11} * \frac{25}{hZ_0} = \left[0.134+0.0436\ln\frac{h}{W}\right] \exp\left[-1\left(3.656+0.246\frac{h}{W}\right)\left(\frac{S}{h}\right)^{1.739+0.39\ln\frac{W}{h}}\right], \tag{11}$$

$$L_{12} * \frac{25}{hZ_0} = \left[0.008285\tanh\left(0.5665\frac{W}{h}\right)+0.0103\right] + \left[0.1827+0.00715\ln\frac{W}{h}\right] \exp\left[-1\left(5.207+1.283\tanh\left(1.656\frac{h}{W}\right)\right)\left(\frac{S}{h}\right)^{0.542+0.873\tan^{-1}\frac{W}{h}}\right], \tag{12}$$

$$\frac{R_1}{Z_0} = 1.024\tanh\left(2.025\frac{W}{h}\right) \tanh\left[\left(0.01584+0.0187\frac{h}{W}\right)\frac{S}{h} + \left(0.1246+0.0394*\sinh\left(\frac{W}{h}\right)\right)\right], \tag{13}$$

$$C_2 * \frac{25Z_0}{h} = \left[0.1776+0.05104\ln\left(\frac{W}{h}\right)\right]\frac{h}{S} + \left[0.574+0.3615\frac{h}{W}+1.156\ln\left(\frac{W}{h}\right)\right] \sec h\left(2.3345\frac{S}{h}\right), \tag{14}$$

$$L_2 * \frac{25}{hZ_0} = \left[0.00228+\frac{0.0873}{\cosh\left(\frac{W}{h}\right)+7.52\left(\frac{W}{h}\right)}\right] \sinh\left(2.3345\frac{S}{h}\right), \tag{15}$$

$$\frac{R_2}{Z_0}=\left[-1.78+0.749\frac{W}{h}\right]\frac{S}{h}$$
$$+\left[1.196-0.971\ln\left(\frac{W}{h}\right)\right]\sinh\left(2.3345\frac{S}{h}\right). \quad (16)$$

The equivalent circuit modeling procedure can be divided into two steps: produce S-parameter for the lack of coherence in the microstrip line and construct lumped circuit model which is independent of frequencies and describable using a set of equations based on physics of the structure. For the case in Fig. 4, the equivalent circuit satisfies a microstrip gap starting from a fraction until the gap approaches infinity.

Ground planes irregularity has very small effect on the coupled structure which can be ignored. The small microstrip rectangle in the middle of the ground plane works as the finite ground plane for the coupled microstrip lines of the patch.

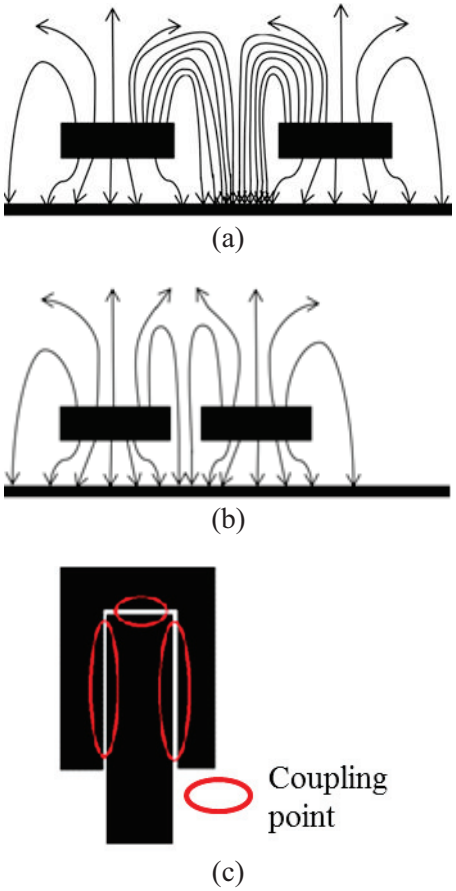

Fig. 3. (a) Coupled microstrip lines at a distance, (b) decreased gap between coupled lines, and (c) coupling points of the proposed antenna.

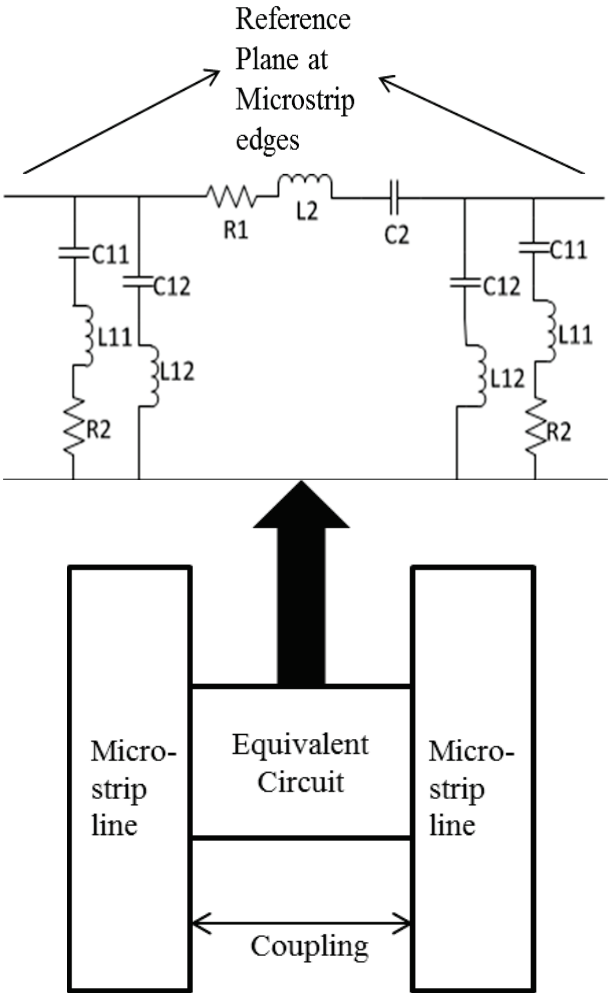

Fig. 4. Equivalent circuit of a microstrip coupled line gap.

The ground plane in Fig. 1 (b) has a circular slot in the middle which indicates the antenna can be classified as aperture type antenna. By Babbinet's principle, the complementary of that circular slot of the aperture type antenna radiation can be compared with the antenna radiation of a circular patch antenna. The principle is supported by the equations:

$$E_{\theta p}=H_{\theta c}, \quad (17)$$
$$E_{\varphi p}=H_{\varphi c}, \quad (18)$$
$$E_{\theta p}=-\frac{E_{\theta c}}{\eta_0^2}, \quad (19)$$
$$H_{\varphi p}=-\frac{E_{\varphi c}}{\eta_0^2}, \quad (20)$$

where, E_p=Electric field of circular patch, η_0=Intrinsic impedance of free space, E_c=Electric field of the complementary patch, H_p=Magnetic field of circular patch, and H_c=Magnetic field of complimentary patch. A microstrip rectangle is introduced in the middle of the circular slot in the ground plane.

Figure 5 shows the antenna along with its complementary structure:

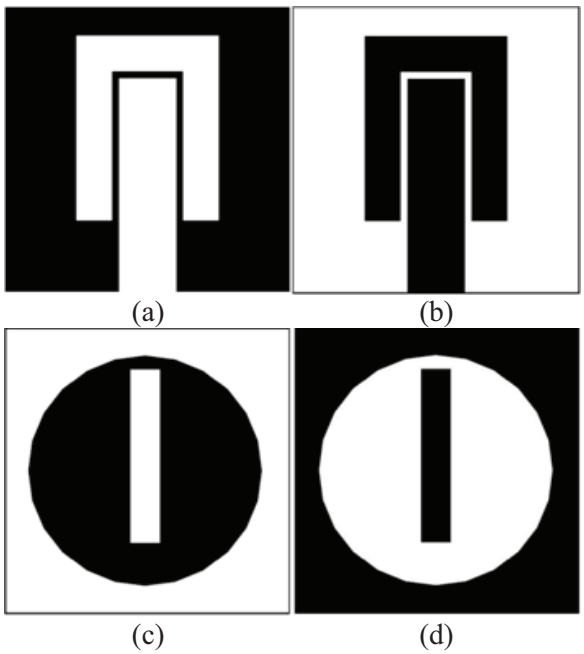

Fig. 5. (a) patch, (b) complementary of the patch, (c) ground plane, and (d) complementary of the ground plane.

The microstrip rectangle in the middle of the ground plane works as a finite ground for the coupled lines.

III. PARAMETRIC STUDIES

The antenna structure is simulated using a high and a low dielectric constant compared to FR4 substrate to investigate the behaviour of the planar structure for various existing substrate with same thickness, n=1.6 mm. Figure 6 shows the concluded study using different dielectric constant. Polyester with a dielectric constant, ε_{rp}=3.2 has a close relation (0.15 GHz first resonance frequency difference) with the S_{11} response of FR4 substrate. Moreover, Gallium Arsenide with a dielectric constant, ε_{rg}=12.9 shows a difference of 0.33 GHz with the primary resonance frequency of FR4. With high dielectric constant, the second resonance response of the antenna starts to degrade confirming that, FR4 is a valid choice for the proposed antenna design which is quite chip and available. Another widely used [21, 22] substrate from Rogers RO4350B with dielectric constant of 3.66 is compared in Fig. 5. The primary resonance response tends to shift 0.78 GHz towards frequency increment. From the discussions described, the observation is that the antenna design is more depended on the pattern of the microstrip lines over the substrate than the properties of substrate material itself.

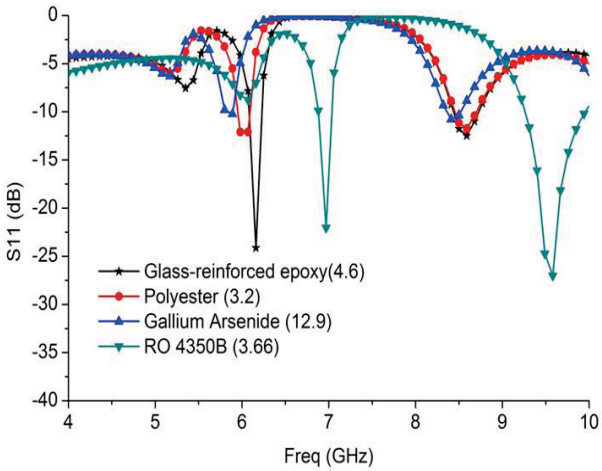

Fig. 6. S_{11} response with different dielectric constants.

Figure 7 shows a study of changing the radius 'R' of the circular slot at the ground plane. When R=6 mm the outer part of the circle already touches the microstrip rectangle situated in the middle and gives a lower frequency response at 4.51 GHz. The second resonance frequency however, fades away. R=7 mm follows the same resonance response as for R=6 mm. At R=9 mm, the first resonance shifts left but also loses its resonance behaviour which narrows at 5.89 GHz barely passing the first resonance. In the case of second resonance, the antenna shows 330 MHz bandwidth with a resonance at 8.05 GHz. The antenna resonance response shows a harmonic relation with the change of the circular slot radius which can be seen when R=10 mm. At R=10 mm, the first resonance shifts to 5.35 GHz with a -10 dB bandwidth of 120 MHz

with a second and a third resonance response at 7.96 GHz and 10 GHz.

Figure 8 shows the behaviour change with the change of length of microstrip rectangle in the middle of the ground plane. The copper line in the middle plays important role on controlling the first resonance of the antenna. The results show that if the length of 'j' is decreased, the first resonance is fully missed. Also, the placement of the microstrip rectangle is optimized manually.

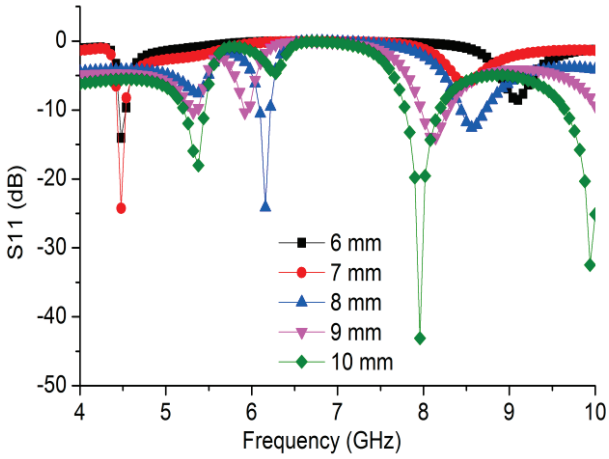

Fig. 7. Antenna resonance response with changed radius of circular slot.

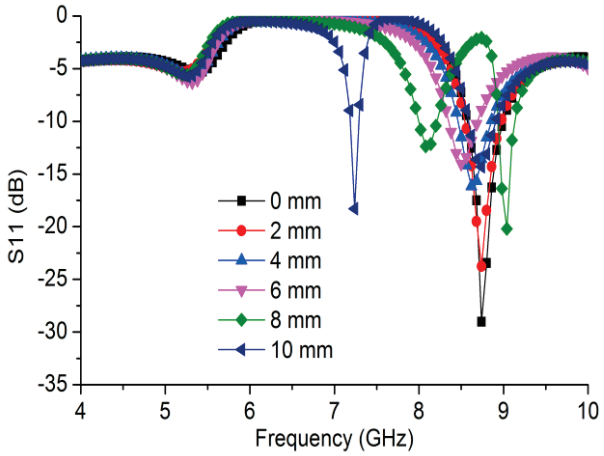

Fig. 8. Antenna resonance response with changed length of rectangle in the middle of the ground plane.

By changing the width 'k' of the microstrip rectangle in the middle of the ground plane, the behaviour change of resonance response found is shown in Fig. 9.

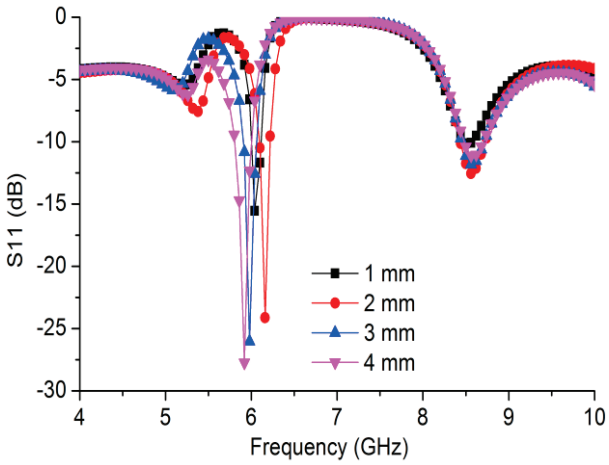

Fig. 9. Antenna resonance response with changed width of rectangle in the middle of the ground plane.

From the current distribution pattern, it can be seen that at the frequency 6.18 GHz, the current distribution over the strip line situated in the middle of the circular slot at the ground plane is high, as shown in Fig. 10, which also indicates a better result in that frequency. Minor perturbations can be seen at the patch of the antenna. By adjusting the length of the strip line in the ground plane, the resonance at 6.18 GHz can be tuned.

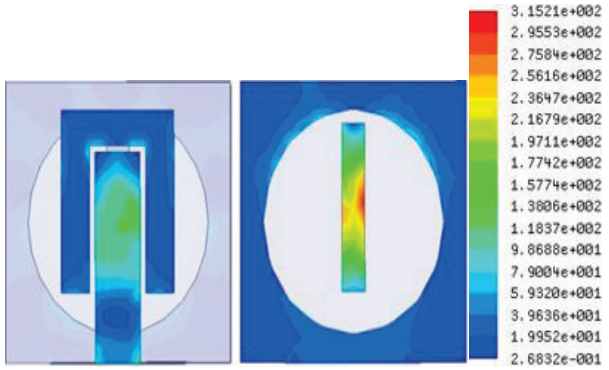

Fig. 10. Current distribution of the antenna at 6.18 GHz.

IV. OPTIMIZATION USING PSO ALGORITHM

PSO is a PSO based algorithm that is

specifically designed for antenna gain optimization. PSO can work with any finite number of variables given enough computation time [23]. Key problems with PSO are Curse of Dimensionality and Premature Convergence. The multi-start algorithm breaks the searching area into pieces of 2 and 3 dimensional spaces and edits it with a rapidly converging PSO. The multi-start technique removes the Premature Convergence issue completely. The k-dimensional breakdown approach improves the algorithm's performance highly dimensional problems. Until a predetermined termination criterion is met, the process is repeated up to a pre-determined number of iterations. PSO updates the particle position according to equations below:

$$v_{i+1} = wv_i + \varphi_1 r_1 (d_{localbest} - d_i) + \varphi_2 r_2 (d_{globalbest} - d_i), \quad (21)$$

$$d_{i+1} = d_i + v_{i+1}, \quad (22)$$

here, w=inertia coefficient, r_1, r_2=uniformly distributed random values between zero and one, v_i, d_i=velocity, dimensions of a particle at i^{th} iteration, φ_1, φ_2=cognitive and social coefficients.

The algorithm is modified for aperture type antenna design optimization. IE3D software is used to collaborate with the PSO algorithm executed in Matlab environment. A total number of 9 dimensions were optimized using this PSO algorithm.

The algorithm applied traditional PSO on 5 dimensions while holding the other dimensions constant. After 9 generations, the algorithm re-initialized the population and making two active dimensions inactive and replacing them two previously inactive dimensions. The swapping of active dimensions with inactive dimensions is done at random. After 246 generations, the optimized result is achieved. The pre-optimized and post-optimized dimensions are given in Table 1.

In this paper, the average gain and resonance over C-band and X-band was optimized; hence, it was the fitness function for this maximization problem. Figure 15 illustrates the improvement of the best fitness achieved during optimization. This validates the performance of the PSO.

Table 1: Design specification of the proposed antenna

Antenna Dimension	Before Optimization	After Optimization
Substrate	FR4	FR4
Relative permittivity of the substrate, (ε_r)	4.55	4.55
Thickness of the dielectric substrate, (n)	1.6 mm	1.6 mm
Ground plane (a × a)	20 mm × 20 mm	20 mm × 20 mm
Hands length of the coupling element, (b)	13.5 mm	16.2 mm
Hands length of the coupling element, (p)	13.5 mm	14.3 mm
Length of the primary patch, (c)	15 mm	16.9 mm
Distance from the boundary to coupling element, (d)	2 mm	0.15 mm
Gap between primary and coupling element, (e)	0.5 mm	0.61 mm
Distance from the boundary to the hand of the Coupling element, (f)	5 mm	6.2 mm
Width of the coupling element, (g)	2.5 mm	1.2 mm
Width of the coupling element, (q)	2.5 mm	1.23 mm
Width of the primary patch, (m)	4 mm	4 mm
Distance from the circular slot to the rectangle,(h)	1 mm	1 mm
Width of the rectangle, (k)	2 mm	2 mm
Length of the rectangle, (j)	12 mm	12 mm
Distance from the boundary to the rectangle, (i)	9 mm	9 mm
Radius of the circular slot, (R)	8 mm	8 mm

V. ANTENNA MEASUREMENT

The measurements of two antennae are done using Agilent PNA analyser with model no. E8358A. An anechoic chamber with length and width of 4.5 meter by 3.5 meter and a height of 4 meter is used to measure the polarization and gain of the antenna. A three antenna measurement technique is applied with a gap of 3 meter from each other. For the far field measurement, as the antenna is an electromagnetically short at 5.5 GHz, the minimum far field distance can be calculated as $d_f >> 2\lambda$. So, for this case, a 3 meter distance will serve the far field pattern quite nicely. Among three antennae two of the antennae are linearly polarized horn antennae with model no. SAS 571 and the other antenna is the AUT. At first the two antennae (horn antennae) with known gains are measured for the gain among each other and then the AUT is measured. The calculation based on Friis transmission equation demonstrates the calculation for the gain measurement shown in equation (13):

$$G_i dB + G_j dB = 20\log_{10}\left(\frac{4\pi R}{\lambda}\right) + 10\log_{10}\left(\frac{P_r}{P_t}\right)^k, \quad (23)$$

here, i=1, 2, 3, j=1, 2, 3, i≠j and k=1, 2, 3. R=distance between two antennae, P_t=transmitted power, P_r=received power, G=gain of the antenna.

VI. RESULTS OF THE DESIGNED ANTENNAE

Figure 11 shows the fabricated antennae using FR4 substrate with a thickness of 1.6 mm and a dielectric constant of 4.55. In Fig. 11 (a) shows the antenna fabricated before optimization and (b) shows the antenna after optimization.

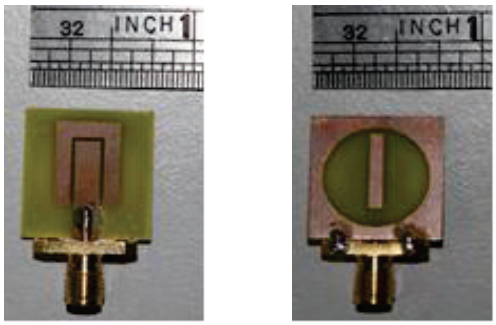

(a)

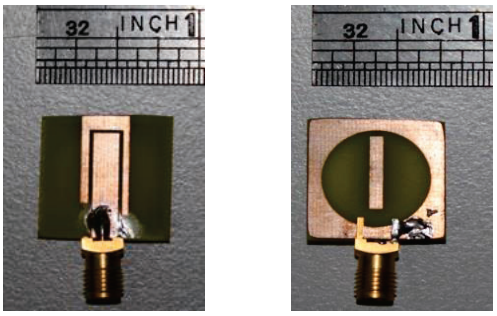

(b)

Fig. 11. (a) Antenna before optimization, and (b) antenna after optimization.

Clearly with naked eyes, it can be seen that there are changes in the pattern of the dimensions of the patch. The ground plane remains unchanged as no optimization algorithm was applied to the ground plane.

Figure 12 shows the resonance response of the antennae. The S_{11} response of the first antenna (before optimization) is less than -10 dB for the frequency starting from 5.89 GHz to 6.52 GHz with a notch at 6.25 GHz which degrades the total bandwidth performance of the antenna. Another resonance can be found starting at 8.71 GHz and ending at 8.77 GHz. The bandwidth at this resonance (X-band) is low. From the simulation results, it is clear that the second resonance is missed from the graph of the measured performance of the antenna before optimization.

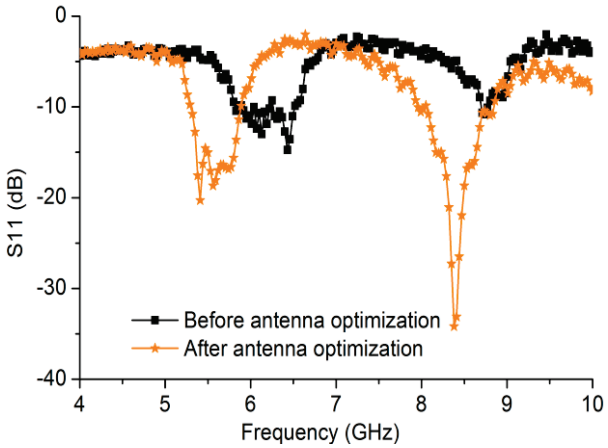

Fig. 12. Measured S_{11} response of the proposed multiband antenna.

After optimization, the resonance response of the optimized antenna can be found in Fig. 12. It is clear from the graph that the antenna is optimized to gain resonance frequency response at C-band and X-band with best bandwidth possible. A bandwidth of 0.6 GHz starting from 5.29 GHz to 5.89 GHz is achieved at the first resonance (C-band) [29], and a bandwidth of 0.93 GHz is achieved at the frequency starting from 7.93 GHz to 8.86 GHz (X-band). At C-band the lowest resonance response is less than -20 dB and at X-band the lowest resonance response is less than -34 dB. No notch is detected at the resonance frequency of the optimized antenna.

Figure 13 shows the measured gain of both the antennae. The gain of the antenna before optimization has an average gain of 2.7 dBi at the frequency starting at 6.05 GHz to 6.24 GHz with a peak gain of 4.07 dBi at 6.15 GHz. The range of frequency is quite low considering high gain at the resonance frequency. At the X-band, the gain is lower than 0 dBi for the first antenna.

For the optimized antenna, at C-band, the average gain starting from 5.29 GHz to 5.93 GHz is 3.2 dBi with a peak gain of 5.65 dBi at 5.84 GHz. At the X-band, with a high bandwidth a peak gain of 6.62 dBi is achieved at 8.16 GHz frequency. The average gain at X-band is 4.3 dBi starting from 7.93 GHz till 8.68 GHz.

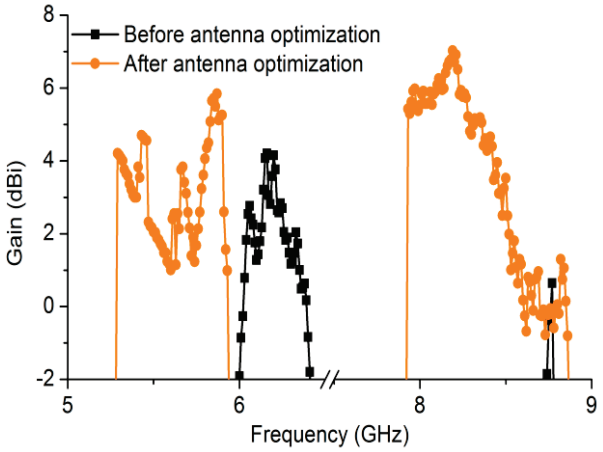

Fig. 13. Measured peak gain of the dual-band antenna.

Figure 14 shows the polarization of the optimized antenna at 5.5 GHz and 8.3 GHz. Observe that at 5.5 GHz in the E-plane, the antenna shows an omni-directional pattern at both co- and cross-pol. However, at 5.5 GHz, H-plane shows irregularity of co-polarization from 270° till 360°. Again for 8.3 GHz, the radiation pattern is somewhat omni-directional at the E-plane, whereas, at H-plane an irregularity can be seen at the co-pol which can be ignored due to the overall omni-directional performance.

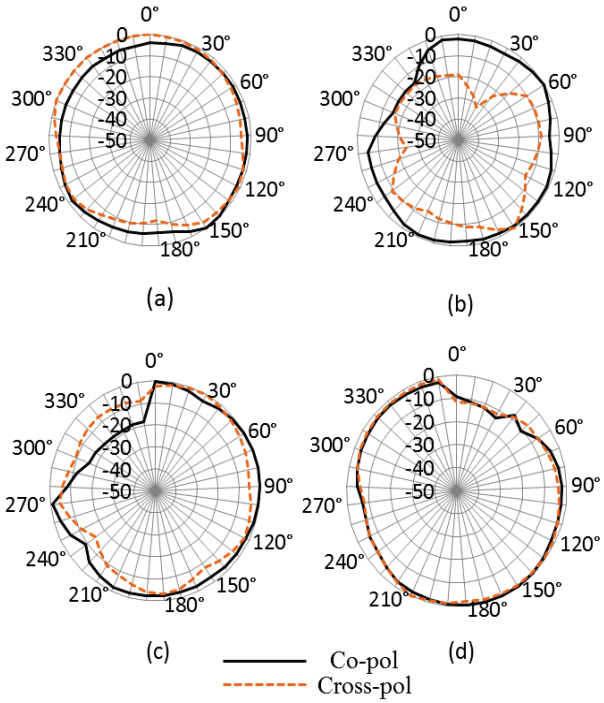

Fig. 14. Normalized radiation pattern of the antenna at: (a) 5.5 GHz (E-plane), (b) 8.3 GHz (E-plane), (c) 5.5 GHz (H-plane), and (d) 8.3 GHz (H-plane).

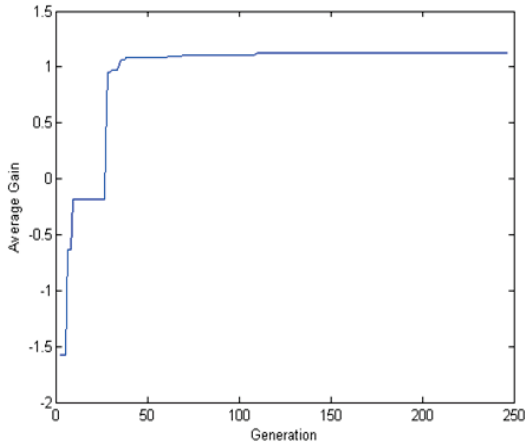

Fig. 15. Average gain increment after 246 generations (taken from Matlab).

VII. CONCLUSION

A new method for the design of microstrip patch antenna is described in this paper. A U-shaped parasitic element is introduced covering the active patch body of the antenna. The dimension of the patch and U-shaped element is optimized using modified PSO algorithm. Two antennae are fabricated to compare the result before and after the optimization were done. By changing the width of the U-shaped parasite, resonance frequency of the antenna can be changed. The antenna design is optimized for C-band and X-band frequency responses. After the optimization, the antenna at 5.84 GHz shows a maximum gain of 5.65 dBi and at 8.16 GHz the gain is 6.62 dBi. The resonance response of the antenna falls sharply at the desired frequencies of C-band and X-band. For future work, an array of this antenna can be proposed to have increased gain and more practical for the C-band and X-band applications.

REFERENCES

[1] M. Tzortzakakis and R. Langley, "Quad-band internal mobile phone antenna," *IEEE Trans. Antennas Propag*., vol. 55, no. 7, pp. 2097-2103, Jul. 2007.

[2] Y. Chi and K. Wong, "Compact multiband folded loop chip antenna for small-size mobile phone," *IEEE Trans. Antennas Propag*., vol. 56, no. 12, pp. 3797-3803, Dec. 2008.

[3] J. J. Tiang, M. T. Islam, N. Misran, et al., "Slot loaded circular microstrip antenna with meandered slits," *Journal of Electromagnetic Waves and Applications*, vol. 25, issue 13, pp. 1851-1862, 2011.

[4] K. Wong and C. Huang, "Printed loop antenna with a perpendicular feed for penta-band mobile phone application," *IEEE Trans. Antennas Propag*., vol. 56, no. 7, pp. 2138-2141, Jul. 2008.

[5] K-J. Kim, S-H. Lee, B-N. Kim, et al., "Small antenna with a coupling feed and parasitic elements for multiband mobile applications," *IEEE Antennas and Wirelesss Propagation Letters*, vol. 10, pp. 290-293, 2011.

[6] R. Azim, M. T. Islam, and N. Misran, "Printed planar antenna for wideband applications," *Journal of Infrared Millimeter and Terahertz Waves*, vol. 31, issue 8, pp. 969-978, 2011.

[7] X. Qu, Z. He, W. Shi, et al., "Multiband analysis of Sierpinski Gasket antenna with an iterative method," *Wireless Communications & Signal Processing, WCSP International Conference on*, pp. 1-4, Nov. 2009.

[8] J. Costantine, K. Y. Kabalan, A. El Hajj, et al., "New multi-band design for a microstrip patch antenna," *Antennas and Propagation, EuCAP, The Second European Conference on*, pp. 1-4, Nov. 2007.

[9] J. Costantine, C. G. Christodoulou, and S. E. Barbin, "A new reconfigurable multi band patch antenna," *Microwave and Optoelectronics Conference, IMOC, SBMO/IEEE MTT-S International*, pp. 75-78, Oct. 2007.

[10] L. Liu, S. Zhu, and R. Langley, "Dual-band triangular patch antenna with modified ground plane," *Electronics Letters*, vol. 43, issue 3, pp. 140-141, Feb. 2007.

[11] R. Azim, M. T. Islam, N. Misran, et al., "Planar UWB antenna with multi-slotted ground plane," *Microwave and Optical Technology Letters*, vol. 53, issue 5, pp. 966-968, 2011.

[12] B. Yildirim, "Multiband and compact WCDMA/WLAN antenna for mobile equipment," *IEEE Antennas and Wireless Prop. Letters*, vol. 10, pp. 14-16, 2011.

[13] K. Y. Lam, K-M. Luk, K. F. Lee, et al., "Small circularly polarized U-slot wideband patch antenna," *IEEE Antennas and Wireless Prop. Letters*, vol. 10, pp. 87-90, 2011.

[14] M. T. Islam, M. Moniruzzaman, N. Misran, et al., "Curve fitting based particle swarm optimization for UWB patch antenna," *Journal of Electromagnetic Waves and Applications*, vol. 23, issue 17-18, pp. 2421-2432, 2009.

[15] Y. Rahmat-Samii and N. Jin, "Particle swarm optimization (PSO) in engineering electromagnetics: a nature-inspired evolutionary algorithm," *ICEAA*, pp. 177-182, Sept. 2007.

[16] S. Singh, S. Tayal, and G. Sachdeva, "Evolutionary performance of BBO and PSO algorithms for Yagi-Uda antenna design optimization," *WICT 2012*, pp. 861-865, 2012.

[17] F. A. Ali and K. T. Selvan, "A study of PSO and its variants in respect of microstrip antenna feed point optimization," *Asia-Pacific Microwave Conf., 2009*, pp. 1817-1820, 2009.

[18] K. Y. Lam, K-M. Luk, K. F. Lee, et al., "Small circularly polarized U-slot wideband patch antenna," *IEEE Antennas and Wireless Prop. Letters*, vol. 10, pp. 87-90, 2011.

[19] M. N. O. Sadiku, *Boundary Conditions*, in Elements of Electromagnetics, 4th ed., New York, Oxford University Press, ch. 5, sec. 9, pp. 190, 2007.

[20] N. G. Alexopoulos and S. Wu, "Frequency-independent equivalent circuit model for microstrip open-end and gap discontinuities," *IEEE Transactions on Microwave Theory and Techniques*, vol. 42, no. 7, pp. 1268-1272, Jul. 1994.

[21] C-J. Hwang, L. B. Lok, I. G. Thayne, et al., "A wide bandpass filter with defected ground structure for wide out-of-band suppression," *Microwave Conference, Asia Pacific*, pp. 2018-2021, Dec. 2009.

[22] Y. M. Kempa, Z. E. Kazanivsky, H. H. Masyutin, et al., "Specific features of wide-band microwave filters constructive design," *Microwave & Telecommunication Technology*, pp. 481-483, Sept. 2007.

[23] M. Wu, "Improved intelligent optimization algorithm for the application of feedback design," *Journal of Convergence Information Technology*, vol. 6, no. 9, Sept. 2011.

[24] D. M. Pozar, *Microwave Engineering*, Edition 4, John Wiley & Sons, Inc., pp. 347.

[25] J. Zhang, X. Yang, J. Li, et al., "Triangular patch Yagi antenna with reconfigurable pattern characteristics," *Applied Computational Electromagnetics Society (ACES) Journal*, vol. 27, no. 11, pp. 918-924, Nov. 2012.

[26] Y. Li, W. Li, and W. Yu, "A multi-band/UWB MIMO/diversity antenna with an enhanced isolation using radial stub loaded resonator," *Applied Computational Electromagnetics Society (ACES) Journal*, vol. 28, no. 1, pp. 8-20, Jan. 2013.

[27] H. Oraizi and B. Rezaei, "Application of inductive loadings for the dual and broad banding of CPW-fed ring antennas," *Applied Computational Electromagnetics Society (ACES) Journal*, vol. 27, no. 7, pp. 587-595, Jul. 2012.

[28] P. Wang, G. Wen, and Y. Huang, "Compact CPW-fed planar monopole antenna with triple-band operation for WLAN/WiMAX applications," *Applied Computational Electromagnetics Society (ACES) Journal*, vol. 27, no. 8, pp. 691-696, Aug. 2012.

[29] *IEEE Standard Letter Designations for Radar-Frequency Bands*, IEEE Std. 521-2002 (Revision of IEEE Std. 521-1984), pp. 1-3, 2003.

[30] L. Liu, S. W. Cheung, et al., "A compact circular-ring antenna for utra-wideband applications," *Microwave and Optical Technology Letters*, vol. 53, issue 10, pp. 2283-2288, 2011.

[31] A. T. Mobashsher, M. T. Islam, et al., "Wideband compact antenna with partially radiating coplanar ground plane," *Applied Computational Electromagnetics Society (ACES) Journal*, vol. 26, no. 1, pp. 73-81, Jan. 2011.

[32] M. S. Alam, M. T. Islam, and N. Misran, "A novel compact split ring slotted electromagnetic bandgap structure for microstrip patch antenna performance enhancement," *Progress in Electromagnetic Research (PIER)*, vol. 130, pp. 389-409, 2012.

Md. Rokunuzzaman was born in Dhaka, Bangladesh in 1989. He was awarded his B.Eng. (Hons) Electronics majoring in Microwave and Communications from Multimedia University (MMU), Malaysia. Currently he is pursuing his M.Sc. degree in Universiti Kebangsaan Malaysia and worked as a Research Assistant at Centre for Space Science (ANGKASA) in a research project funded by Malaysian government. His research interest focuses on microstrip antenna design, MMICs, RFID passive tag antenna, microwave filter, microwave power divider, amplifier, telecommunication, wireless communication, etc.

Mohammad Tariqul Islam is a Professor in the Department of Electrical, Electronic and Systems Engineering of the Universiti Kebangsaan Malaysia (UKM). He is also the Group Leader of Radio Astronomy Informatics Group at UKM. Prior to joining UKM, he was a Lecturer in Multimedia University, Malaysia. He is a Senior Member of the IEEE, regular Member of Applied Computational Electromagnetic Society (ACES) and serving as the Editor-in-Chief of the International Journal of Electronics & Informatics (*IJEI*). Tariqul has been very promising as a Researcher, with the achievement of several International Gold Medal awards, a Best Invention in Telecommunication award and a Special Award from Vietnam for his research and innovation. Over the years, he has carried out research in the areas of communication antenna design, radio astronomy antennas, satellite antennas, and electromagnetic radiation analysis. His publications include over 160 research journal papers, nearly 150 conference papers, and few book chapters on various topics related to antennas, microwaves and electromagnetic radiation analysis with 8 inventory patents filed. Thus far, his publications have been cited 1578 times, and the H-index is 24 (Source: Scopus). For his contributions, he has been awarded "Best Researcher Award" in 2010 and 2011 at UKM. He is now managing many research projects from the Ministry of Science, Technology and Innovation (MOSTI), Ministry of Higher Education Malaysia (MOHE) and some

International research grants from Japan.

Salehin Kibria was born in Dhaka, Bangladesh in 1988. He was awarded his B.Eng. (Hons) Electronics majoring in Telecommunications from Multimedia University (MMU), Malaysia. He was awarded his M.Sc. degree in Universiti Kebangsaan Malaysia and employed as a Research Assistant at Centre for Space Science (ANGKASA) in a research project funded by Malaysian government. His research interest focuses on RFID Reader Antenna designs, telecommunication, Particle Swarm Optimization, etc.

Wideband Power Divider Using Novel Split-Ring Resonator

Tao Huang [1], Di Jiang [1], and Hongzhi Hu [2,3*]

[1] School of Communication and Information Engineering
University of Electronic Science and Technology of China, Chengdu, 611731, China

[2] School of Automation Engineering
University of Electronic Science and Technology of China, Chengdu, 611731, China

[3] School of Electronic Engineering and Automation
Guilin University of Electronic Technology, Guilin, 541004, China

Abstract ─ A set of novel split-ring resonator basic block Hybrid-Microwave Integrated-Circuit (HMIC) components (transmission line, open and short stubs) is presented with applications to the RF/Microwave power divider. This new open and short LH HMIC resonators have compact sizes of 0.81 and 1.44 mm^2, respectively. The prototypes of an LH power divider constructed from these basic components have been designed, fabricated, and characterized. The LH power divider including two LH branches shows equal power split from 1 to 7 GHz. The proposed power divider benefit from the miniaturized LH HMIC components and have compact sizes of 2.205 mm^2, respectively. There is a good agreement between the full-wave simulations and measurement results with 0.254-mm thick RT5880 substrate. While maintaining similar performance, a 50% reduction in impedance transformer is achieved in comparison to a conventional design.

Index Terms ─ Compact, power divider, Split Ring Resonators (SRRs).

I. INTRODUCTION

There is an increasing demand to design compact broad-band components for modern wireless communication systems. A key aspect in such components is to achieve their functionality at the required system frequencies. In this regard, due to the possibility of engineering their dispersion diagram, metamaterial-based artificial lines provide a good solution [1]. Such artificial lines have been applied to the design of broad-band power dividers, among other microwave components [2]. Recently, several works have demonstrated the possibility of implementing broad-band and even multiband components by means of metamaterial-based artificial lines, including the experimental validation of a broad-band microwave passive circuit. One of these approaches consists on the implementation of microwave components by means of metamaterial transmission lines. Such lines are artificial lines consisting on a host line loaded with reactive elements, and they can be implemented by means of two main approaches: (i) the CL-loaded approach, where conventional transmission lines are loaded with series capacitances and shunt inductances, and (ii) the resonant-type approach, where the lines are loaded with sub-wavelength resonators, such as Split-Ring Resonators (SRRs) or Complementary Split-Ring Resonators (CSRRs) combined with shunt inductances and series capacitances, respectively [3]. These lines exhibit controllable electrical characteristics, beyond what can be achieved in conventional lines, because of the fact that there are more degrees of freedom. In addition, metamaterial transmission lines can be designed to be electrically small, which makes them suitable for the synthesis of compact microwave circuits. In the case of the resonant-type approach, the size of the line is determined by the size of the resonators; for this reason, it is possible to obtain an important level of miniaturization (the use of electrically

Submitted On: May 17, 2013
Accepted On: October 6, 2014

small resonators and the possibility to implement artificial lines with the required phase and impedance with a single unit cell is relevant for size reduction).

The power divider and combiner are very important components for microwave power amplifiers [4-6]. Recent years have seen a worldwide effort to develop wide-band power dividers due to the trend of broad band mobile systems. A conventional power divider operates only at one design frequency. Therefore, it is not suitable for some broad-band operations. In some applications, a broad-band operation is needed. In the literature, most of the papers are based on the power divider and their multi-band operation is achieved by using open and short-ended stubs, by multiple transmission line transformers or by coupled lines. All these devices use the classical microstrip transmission line and therefore show low performances regarding miniaturization or operating bandwidth. The Split Ring Resonators (SRRs) is a practical implementation of a left-handed metamaterial which is generally defined as an artificial, effectively homogeneous electromagnetic structure with unusual properties, not readily available in nature [7]. Several power dividers based on the Split Ring Resonators (SRRs) have been proposed. However, they are single band and have either high insertion loss or narrow band between output ports. This paper presents a novel broad-band power divider also based on the SRRs, but with improved performances as compared to the previous mentioned work.

II. POWER DIVIDER DESIGN

The geometry of the proposed novel broadband power divider is shown in Fig. 1. This power divider printed on a 0.254-mm thick RT5880 (substrate with dielectric constant ε_r=2.2 and loss tangent tan=0.0009) with dimension of 15×14.97 mm^2. The size of inner-square (R_1, R_2) should be adjusted to determine the central frequency of power divider as simulated in Fig. 2. If other parameters are fixed, the central frequency will increase with the decrease of R_1 and R_2. If R_1 and R_2 are fixed, the central frequency could be also enhanced by increasing slit width of squares (g) as simulated in Fig. 3. For the convenience of optimization, the width of squares (d_1, d_2) and distance between squares are set to be the same as (g). After that, the height (h) and length(s) should be also optimized. These optimization works were managed by using commercial 3-D electromagnetic software HFSS [8].

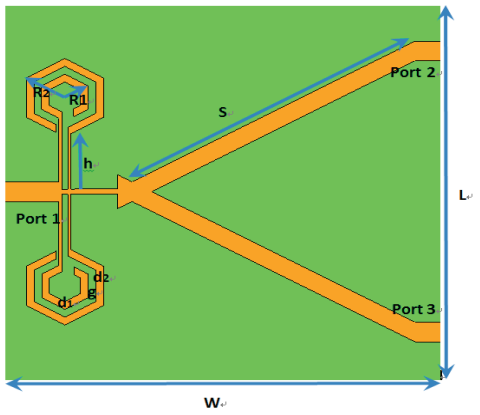

Fig. 1. Geometry of power divider, the dimensions are: R_1=0.9 mm, R_2=1.29 mm, d_1=0.2 mm, d_2=0.2 mm, g=0.19 mm, S=10.9 mm, h=1.02 mm, W=15 mm, and L=14.97 mm.

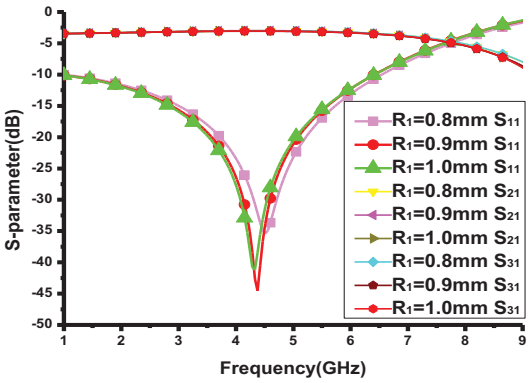

(a)

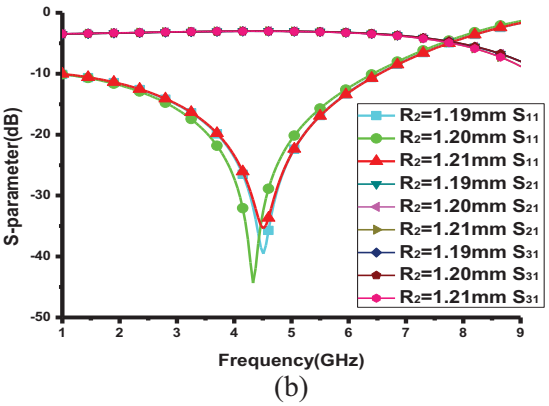

(b)

Fig. 2. (a) Simulated S-parameters of different radius of R_1, and (b) simulated S-parameters of different radius of R_2.

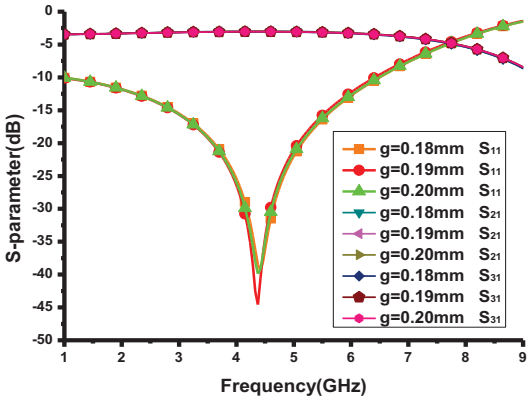

Fig. 3. Simulated S-parameters of different slit width of squares (g).

III. RESULTS AND DISCUSSION

To validate the proposed design, the novel split-ring resonator unit cell based power divider was fabricated [9]. The photograph of the fabricated device is shown in Fig. 4, and we can see its compact size from Table 1. The prototype has been characterized and its relevant measured scattering parameters (return losses and transmission coefficient) are shown in Fig. 5. By comparing Fig. 5 and Fig. 6, it can be seen that there is good agreement between simulated and measured results for the novel broadband microstrip power divider. However, the measured central frequency (4.45 GHz) is higher by approximately 2.2% than the simulated frequency (4.35 GHz). This shift can be attributed to fabrication tolerances, connectors, and the substrate properties [15-17]. The measured return loss is below -45 dB, and the measured insertion loss at each branch, is approximately -3.5 dB. The slightly higher loss value approximately 0.5 dB is attributed to inaccuracies in fabrication of the structure. The measured results show that this new unit cell can be used in the design and fabrication of miniaturized RF and microwave circuits.

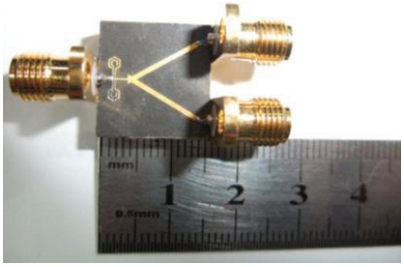

Fig. 4. Photograph of the proposed novel power divider.

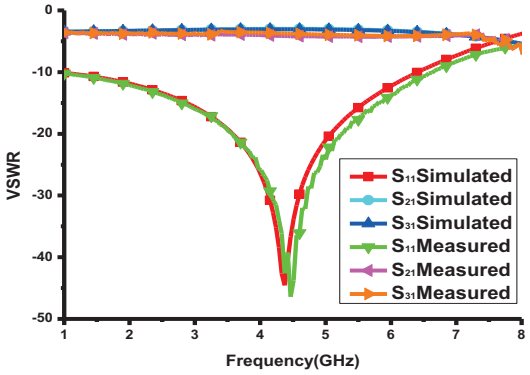

Fig. 5. Measured and simulated frequency responses for the thrus (S_{21} and S_{31}), and the return loss (S_{11}) of the broadband power divider.

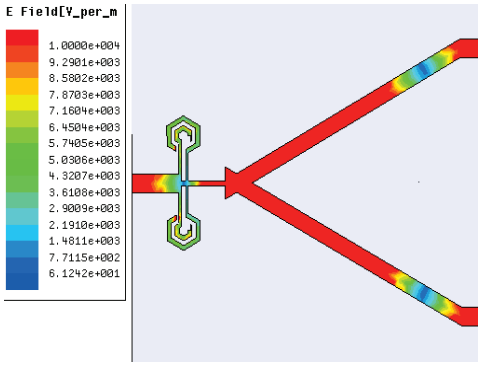

Fig. 6. Simulated electric field (4.35 GHz) on the proposed broadband power divider.

Table 1: Comparison of sizes with reported power dividers

	[10]	[11]	[12]	[13]	[14]	This work
Frequency Range (GHz)	3.1~10.6	3~4.7	1.15~2.21	4.25~4.75	2.7~4.7	1~7
Power-Dividing Radio	1:1	1:1	1:1	2:1	1:1	1:1
Size ($\lambda_g \times \lambda_g$)	0.75x1.12	1.04x0.28	0.69x0.59	0.98x0.98	0.81x0.40	0.33x0.33

IV. CONCLUSION

In this paper, a novel broadband microstrip power divider utilizing Split Ring Resonators (SRRs) has been proposed. Based on the unique properties of the split ring resonators, the designed wideband power divider that can operate multi-frequency bands, covering the requirements of the most common telecommunication systems. The power divider shows good performances, low insertion loss and compact size. In contrast to the conventional power divider, its size does not depend on the operating frequency. The proposed broadband microstrip power divider is a promising device for microwave and millimeter wave communication systems.

REFERENCES

[1] A. Lai, C. Caloz, and T. Itoh, "Composite right/left-handed transmission line metamaterials," *IEEE Microw. Mag*, (9), pp. 34-50, 2004.

[2] M. A. Antoniades and G. V. Eleftheriades, "A broadband Wilkinson balun using microstrip metamaterial lines," *IEEE Antennas Wirel. Propag. Lett.*, 4, pp. 209-212, 2005.

[3] S. G. Mao and Y. Z. Chueh, "Broadband composite right/left-handed coplanar waveguide power splitters with arbitrary phase responses and balun and antenna applications," *IEEE Trans. Antennas Propag.*, 54, (1), pp. 243-250, 2006.

[4] I. H. Lin, M. Devincentis, C. Caloz, and T. Itoh, "Arbitrary dual-band components using composite right/left-handed transmission lines," *IEEE Trans. Microw. Theory Tech.*, 52, (4), pp. 1142-1149, 2004.

[5] B. Xiao, J. Hong, and B. Wang, "A novel UWB out-of-phase four-way power divider," *Applied Computational Electromagnetics Society (ACES) Journal*, vol. 26, no. 10, pp. 863-867, October 2011.

[6] V. Demir, D. Elsherbeni, D. Kajfez, and A. Z. Elsherbeni, "Efficient wideband power divider for planar antenna arrays," *Applied Computational Electromagnetics Society (ACES) Journal*, vol. 21, no. 3, pp. 318-324, November 2006.

[7] C. H. Tseng and T. Itoh, "Dual-band bandpass and bandstop filters using composite right/left-handed metamaterial transmission lines," *IEEE MTT-S Int. Microw. Symp. Dig.*, San Francisco, CA, USA, pp. 931-934, 2006.

[8] C. Caloz and T. Itoh, "Electromagnetic metamaterials: transmission line theory and microwave applications," *Wiley*, 2006.

[9] V. Piatnitsa, D. Kholodnyak, P. Kapitanova, I. Fischuk, T. Tick, J. Jantti, H. Jantunen, and I. Vendik, "Right/left-handed transmission line LTCC directional couplers," *Proc. of 37th European Microwave Conf.*, Munich, Germany, pp. 636-639, 2007.

[10] A. M. Abbosh, "Ultra wideband inphase power divider for multilayer technology," *IET Microw., Antennas, Propag.*, vol. 3, no. 1, pp. 148-153, February 2009.

[11] B. L. Ooi, W. Palei, and M. S. Leong, "Broad-banding technique for in-phase hybrid ring equal power divider," *IEEE Trans. Microw. Theory Tech.*, vol. 50, no. 7, pp. 1790-1794, July 2002.

[12] H. Oraizi and A. R. Sharifi, "Optimum design of a wideband two-way Gysel power divider with source to load impedance matching," *IEEE Trans. Microw. Theory Tech.*, vol. 57, no. 9, pp. 2238-2248, September 2009.

[13] H. Oraizi and A. R. Sharifi, "Optimum design of asymmetrical multi-section two-way power dividers with arbitrary power division and impedance matching," *IEEE Trans. Microw. Theory Tech.*, vol. 59, no. 6, pp. 1478-1490, June 2011.

[14] Z. Sun, L. Zhang, Y. Yan, and H. Yang, "Design of unequal dual-band Gysel power divider with arbitrary termination resistance," *IEEE Trans. Microw. Theory Tech.*, vol. 59, no. 8, pp. 1955-1962, August 2011.

[15] H. Zhang and H. Xin, "Designs of dual-band Wilkinson power dividers with flexible frequency ratios," *Proceedings of 2008 IEEE MTT-S International Symposium*, Atlanta, Georgia, USA, June 15-20, 2008.

[16] Y. Wu, Y. Liu, and S. Li, "An unequal dual-frequency Wilkinson power divider with optional isolation structure," *In Progress In Electromagnetics Research, PIER 91*, pp. 393-411, 2009.

[17] Z. Lin and Q. X. Chu, "A novel approach to the design of dual-band power divider with variable power dividing ratio based on coupled-lines," *In Progress In Electromagnetics Research, PIER 103*, pp. 271-284, 2010.

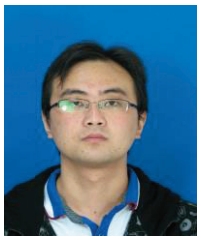

Tao Huang received the B.S. degree in Communication and Information Engineering from the University of Electronic Science and Technology of China (UESTC) in 2010. He has been read the Ph.D. degree in UESTC since 2013. His research interests include microwave and millimeter wave circuit designing and frequency synthesis.

Circular Ring Optically Transparent Antenna for Ultra-Wideband Applications

M. R. Haraty [1], M. Naser-Moghadasi [1], A. A. Lotfi-Neyestanak [2], and A. Nikfarjam [3]

[1] Department of Electrical Engineering, Science and Research Branch
Islamic Azad University, Tehran, 14778-93855, Iran
m.haraty@srbiau.ac.ir, mn.moghaddasi@srbiau.ac.ir

[2] Department of Electrical Engineering,Yadegar-e-Imam Khomeini (RAH) Shahre-Rey Branch
Islamic Azad University, Tehran, 18155-144, Iran
alotfi@iust.ac.ir

[3] Faculty of New Sciences & Technologies
University of Tehran, P.O. Box:14395-1561, Tehran, Iran
a.nikfarjam@ut.ac.ir

Abstract ─ This paper presents the results of a simple and novel optically transparent Ultra-Wideband (UWB) antenna consisting of a coplanar waveguide fed circular ring-shaped monopole that is constructed on a transparent conductive Indium Tin Oxide (ITO) film. The proposed antenna exhibits an impedance bandwidth of 163% between 2 to 20 GHz, which exceeds Federal Communication Commission's UWB frequency range, with a return-loss performance more than 10 dB. The antenna radiates omni-directionally in the *H*-plane and bi-directionally in the *E*-plane. The measured results confirm the antenna is a feasible proposition for integration with various ultra-wideband applications requiring transparent aesthetics. Details of the antenna design, simulation and measurement results are presented.

Index Terms ─ Coplanar Waveguide (CPW) fed antennas, Indium Tin Oxide (ITO), transparent antenna, transparent conductive, Ultra-Wideband (UWB) antennas.

I. INTRODUCTION

Optically transparent antenna are gaining prominence and becoming a very attractive proposition for various applications such as car windshields, building windows, touch panel controls, and display panels of wireless communications equipment. These antennas can enhance security and aesthetics of vehicles, and can be integrated within satellites' solar cell panels [1]. Such antennas can be constructed on transparent conductive film such as Indium Tin Oxide (ITO), Fluorine-doped Tin Oxide (FTO) and silver coated polymer (AgHT) films [2-4]. ITO is more desirable as it offers reasonable trade-off between optical transparency and conductivity. However, due to the difficulty of fabrication and lossy nature of the transparent materials, the R&D work on transparent antennas is limited and sparse in the literature [5-8]. In [5], the transparent antenna operates in 2.3 and 19.5 GHz, in [6], the AgGL meshed transparent antenna operates in 60 GHz and it has transparency above 80% in wavelength 550 nm. Katsounaros [7] has been presented an UWB Transparent antenna which works from 1 GHz to 8.5 GHz. The authors used an AgHT-4 optically transparent conductive coating on a clear polyester substrate.

After releasing by the Federal Communications Commission (FCC) for a bandwidth of 7.5 GHz (3.1-10.6 GHz) for UWB wireless communications, UWB is rapidly advancing as a high data rate wireless communication technology [9]. The UWB system has wide applications in short range and high speed wireless systems such as local area communications, radar, medical imaging and other military applications. This technology

Submitted On: July 27, 2013
Accepted On: September 27, 2014

requires antennas that are small in size with a wide bandwidth, possess omni-directional radiation patterns and exhibit minimum distortion in the received waveform. Although recently numerous planar broadband antenna configurations have been studied and reported [10-12], these antennas have not been implemented on the transparent media to date. In this paper, a new optically transparent antenna is proposed with a ring-shaped patch that is excited by CPW-fed structure and fabricated on ITO conductive film for UWB applications. Although the annular ring structure in opaque substrate is not new, in this paper we have studied various types of transparent substrates to achieve high transparency, higher bandwidth than nontransparent substrate and investigated the effect of them in antenna design. The antenna's impedance bandwidth of 163% extends between 2-20 GHz with return-loss better than 10 dB. This simulation result is compared with measurement which shows a good agreement.

II. ANTENNA CONFIGURATION

The geometry and parameters defining the proposed transparent UWB antenna are shown in Fig. 1. The antenna comprises of circular ring monopole patch with a CPW feed structure. It is fabricated on an ITO conductive film that has a thickness and surface resistance of 100 nm and 15 Ω/sq, respectively. Its transparency is also above 85% at a wavelength of 550 nm. Figure 2 shows the transparency of Antenna (ITO+substrate) for various wavelengths.

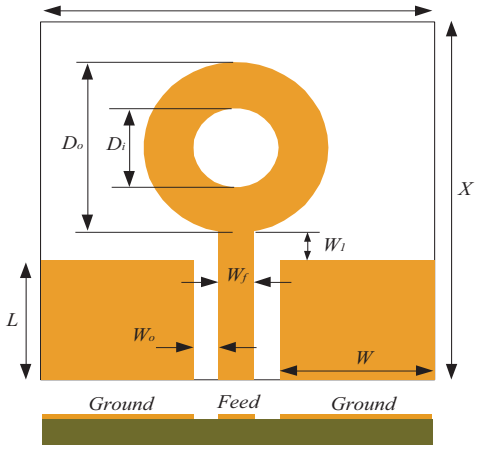

Fig. 1. Geometry and characterizing parameters of the proposed antenna.

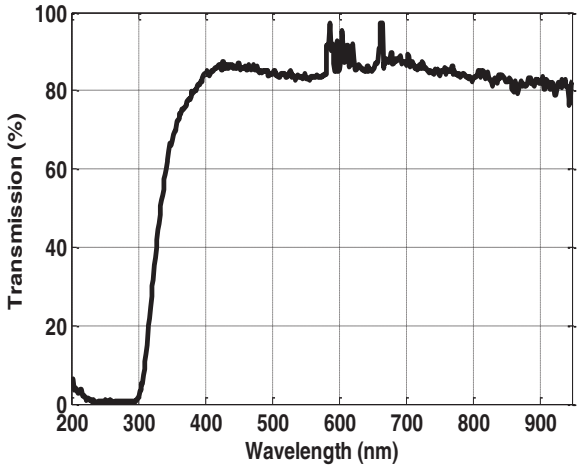

Fig. 2. Measured transparency of the antenna for various wavelengths.

The antenna is mounted on a 1.3 mm thick glass substrate with ε_r=4.6. The antenna located in the *x-y* plane, has a total substrate size of 50×50 mm^2. The antenna characterizing dimensions are given in Table 1. A photograph of the fabricated antenna is shown in Fig. 3. In order to obtain 50 Ω input impedance, a CPW feed-line is used, which has width, W_f of 2.0 mm and is separated from the coplanar ground-plane with gap, W_o of 0.34 mm.

Table 1: Characterizing parameter values of the antenna

Parameters	*X*	*W*	*L*	*W1*	*D0*	*Di*
Units (mm)	50	23.45	18.7	1	25.2	11

Fig. 3. Photograph of the fabricated antenna.

III. SIMULATION AND MEASURMRNT RESULTS

The proposed antenna in Fig. 1 is fabricated using parameter values given in Table 1. The antenna design was conducted using Ansoft High-Frequency Structure Simulator (HFSS™). The return-loss was measured in an anechoic chamber using the Agilent 8722ES network vector analyzer (50 MHz - 40 GHz). Simulated and measured reflection coefficient (S_{11}) presented in Fig. 4, are in good agreement.

The measured response is better than the simulated one. The discrepancy is attributed to a lesser extent of the fabrication tolerance and the effect of Ag adhesive applied to mount the antenna on the glass substrate. Also, the dielectric constant of the substrate in the measurement may be different than one used in the simulation.

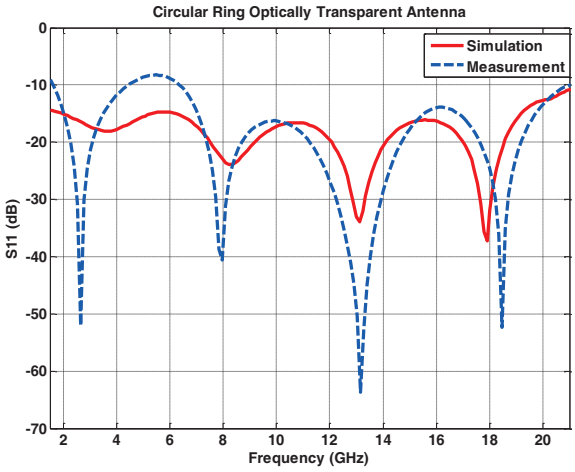

Fig. 4. Simulated and measured reflection coefficient of the proposed antenna.

The bandwidth of the fabricated antenna is 163% across the frequency range of 2-20 GHz for S_{11} <-10 dB. The normalized radiation patterns of the proposed antenna at three spot frequencies, i.e., 3, 8 and 13 GHz, are shown in Fig. 5. The results show that the *H*-plane radiation pattern of the antenna is omni-directional, while the *E*-plane one is bi-directional. The frequency range of this antenna exceeds the UWB frequency region defined by FCC (3.1-10.6 GHz), which validates the effectiveness of the proposed antenna. Table 2 compares the proposed transparent antenna using ITO coated glass with copper plate antenna.

Figure 6 shows the effect of antenna dimension on the reflection coefficient. As it can be seen, by reducing the external diameter and increasing the internal one, antenna bandwidth can be improved. Figure 7 shows variation of dielectric constant of the transparent antenna using various transparent materials. As it can be seen, the use of PEC allows achieving maximum bandwidth while preserving the transparency.

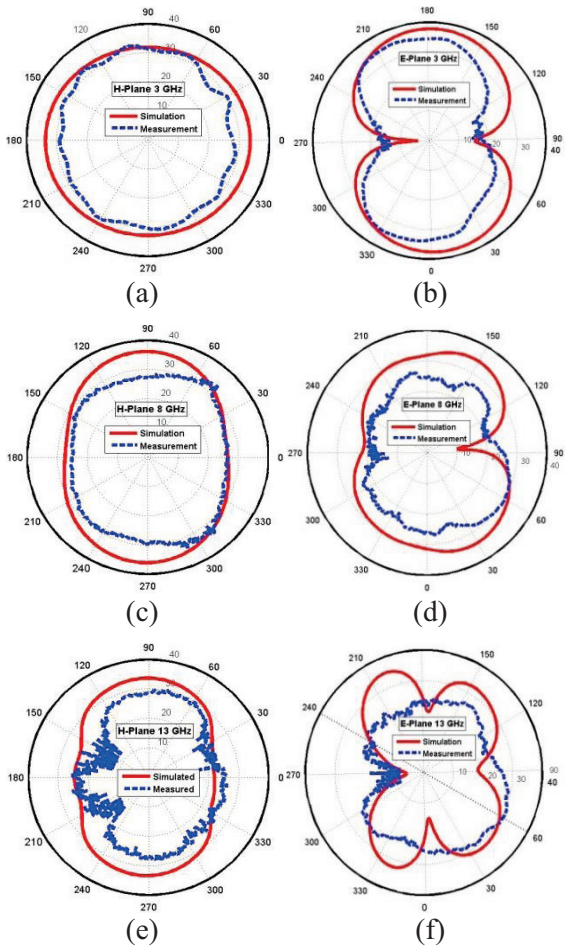

Fig. 5. Simulated and measured E- and H-plane radiation patterns: (a) H-plane 3 GHz, (b) E-plane 3 GHz, (c) H-plane 8 GHz, (d) E-plane 8 GHz, (e) H-plane 13 GHz, and (f) E-plane 13 GHz.

Table 2: Measured gain and parameters of antenna

Frequency (GHz)	3	5	8	13	T (%)	BW (%)
ITO+glass (dB)	-4	-2	0.5	2	88	163
Copper+FR4 (dB)	0.5	3	5	5.2	0	138

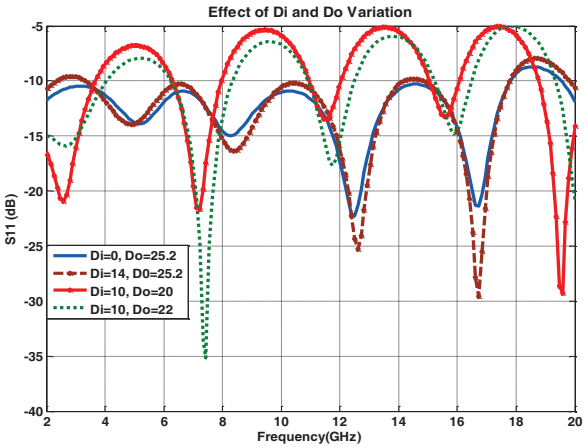

Fig. 6. Effect of Di and Do variation.

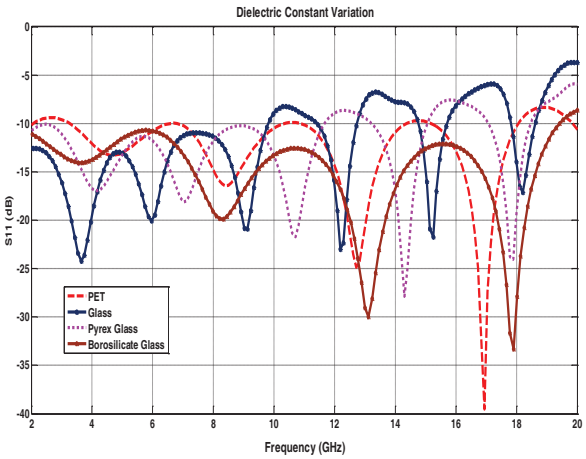

Fig. 7. Effect of dielectric constant variation.

IV. CONCLUSIONS

An optically transparent monopole antenna consisting of a circular ring patch, which is excited through a coplanar waveguide is proposed. This antenna exhibits return-loss performance exceeding FCC's ultra-wideband frequency range. Its performance is assessed by simulation and verified experimentally. The antenna is fabricated on a transparent conductive ITO film and mounted on a glass substrate with dimension of 50×50 mm^2. Its bandwidth is 163% (2-20 GHz) for a return-loss better than 10 dB (VSWR<2). In addition, the antenna radiates omni-directionally in the *H*-plane and bi-directionally in the *E*-plane. The compact size, low profile and transparent feature of the proposed antenna allows it to be integrated in a mini solar panel or cell for harnessing solar energy to provide backup power for efficient management and use of the battery in the compact UWB devices.

REFERENCES

[1] J. Saberin, "Optically transparent antenna for small satellites," *M.S. Thesis, Dept. Elect. Eng., Univ. of Utah*, Salt Lake City, UT, 2010.

[2] C. T. Lee, C. M. Lee, and C. H. Luo, "The transparent monopole antenna for WCDMA and WLAN," *Proc. IEEE WAMICON*, pp. 1-3, December 2006.

[3] N. Outaleb, J. Pinel, M. Drissi, and O. Bonnaud, "Microwave planar antenna with RF sputtered indium tin oxide," *Microw. Opt. Technol. Lett*., 24, (1), pp. 3-7, 2000.

[4] T. Peter, R. Nilavalan, H. F. A. Tarboush, and S. W. Cheung, "A novel technique and soldering method to improve performance transparent polymer antennas," *IEEE Antennas Wireless Propag. Lett*., 9, pp. 918-921, 2010.

[5] R. N. Simons and R. Q. Lee, "Feasibility study of optically transparent microstrip patch antenna," *Proc. IEEE Antennas Propag. Soc. Int. Symp*., 4, pp. 2100-2103, July 1997.

[6] J. Hautcoeur, L. Talbi, and K. Hettak, "Feasibility study of optically transparent CPW-fed monopole antenna at 60-GHz ISM bands," *IEEE Transactions on Antennas and Propagation*, 61, (4), pp. 1651-1657, 2013.

[7] A. Katsounaros, Y. Hao, N. Collings, and W. A. Crossland, "Optically transparent ultra-wideband antenna," *Electron. Lett*., 45, (14), pp. 722-723, 2009.

[8] N. Guan, H. Furuya, D. Delaune, and K. Ito, "Radiation efficiency of monopole antenna made of a transparent conductive film," *Proc. IEEE AP-URSI*, pp. 221-224, June 2007.

[9] *Federal Communications Commission*, "Revision of part 15 of the commission's rules regarding ultra wideband transmission system first report and order," Tech. Rep. ET Docket 98-153, FCC02-48, FCC, February 2002.

[10] M. R. Haraty, S. M. Seyed-Momeni, and R. A. Sadeghzadeh, "Candelabra shaped microstrip antenna for ultra-wideband applications," *Microw. Opt. Technol. Lett*., 53, (3), pp. 669-672, 2011.

[11] M. Naser-Moghadasi, S. M. Seyed-Momeni, M. R. Haraty, and B. S. Virdee, "A novel compact ultra-wideband dual-notch microstrip antenna," *Francis & Taylor Electromagn*., 32, (5), pp. 233-243, 2012.

[12] J. Liang, C. Chiau, X. Chen, and C. G. Parini, "Study of CPW-fed circular disc monopole antenna for ultra-wideband applications," *IEE Proc. Microw. Antennas Propag*., 152, (6), pp. 520-526, 2005.

Mohammad Reza Haraty was born in Tehran, Iran, in 1984. He received his B.Sc. degree in Electrical Engineering (Communication) from Yadegar-e-Imam Khomeini (RAH) Shahre-Rey Branch, Islamic Azad University, Tehran-Iran in 2008 and M.Sc. degree in Electrical Engineering (Communication) from Islamic Azad University, Science & Research Branch, Tehran, Iran, in 2011. Since 2011, he has been working towards his Ph.D. degree at Islamic Azad University, Science & Research Branch, Tehran, Iran. From 2010 he was teaching in the Department of Electrical Engineering at the Yadegar-e-Imam Khomeini (RAH) Shahre-Rey Branch, Islamic Azad University, Tehran-Iran. His main areas of research interest are Microstrip antenna, Microwave passive and active circuits, Transparent antenna and shielding, Optimization methods in electromagnetic, Microwave measurement, Numerical methods in electromagnetic problems and RF MEMS.

Mohammad Naser-Moghadasi was born in Saveh, Iran, in 1959. He received the B.Sc. degree in Communication Eng. in 1985 from the Leeds Metropolitan University (formerly Leeds Polytechnic), UK. Between 1985 and 1987, he worked as an RF Design Engineer for the Gigatech Company in Newcastle Upon Tyne, UK. From 1987 to 1989, he was awarded a full scholarship by the Leeds Educational Authority to pursue an M.Phil. studying in CAD of Microwave circuits. He received his Ph.D. in 1993, from the University of Bradford, UK. He was offered then a two years Post Doc. to pursue research on Microwave cooking of materials at the University of Nottingham, UK. From 1995, Naser-Moghadasi joined Islamic Azad University, Science & Research Branch, Iran, where he currently is an Associate Professor and Head of Postgraduate Studies. His main areas of interest in research are Microstrip antenna, Microwave passive and active circuits, RF MEMS. Naser-Moghadasi is Member of the Institution of Engineering and Technology, MIET and the Institute of Electronics, Information and Communication Engineers (IEICE). He has so far published over 140 papers in different journals and conferences.

Abbas Ali Lotfi-Neyestanak was born in Tehran, Iran. He received his B.Sc. degree in Communication Eng. (1993) and M.Sc. degree in Electronic Engineering (1997) and Ph.D. degree in communication Engineering (2004) from Iran University of Science and Technology (IUST) Tehran, Iran, respectively. From 1997 he was teaching in the Department of Electrical Engineering at the Yadegar-e-Imam Khomeini (RAH) Shahre-Rey Branch, Islamic Azad University, Tehran-Iran. In 2011, he joined the Radio Science Lab at the University of British Columbia as visiting researcher. Currently, he is collaborating with the Department of Electrical Engineering, University of Waterloo, Ontario, Canada. His main areas of research interest are Microstrip antenna, Microwave passive and active circuits, Electronic circuits design, EMC & EMI in High voltage, Optimization methods in electromagnetic, Radio wave propagation, Microwave measurement, Numerical methods in electromagnetic problems, RF MEMS and bio electromagnetic. Dr. A. A. Lotfi Neyestanak is a Senior Member of IEEE and has published two books and more than 100 papers in international journals and conferences.

Alireza Nikfarjam was born in Tehran on 1975. He obtained his BSc and MSc degrees in electronics both in Iran in 1998 and 2001, respectively. In 2007 he obtained his PhD in microelectronics from K. N. Toosi University of Technology. He joined the Sharif University of Technology in Tehran in 2009 as Post-Doctoral researcher to work on nano-sensors. Then he joined the Faculty of New Sciences and Technologies of University of Tehran in Tehran in 2011 as assistant professor. His research interests are semiconductor micro&nano-devices especially gas sensors, MEMS&NEMS and Organic Electronics.

A New Meandered-Stripline Fed Dual Band Patch Antenna

M. R. Ahsan [1], M. T. Islam [1], and M. Habib Ullah [2]

[1] Dept. of Electrical Electronic and Systems Engineering, Faculty of Engineering and Built Environment
Universiti Kebangsaan Malaysia, Bangi, Selangor, 43600, Malaysia
rezwanul.ahsan@yahoo.com, titareq@yahoo.com

[2] Department of Electrical Engineering, Faculty of Engineering
University of Malaya, Kuala Lumpur, 50603, Malaysia
habib_ctg@yahoo.com

Abstract ─ A new circular shaped patch antenna loaded with vertical slots and fed by meandered-stripline on a high dielectric material substrate is proposed in this paper, and experimentally verified the performance of the printed prototype. With the deployment of meandered-stripline structure to excite in the assistant of partial ground plane, the experimental results show that the proposed antenna has achieved wider bandwidth with satisfactory gain. The measured impedance bandwidth (voltage wave stand ratio, VSWR <= 2) of the proposed antenna at lower band is 400 MHz (600 MHz - 1 GHz) and at upper band is 700 MHz (2.25 GHz - 2.95 GHz). The peak gains of -1.18 dBi and 4.87 dBi have measured with topmost radiation efficiencies of 82.0% and 92.6% and have observed at lower band and upper band respectively. The performance criteria and almost consistent radiation pattern make the proposed antenna as a suitable candidate for UHF RFID, WiMAX and WLAN applications. The designing of antenna model and the parametric study have been performed with commercially available EM simulation software on 64-bit windows PC. The proposed antenna model has been validated by comparing the obtained experimental results with the output from the numerical simulation and apparently shows good agreement between them.

Index Terms ─ Bandwidth enhancement, finite element method, meandered-stripline feed, microstrip antenna, patch antenna, planar antenna, RFID, WiMAX, WLAN.

I. INTRODUCTION

The last couple of years, the innovative research ideas with the help of cutting-edge technology have contributed an intense boost to the wireless communications. Our todays social life always demanded cost effective, portable, compact, radiation efficient and reliable wireless communication devices. Thus, the request for designing printed, planar, small-sized, wideband, multiband and highly efficient antennas are escalated. The wideband and multiband functionality in antennas is a fundamental requirement nowadays to equip with the communication systems so that it can utilize the space effectively to increase portability and satisfy the standard operating frequency bands [1-3]. The microstrip antennas are being increasingly used in communication systems since they inherently got some promising preferences other than conventional antennas while considering size, cost, manufacturing process, durability and conformability [4]. On the other hand, intrinsically the microstrip patch antennas also suffer from narrow bandwidth which in turn deteriorates the performance while covering up some specific bands. The review process unfolds numerous patch antennas of various sizes and shapes of radiating patch with a number of dissimilar techniques that proposed in widening the impedance bandwidth. Out of the bandwidth broadening techniques, some can be mentioned here as for example, introducing separate slit lines [5-6], implementing unusual feeding techniques [7-8], integrating metallic strip

Submitted On: June 25, 2013
Accepted On: September 27, 2014

surrounding the radiating patch or some of its parts as parasitic element [9], using thick substrate or higher dielectric substrate [10], embedding array of similar geometric pattern based patch structure named differently as electromagnetic band gap (EBG) [11] and metasurface [12], employing metamaterial [13]. However, not all the above mentioned designs can significantly increase the bandwidth and gain of the antenna. Moreover, the extensive review of the recent articles has revealed the presence of trade-off between the antenna characteristics and the complex structure, time inefficient, cost ineffective antenna designs.

In the recent couple of years, the idea of meandered-stripline-fed patch antenna has gained potential interest among the antenna researchers. This technique is less cumbersome and cost effective in widening the bandwidth of patch antenna [14]. The microstrip-line-fed patch antennas ensure several stunning properties, as for example less radiation loss, low cross-polarization, easy fabrication and integration, no need to use via hole in the existing microstrip technology. Taking the advantage from strip-line-fed, a meandered-stripline-fed circular type patch antenna loaded with slits of similar width has been designed to cover two important frequency bands, namely ultra-high frequency (UHF) band for Radio Frequency Identification (RFID) and lower wireless/ Worldwide Interoperability for Microwave Access (WiMAX) band. A considerable amount of interest has been paid to the RFID system in UHF band due to its organizational and commercial use of its tracking and identification capabilities. In general, the UHF RFID system functions at the bands of Europe (865-867 MHz) and/or North America (902-928 MHz) [15-16]. On the other hand, WiMAX is based upon IEEE 802.16-2004, which is later modified to IEEE Std. 802.16e-2005 and it has different spectrum allocation in different parts of the world based on the standard band 2.3 GHz, 2.5 GHz and 3.5 GHz [17-18].

A new planar microstrip antenna has been proposed in this paper with detail configuration and the process of obtaining optimal design structure where the circular radiating element is loaded with a couple of vertical slots (along the y axis) and fed by meandered stripline structure. To demonstrate and analyze the performance characteristics of the proposed antenna, a physical model has been fabricated with a patch diameter of 38 mm (0.114λ), substrate thickness of 2 mm (0.006λ) and fed by meandering-stripline structure. Through numerous parametric studies, it has been revealed that the appropriate placement of slots on the circular patch along with the advantages of partial ground [19] and meandered-stripline structure can facilitate to attain the extended impedance bandwidth and good radiation properties, which make it suitable for dual-band wireless communication systems like UHF RFID and WiMAX applications.

II. DESIGNING ANTENNA STRUCTURE

The full wave 3-dimensional high frequency electromagnetic structural simulation (HFSS) tool [20] is used for the design and simulation of the proposed meandered-stripline-fed vertical slot loaded circular patch antenna. Like other typical microstrip patch antennas, the proposed antenna contains an SMA connector in its side, a meandered structure microstrip line to feed the radiating patch, a circular type radiating patch introduced with slotline of the same width on top and a rectangular ground plane at the bottom. The meandered-line-fed microstrip patch antenna structure and its associated detail dimensions are given by Fig. 1. The radiating patch is circular type where three types of different vertical rectangular slots of similar width (1.5 mm) are introduced. The radius of the circular patch (R) is chosen as 19 mm (0.057λ) and the length of its narrow rectangular slot lines are 32 mm (L3, L4), 24 mm (L2, L5) and 18 mm (L1, L6) for middle slots, side slots and outer side slots respectively. Therefore, half of the circular radiating patch is symmetrical to the other half along x-axis, thus effectively help to enhance the radiation by cancelling the cross-polarization effect. In between the radiating patch and partial ground plane, a 2 mm thick ceramic filled bio-plastic substrate of relative permittivity (ε_r) 15 is being inserted. Since impedance agreement is considered as very much sensitive to the geometry of the feed arrangement, a parametric study has been performed to find out best choice of meandered structure to feed the patch antenna. The radiating patch is excited by an optimized meandered stripline structure which is also coupled to the SMA connector by impedance matching. The optimal dimensions of the proposed antenna are offered in Table 1.

Table 1: Optimal dimension of the design antenna

Param.	Dim., mm	Param.	Dim., mm
W	41	L	51
W1	7	L1, L6	16
W2	33	L2, L5	24
SW	1.5	L3, L4	32
R	19	L*g*	5
-	-	L*f*	5

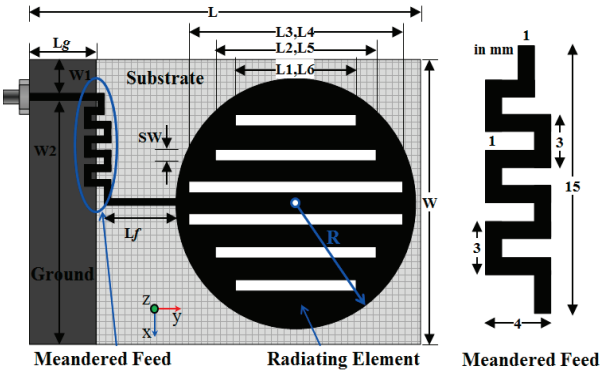

Fig. 1. Geometric configuration of the meandered stripline-fed patch antenna.

III. PARAMETRIC STUDY

The parametric studies are performed on several antenna variables to achieve optimized geometric structure and hence better impedance matching for the microstrip planar antenna. For the parametric studies, the numerical simulations have been done by finite element method (FEM) based commercial 3D simulator HFSS – has well established reputation in terms of accuracy. The parametric studies consider only the cutting slot inside the circular shaped radiating patch and the feeding structure to it. It is already known to the antenna researchers that some of the parameters (e.g., dimension of antenna, feed location) and performances (e.g., gain, radiation efficiency) have an effect on the patch antenna, these are excluded from parametric studies. For better understanding the impact of the parameter on the antenna performance, only one parameter has been picked for investigation while other parameters were left as it is. The Optimetrics engine from HFSS has been utilized successfully by setting up variables to carry out different parametric studies.

On a priority basis, the parametric study is being focused on the numbers of slots inside the circular radiating patch and its placement variation while considering the constant width of 1.5 mm. The graphical presentation in Fig. 2 validates the study and outcome. At the center of the radiating patch, the slots are etched out symmetrically by placing at the same distance from the central line. In this arrangement, the lower frequency is said to be getting closer to the achieved resonant frequency at VSWR less than 2. The symmetrical placement of the two side slots is responsible for the higher frequency band. The outer side slots inside the circular patch significantly affect the excitation, and the resonant frequencies are achieved at 0.9 GHz and 2.5 GHz with VSWR 1.24 and 1.3 respectively.

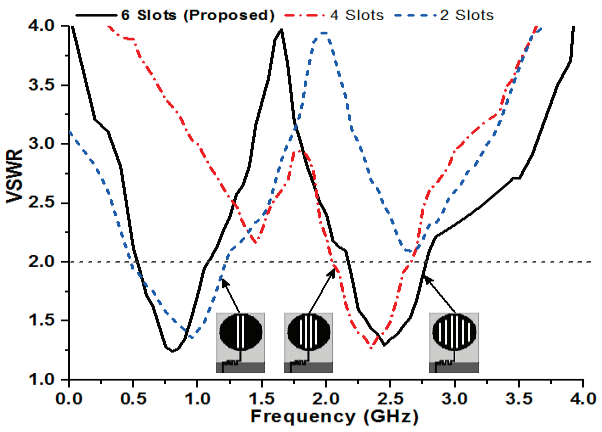

Fig. 2. Simulated VSWR for different numbers of slot inside radiating patch.

The parametric study has extended to analyze the effect of slot width and thus finding the optimal width to attain satisfactory VSWR with broader bandwidth. Figure 3 exhibits the graph for VSWR vs frequency for different width of the slots on circular patch structure. It is clearly understood from the figure that, the slot width of 1.5 mm is optimal for achieving comparatively wider impedance bandwidth and lower VSWR other than the slots of 1 mm and 2 mm width. Further investigations have been performed on the feeding structure to the patch which is responsible to contribute in the bandwidth widening process through good impedance matching. Figure 4 illustrates the antenna performance in terms of VSWR for different feeding arrangement. In the case of the L - strip and straight stripline feed, the return loss at center frequency and bandwidth are close by those of the meander strip feeding.

However, under the situation of 50 Ω impedance matching, the meander stripline feed structure offers the best agreement and exhibits broader bandwidth compared to other feeding method. Additionally, with the assist of partial ground plane the meander stripline structure promotes longer resonant mode by adapting the electric length which play vital role in bandwidth enhancement. The adjustable electrical length for different excitation in the case of meandered stripline feed also liable to produce comprehensible current phase distribution along the proposed antenna which may lead to reduce cross-polarization effect.

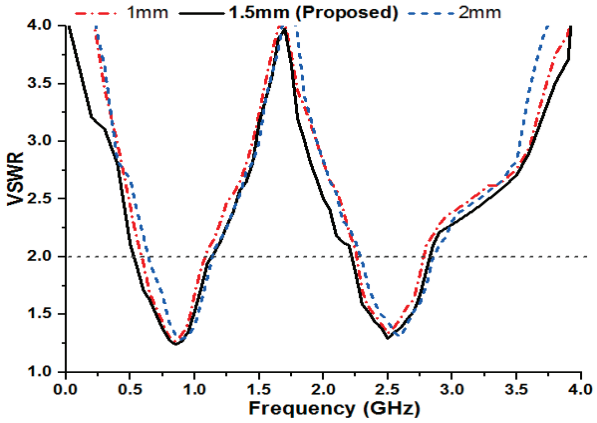

Fig. 3. Simulated VSWR against frequency for different width of the slot.

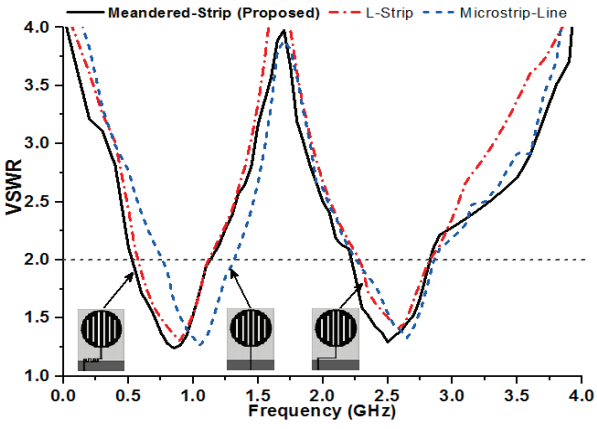

Fig. 4. Simulated VSWR for different feeding structure.

IV. RESULTS AND DISCUSSIONS

The 3D electromagnetic structure solving functionality of FEM based HFSS simulator has been utilized for performing numerical analysis and finding the optimized structure of the meandered-stripline fed circular type microstrip patch antenna. The accomplishment of the parametric study gives an optimized geometric structure of the proposed antenna, which is realized through in house PCB LPKF prototyping machine to get a physical test model and present in Fig. 5. Afterwards, the antenna parameters have been measured with the help of Agilent's Vector Network Analyzer (Agilent E8362C) in a standard sized anechoic measurement chamber. The simulation and measured antenna parameters have been further evaluated and graphically presented by available software package and computer aided tools.

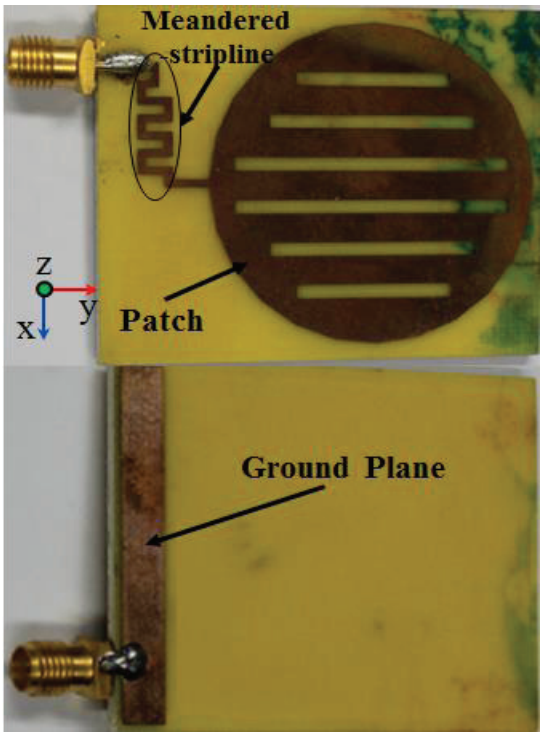

Fig. 5. Photograph for the prototype of the proposed antenna

Figure 6 shows the measured and simulated VSWRs against the frequency of the proposed two band antenna. The graphical output undoubtedly presents an excellent agreement between the simulated and measured VSWR. However, a diminutive deviation can be seen in between the simulated and measured results, which may occur on behalf of the fabrication tolerance affected by thickness uncertainty and/or existed inconsistency

in the substrate material. The measured impedance bandwidth (VSWR <= 2) range from 600 MHz to 1 GHz (44.4%) and 2.25 GHz to 2.95 GHz (28%) respectively. It is apparent that the attained bandwidth of the proposed antenna can successfully cover the UHF RFID and 2.3/2.5 GHz WiMAX/WLAN bands.

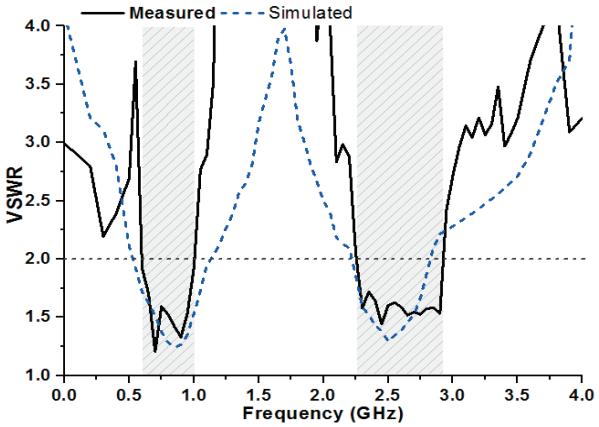

Fig. 6. The simulated and measured VSWR of the proposed meandered-strip-fed patch antenna.

The full-wave electromagnetic simulation software HFSS also make available the distribution of surface currents along the radiating patch and feed line. The proposed antenna further studied in terms of surface current distribution at two of its resonant frequencies, more specifically at 0.9 GHz and 2.5 GHz which are furnished through Fig. 7. At lower frequency of 0.9 GHz, an increased amount of surface current is seen to flow through the lower part of the radiating patch and also nonuniformity of current distribution can be seen along the meandered-stripling-fed structure. The surface current path in this case is less disturbed, which lead to generation of almost homogeneous electric and magnetic fields and thus provides less cross-polarization. Whereas at high frequency of 2.5 GHz, the distribution of surface current along the radiating patch and meandered-stipline-fed structure is almost uniform except the middle stripline of the patch which seems to carry slightly more surface currents. Stronger current distributions are also noticeable at the start and end terminal of the meandered-stripline-fed structure. Furthermore, in comparison to the lower frequency the variation of the current phase along the storylines of the radiating patch are clearly visible. The resulted effect can be validated through radiation pattern where a slight increase of cross-polarization and little discrepancy in E- and H-field can be realized.

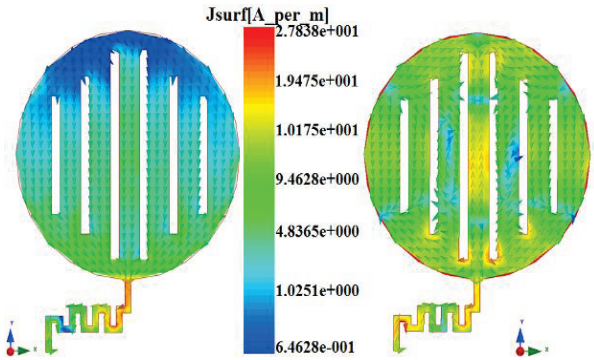

Fig. 7. Distribution of surface current at 0.9 GHz and 2.5 GHz.

The analysis of the proposed antenna performance has further carried out in terms of radiation characteristics. Figure 8 exhibits the far-field radiation patterns in E-plane and H-plane for the frequencies at 0.9 GHz and 2.5 GHz respectively. In the typical case of patch antenna, the radiation pattern in the E-plane is marginally widespread than that of the H-plane which is readily observable from the figure. For lower frequency, the co-polarization patterns for E- and H-plane are almost symmetric and directional. However, in the event of higher frequency the co- and cross-polarization patterns over the off-boresight angles for E-plane are much disturbed due to the fact of abnormal current phase along the length of the antenna. However, the effect of cross-polarization for both E- and H-plane at high frequency is increased to some extent, since the variation of the current phase suppresses the excitation responsible to increase cross-polarization effect. Typically, excitation from higher order modes distorts the electric currents, more specifically near to feed-patch joint which lead to degraded radiation. Use of a meander-stripline-feed essentially diminishes this issue as seen the current distribution patterns in Fig. 7. Through critical analysis, it can be concluded that the designed meandered-stripline-fed vertical slot-loaded circular patch antenna performs well in by providing a nearly conformal radiation pattern radially for operating bands by maintaining low cross-polarization.

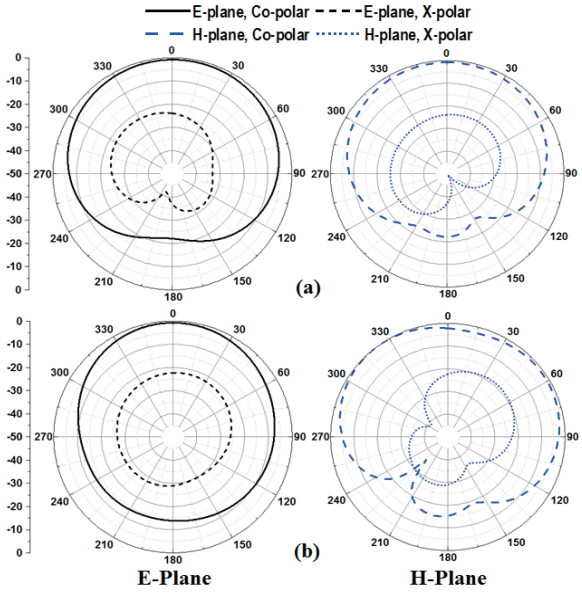

Fig. 8. Radiation patterns for the proposed antenna at: (a) 0.9 GHz, and (b) 2.5 GHz.

It is often typically considered that the antenna performance is being compromised in between the realized gain and operating bandwidth. For comparatively wider bandwidth of the antenna, it is necessary to ensure the measured antenna gain can meet the requirement for specific application. Free-space ranges are used to measure the gain of the designed dual-band antenna by utilizing two identical horn antennas whose gain and radiation patterns are known. Figure 9 shows the measured and simulated gains against the corresponding operating frequency bands. For the lower operating band at 0.6 GHz - 1 GHz the average and maximum gains are -3.34 dBi and -1.18 dBi respectively. Whereas, for the upper band at 2.25 - 2.95 GHz, the average and maximum gain are 3.15 dBi, 4.87 dBi and 2.85 dBi respectively, and this is why directivity of the designed antenna increased at high frequency. Figure 10 exhibits the radiation efficiency of the proposed antenna. It has been observed that the maximum radiation efficiency 76.65% is achieved at a lower UHF RFID band with average efficiency over the band is 63.03%. On the contrary, for WiMAX/WLAN band the achieved average and maximum radiation efficiencies are 82.02% and 92.6% respectively.

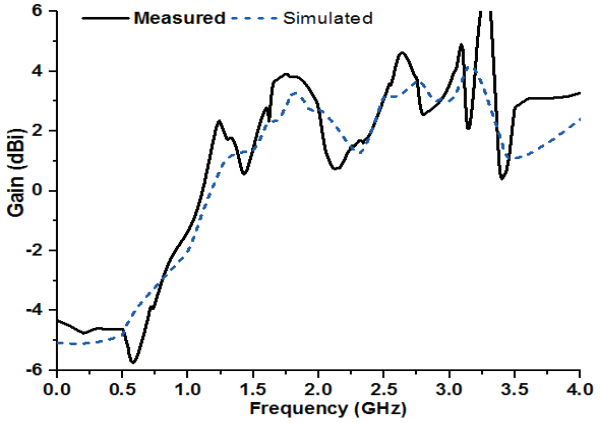

Fig. 9. Simulated and measured gain of the proposed antenna.

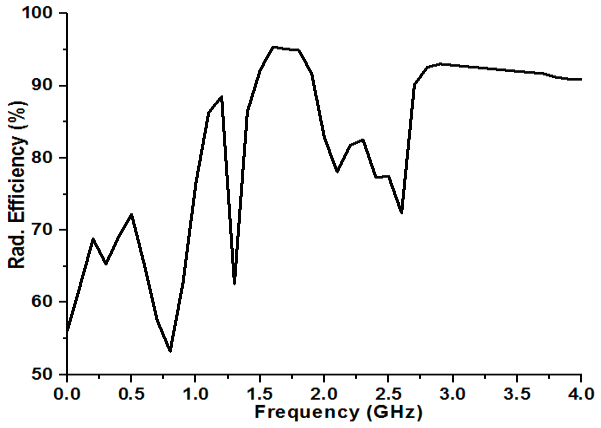

Fig. 10. Radiation efficiency of the proposed antenna.

Table 2 presents a concise comparative study between the performances of proposed and some existing antennas. The tabulated data clearly shows that, the proposed antenna is comparatively smaller in dimension with enhanced bandwidth and higher gain. On the contrary, some of the specified antennas have reported a higher gain with compromised fractional bandwidth and dimension. Additionally, these antennas would require more space to accommodate inside small, portable device which is not a preferable situation.

Table 2: Comparison between the proposed and some existing antenna

Ref.	Overall Dimension (mm^2)	Fract. Bandwidth (%)	Gain (dBi)
Proposed	40x50	44.4, 28	-1.18, 4.87
[6]	50x100	6.26, 8.16	-2.4, -0.64
[8]	40x40	28, 21	1.77, 1.72
[13]	25.4x29.2	1.36, 2.96	-3.5, 1.6
[21]	108x108	26.2, 22.2	3.5, 4.2

V. CONCLUSIONS

In this article, we have proposed a new slotline loaded circular shaped microstrip planar antenna with meandered-stripline feed structure. The design parameters of the antenna have been critically analysed through EM simulator to achieve the optimum geometric structure for the prototype antenna. The final optimized dimensions of the antenna is of 0.114λx0.114λx0.006λ, which is fabricated using in-house machineries. The experimental results from the fabricated antenna prototype represent that enhance bandwidth have been achieved for using the partial ground assisted meandered-stripline fed structure. The achieved fractional bandwidth of 44.4% (0.6-1 GHz, resonant frequency 0.9 GHz) for the lower band and 28% (2.25-2.95 GHz, resonant frequency 2.5 GHz) for the upper band with respect to their corresponding lower frequency cut at VSWR=2. The proposed antenna design with its optimal dimensions offer good agreement between the simulated and measured data. The antenna performance and communication quality in terms of bandwidth, radiation and gain, the proposed dual-band planar antenna comply with the requirements from UHF RFID and WiMAX/WLAN applications.

REFERENCES

[1] C. Y. D. Sim, F. R. Cai, and Y. P. Hsieh, "Multiband slot-ring antenna with single-and dual-capacitive coupled patch for wireless local area network/worldwide interoperability for microwave access operation," *IET Microwaves Antennas Propag. Let*., vol. 5, no. 15, pp. 1830-1835, 2011.

[2] J. William and R. Nakkeeran, "A new UWB slot antenna with rejection of WiMax and WLAN bands," *Appl. Comp. Electro. Society (ACES) J*., vol. 25, no. 9, pp. 787-793, 2010.

[3] R. Azim, M. T. Islam, and N. Misran, "Compact tapered-shape slot antenna for UWB applications," *IEEE Antennas Wirel. Propag. Lett*., vol. 10, pp. 1190-1193, 2011.

[4] S. Noghanian and M. K. Jung, "Ultra wide band planar slot antenna," *J. Electromagn. Waves Appl*., vol. 22, no. 8-9, pp. 1299-1308, 2008.

[5] M. H. Ullah, M. T. Islam, and J. S. Mandeep, "Printed prototype of a wideband S-shape microstrip patch antenna for Ku/K band applications," *Appl. Comp. Electro. Society (ACES) J*., vol. 28, no. 4, pp. 307-313, 2013.

[6] J. W. Park and H. M. Lee, "Isolation improvement of two-port multiple-input-multiple-output antenna using slits and split ring resonators on the ground plane," *in 2011 International Workshop on Antenna Technology (iWAT)*, pp. 392-395, 2011.

[7] M. T. Islam, M. N. Shakib, and N. Misran, "Design analysis of high gain wideband L-probe fed microstrip patch antenna," *Prog. Electromagn. Res*., vol. 95, pp. 397-407, 2009.

[8] H.-W. Liu, C.-H. Ku, and C.-F. Yang, "Novel CPW-fed planar monopole antenna for WiMAX/WLAN applications," *IEEE Antennas Wirel. Propag. Lett*., vol. 9, pp. 240-243, 2010.

[9] X.-L. Ma, W. Shao, and G.-Q. He, "A novel dual narrow band-notched CPW-Fed UWB slot antenna with parasitic strips," *Appl. Comp. Electro. Society (ACES) J*., vol. 27, no. 7, pp. 581-586, 2012.

[10] M. Habib Ullah, M. T. Islam, J. S. Mandeep, N. Misran, and N. Nikabdullah, "A compact wideband antenna on dielectric material substrate for K band," *Electron. Electr. Eng*., vol. 123, no. 7, pp. 75-78, 2012.

[11] A. Pirhadi, H. Bahrami, and A. Mallahzadeh, "Electromagnetic band gap (EBG) superstrate resonator antenna design for monopulse radiation pattern," *Appl. Comp. Electro. Society (ACES) J*., vol. 27, no. 11, pp. 908-917, 2012.

[12] K. L. Chung and S. Chaimool, "Broadside gain and bandwidth enhancement of microstrip patch antenna using a MNZ-metasurface," *Microw. Opt. Technol. Lett*., vol. 54, no. 2, pp. 529-532, 2012.

[13] K. L. Sheeja, P. K. Sahu, S. K. Behera, and N. Dakhli, "Compact tri-band metamaterial antenna for wireless applications," *Appl. Comp. Electro. Society (ACES) J*., vol. 27, no. 11, pp. 947-955, 2012.

[14] H.-W. Lai and K.-M. Luk, "Wideband patch antenna fed by printed meandering strip," *Microw. Opt. Technol. Lett*., vol. 50, no. 1, pp. 188-192, 2008.

[15] Z. Wang, S. Fang, S. Fu, and S. Jia, "Single-fed broadband circularly polarized stacked patch antenna with horizontally meandered strip for universal UHF RFID applications," *IEEE Trans. Microw. Theory Tech*., vol. 59, no. 4, pp. 1066-1073, 2011.

[16] Y. Sun, G. Wen, P. Wang, Y. Huang, and Z. Du, "A compact printed end-fire antenna for radio frequency identification (RFID) handheld reader," *Appl. Comp. Electro. Society (ACES) J*., vol. 28, no. 1, pp. 71-76, 2013.

[17] C.-Y. Pan, T.-S. Horng, W.-S. Chen, and C.-H. Huang, "Dual wideband printed monopole antenna for WLAN/WiMAX applications," *IEEE Antennas Wirel. Propag. Lett*., vol. 6, pp. 149-151, 2007.

[18] P. Wang, G.-J. Wen, Y.-J. Huang, and Y.-H. Sun, "Compact CPW-fed planar monopole antenna with distinct triple bands for WiFi/WiMAX applications," *Electron. Lett*., vol. 48, no. 7, pp. 357-359, 2012.

[19] A. T. Mobashsher, M. T. Islam, and N. Misran, "Wideband compact antenna with partially radiating coplanar ground plane," *Appl. Comp. Electro. Society (ACES) J*., vol. 26, no. 1, pp. 73-81, 2011.

[20] ANSYS® High Frequency Structural Simulator (HFSS). ANSYS, Inc., USA.

[21] J.-J. Tiang, M. T. Islam, N. Misran, and J. S. Mandeep, "Circular microstrip slot antenna for dual-frequency RFID application," *Prog. Electromagn. Res*., vol. 120, pp. 499-512, 2011.

Md. Rezwanul Ahsan was born in Bogra, Bangladesh in January, 1978. He received his B.Sc. degree in Engineering (Electrical and Electronics) from faculty of Electrical and Electronics Engineering, Khulna University of Engineering and Technology (KUET) in 2001 and M.Sc. in Engineering (Electronics) degree from the Faculty of Engineering, International Islamic University Malaysia (IIUM) in 2012. Currently he is a Ph.D. candidate at the Faculty of Engineering and Built Environment, Universiti Kebangsaan Malaysia (UKM) and working as a graduate Research Assistant at the Institute of Space Science (ANGKASA) in a research project funded by the Malaysian government. His research interests include signal processing, VLSI design, artificial intelligences, antenna engineering, RF Circuit design, microwave engineering etc. He is a member of the Institution of Engineers, Bangladesh (IEB), Bangladesh Computer Society (BCS), International Association of Engineers (IAENG) and the International Association of Computer Science and Information Technology (IACSIT). He is the author of about 28 research articles published in peer reviewed journals and international conference proceedings.

Mohammd Tariqul Islam is a Professor with the Department of Electrical, Electronic and Systems Engineering of the Universiti Kebangsaan Malaysia (UKM). He is also the group leader of the Radio Astronomy Informatics group at UKM. Prior to joining UKM, he was a Lecturer in Multimedia University, Malaysia. He is a Senior Member of the IEEE, regular member of Applied Computational Electromagnetic Society (ACES) and serving as the Editor-in-Chief of the International Journal of Electronics & Informatics (IJEI). Islam has been very promising as a Researcher, with the achievement of several International Gold Medal awards, a Best Invention in Telecommunication award and a Special Award from Vietnam for his research and innovation. Over the years, he has carried out research in the areas of communication antenna design, radio astronomy antennas, satellite antennas, and electromagnetic radiation analysis. His publications include over 160 research journal papers, nearly 150 conference papers, and few book chapters on various topics related to antennas, microwaves and electromagnetic radiation analysis with 8 inventory patents filed. Thus far, his publications have been cited 1578 times, and the H-index is 24 (Source: Scopus). For his contributions, he has been awarded "Best Researcher Award" in 2010 and 2011 at UKM. He is now managing many research projects from the Ministry of Science, Technology and Innovation (MOSTI), Ministry of Higher Education Malaysia (MOHE) and some International research grants from Japan.

Mohammad Habib Ullah was born in Chittagong, Bangladesh in 1980. He has awarded his Ph.D. in Electrical, Electronics and System Engineering from Universiti Kebangsaan Malaysia (UKM) in 2014 and currently with the University of Malaya (UM) as Postdoctoral Research Fellow. He also has awarded his B.Sc. Honors in Computer and Communication Engineering from the International Islamic University Chittagong (IIUC), Bangladesh and M.Sc. degree in Communication Engineering from the International Islamic University Malaysia (IIUM) in 2003 and 2011. He has worked with several national and international companies in Bangladesh, Kingdom of Saudi Arabia and Malaysia as Engineer and Academician. He worked as

Research Assistant in several research projects funded by government and non-government organizations. Currently, he is working as Researcher at Universiti Kebangsaan Malaysia in a research project funded by the Malaysian government. He has authored and co-authored 40 International refereed journal articles and 6 conference proceedings.

Design of a Compact Planar Antenna for Ultra-wideband Operation

M. N. Shakib [1,2,4], M. Moghavvemi [1,2,3], and W. N. L. Mahadi [1,4]

[1] Department of Electrical Engineering
[2] Center for Research in Applied Electronics (CRAE), Faculty of Engineering
[4] Electromagnetic Radiation & Devices Research (EMRD), Faculty of Engineering
University of Malaya, Kuala Lumpur, 50603, Malaysia
engmdns@yahoo.com, mahmoud@um.edu.my, wnliza@um.edu.my

[3] Engineering Department
University of Science & Culture, Tehran, Iran

Abstract ─ In this paper, a new compact planar antenna is proposed for UWB (Ultra-wideband) operations. The proposed antenna has a low profile structure, consisting of a radiating patch, notched ground plane, and a novel arc-shaped strip connected between the microstrip feed line and the radiating patch. By using the proposed structure, broadband antenna with good impedance matching is obtained. Measured results show that the antenna can achieve a bandwidth of 96.22%. The proposed antenna is optimized in order to satisfy the required band with a good radiation pattern. The fabricated antenna has a compact size of $16\times 20\times 1.6$ mm^3. These features demonstrate that the proposed antenna is a suitable candidate for UWB applications, due to its simple configuration, compactness, and low fabrication costs.

Index Terms ─ Broadband antenna, planar antenna, ultra-wideband antenna.

I. INTRODUCTION

Ultra-wideband system has been widely used for the last few years due to its amazing frequency spectrum in wireless communication. According to the Federal Communications Commission (FCC), UWB system is defined as any radio system operating in the band of 3.1-10.6 GHz, has a 10 dB bandwidth larger than 25% percent of the center frequency and a maximum equivalent isotropic radiated power spectral density of -41.3 dBm/MHz [1-3]. In applications such as wireless personal area networks, low data rate communication and low power consumption with location and tracking, UWB technology became a favorable candidate in wireless system [4-7]. It is a known fact that UWB antenna is one of the promising key parts in a UWB system [8]. Also, any antenna implemented in a UWB system plays a more unique role than it does in conventional narrowband systems. However, antenna design for UWB applications faces many challenges.

Planar antennas present appealing physical features, such as low profile, small in size, conformability, easy to integrate with other devices and low cost. Owing to these attractive characteristics, planar antennas have gained the attention for use in UWB operations, especially in the Body Area Network (BAN) for medical applications [9-13]. However, the size optimization in the UWB frequency band remains a challenge for antenna designers.

Various structures have been studied to achieve ultra-wideband antennas [14-16] in practical applications, such as the waveguide horn [17], log periodic [18], planar inverted cone [19], and biconical [20]. A new bi-arm rolled monopole antenna with small characteristics for UWB has been investigated in [21]. In [22], planar ultra-wideband (UWB) dipoles used by elliptical elements are introduced. Again, small sized UWB antennas printed with quasi transmission lines and band dispensation are presented in [23-25]. However, these designs require large grounding area or a large radiator. In addition, antennas with circular, square, elliptical, pentagonal shapes are

Submitted On: July 30, 2013
Accepted On: December 10, 2014

proposed in [26-29] for UWB applications. However, the ground planes of these structures are perpendicular to the radiator, which leads difficulty to use for integration with PCB technology.

Recently, a double sided microstrip antenna using modified ground plane is investigated [30-32]. In [31], the antenna comprises of a rectangular patch with an inverted L-shaped slits, cut out in the ground to control the antenna's resonant frequency and bandwidth. Although these antennas can cover the UWB band, it cost more with a larger antenna size. In this paper, a new compact planar antenna with arc-shaped strip, connected to microstirp feed line and radiating patch is introduced for UWB applications. The proposed antenna is smaller and more compact compared to the designs reported in [30-32].

II. ANTENNA DESIGN

Figure 1 shows the layout of the proposed planar antenna. The antenna is fed by a microstrip line and printed on an FR4 substrate with a thickness of 1.6 mm and a permittivity of 4.4. The width of the microstrip feed line is fixed at 2.8 mm. The proposed antenna consists of a notched radiating patch, feed line, a ground plane, and a new arc-shaped strip. The patch is connected to the feed line with a width and length of W_x and L_x, respectively. In this design, a new arc-shaped strip, connected from the microstrip feed line to the radiating patch is proposed. This extended arc-shaped protruded strip acts as an impedance matching element to control the impedance bandwidth of the proposed antenna by creating additional surfaces of current paths in the antenna. Therefore, the excited current shifts its upper resonances, so much so that a wider impedance bandwidth can be produced, especially at upper band. Further more, the ground plane comprises of a rectangular slit that is almost centered under the feed-line, which creates an extra resonance, leading to the improvement in the bandwidth. The introduction of a notch on the left corner of the radiating patch reduces the size of patch and helps to acquire better matching at lower frequency band. There is a gap that is equal to s between the radiating element at the top layer and the ground plane at the bottom layer. Parametric analysis concerning the choice of the optimum value of s indicated that it should not be larger than the thickness of the substrate h, in order to get the wider operation bandwidth. The photograph of the antenna is shown in Fig. 2, which has a surface area of 20×16 mm^2. The proposed antenna is significantly smaller by 51.5%, 87.2%, and 46.7% compared to the recently designed antennas reported in [30], [31] and [32], respectively. A 50 Ω SMA connector is connected to the end of the feeding strip and grounded to the edge of the ground plane. The proposed antenna is analyzed by the electromagnetic simulator HFSS, based on finite element method. The optimized values of the proposed antenna design parameters are as follows: L=20 mm, W=16 mm, L_x=8 mm, W_x=11 mm, L_{x1}=6 mm, L_g=8 mm, W_f=2.8 mm, W_s=3.7 mm, L_s=4 mm, s=0.3 mm, L_{arc}=2.7 mm, h=1.6 mm, L_{x2}=2 mm, and W_{x1}=0.5 mm.

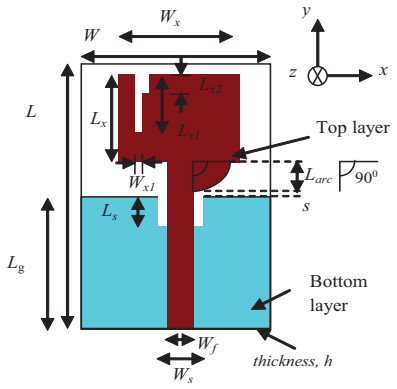

Fig. 1. Geometry of the proposed antenna.

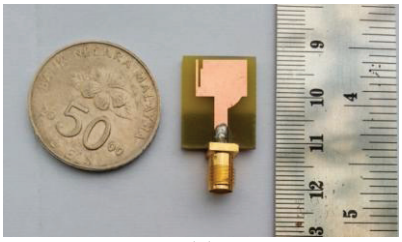

(a)

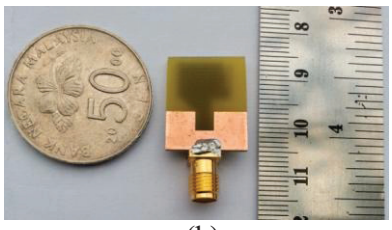

(b)

Fig. 2. Photo of the proposed antenna: (a) top layer, and (b) bottom layer.

III. RESULTS AND DISCUSSIONS

The microstrip antenna has been constructed and optimized to exhibit the effect of the bandwidth enhancement technique. Figure 3 shows the simulated reflection coefficient of the optimized proposed antenna and proposed antenna without an arc-strip, notched in radiator and ground plane slit.

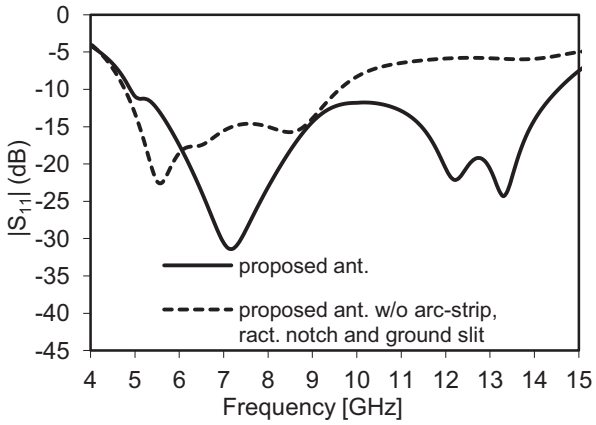

Fig. 3. Simulated reflection coefficient: (a) proposed antenna, and (b) proposed antenna without arc strip and ground slit.

As shown in the figure, firstly, the proposed antenna was configured with a compact microstrip fed rectangular patch, with a partial ground plane on the bottom layer to provide the fundamental and next higher resonances at 5.6 GHz and 8.6 GHz, respectively. Then, a newly proposed arc-shape strip is integrated with the design that produces higher current flow at higher frequencies. This results in the fundamental frequency shifting to 7.2 GHz, and next higher resonant frequency shifts to 9.7 GHz, resulting in a wider frequency band from 4.8 to 11.7 GHz. This technique implies that the arc-strip plays an important role in the broadband characteristics and in determining the sensitivity of impedance matching. A small rectangular slit of 4 mm by 3 mm is inserted into the ground plane as reported in [7], to obtain better matching on the frequency band. The integration of this technique causes the upper resonance of the designed antenna to shift from 9.7 GHz to 12.1 GHz, and a new resonance is introduced at 13.1 GHz, leading to the achievement of higher frequency band to up to 14.5 .GHz.

Figure 4 shows the simulated and measured VSWR of the proposed antenna. The proposed antenna is measured with a Rohde & Schwarz ZVA24 vector network analyzer. The simulated bandwidth covers from 4.8 GHz to 14.5 GHz, while the measured bandwidth covers from 4.8 GHz to 13.7 GHz. The discrepancies between the simulated and measured results may be attributed to the connector, which is not taken into account in the simulation. Figure 5 shows the current distribution at 6 GHz and 9 GHz. At 6 GHz, it can be observed that most of the electric currents are distributed on the bottom edge of the feeding strip, the junction of the rectangular radiator, and the left side of the notched ground plane. Again, at 9 GHz, the majority of the electric current is concentrated around the arc-shaped strip and the bottom edge of the radiator. This suggests that the arc-shaped strip has a significant effect on the antenna performance at higher operating frequencies.

To measure and identify S_{21} and group delay values, a distance of 50 cm between the two equal (Tx/Rx) antennas was chosen. Figure 6 shows the measured values of S_{21} in the face-to-face scenarios. Figure 7 indicates group delay on the antennas. The measured group delay is almost flat, at about 2ns, while the variation is about 0.48ns. This small variation in group delay signifies a good linear transmission function characteristics of the proposed antenna for UWB applications. Figure 8 shows the variation of the simulated and measured peak gain of the antenna. It is observed that the proposed antenna has a gain above 2.56 dBi in the entire operating band.

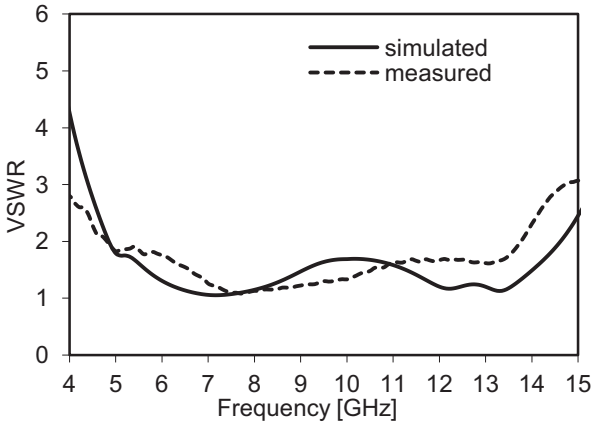

Fig. 4. Simulated and measured VSWR of proposed antenna.

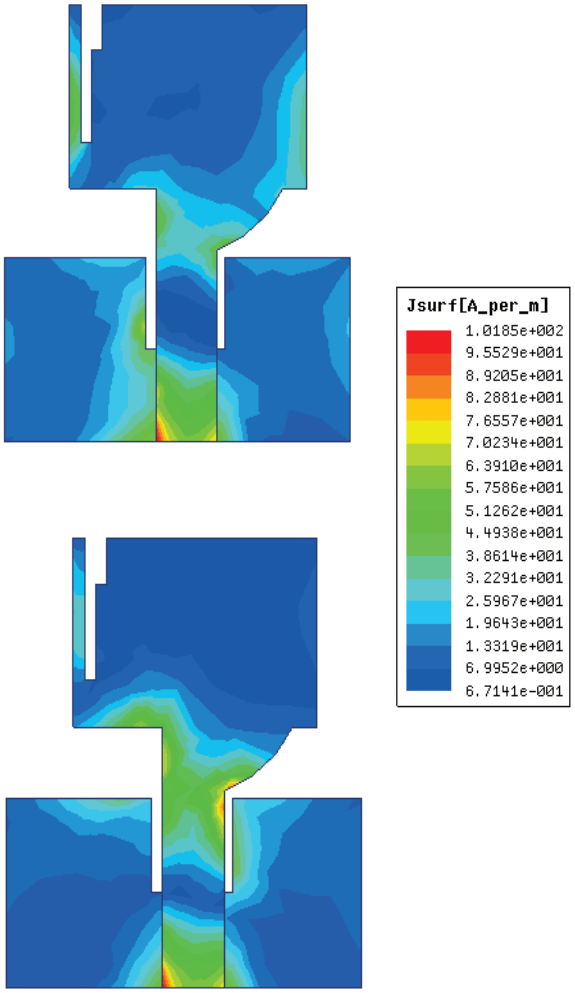

Fig. 5. Current distribution of the proposed antenna at: (a) 6 GHz, and (b) 9 GHz.

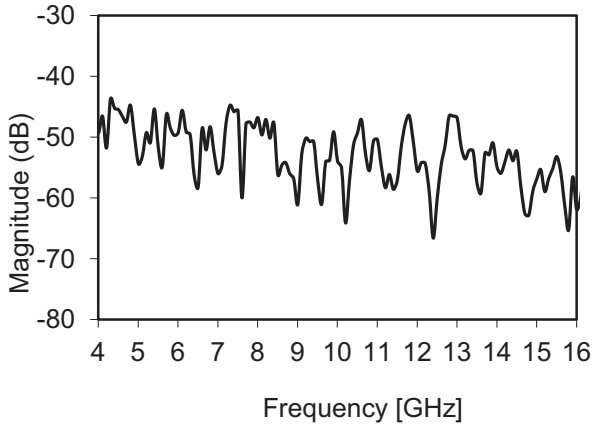

Fig. 6. Measured S_{21} (magnitude) of the proposed antenna.

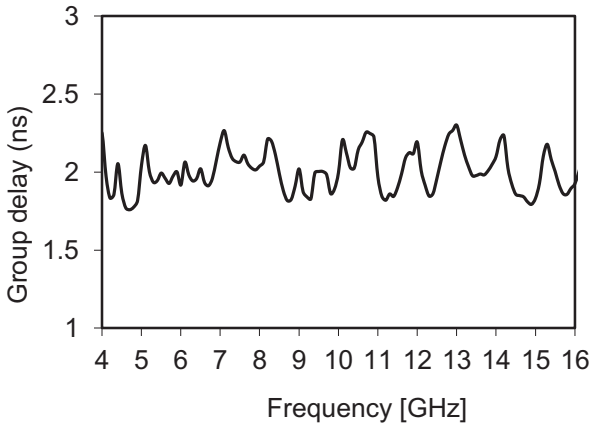

Fig. 7. Measured group delay of the proposed antenna.

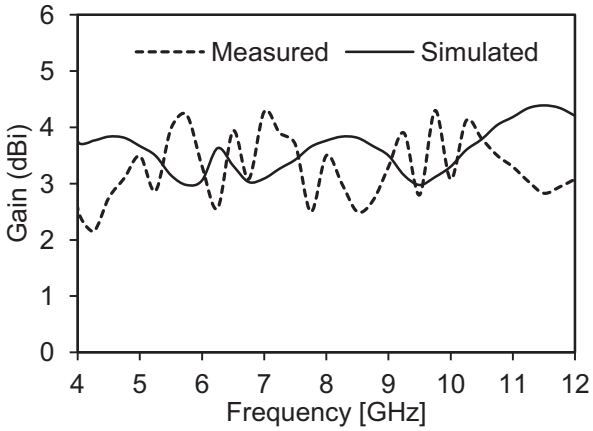

Fig. 8. Simulated and measured gain of the proposed antenna.

Figure 9 illustrates the simulated and measured radiation patterns, including the co-polarization and cross-polarization in the E-plane (*xz*-plane) and H-plane (*yz*-plane) at 6 GHz. It can be seen that the radiation patterns in *xz*- and *yz*-plane are quasi omni-directional at 6 GHz.

A parameter study has been performed to observe the effect on the antenna performances on the impedance matching, due to changes in the *s* parameter. As shown in Fig. 10, increasing or decreasing the *s* parameter experiences better matching at the lower frequency band, but at the expense of reducing the upper edge frequency, resulting in a reduction in the bandwidth. Hence, *s*=0.3 mm was chosen as the control model. In Fig. 11, with decreasing L_{arc}, a mismatch on the

antenna leads to small bandwidth drop on the upper frequency. With increasing L_{arc}, the lower and upper resonances shift upward which causes band reduction on the antenna. Hence, L_{arc}=2.7 mm was chosen as control model.

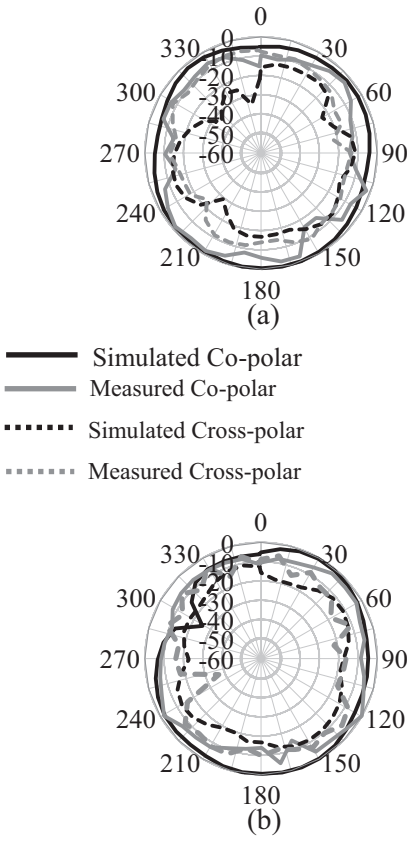

Fig. 9. Simulated and measured radiation pattern of the antenna at 6 GHz: (a) *xz*-plane, and (b) *yz*-plane.

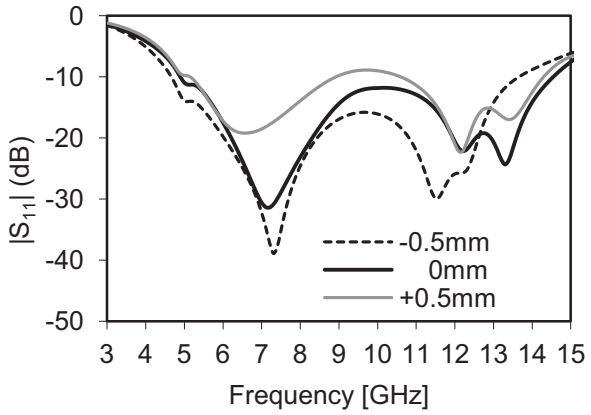

Fig. 10. Effects on reflection coefficient with changing *s* parameter.

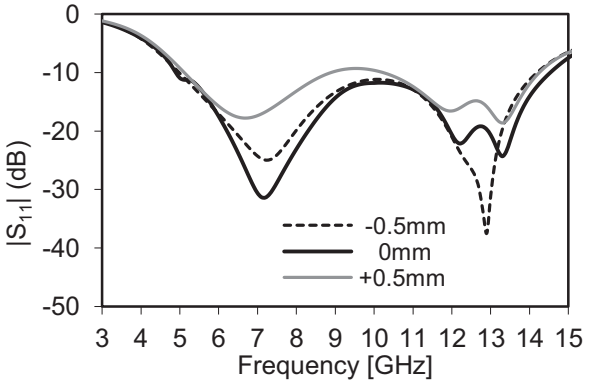

Fig. 11. Effects on reflection coefficient with changing L_{arc} parameter.

In Fig. 12, with increasing or decreasing L_s, a mismatch is occurred on the entire band, leads to a bandwidth reduction on the antenna. At Fig. 13, with decreasing L_g, a mismatch is occurred in the frequency. But, the operating bandwidth remains the same. With increasing L_g, the resonances shift upwards, causing bandwidth fall on the antenna. Hence, L_g=8 mm was chosen as control model.

In Fig. 14, with increasing W_s, the lower frequency shifts upward, leads to a bandwidth drop on the antenna. With decreasing W_s, a mismatch occurs in the frequency, but the operating band remains the same. Hence, W_s=3.7 mm was chosen as control model. In Fig. 15, with changing L, the designed structure performs good matching on the antenna. In Fig. 16, with increasing W, a good matching is observed. But, with decreasing W, the upper resonant shifts upward, causing a bandwidth drop on the upper frequency. Hence, W=16 mm was chosen as control model.

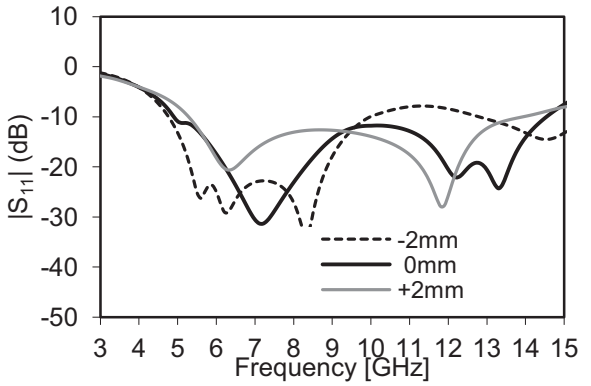

Fig. 12. Effects on reflection coefficient with changing L_s parameter.

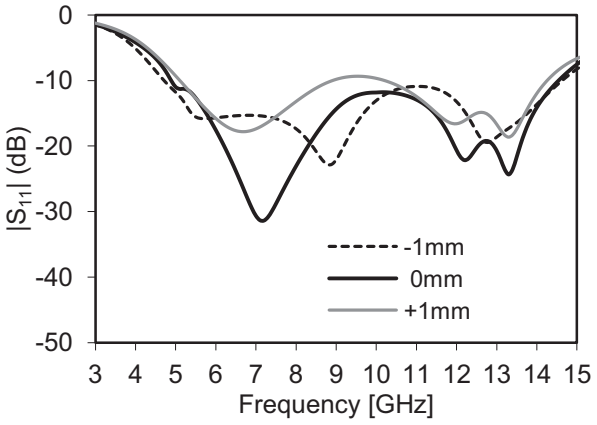

Fig. 13. Effects on reflection coefficient with changing L_g parameter.

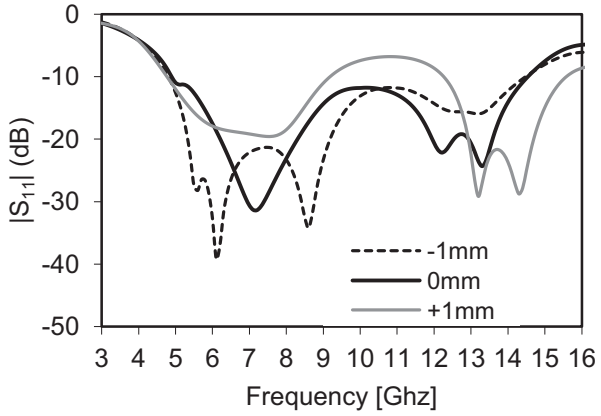

Fig. 14. Effects on reflection coefficient with changing W_s parameter.

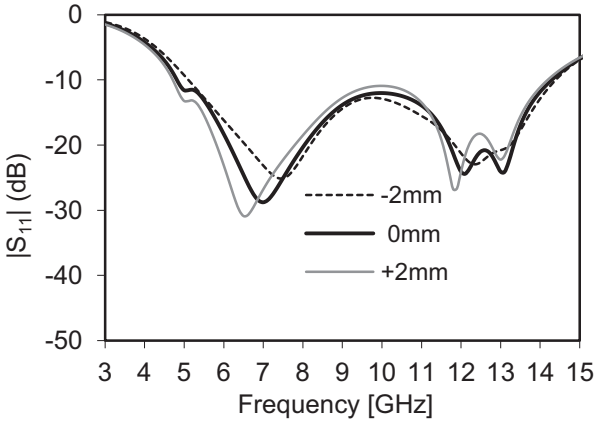

Fig. 15. Effects on reflection coefficient with changing L parameter.

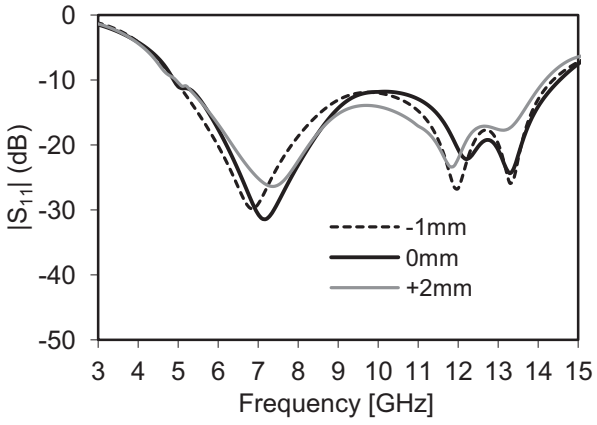

Fig. 16. Effects on reflection coefficient with changing W parameter.

IV. CONCLUSION

In this paper, a new compact planar UWB antenna has been presented and analyzed in detail. By successfully utilizing the arc-shaped strip structure, radiating plate, notched ground plane and adjusting the parameters, the antenna has obtained a wide bandwidth with quasi omni-directional radiation pattern. Despite exhibiting wide impedance bandwidth, the antenna has achieved compact and low profile characteristics. The prototype has been fabricated and measured. The results have shown a good agreement between simulations and measurements. Therefore, these characteristics have made the proposed antenna a suitable candidate for UWB applications.

ACKNOWLEDGMENT

The authors would like to thank the support of the Bright Spark Grant (No: BSP/APP/1133/2012) and PPP Grant (No: PG131-2013A) of the University of Malaya.

REFERENCES

[1] X. H. Wu and A. A. Kishk, "Study of an ultra-wideband omnidirectional rolled monopole antenna with trapezoidal cuts," *IEEE Trans. Antennas Propagat.*, vol. 56, no. 1, pp. 259-263, Jan. 2008.

[2] Y. S. Li, W. Li, and W. Yu, "A multi-band/UWB MIMO/diversity antenna with an enhanced isolation using radial stub loaded resonator," *Applied Computational Electromagnetics Society (ACES) Journal*, vol. 28, no. 1, pp. 8-20, Jan. 2013.

[3] M. N. Shakib, M. T. Islam, and N. Misran,

"Stacked patch antenna with folded patch feed for ultra-wideband application," *IET Microw. Antennas Propag.*, vol. 4, no. 10, pp. 1456-1461, 2010.

[4] H. B. Li and R. Kohno, "Introduction of SG-BAN in IEEE 802.15 with related discussion," *Proc. 2007 IEEE Int. Conf. Ultra-Wideband*, Singapore, pp. 134-139, Sept. 2007.

[5] R. Kohno, K. Hamaguchi, H. B. Li, and K. Takizawa, "R&D and standardization of body area network (BAN) for medical healthcare," *Proc. 2008 IEEE Int. Conf. Ultra-Wideband*, Hannover, pp. 5-8, Sept. 2008.

[6] L. Huang, P. Harpe, C. Zhou, S. Rampu, M. Vidojkovic, G. Dolmans, H. Groot, and K. Imamura, "Performance evaluation of an ultra-low power receiver for body area networks (BAN)," *Proc. 2010 IEEE 21st Int. Symp. Personal, Indoor Mobile Radio Commun. Workshops*, Istanbul, pp. 89-94, Sept. 2010.

[7] J. Jung, W. Choi, and J. Choi, "A small wideband microstrip-fed monopole antenna," *IEEE Microw. Compon. Lett.*, vol. 15, no. 10, pp. 703-705, Oct. 2005.

[8] K. S. Ryu and A. A. Kishk, "Ultra-wide band dielectric resonator antenna with broadside patterns mounted on a vertical ground plane edge," *IEEE Trans. Antennas and Propagat.*, vol. 58, no. 4, pp 1047-1053, Apr. 2010.

[9] M. Mighani, M. Akbari, and N. Felegari, "A novel SWB small rhombic microstrip antenna with parasitic rectangle into slot of the feed line," *Applied Computational Electromagnetics Society (ACES) Journal*, vol. 27, no. 1, pp. 74-79, Jan. 2012.

[10] M. Mighani, M. Akbari, and N. Felegari, "A CPW dual band notched UWB antenna," *Applied Computational Electromagnetics Society (ACES) Journal*, vol. 27, no. 4, pp. 352-359, Apr. 2012.

[11] M. N. Jahromi and N. K. Barchloui, "Analysis of the behavior of Sierpinski carpet monopole antenna," *Applied Computational Electromagnetics Society (ACES) Journal*, vol. 24, no. 1, pp. 32-36, Feb. 2009.

[12] M. Mehranpour, J. Nourinia, C. Ghobadi, and M. Ojaroudi, "Dual band-notched square monopole antenna for ultra-wideband applications," *IEEE Antennas Wireless and Propag. Lett.*, vol. 11, pp. 172-175, 2012.

[13] N. Ojaroudi, M. Ojaroudi, and S. Amiri, "Enhanced bandwidth of small square monopole antenna by using inverted U-shaped slot and conductor-backed plane," *Applied Computational Electromagnetics Society (ACES) Journal*, vol. 27, no. 8, pp. 685-690, Aug. 2012.

[14] H. Schantz, "A brief history of UWB antennas," *Proc. Ultra Wideband Systems and Technologies*, pp. 209-213, Nov. 2003.

[15] Z. Zhang and J. T. Bernhard, "A circular wire antenna for ultra wideband applications," *Proc. IEEE Int. Symp. Microwave, Antenna, Propagation, and EMC Technologies for Wireless Communications*, 2007, Hangzhou, pp. 496-499, Aug. 2007.

[16] N. Behdad and K. Sarabandi, "A compact antenna for ultrawide-band applications," *IEEE Trans. Antenna Propag.*, vol. 53, no. 7, pp. 2185-2192, 2005.

[17] C. H. G. Henrique, M. M. Afonso, R. S. Alfpio, U. C. Resende, M. A. O. Schroeder, and L. A. L. Santos, "Approximated raising of the curvature of a double-ridged waveguide horn in a computational model," *IEEE MTT-S Int. Conf.*, pp. 435-438, Oct. 2007.

[18] G. Engargiola, W. Holzapfel, and A. Lee, "Planar channelized log-periodic antenna," *IEEE Int. Symp.*, pp. 306-309, Aug. 2005.

[19] S. Y. Suh, W. L. Stutzman, and W. A. Davis, "A new ultra-wideband printed monopole antenna: the planar inverted cone antenna (PICA)," *IEEE Trans. Antennas Propagat.*, vol. 54, no. 5, pp. 1361-1365, May 2004.

[20] H. Ghannoum, S. Bories, C. Roblin, and A. Sibille, "Biconical antennas for intrinsic characterization of the UWB channel," *IEEE Int. Workshop Antenna Technology*, pp. 101-104, Mar. 2005.

[21] Z. N. Chen, "Novel bi-arm rolled monopole for UWB applications," *IEEE Trans. Antennas Propagat.*, vol. 53, no. 2, pp. 672-677, Feb. 2005.

[22] H. G. Schantz, "Planar elliptical element ultra-wideband dipole antennas," in *Proc. 2002 IEEE AP-S Int. Symp.*, San Antonio, TX, USA, pp. 44-47, Jun. 2002.

[23] C. W. Ling and S. J. Chung, "A simple printed ultra-wideband antenna with a quasi-transmission line section," *IEEE Trans. Antennas Propagat.*, vol. 57, no. 10, pp. 3333-3336, Oct. 2009.

[24] K. G. Thomas and M. Sreenivasan, "A simple ultra-wideband planar rectangular printed antenna with band dispensation," *IEEE Trans. Antennas Propagat.*, vol. 58, no. 1, pp. 27-34, Jan. 2010.

[25] Z. N. Chen, T. S. P. See, and X. Qing, "Small printed ultra-wideband antenna with reduced ground plane effect," *IEEE Trans. Antennas Propagat.*, vol. 55, no. 2, pp. 383-388, Feb. 2007.

[26] M. J. Ammann and Z. N. Chen, "Wideband monopole antennas for multiband wireless systems," *IEEE Antennas and Propagation Magazine*, vol. 45, no. 2, pp. 146-150, Apr. 2003.

[27] N. P. Agrawall, G. Kumar, and K. P. Ray, "Wide-

band planar monopole antennas," *IEEE Trans Antennas Propagat.*, vol. 46, no. 2, pp. 294-295, Feb. 1998.

[28] E. Antonino-Daviu, M. Cabedo-Fabre's, M. Ferrando-Bataller, and A. Valero-Nogueira, "Wideband double-fed planar monopole antennas," *Electron. Lett.*, vol. 39, no. 23, pp. 1635-1636, Nov. 2003.

[29] Z. N. Chen, M. Y. W. Chia, M.Y.W. and M. J. Ammann, "Optimization and comparison of broadband monopoles," *IEE Proc. Microw. Antennas Propag.*, vol. 150, no. 6, pp. 429-435, Feb. 2003.

[30] R. Azim, M. T. Islam, and N. Misran, "Ground modified double-sided printed compact UWB antenna," *Electron. Lett.*, vol. 47, no. 1, pp. 9-11, Jan. 2011.

[31] M. M. Azer, S. I. Shams, and A. M. M. A. Allam, "Compact double-sided printed omni-directional ultra wideband antenna," *Int. Symp. on Antenna Technology and Applied Electromagnetics and the American Electromagnetics Conf.*, Toronto, ON, pp. 1-4, Jul. 2010.

[32] M. Koohestani and M. Golpour, "Very ultra wideband printed CPW-fed slot antenna," *Electron. Lett.*, vol. 45, no. 21, pp. 1066-1067, Oct. 2009.

Mohammed Nazmus Shakib received his B.Sc. degree in Engineering from Multimedia University, Malaysia, the M.Sc. degree from National University of Malaysia, Malaysia. He was a Research Assistant at National University of Malaysia from 2008 to 2010. He is a Faculty Member in the Department of Electronics and Communication Engineering, Manarat International University at Bangladesh since 2011. Currently, he is pursuing the Ph.D. at The University of Malaya, Malaysia under the Bright Spark Program. He has published many international conferences and journals. He is also a Reviewer of a few journals such as IET, PIER, JEMWA, etc. His research interests mainly include RF, measurement antennas, patch antennas, implantable antennas and UWB technology.

Mahmoud Moghavvemi graduated from The State University of New York (SUNY) at Buffalo with a B.Sc. (CIE) and B.Sc. (Electrical Engineering). He obtained his M.S. degree from Bridgeport University and later on a Ph.D. from The University of Malaya. He is currently attached to the Department of Electrical Engineering, University of Malaya. Besides teaching duties, he is actively involved in various research projects and has published more than 200 articles in peer reviewed technical journals and conferences. He is the Founder and Director of The University of Malaya Center for Research in Applied Electronics (CRAE).

Wan Nor Liza Mahadi graduated in Electrical and Electronics Engineering from The University College Cardiff, Cardiff, United Kingdom. She later obtained her Ph.D. in Electrical and Electronic (Electromagnetic) Engineering in 1996 from The Wolfson Centre for Magnetic Technology, University of Wales College of Cardiff, Cardiff, United Kingdom. She is currently attached to the Department of Electrical Engineering, Faculty of Engineering, University of Malaya. She is the Head of Electromagnetic Radiation and Devices (EMRD) Research group that actively researches into studies on the influence of Electromagnetic Field (EMF) exposure on public and environment, Electromagnetic Field (EMF) exposure and its mitigations, magnetic materials and its applications as well as antenna design, among others. She has published many journal and conference proceeding in the field of antenna propagation and electromagnetics.

Pattern Synthesis for a Conformal Array Antenna Mounted on a Paraboloid Reflector Using Genetic Algorithms

M. A. Nikooharf Fakher

Faculty of Engineering
Shahed University, Tehran, Iran
nikooharfefakher@gmail.com

Abstract ─ In this article a 12×1 conformal array antenna is designed for Identification Friend or Foe (IFF) applications. Using Genetic Algorithm (GA), the phase and amplitude weights of each element mounted on a paraboloid reflector surface is calculated. To have a broadband array with adjusted integrated balun, an optimized printed dipole is chosen as an array element. The effect of mutual coupling between the elements is taken into account through using the Multi-Level Fast Multipole Method (MLFMM). The gain of the antenna is about 15.4 dBi with a 3 dB beam width of 67° and 12° in the two principal planes. Also, the side lobe level of the H-plane pattern is below -25 dBi.

Index Terms ─ Conformal array antenna, Genetic Algorithm (GA), Identification Friend or Foe (IFF).

I. INTRODUCTION

Conformal array antennas are used in many different applications due to their advantages of volume saving, reduction of radar cross-section, reduction of aerodynamic drag, potential increase in available aperture, etc. [1], [2]. There are a wide variety of techniques that have been developed for their analysis and synthesis, which include matrix method using near-field data [3], Least-Mean-Squares methods (LMS) [4], projection methods [5], optimization methods [6]-[9], Volume-Surface Integral Equation (VSIE) formulation and pre-corrected-Fast Fourier Transform method (p-FFT) fast solver [10]. Another approach for the fast analysis of irregular arrays is based on the use of p-series expansion and NUFFT routines [11]. Also, adaptive array methods have been successfully applied to synthesizing pattern of conformal antenna array [12].

Iterative methods based on optimization techniques are very powerful tools for pattern synthesis [2]. Particle Swarm Optimization (PSO) [13] and Differential Evolution Algorithm [14], were used in the array pattern synthesis.

One possible optimization method is Genetic Algorithm (GA) technique, which using to select the excitation magnitudes and phasing that would synthesis best array radiation pattern. Genetic algorithm techniques have been used to optimize array characteristics; for example, in [15] for the reduction of side lobes.

In [16], a hexagonal configuration of an array is placed on a paraboloidal surface and is compared with a planar array of the same projected aperture. In this paper, we synthesize a twelve-element array antenna to conform to a parabolic reflector surface for volume saving. The parabolic reflector is a common surface for radar application. In portable vehicles, the available space for antennas is limited. The proposed structure designed for IFF frequency band and the parabolic surface can be used for an antenna at X-band as a reflector at the same time. However, this method can be applied on the other kinds of surfaces. Therefore, the projection method is used to select element excitations for conformal arrays. This method is not respondent alone, but the achieved values would be useful for characterizing the range of optimization parameters to reduce the time of calculations by genetic algorithm.

For synthesis of the conformal array, we will use genetic algorithm and take the amplitude and phase weights as optimization parameters to give an antenna pattern with low side lobe level, low

Submitted On: April 6, 2013
Accepted On: September 5, 2014

HPBW in elevation plane and maximum gain to satisfy the pattern characteristic required to IFF systems. The proposed array structure is modeled through the software package CST Microwave Studio 2011, using the integral equation solver which is of special interest for electrically large models. In [17], an approximated method is proposed to solve the time consuming issue of a large array modeled with MOM which it neglects the coupling. For calculation efficiency, the equation system is solved by the Multi-Level Fast Multipole Method (MLFMM) for electrically large models. The system matrix is dense because every element couples to all other elements. The single level Fast Multipole Method (FMM) uses boxes to combine the couplings. A recursive scheme is used for the MLFMM to increase the efficiency.

II. ANTENNA ELEMENT DESIGN

We select the printed dipole with adjusted integrated balun proposed in [18] as array element which features a broadband performance. Since the position of feed point (illustrated in Fig. 1) is an adjustable parameter, the adjusted integrated balun match to different impedance values, which is useful for antenna arrays because the mutual coupling between array elements change the input impedance of each antenna element.

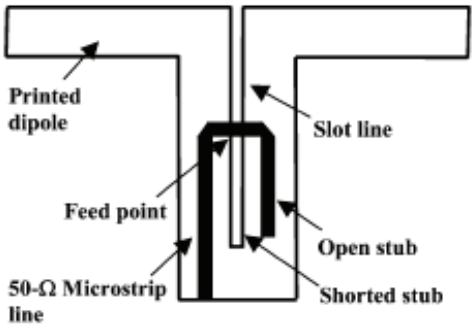

Fig. 1. Printed dipole with a modified integrated balun [18].

This antenna is designed for IFF applications at the L-band and is simulated on a substrate of RO4003 with a dielectric constant of ε_r=3.55 and a loss tangent of 0.0027. The dipole and a slot line are printed on the back side and microstrip line of integrated balun printed on the front side of the substrate. The printed dipole with adjusted integrated balun fed by a coaxial line underneath the ground plane as illustrated in Fig. 2.

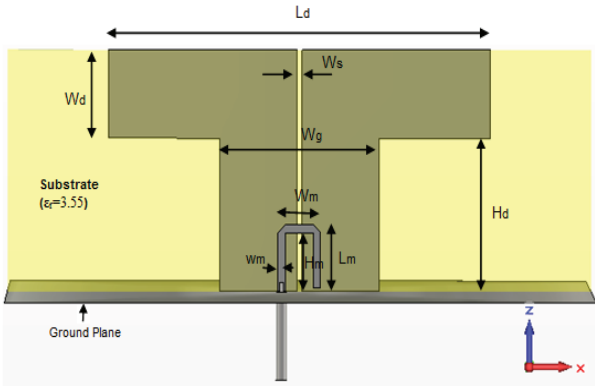

Fig. 2. Geometry of the printed dipole with adjusted integrated balun.

The geometric parameters of the antenna element are listed in Table 1. Figure 3 shows the CST simulated S11 of the printed dipole antenna. The simulated S11-10 dB bandwidth is from 0.86 to 1.22 GHz, which means the impedance bandwidth is ~34%. The simulated E- and H-plane radiation patterns of the printed dipole at the center frequency of 1.06 GHz are shown in Fig. 4.

Table 1: Geometric parameters of the printed dipole with adjusted integrated balun

L_d	144 mm	W_m	16 mm
W_d	30 mm	H_m	20 mm
H_d	52 mm	W_s	1.8 mm
W_g	60 mm	w_m	1.8 mm
L_m	23 mm	t (thickness of substrate)	0.81 mm

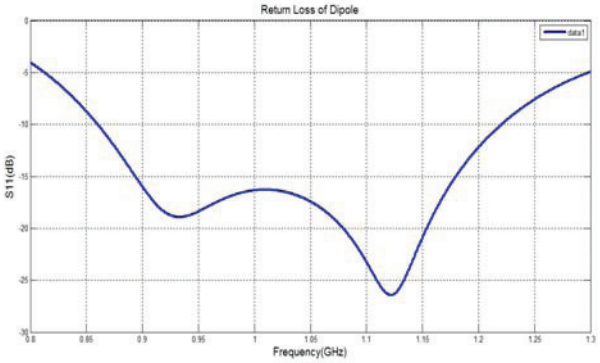

Fig. 3. Input reflection coefficient of the dipole.

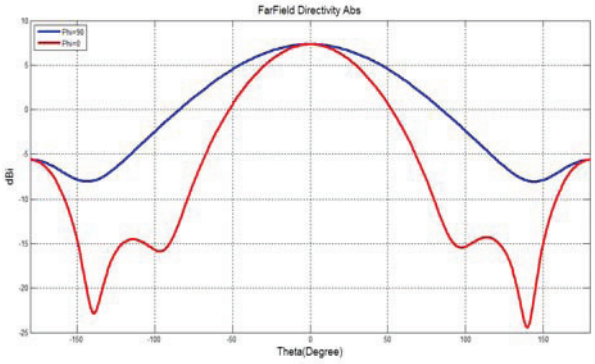

Fig. 4. Radiation pattern of the dipole.

III. CONFORMAL ARRAY SYNTHESIS

A. Theory

We consider a conformal array composes N elements which are mounted on a parabolic reflector surface, as shown in Fig. 5. The equation for a paraboloid of revolution can be written as:

$$4f(z-h) = -(x^2 + y^2), \tag{1}$$

where f is the focal distance. We consider an array of antenna elements uniformly spaced in a straight line along the surface of a parabolic platform of finite length according to above equation.

Since the desired polarization of the reflector is horizontal, the printed dipoles lying in x-z plane orthogonally in order to obviate the mutual coupling effects between the reflector and the array antenna.

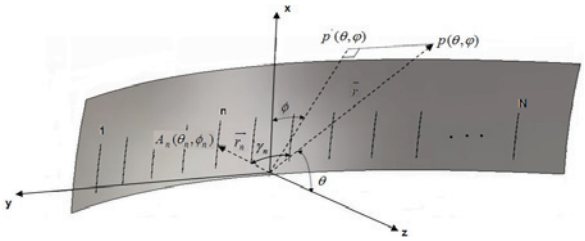

Fig. 5. The conformal antenna array element mounted on a parabolic reflector surface.

The total far-field radiation pattern of the array contains N elements can be expressed as:

$$E(\theta,\phi) = \sum_{n=1}^{N} I_n f_n(\theta,\phi) e^{j(kR_n \cos\gamma_n + \varphi_n)}, \tag{2}$$

where I_n is the element excitation current amplitude, φ_n is the excitation current phase, and $f_n(\theta,\phi)$ characterizes the individual element pattern for A_n. R_n is the distance between A_n and the coordinate origin o. γ_n is the angle between reference direction vector $\vec{r}$ and element position vector $\vec{r_n}$, and k is the free-space wave-number. Moreover, there are the following parameters in the array of Fig. 5 which expressed as:

$$\hat{r} = \hat{x}\sin\theta\cos\phi + \hat{y}\sin\theta\sin\phi + \hat{z}\cos\theta, \tag{3}$$

$$\hat{r_n} = \hat{x}\sin\theta_n\cos\phi_n + \hat{y}\sin\theta_n\sin\phi_n + \hat{z}\cos\theta_n, \tag{4}$$

$$\begin{aligned}\cos\gamma_n &= \hat{r}\hat{r}_n = \sin\theta\sin\theta_n\cos\phi\cos\phi_n \\ &+ \sin\theta\sin\theta_n\sin\phi\sin\phi_n + \cos\theta\cos\theta_n \\ &= \cos^2[(\phi-\phi_n)/2]\cos(\theta-\theta_n) \\ &+ \sin^2[(\phi-\phi_n)/2]\cos(\theta+\theta_n),\end{aligned} \tag{5}$$

$$\vec{r}_n = \hat{x}A_n(x) + \hat{y}A_n(y) + \hat{z}A_n(z), \tag{6}$$

$$\begin{aligned}R_n\cos\gamma_n &= \vec{\gamma}_n\hat{\gamma} = A_n(x)\sin\theta\cos\phi \\ &+ A_n(y)\sin\theta\sin\phi + A_n(z)\cos\theta.\end{aligned} \tag{7}$$

The phasing parameter φ_n may be used to steer the main beam of the array radiation pattern by selecting its value according to:

$$\begin{aligned}\varphi_n &= -k[A_n(x)\sin\theta_0\cos\phi_0 \\ &+ A_n(y)\sin\theta_0\sin\phi_0 + A_n(z)\cos\theta_0],\end{aligned} \tag{8}$$

where (θ_0, φ_0) is the desired steering angle.

With above conditions, Eq. (2) may be written as:

$$\begin{aligned}E(\theta,\phi) &= \sum_{n=1}^{N} I_n f_n(\theta,\phi)\exp\{j[k(A_n(x)\sin\theta\cos\phi \\ &+ A_n(y)\sin\theta\sin\phi + A_n(z)\cos\theta) + \varphi_n]\}.\end{aligned} \tag{9}$$

B. MLFMM

The radiation pattern of the individual array element that mounted on the parabolic surface is influenced by their location on the platform. Thus, each individual array element pattern is different. This subject makes the radiation pattern synthesis procedure complicated. The radiation pattern of the elements with considering the effect of the mutual coupling between the elements achieve by calculating the antenna array using the Multi-Level Fast Multipole Method (MLFMM). Here, we use genetic algorithm as a synthesis technique for determining the optimal set of excitation amplitudes and phases required to make desired

pattern by the actual radiation patterns of each element in presence of other elements and platform determined by MLFM method.

The MLFMM is an alternative formulation of the technology behind the MoM and is applicable to much larger structures than the MoM, making full-wave current-based solutions of electrically large structures a possibility. This fact implies that it can be applied to most large models that were previously treated with the MoM without having to change the mesh.

The effects of parabolic reflector and dipole placement on the radiation patterns of the individual array elements are considered in Fig. 6.

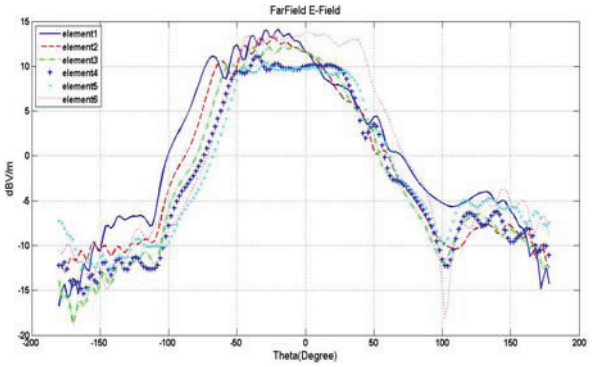

Fig. 6. Element patterns for the array elements mounted on the parabolic reflector illustrated in Fig. 5. Because of symmetry, the radiation patterns of other elements are identical.

The MLFMM is used to calculate the radiation pattern associated with each of the twelve printed dipole antennas for the configuration shown in Fig. 5. Because of the mutual couplings of all elements, the system matrix is considerably dense. Therefore, MLFMM is used because it is suitable for electrically large models. The plots of Fig. 6 clearly show that the radiation pattern produced by an individual printed dipole antenna element is strongly dependent upon the location at which it is placed on the doubly curved parabolic reflector platform. These plots specify that the closer to the end of the reflector the element is placed, the pattern will become more distorted. The far field radiation pattern for this parabolic reflector-mounted array must be calculated using (9).

C. Genetic algorithm

Genetic algorithms are a family of computational models inspired by evolution. These algorithms encode a potential solution to a specific problem on a simple chromosome-like data structure and apply recombination operators to these structures as to preserve critical information. Genetic algorithms are often viewed as function optimizer; although, the ranges of problems to which genetic algorithms have been applied are quite broad. An implementation of genetic algorithm begins with a population of (typically random) chromosomes. One then evaluates these structures and allocated reproductive opportunities in such a way that these chromosomes which represent a better solution to the target problem are given more chances to 'reproduce' than those chromosomes which are poorer solutions. The 'goodness' of a solution is typically defined with respect to the current population. To illustrate the working principles of GA, an unconstrained optimization problem is considered. We consider following minimization problem:

$$Minimizef\,(x), x_i^l \le x_i \le x_i^u, i = 1,2,...,N, \qquad (10)$$

where x_i^l and x_i^u are the lower and upper bound the variable x_i can take.

The advantage of the GA approach is the ease with which it can handle arbitrary kinds of constraints and objectives; all such things can be handled as weighted components of the fitness function, making it easy to adapt the GA scheduler to the particular requirements of a very wide range of possible overall objectives.

In this paper, the GA will be used to choose the optimal excitation amplitude and phase parameters for each element. The main tasks of the optimization are to minimize the side-lobes, HPBW to a certain level, and achieve the maximum gain. Thus, the fitness function can be written as:

$$Fitness(\overline{X}) = w_1 \left| 20\log\left(\frac{1}{\theta_{SLL}} \sum_{\theta \in \theta_{SLL}} E(\overline{X}, \theta, \phi_0) \right) - SLL_d \right|$$
$$+ w_2 \left| 20\log\left(\frac{1}{\theta_G} \sum_{\theta \in \theta_G} E(\overline{X}, \theta, \phi_0) \right) - G_d \right|$$
$$+ w_3 \left| 20\log\left(\frac{1}{\theta_{HPBW}} \sum_{\theta \in \theta_{HPBW}} E(\overline{X}, \theta, \phi_0) \right) - HPBW_d \right|, \qquad (11)$$

where $E(\overline{X}, \theta, \phi_0)$ is the far-field values calculated from (9). SLL_d and G_d represent desired Side

Lobe Level and Gain, respectively, and $HPBW_d$ is target 3 dB beam width at angle of $\phi_0 = 90^\circ$. w_1, w_2, w_3 are the weight coefficients in the fitness function.

IV. RESULTS

A twelve-element conformal antenna array mounted on a parabolic reflector was modeled via CST to yield radiation pattern of each element in presence of others. The simulated conformal array antenna is shown in Fig. 7.

Fig. 7. Twelve-element conformal array of the printed dipole with adjusted integrated balun.

When the inter-element spacing is more than 1λ, the grating lobes are formed, because of the periodicity of the array factor. Also, we should consider mutual coupling effects on array design. Thus, with aspect to this consideration, the element spacing is chosen 18.5 cm. The parabolic reflector under consideration has a length of 240 cm and a focal distance of 90 cm. Analysis and optimization together with CST is a time- and memory-consuming method. For optimization, first the pattern of each element was obtained by MLFMM in CST MWS solver and then was transformed to MATLAB for optimization by GA. The excitation distribution is optimized using genetic algorithm to achieve a minimum Side Lobe Level (SLL) of -25 dB and a 3 dB beam width of 67° and 12° in E-plane and H-plane, respectively, and the gain of 15 dBi at the center frequency.

The population size durig process and the maximum of generations are 140 and 85, respectively. Figure 8 represents the fitness function value in the iterations of genetic algorithm. The optimization parameters SLL=-25 dB, Gain=15 dB and HPBW of 12° obtained in the operational plane (YZ-plane). Figure 9 shows some selected radiation patterns in relative iterations during optmization. The optimization time was about 1 hour on a core-i5 CPU PC. The resulting radiation pattern of the conformal array antenna achieved by optimization using genetic algorithm shows in Fig. 10.

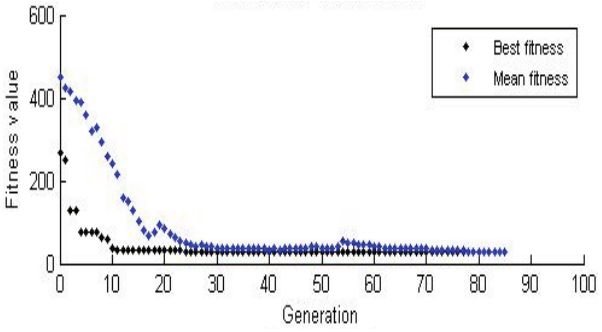

Fig. 8. The objective function value of the best point in the population for GA runs.

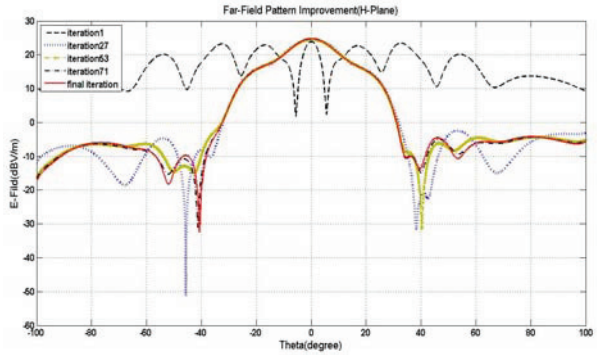

Fig. 9. Far-Field E-Field pattern improvement in some selected iterations during genetic algorithm optimization.

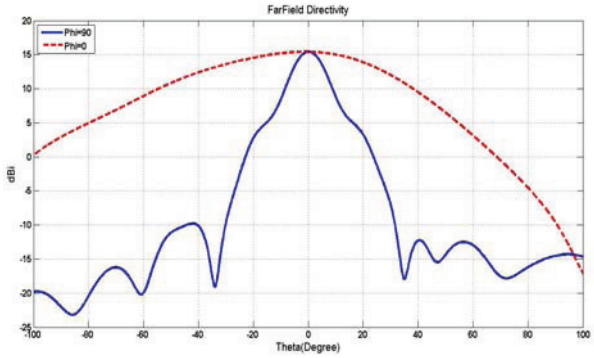

Fig. 10. Optimized E and H-plane radiation patterns of the conformal array antenna at center frequency.

Amplitude and phase weights of the 6 elements of the conformal array which optimized

by genetic algorithm are shown in Table 2. Because of the symmetrically of the structure, weights of other 6 elements are identical. In optimization, we consider the location of the elements 6th and 7th as reference points, and other phase weights are based on their distances of these elements.

Table 2: Optimized amplitude and phase weights of the conformal array by GA

Element	Amplitude	Phase (degree)
1	0.03183	-351.038
2	0.22667	-243.916
3	0.0532	-136.87
4	0.4948	-50.713
5	0.9997	-25.4
6	0.97015	0

The sum radiation patterns in the two principal planes are shown in Fig. 11 and Fig. 12 at both frequencies of 1030 MHz and 1090 MHz. Figure 13 shows the difference pattern of the array which is obtained by 180° phase shifting in the half of elements phase weights.

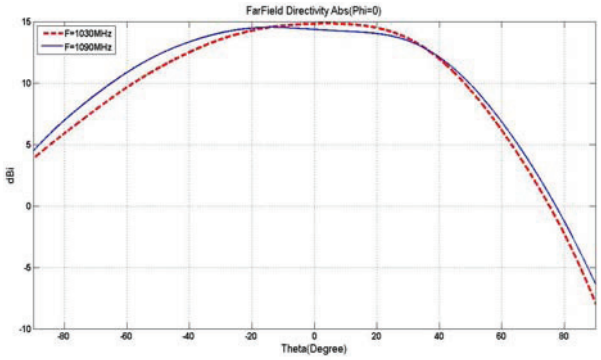

Fig. 11. Sum radiation pattern (E plane).

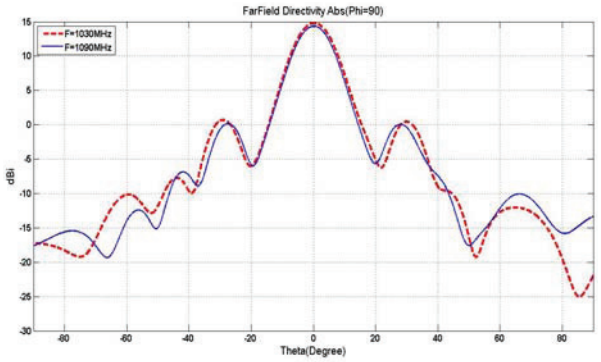

Fig. 12. Sum radiation pattern (H plane).

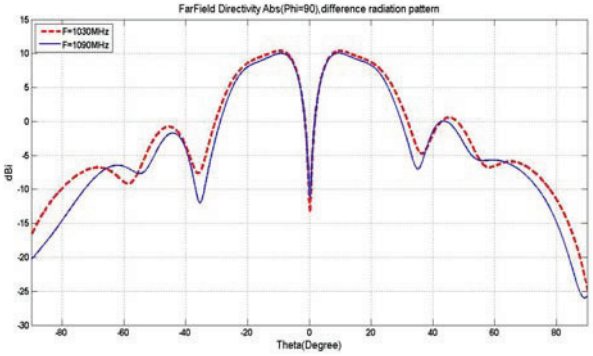

Fig. 13. Delta radiation pattern (H plane).

V. CONCLUSION

A 12x1 conformal antenna array mounted on a parabolic reflector surface is proposed for serving L band (1025-1095 MHz) IFF systems. The basic array element is an optimized printed dipole with adjusted integrated balun. In this array structure, all elements of the array have not identical element pattern, so the synthesis of the conformal array is difficult. In this paper, we used genetic algorithm to synthesize the radiation pattern of the conformal array antenna. This synthesis technique yields the optimal set of excitation current amplitudes and phases required to compensate as much as possible for platform effects and mutual coupling effects on the individual array element patterns. The coupling of antennas and their platform can be taken into account by using of the Multi-Level Fast Multipole Method.

ACKNOWLEDGMENT

The author greatly thanks Dr. Mallahzadeh of Shahed University, Tehran, Iran, for supporting this work and Eng. M. Salavati.

REFERENCES

[1] B. Thors and L. Josefsson, "Radiation and scattering tradeoff design for conformal arrays," *IEEE Trans. Antennas Propagat.*, vol. 51, no. 5, pp. 1069-1076, May 2003.

[2] L. Josefsson and P. Persson, "Conformal array antenna theory and design," *Piscataway, NJ: IEEE Press*, 2006.

[3] O. M. Bucci, A. Capozzoli, and G. D'Elia, "Power pattern synthesis of reconfigurable conformal arrays with near-field constraints," *IEEE Trans. Antennas Propagat.*, vol. 52, no. 1, pp. 132-141, July 2004.

[4] L. I. Vaskelainen, "Iterative least-squares synthesis methods for conformal array antennas with optimized polarization and frequency porperties," *IEEE Trans. Antennas Propagat*., vol. 45, no. 7, pp. 1179-1185, July 1997.

[5] O. M. Bucci, G. D'Elia, and G. Romito, "Power synthesis of conformal arrays by a generalized projection method," *Proc. IEEE Microwave Antennas and Propagation*, vol. 142, no. 6, pp. 467-471, 1995.

[6] J. A. Ferreira and F. Ares, "Pattern synthesis of conformal arrays by the simulated annealing technique," *Electron. Lett*., vol. 33, no. 14, pp. 1187-1189, 1997.

[7] F. J. Ares-Pena, J. A. Rodriguez-Gonzalez, E. Villanueva-Lopez, and S. R. Rengarajan, "Genetic algorithms in the design and optimization of antenna array patterns," *IEEE Trans. Antennas Propagat*., vol. 47, no.1, pp. 506-510, March 1999.

[8] D. W. Boeringer and D. G. Werner, "Particle swarm optimization versus genetic algorithms for phased array synthesis," *IEEE Trans. Antennas Propagat*., vol. 52, no. 3, pp. 771-779, March 2004.

[9] T. Su and H. Ling, "Array beamforming in the presence of mounting tower using genetic algorithms," *IEEE Trans. Antennas Propagat*., vol. 53, no. 6, pp. 2011-2019, June 2005.

[10] K. Xiao, Y. Li, F. Zhao, S. Chai, and J. Mao, "Analysis of microstrip antennas using the volume surface integral equation formulation and the pre-corrected fast fourier transform method," *Applied Computational Electromagnetics Society (ACES) Journal*, vol. 26, no. 11, pp. 922-929, November 2011.

[11] A. Capozzoli, C. Curcio, G. D`Elia, A. Liseno, and P. Vinetti, "Fast CPU/GPU pattern evaluation of irregular arrays," *Applied Computational Electromagnetics Society (ACES) Journal*, vol. 25, no. 4, pp. 355-372, April 2010.

[12] C. Dohmen, J. W. Odendaal, and J. Joubert, "Synthesis of conformal arrays with optimized polarization," *IEEE Trans. Antennas Propagat*., vol. 55, no. 10, pp. 2922-2925, October 2007.

[13] D. W. Boeringer and D. G. Werner, "Particle swarm optimization versus genetic algorithms for phased array synthesis," *IEEE Trans. Antennas Propagat*., vol. 52, no. 3, pp. 771-779, March 2004.

[14] J. L. Guo and J. Y. Li, "Pattern synthesis of conformal array antenna in the presence of platform using differential evolution algorithm," *IEEE Trans. Antennas Propagat*., vol. 57, no. 9, September 2009.

[15] R. L. Haupt, "Thinned arrays using genetic algorithms," *IEEE Trans. Antennas Propagat*., vol. 42, pp. 993-999, July 1994.

[16] A. Zaghloul, M. Parsa, and S. Kumar, "Investigation of a microstrip antenna array conformal to a paraboloidal surface," *23rd Annual Review of Progress in Applied Computational Electromagnetics (ACES)*, pp. 1608-1615, Verona, Italy, March 2007.

[17] F. Chauvet, R. Guinvarc'h, and M. Hélier, "Approximated method neglecting coupling for conformal array," *Applied Computational Electromagnetics Society (ACES) Journal*, vol. 22, no. 1, pp. 105-111, March 2007.

[18] R. L. Li, T. Wu, B. Pan, K. Lim, J. Laskar, and M. M. Tentzeris, "Equivalent-circuit analysis of a broadband printed dipole with adjusted integrated balun and an array for base station applications," *IEEE Trans. Antennas Propagat*., vol. 57, no. 7, July 2009.

Mohammad Ali Nikooharf Fakher was born in Qom, Iran, in 1985. He received the B.Sc. degree in Electronic Engineering from Imam Hussein University, Tehran, Iran, in 2009, and his M.Sc. degree in Communication Engineering at Shahed University, Tehran, Iran, in 2013. His current research interests include conformal antennas, microstrip antennas, and electromagnetic theory.

An Efficient Approach for Reducing the Complexity of Reconfigurable Antennas

Chang-Ying Wu, Yan-Ping Ma, and Jin Xu

School of Electronics and Information
Northwestern Polytechnical University, Xi'an, Shaanxi 710129, China
aaawucy@nwpu.edu.cn, mayp0309@163.com, xujin227@nwpu.edu.cn

Abstract ─ This paper proposes a new method of characterizing reconfigurable antennas for reducing its complexity while still maintaining its reconfigurability. The proposed method is performed by removing the less important switches of a conventional reconfigurable antenna. Therefore, the proposed antenna only has the switches that play important roles in the reconfigurability. The importance of each switch is evaluated by the correlation coefficient of the two envelopes of frequency responses of the antenna. During the evaluating process, the switch to be determined is turned on and off, respectively; whereas, the other switches are in ON and OFF states randomly to provide sufficient number of antenna configurations. To verify the concept of this approach, a frequency configurable antenna is designed and simulated. After reducing the switch number of the antenna from 40 to 8, the final structure still has an evenly-distributed reconfigurable coverage of reflection coefficients which are less than -20 dB within the band of 1.7 GHz ~ 2.7 GHz.

Index Terms ─ Complexity reduction, correlation coefficient, multi-port network method, reconfigurable antenna.

I. INTRODUCTION

Reconfigurable antennas have received much attention in recent years, and they are playing important roles in smart and adaptive systems nowadays. Antenna properties such as frequency, radiation pattern or polarization can be changed dynamically by external control. In most cases, the external control is implemented with switches such as PIN diodes [1], field effect transistors (FETs) [2], micro electro mechanical system (MEMS) switches [3], and so on. To increase the antenna reconfigurability, the number of switches has to be increased. As a result, the number of antenna configurations according to the combination of different states of all the switches is also increased. However, the number of antenna configurations is an exponential function of the number of switches and increases faster as the number of switches increases, especially when a lot of switches are used. A mentionable shortcoming with this kind of antenna is that increasing the number of switches renders finding optimum solutions to different application scenarios much difficultly and slowly, due to the extremely large number of antenna configurations. The cost is also strongly affected by the large number of high-quality switches required, together with complex biasing networks and control circuitry. This is also true of reconfigurable reflectarrays, which have a lot of switches to adjust the delay [4].

With the increasing complexity caused by the increasing number of the switches, the problem of optimizing the overall structure of the antenna was investigated through various methods. If the switches are not evenly deployed in the antenna or some switches that do not affect the properties of the antenna a lot are removed, fewer switches could provide almost the same reconfigurability as the evenly deployed switches do. Several clever methods have been reported to remain the reconfiguration properties while minimizing the number of necessary switches, so as to release the burden of configurations finding and financial cost [5-8].

The approaches to reducing the number of switches of frequency reconfigurable antennas can

Submitted On: June 19, 2014
Accepted On: October 5, 2014

be categorized into two groups. The first group intuitively deploys the switches based on the mechanism of antennas. The Ref. [5] mitigates the inherent complexity of pixel antennas by including multiple sized pixels divided over driven and parasitic regions. The asymmetric pin layout is used in [6] to preclude any duplicated states. The second group uses optimization techniques to search the best number and positions of switches according to a fitness function. Graph models are developed and formulated to reduce the number of switches and parts in the antenna structure [7]. Moreover, optimizations via genetic algorithms and evolutionary algorithms have received widespread attention and have been successfully applied in the reconfigurable antenna design [8].

This paper presents a method of reducing the complexity of the antenna while still fulfilling the requirements of the reconfigurability by removing the switches with less effect on the reconfigurability of the antenna. The effect of each switch is evaluated by the correlation coefficients of the two envelopes of frequency responses of the antenna. During the evaluating process, the switch to be determined is turned on and off, respectively; whereas, the other switches are in ON and OFF states randomly to provide sufficient number of antenna configurations. During the processing of discriminating the switches, the antenna properties of a large number of configurations should be computed, of which it happens to other optimization methods. Since the computation burden of full-wave simulations for each configuration is too heavy, the multi-port network method using the Y matrix is applied to compute the properties of the antenna under different configurations, and the full-wave simulation is only used to get the Y matrix of the antenna at the beginning of the optimization. The simulation results show that the proposed method works efficiently in choosing the best 8 switches from 40 switches.

II. THE PROPOSED METHOD

The optimization scheme of discriminating the switches with more importance can be divided into three steps:

1). assuming the antenna as a multi-port network and filling the Y matrix;
2). computing the importance of the switches on the return loss of the antenna;
3). removing the switches with less importance and verifying the optimized structure.

This paper is focused on the frequency reconfigurable antennas, so only the input impedance of the antenna under different configurations is computed. The multi-port method can also be used to analyze the radiation-pattern reconfigurability of antennas [9]. To do that, the importance of the switches on the radiation pattern has to be considered, yet this would not change the structure of the procedure.

A. Multi-port network method

Since the full-wave simulation is time-consuming and a large number of simulations are needed during the optimization, it is not practical to perform the full-wave simulation for every antenna configuration. Multi-port network method is especially efficient for such case [8,9]. In spite of the fact that to fill the Y matrix is time-consuming, it does not contribute much to the overall computation time because it is only calculated once at the beginning of the optimization.

The multi-port method is achieved by considering both the actual feeding port and the switches as simulation ports, so that the antenna is considered as an (N+1)-port network, N being the number of switches presented in the structure. The port model of the structure is shown in Fig. 1. In this way, the Y matrix of the structure is then used to compute the input impedance of the antenna.

The method of moment (MoM) analysis is especially efficient in dealing with the problem. In this paper, the MoM simulations are performed by FEKO, a computational electromagnetics software product developed by EM Software & Systems - S.A. (Pty) Ltd. The simulations run with a unit voltage source across the kth port and short circuits on the other ports, yielding current $y_{jk}=i_j$, where i_j is the current flowing into the jth port, y_{jk} is the element at the jth row and kth column of the Y matrix. Repeating this procedure successively for each port (k=1, 2, 3, …, N+1), the Y matrix is filled.

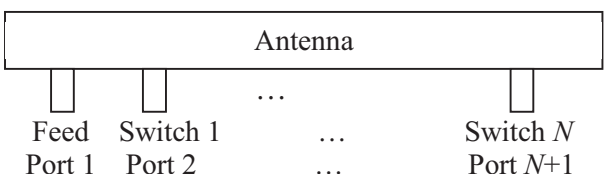

Fig. 1. Port model of the structure.

Y matrices are used to present the relation between the vector of voltages and the vector of currents on the ports, as:

$$\mathbf{i} = \mathbf{Y}\mathbf{v}. \quad (1)$$

Here, the Y matrix can be partitioned into blocks as follows:

$$\begin{bmatrix} i_1 \\ \mathbf{i}_2 \end{bmatrix} = \begin{bmatrix} y_{11} & \mathbf{y}_{12} \\ \mathbf{y}_{21} & \mathbf{Y}_{22} \end{bmatrix} \begin{bmatrix} v_1 \\ \mathbf{v}_2 \end{bmatrix}, \quad (2)$$

where i_1 and v_1 are the scalar current and voltage of port 1 on the feed, $\mathbf{i}_2$ and $\mathbf{v}_2$ are the vectors of currents and voltages on the reconfigurable ports from 2 to N+1, respectively. In Eq. (2), the Y matrix is partitioned into four sub-matrices corresponding to the feed and the reconfigurable ports.

The Y matrix is then used to compute the input impedance of the antenna for any switch state by terminating port k+1 with admittance $y_{L,k}$, k=1, 2, …, N. For an ideal switch, the corresponding switch port is terminated in short circuit for ON state and open circuit for OFF state; for a real switch, the port is terminated in the appropriate ON/OFF impedance. In this paper, for analysis simplicity we only consider the switch with ideal characteristics.

Due to the definition of the polarities of the voltage and current on each port, the current and voltage of each port satisfy:

$$i_{k+1} = -y_{L,k} v_{k+1}. \quad (3)$$

It can be also expressed in the form of matrix:

$$\mathbf{i}_2 = -\mathbf{Y}_L \mathbf{v}_2, \quad (4)$$

where $\mathbf{Y}_L$ is a diagonal matrix with $Y_{L,kk}$=$y_{L,k}$.

Combining (2) and (4), the input admittance looking into the feed for the given terminations at the reconfigurable ports is:

$$y_{in} = \frac{v_1}{i_1} = y_{11} - \mathbf{y}_{12}\left(\mathbf{Y}_{22} + \mathbf{Y}_L\right)^{-1}\mathbf{y}_{21}. \quad (5)$$

The reflection coefficients are then given by:

$$\Gamma = \left(1 - y_{in}Z_0\right)/\left(1 + y_{in}Z_0\right), \quad (6)$$

where Z_0=50 Ω is the normalizing port impedance of the antenna.

For any switch state and any ON/OFF characteristics of the switch, the antenna reflection coefficients can be obtained from the multi-port structure in Fig. 2 and Eq. (6). Comparing with results from full-wave simulations, the above network-analysis technique is more efficient and the simulation procedure is not constrained by the number or type of configurable elements. In this way, it only needs to compute the Y matrix of the multi-port structure once at the start, which is then used to analyze all the possible switch states. The performance is not constrained by practical limitations of existing switch technology, biasing, substrate losses, etc.

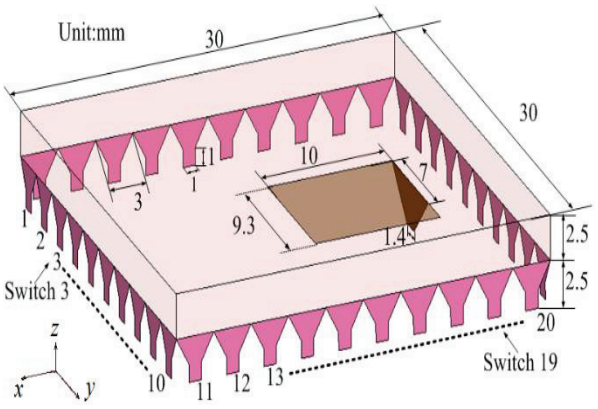

Fig. 2. Initial structure (ground plane removed) [8].

B. Importance of the switches

The importance of one switch means how much this switch impacts on the properties of the antenna or how big the difference of the properties of the antenna when the switch is in ON and OFF states, respectively. However, the difference of the properties of the antenna caused by one switch should not be too big. For example, if the antenna cannot work properly in the whole band of interest when one switch is in ON state, this switch ought to be always tuned off or be removed and should not be treated as a reconfigurable port, although the antenna works properly at some frequency when the switch is in OFF state. This happens when a switch is placed too close to the feed port. Obviously, a switch cannot be placed too close to the feed port, otherwise the antenna will be shorted.

Here, the importance of the switches to a frequency reconfigurable antenna is evaluated as follows:

1). selecting sufficient number of antenna configurations by turning the switches on and off randomly;
2). computing the reflection coefficients of all the selected antenna configurations by the multi-port network method;
3). categorizing all the antenna configurations into two groups for each switch according to the ON and OFF states of this switch;
4). obtaining the two envelopes for the two configuration groups of each switch by the

minimum reflection coefficients obtainable at every frequency in the band from the data in each group;

5). evaluating the importance of each switch by the correlation coefficients of the two envelopes of the switch to be determined.

After the five steps, an evaluation for discrepancy of each pair of envelopes is established by the correlation coefficients to determine the importance of this switch on the antenna, which is expressed as follows:

$$\rho_{X,Y} = \frac{E(XY) - E(X)E(Y)}{\sqrt{E(X^2) - E^2(X)}\sqrt{E(Y^2) - E^2(Y)}}, \quad (7)$$

where X and Y stand for the envelops of the reflection coefficients curves when the switch to be determined remains ON state and OFF state, respectively, E is the expectation, and $\rho_{X,Y}$ is the correlation coefficients of them. In mathematics, correlation coefficients are a measure of the interdependence of two random variables that ranges in value from −1 to +1, indicating perfect negative correlation at −1, absence of correlation at zero, and perfect positive correlation at +1. Herein, the correlation coefficients are factors which determine the relative importance of the switch on the antenna. Obviously, the switch with lower correlation coefficient has a greater effect since the two states make greater different performance of the antenna.

C. Final structure

Suppose that the proposed structure has N switches, then, the number of antenna configurations is 2^N. When N is big, the 2^N is much bigger. So the sufficient number of configurations that is used to determine the importance of the switch is M, which is less than 2^N. After one switch with least importance is eliminated, the state of this switch is always fixed. Therefore the number of configurations to be computed is no longer M but $M/2$, which is not sufficient enough. To eliminate another switch, the number of configurations has to be replenished up to M again with another $M/2$ new configurations, which are randomly selected and different from the previous configurations. When there are only a few more switches left and the overall number of configurations is less than M, all the configurations are used.

III. OPTIMIZATION RESULTS

To verify the concept of this method, a frequency reconfigurable antenna in [8] is optimized.

Figure 2 shows the geometry of the reconfigurable antenna with 40 switches to be reduced. It consists of a 30 mm × 30 mm square patch in air 5 mm above the ground plane, and a planar L-feed in air 2.5 mm above the ground plane. The horizontal part of the L-feed is a 9.3 mm × 7 mm rectangle, and the L-feed is connected to a 50 Ω SMA connector below the ground plane via a vertical tapering strip. The square patch is circumscribed by a 2.5-mm-wide strip with its top touching the edge of the patch. The patch and the strip are equipped with 40 tapered shorting straps connecting to the ground plane via switches. There are 10 evenly-spaced straps on each side. The reconfigurability is achieved by switches that connect each tapered strap to the ground plane. The ground plane is assumed to be infinite in extend.

The structure was firstly adopted in [8]. In Ref. [8], the optimization procedure was carried with a globe optimizer (genetic algorithm), a local optimizer (1-bit neighborhood) for the geometry, and exhaustive search for the switching patterns. The fitness function is constructed as a combination of the structural complexity of the antenna and the return loss over the entire frequency band. The same structure is used here because it has been verified working well as a frequency reconfigurable antenna in the entire band by [8] and it provides an optimized result obtained by other technique to compare with.

The 40 switches shown in Fig. 2 are uniformly distributed around the four edges of the patch. However, uniform distribution is a suboptimal geometry in terms of complexity, because the contribution of each switch to the antenna reconfigurability is not uniform. Some switches which are with more importance might have a much stronger influence over the antenna performance than those at other locations. Through only these switches with more importance, the antenna might have nearly the same reconfigurability compared with the antenna having all the 40 switches.

The performance of the prototype in Fig. 2 was simulated through FEKO in the band of 1.7 to 2.7

GHz at each of 101 frequencies. Although the multi-port network method is used, the antenna is not treated as a multi-port antenna in FEKO because the time consumed for simulating multi-port antennas is proportional to the square of the number of ports. Here, the antenna is assumed only having one port.

Each port among the actual feed and the reconfigurable ports is assigned as the feed, and all the other ports are shorted. If a unit voltage source is applied across the feed, then the currents through all the ports form one column of the Y matrix. After all the ports have been selected as a feed individually, the Y matrix is filled. Every element in the Y matrix is not a single number. Each one consists of the admittances at all the frequencies.

Using Eq. (5) and assuming that the value of $y_{L,k}$ is 0 when the kth switch is in OFF state and is infinite when in ON state for ideal switches, the frequency responses can be calculated in all cases. If non-ideal switches are terminated, the $y_{L,k}$ should be substituted with the actual admittances.

Obviously, the switches operate in a binary state (ON or OFF). All the switches provide 2^{40} configurations to the antenna. It is not possible to determine the reflection coefficients for all 2^{40} configurations. Thus, a random sample of 100,000 without repeat are applied, which can almost represent the tendency of the overall configurations according to the Monte Carlo Methods.

On the basis of simulation results, 100,000 configurations can provide a very good matching within the band of 1.7 to 2.7 GHz as shown in Fig. 3. The thin curves represent the reflection coefficients for the 100,000 configurations, and the thick curve is their envelope. The envelope is the minimum reflection coefficients obtained at every frequency in the band from the 100,000 curves of reflection coefficients, which is the key concern during the process of discriminating switches.

It can be seen from Fig. 3 that the envelope distributes in the band of 1.7 to 2.7 GHz without any gap. Now, we expect to simplify the original structure by reducing the number of switches while still retaining the frequency reconfigurability in the same band. The optimization is firstly carried out by means of comparing correlation coefficients of reflection coefficient envelops.

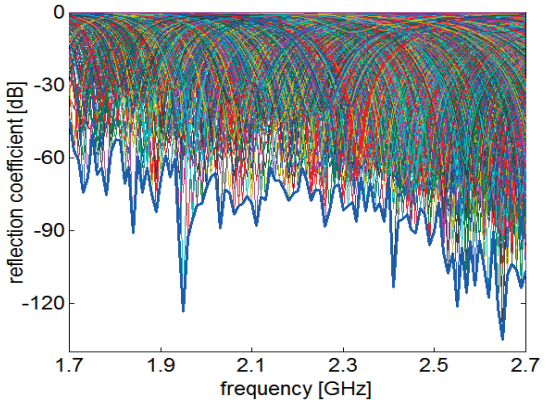

Fig. 3. Curves of a random sample of 100,000 configurations and their envelope.

As an example, to illustrate the importance of switches, Fig. 4 shows two pairs of envelopes of 100,000 configurations according to switch 3 and 16 (their positions are shown in Fig. 2) when they are in ON and OFF states. The discrepancy of each pair of envelopes represents the impact of the switch on the antenna.

As alluded before, a merit figure is obtained to evaluate the importance of switch. The correlation coefficient of the two envelopes of switch 3 (Fig. 4 (a)) is 0.3432, and that of switch 16 (Fig. 4 (b)) is 0.0540. It is obvious that switch 16 has a stronger impact on the antenna.

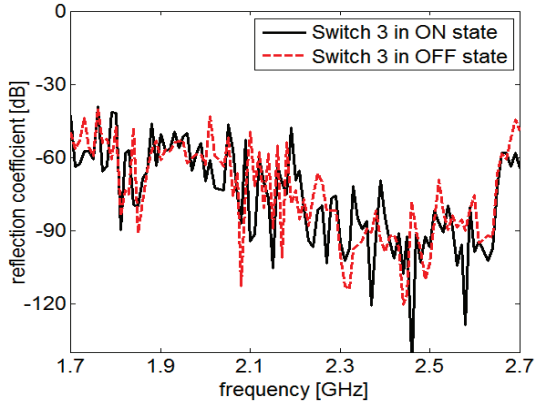

(a)

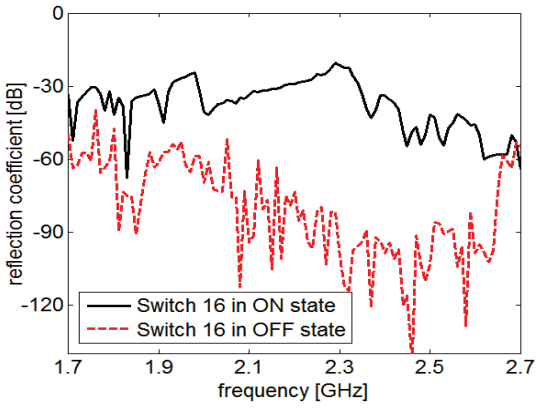

(b)

Fig. 4. Envelopes of curves of 100,000 configurations according to: (a) switch 3, and (b) switch 16.

The correction coefficients of each pair of two envelopes of all switches are given in Table 1 in descending order. As Ref. [8], 8 switches are left in the final structure. The 8 switches with the least correlation coefficients are 19, 14, 16, 35, 37, 8, 20, and 5. The antenna structure with these 8 switches is shown in Fig. 5. The simulated performance of the optimum structure is shown in Fig. 6; the thin curves represent the reflection coefficient of each switch configuration, and the thick envelope is the best performance obtained by 2^8 switch configurations. It can be observed that a very low reflection coefficient in the band can be achieved (the envelope is < -20 dB) for every frequency. Compared with the work reported in Ref. [8], the thin curves of the reflection coefficients for each switch configuration from the final structure are more evenly distributed over the band.

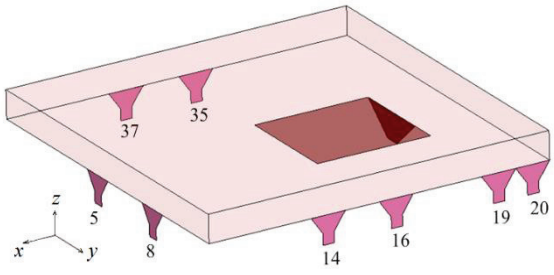

Fig. 5. Final structure (ground plane removed).

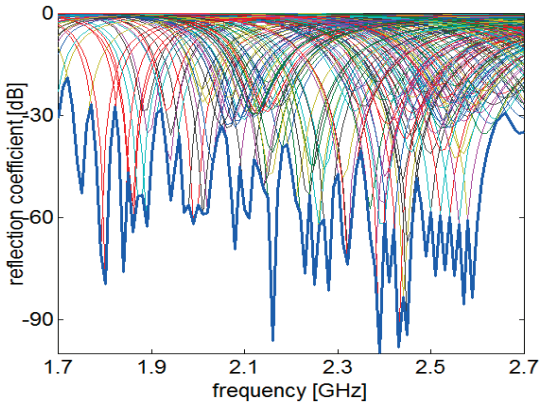

Fig. 6. The performance of the final structure from simulation.

Table 1: Correlation coefficients of 40 switches in descending order

Number of Switches	40	22	3	32	2
Correlation Coefficient	0.401	0.355	0.343	0.326	0.319
Number of Switches	31	34	30	29	39
Correlation Coefficient	0.281	0.265	0.241	0.236	0.235
Number of Switches	11	21	1	23	33
Correlation Coefficient	0.235	0.234	0.231	0.219	0.217
Number of Switches	13	24	4	27	38
Correlation Coefficient	0.214	0.209	0.208	0.198	0.185
Number of Switches	36	28	9	12	7
Correlation Coefficient	0.184	0.181	0.171	0.165	0.157
Number of Switches	26	10	6	18	25
Correlation Coefficient	0.156	0.154	0.134	0.131	0.131
Number of Switches	17	15	19	14	16
Correlation Coefficient	0.122	0.120	0.115	0.114	0.112
Number of Switches	35	37	8	20	5
Correlation Coefficient	0.101	0.096	0.094	0.084	0.014

Antenna radiation pattern simulation was also performed for three different configurations at the frequencies of 1.84 GHz, 2.22 GHz and 2.57 GHz, respectively. Figure 7 shows the simulated radiation patterns in *x-z* plane and *y-z* plane at the three certain frequencies. The simulated reflection coefficients of the proposed antenna of the 3 different configurations are plotted in Fig. 8. The states of the 8 switches of 3 antenna configurations are listed in Table 2 as a binary word where 0 and 1 represent OFF and ON states, respectively.

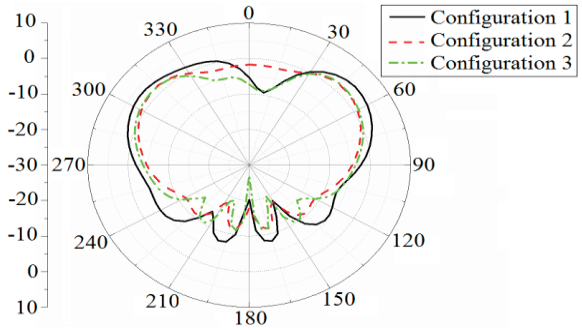

Fig. 7. Simulated gain of the proposed antenna of the 3 different configurations in: (a) *x-z* plane, and (b) *y-z* plane.

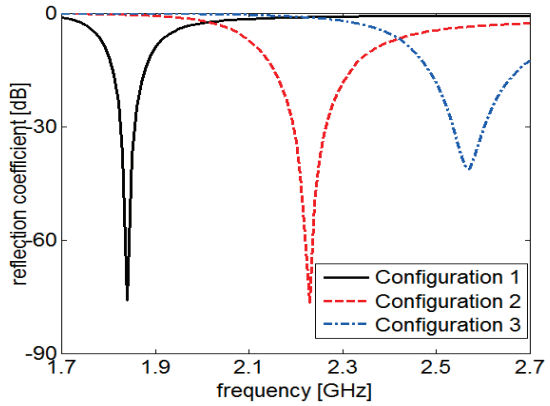

Fig. 8. Reflection coefficients of the proposed antenna of the 3 different configurations.

Table 2: States of the 8 switches of the antenna

Antenna Configuration	Resonant Frequency	States of 8 Switches (0 represents OFF, and 1 represents ON states)							
		19	14	16	35	37	8	20	5
1	1.84 GHz	1	0	0	0	0	1	0	0
2	2.22 GHz	1	1	0	0	0	0	1	0
3	2.57 GHz	1	0	0	0	1	0	1	1

IV. CONCLUSION

In this paper, a new method was presented to simplify reconfigurable antennas by reducing their number of switches which is based on the network analysis and the correlation coefficients. The network analysis is applied for filling the Y matrix and computing the reflection coefficients of the antenna. The correlation coefficients are used to determine the influence of the switches on the antenna. In this way, the reconfigurability of the frequency reconfigurable antenna almost remains the same after removing the switches with less importance. This optimization approach is an efficient tool to reduce the number of switches in reconfigurable antenna structures even though a big number of switches need to be reduced. In addition, this method is also suitable for optimizing radiation-pattern reconfigurable antennas.

REFERENCES

[1] S. Nikolaou, R. Bairavosubramanian, C. Lugo, I. Carrasquillo, D. Thompson, G. E. Ponchak, J. Papapolymerou, and M. M. Tentzeris, "Pattern and frequency reconfigurable annular slot antenna using PIN diodes," *IEEE Trans. Antennas Propagat.*, vol. 54, no. 2, pp. 439-578, 2006.

[2] L. M. Feldner, C. T. Rodenbeck, C. G. Christodoulou, and N. Kinzie, "Electrically small frequency-agile PIFA-as-a-package for portable wireless devices," *IEEE Trans. Antennas Propagat.*, vol. 55, no. 11, pp. 3310-3319, 2007.

[3] C. W. Jung, M. J. Lee, and F. De Flaviis, "Reconfigurable dual-band antenna with high frequency ratio (1.61) using MEMS switches," *Electron. Lett.*, vol. 44, no. 2, pp. 76-77, 2008.

[4] S. V. Hum and J. Perruisseau-Carrier, "Reconfigurable reflectarrays and array lenses for dynamic antenna beam control: a review," *IEEE Trans. Antennas Propagat.*, vol. 62, no.1, pp. 183-198, 2014.

[5] D. Rodrigo and L. Jofre, "Frequency and radiation pattern reconfigurability of a multi-size pixel antenna," *IEEE Trans. Antennas Propagat.*, vol. 60, no. 5, pp. 2219-2225, 2012.

[6] L. Greetis, R. Ouedraogo, B. Greetis, and E. J. Rothwell, "A self-structuring patch antenna: simulation and prototype," *IEEE Trans. Antennas Propagat.*, vol. 52, no. 1, pp. 114-123, 2010.

[7] J. Constantine, S. Al-Saffar, C. G. Christodoulou, and C. T. Abdallah, "Reducing redundancies in reconfigurable antenna structures using graph models," *IEEE Trans. Antennas Propagat.*, vol. 59, no. 3, pp. 793-801, 2011.

[8] J. L. Araque Quijano and G. Vecchi, "Optimization of an innovative type of compact frequency-reconfigurable antenna," *IEEE Trans. Antennas Propagat*., vol. 57, no. 1, pp. 9-18, 2009.

[9] R. Mehmood and J. W. Wallace, "Diminishing returns with increasing complexity in reconfigurable aperture antennas," *IEEE Antennas Wireless Propagat. Lett.*, vol. 9, pp. 299-302, 2010.

Chang-Ying Wu was born in Xi'an, China, in 1977. He received the B.Eng. degree in Electrical and Electronic Engineering in 1999, the M.Eng. degree in Electromagnetic Field and Microwave Technique in 2001, the Ph.D. degree in Circuit and System in 2004 with honors, all from Northwestern Polytechnical University, Xi'an, China. He's been with the School of Electronics and Information, Northwestern Polytechnical University since 2004, where currently he is an Associate Professor. He was a Visiting Scholar with Radio Science Laboratory, Department of Electrical and Computer Engineering, the University of British Columbia in 2011. His research interests include antennas and dielectric measurement.

Yan-Ping Ma was born in Lanzhou, China, in 1991. He received the B.Eng. degree in Electronic and Information Engineering from Northwestern Polytechnical University, Xi'an, China, in 2014, where he is currently working towards the M.Eng. degree in Electromagnetic Field and Microwave Technique. His research interests include antenna design and antenna measurement.

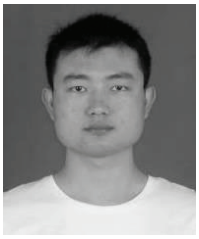

Jin Xu was born in AnHui, China, in 1987. He received the B.Eng. degree in Information Countermeasure Technology and the Ph.D. degree in Information and Communication Engineering from Nanjing University of Science and Technology (NUST), Nanjing, China, in 2009 and 2013, respectively. He is currently an Associate Professor with the School of Electronics and Information, Northwestern Polytechnical University, Xi'an, China. His research interests include UWB technology, MCM technology, microwave passive/active components, microwave and millimeter-wave MMICs developed on SiGe, phased array radar and wireless communication system.

From February 2011 to September 2011, he was an attached Ph.D. student at the Institute of Microelectronics, Singapore. From October 2011 to September 2012, he joined MicroArray Technologies Corporation Limited, Chengdu, P.R. China, where he was an IC R&D Engineer. Since 2011, he has served as a Reviewer for some journals including IEEE Microwave Wireless Component Letters, International Journal of Electronics, PIER and JEMWA.

Liquid Crystal-Based Dielectric-Loaded Plasmonic Ring Resonator Filter

Seyed Mohammad Alavi [1] and Hamed Armand [2]

[1] Electronic & Communication Department
Imam Hossein Comprehensive University, Tehran, Iran
malavi@ihu.ac.ir

[2] Department of Electrical and Computer Engineering
K. N. Toosi University of Technology, Shariati Street, Tehran, Iran
hamed.armand@gmail.com

Abstract ─ A new tunable plasmonic filter based on liquid crystal dielectric loaded plasmonic waveguide is proposed and studied. The transmission spectrum can be controlled easily by applying a constant external electric field to the plasmonic filter. The physical principle of this phenomenon is evaluated from the phase of surface plasmon polaritons (SPPs) in the waveguide and the electro-optical effect of liquid crystals. Our numerical simulations with finite-difference time-domain (FDTD) technique reveal that a large tuning range of the transmission spectrum can be achieved. Both the electrical switching and optical properties of the proposed structure are investigated in the context of designing an optical switch. The special feature of the proposed structure gives it an opportunity to be used as an efficient element in ultrahigh nano-scale integrated photonic circuits for miniaturization and tuning purposes.

Index Terms ─ FDTD, liquid crystal, surface plasmons polaritons.

I. INTRODUCTION

In recent years, optical waveguides based on surface plasmon polaritons (SPPs) are of particular interest in meta-material research. The unique property of these waveguides is the potential to overcome the diffraction limit in conventional dielectric waveguides as a solution to realizing nano-scale photonic devices for high integration [1-2]. Among plasmonic guiding structures, metal-insulator-metal (MIM) waveguides have attracted much interest due to their strong optical subwavelength confinement of electromagnetic energy in the form of a coupled SPP propagating in a deep subwavelength dielectric core [3-5]. Recent research in the plasmonics area has led to important progresses in development of various MIM plasmonic devices, such as bends and splitters [6-8], Mach–Zehnder interferometers [9], Y-shaped combiners [10] and wavelength sorters [11]. SPP filters are one kind of the key components in the SPP integration platform. Different SPP filter structures based on the MIM waveguides have been proposed recently, including ring resonator filters [12-16], tooth-shaped filters [17, 18] and Bragg grating filters [19-22].

However, plasmonics studies have almost exclusively focused on pure metallic nanostructures and passive components whose properties are fixed by their structural parameters. At the same time, real-life applications require active control of plasmonic signals in nano-optic devices to achieve signal switching and modulation, amplification to compensate for losses, and direct generation and detection of plasmons [23-29]. Moreover, it is advantageous to be able to tune plasmonic passive devices. All these can be realized if plasmonic nanostructures are hybridized with functional materials. However, most research studies in this field are still at an early stage.

Submitted On: September 11, 2014
Accepted On: February 21, 2015

There are several methods to implement tunable plasmonic structures, where the optical properties of the device can be actively controlled by temperature tuning [30], optical excitation [31], mechanical control [32], or more technologically appealing, by the application of a voltage [33]. The low frequency, THz transmission of a semiconductor structure consisting of a slit in a silicon wafer surrounded by periodic corrugations has been modulated by optically modifying the propagation lengths of surface waves at the wafer interfaces [34]. Specifically, the active SPP circuit operating in the near infrared or visible optical frequency spectrum have been demonstrated and are currently being explored by using innovative methods such as electrooptical (EO), thermooptical, and all-optical technologies [35-37]. Nonlinear optical devices based on subwavelength metallic structures have been proposed to actively control plasmonic signals [38-40]. The development of electro-optical materials and the integration of such materials with plasmonic nanostructures give rise to the opportunity for electrically controllable active plasmonic devices [41]. Electro-optic control of plasmonic signals can be provided by the use of anisotropic materials. Because of their large and electrooptically controllable birefringence, anisotropic media such as nematic liquid crystals (N-LCs) support the active manipulation of plasmonic signals via external electric fields. Tunability through an applied voltage is a key issue of modern optoelectronics. Liquid crystal is used to electrooptically modulate the phase of incident light; upon applying a voltage, the LC molecules tilt and cause the incident light to see a change in refractive index. The change in refractive index translates directly to a change in the optical path length (OPL), and consequently a phase shift for the incident light [42]. With its low driving voltage and low-cost fabrication technology, liquid crystal technology seems to be an outstanding candidate for tunable plasmonic devices and has been proposed as switches, filters, beam deflectors, electro-optic modulators, etc., in various applications [42-44].

In this paper, we propose and study a hybrid plasmonic filter consisting of MIM waveguides and a ring resonator that are combined with liquid crystal to enable active functionalities and tunability in plasmonic circuitry. The transmission response can be controlled easily by using liquid crystal in the insulator region of the structure and exposing the structure to a constant externally applied electric field. Hence, there is no need to change the geometrical parameters of the filter. The motivation for considering liquid crystal is the possibility of utilizing the liquid crystal parameters in controlling the plasmonic signals. This paper is organized as follows. Following this introduction, a brief review of the theoretical and numerical analysis used in this paper is given in Section 2. The dispersion relations corresponding to both symmetric and antisymmetric modes in metal-liquid crystal-metal (M-LC-M) structure are presented. Then, results of the detailed simulation of a tunable plasmonic ring resonator filter are presented and explained in Section 3. Considering results of Section 3, a new plasmonic optical switch based on a liquid crystal dielectric-loaded ring resonator will be proposed in Section 4. The influence of changes in orientation of the liquid crystal molecules on the transmission response of the plasmonic optical switch is investigated in detail. The dependence of the effective refractive index on the misalignments of the liquid crystal molecules explains the physical principle underlying the phenomenon of active transmission response control. Finally, Section 5 concludes the paper.

II. THEORETICAL AND NUMERICAL ANALYSIS

The structure under study, shown in Fig. 1, comprises a waveguiding slab of thickness $2a$ with its interfaces orthogonal to the x-axis, which is filled with nematic liquid crystal (N-LC) and sandwiched between two silver layers. This structure acts as a waveguide for the SPP propagating along the z-direction in the form of a waveguide mode for TM-polarized waves. To consider only excitation of the fundamental SPP mode, the width $2a$ of the LC layer is chosen to be much smaller than the wavelength of the incident light. The dispersion behavior of silver is estimated using Drude model:

$$\varepsilon(\omega) = \varepsilon_{\infty} - \frac{\omega_{\mathrm{p}}^2}{\omega^2 + \mathrm{i}\gamma\omega}, \qquad (1)$$

where $\varepsilon_{\infty} = 3.7$ is the dielectric constant at an

infinite angular frequency; $\omega_p = 1.38 \times 10^{16}$ rad/s, the bulk plasma frequency, represents the natural frequency of the oscillations of free conduction electrons; $\gamma = 2.73 \times 10^{13}$ rad/s is the damping frequency of the oscillations; and ω is the angular frequency of the incident electromagnetic radiation.

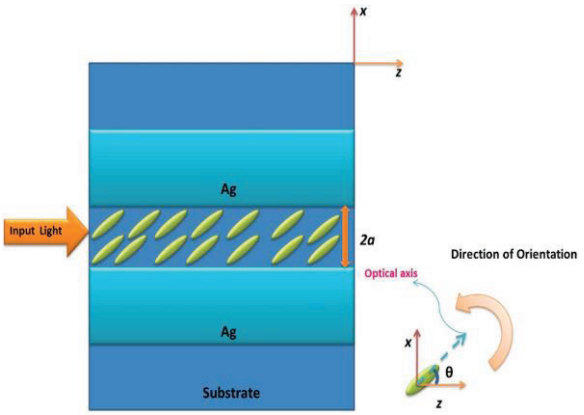

Fig. 1. General schematic of a M-LC-M waveguide structure.

In general, the properties of an anisotropic medium are expressed in a tensor form. By arranging the optical axis of the anisotropic LC molecules in the *x*-*z* plane, the dielectric tensor for the permittivity of the LC is given by:

$$\overline{\overline{\varepsilon}} = \begin{bmatrix} n_e^2\cos^2\theta + n_o^2\sin^2\theta & 0 & \left(n_e^2 - n_o^2\right)\sin\theta\cos\theta \\ 0 & n_e^2 & 0 \\ \left(n_e^2 - n_o^2\right)\sin\theta\cos\theta & 0 & n_o^2\cos^2\theta + n_e^2\sin^2\theta \end{bmatrix}, \quad (2)$$

where n_o and n_e are the ordinary and extraordinary indices of refraction, respectively. In the equation above, θ, called the tilt angle, is the angle between the optical axis of the anisotropic LC molecules and the *z*-direction. In the entire paper, n_e and n_o are taken to be 1.737 and 1.518, respectively, which are the parameters for nematic liquid crystals (E7) at room temperature. The amount of voltage needed to switch a nematic liquid crystal modulator is a function of the specific material used, cell thickness and alignment. In order to investigate the physical properties of SPPs, we derive the dispersion relations corresponding to both symmetric and antisymmetric modes in the M-LC-M waveguide. The dispersion relations for the M-LC-M waveguide of width $2a$ can be found by solving the wave equation inside the anisotropic LC medium and matching the obtained solution with the solution of wave equation inside plasmonic regions using appropriate boundary conditions. The derivation procedure of dispersion relations is out of the scope of this paper. The calculated dispersion relation for M-LC-M structure is:

$$\eta_{zx} i\beta_z - \eta_{zz} i\beta_x - \eta_{zz} k_d \begin{Bmatrix} \tanh(k_d a) \\ \coth(k_d a) \end{Bmatrix} = \frac{k_m}{\varepsilon_m}, \quad (3)$$

where the propagation constant β_x and the attenuation constants k_d and k_m, all in the transverse *x* direction, are defined as $\beta_x = \beta_z \frac{\eta_{xz}}{\eta_{zz}}$, $k_d = \sqrt{\beta_z^2 \frac{\eta_{xx}}{\eta_{zz}} - \frac{\omega^2\mu_0}{\eta_{zz}} - \beta_x^2}$, and $k_m = \sqrt{\beta_z^2 - \varepsilon_m k_0^2}$, respectively; β_z is the complex propagation constant in the longitudinal direction; $\overline{\overline{\eta}} = \overline{\overline{\varepsilon}}^{-1}$ is the relative impermeability tensor of anisotropic layer, ε_m is the dielectric constant of the metal and k_0 is the free-space wave constant. Here, the "tanh" function represents symmetric plasmon modes and the "coth" function represents antisymmetric modes. This dispersion relation equation can be used in the design of active electro-optical plasmonic devices.

By solving Eq. (3), the propagation constant (β_z) of the fundamental SPP mode and, consequently, the effective refractive index ($n_{eff} = \beta_z/k_0$) of the M-LC-M structure for the mode can be obtained which provide physical insight. The real part of n_{eff} of the M-LC-M waveguide as a function of the waveguide width for different tilt angles of the LC molecules is shown in Fig. 2 (a). The wavelength of the input optical wave is taken to be λ = 850 nm. It is clearly seen that for a fixed value of tilt angle, n_{eff} decreases with increasing waveguide width. By increasing the tilt angle for a fixed value of waveguide width, n_{eff} also decreases. Figure 2 (b) shows the real part of n_{eff} versus wavelength for three different tilt angles. The width of the LC layer is chosen to be 100 nm. By increasing the wavelength or increasing the tilt angle, n_{eff} decreases. It is clearly demonstrated that high light confinement can be achieved for small LC tilt angles in the M-LC-M structure. It is also demonstrated that the degree of this light confinement can be varied by

varying the tilt angle of the LC molecules, which can be most conveniently accomplished through an externally applied voltage.

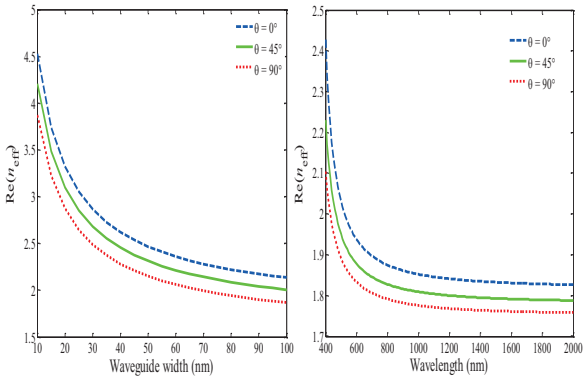

Fig. 2. The real part of n_{eff} of the M-LC-M waveguide as a function of: (a) the waveguide width, and (b) wavelength for different tilt angles.

To simulate the tunable plasmonic ring resonator structures filled with anisotropic LC molecules and to illustrate their new properties, two sets of simulations have been done. The first one is the electrostatic simulations by finite element method (FEM), which gives us the orientation of the electrostatic electric field inside the structure and correspondingly the tilt angles of the liquid crystals for high values of voltages. The outputs of the electrostatic simulations are the tilt angles of the liquid crystals in the structure. Then for the optical simulations, the Anisotropic-Dispersive Finite-Difference Time-Domain (A-D-FDTD) method is used. Convolutional perfectly matched layer (CPML) as absorbing boundary condition is also used to dissipate out-going waves. The simulation dimension is 1×1 μm^2, the FDTD grid size is chosen to be $\Delta x = \Delta y = 1$ nm, and the time step $\Delta t = 2.3115 \times 10^{-18}$ s is achieved following the Courant stability condition. The tilt angles of the liquid crystal, derived from the finite-element simulations, were imported as the inputs to the FDTD solver. In our FDTD solver, the liquid crystals are considered in the realistic way by incorporating a non-diagonal dielectric tensor (Eq. 2) in the FDTD simulations. Figure 3 shows the computational flowchart for finite element and finite-difference time-domain simulations.

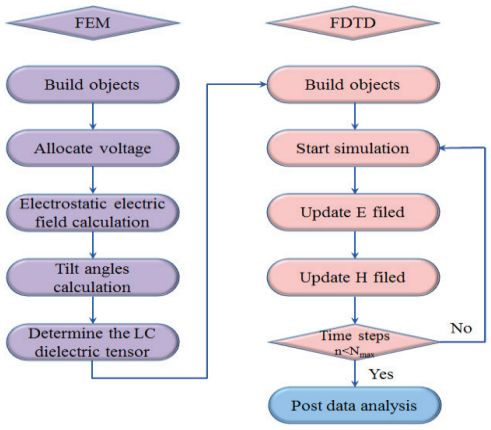

Fig. 3. Computational flowchart for finite element and finite-difference time-domain simulations.

III. TUNABLE PLASMONIC RING RESONATOR FILTER

There are two ways by which the transmission response of a plasmonic filter can be tuned. One approach is by altering the structural parameters of the filter. Clearly, this approach is impractical because the structural parameters of a given fabricated device are difficult to alter; therefore, different plasmonic filters have to be used to tune the transmission response. The other approach is by changing the optical properties of the material inside the structure to tune the transmission characteristics of the filter. In this section, we consider a tunable plasmonic ring resonator filter, shown in Fig. 4, that can be tuned by the second approach. For this purpose, liquid crystal is incorporated in the bus waveguide and in the ring resonator, as shown in Fig. 4.

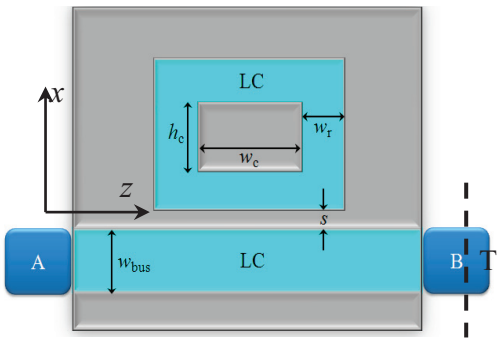

Fig. 4. Tunable plasmonic ring resonator filter filled with liquid crystal in the bus waveguide and in the ring resonator.

A low-frequency voltage of varying value is applied at the upper silver layer, with the electrical path terminating at the grounded lower metal film and metal core. The electric field induces a reorientation of the LC molecules, which tend to align with the applied field, modifying the overall electrical and subsequently optical properties of the LC material. The exact profile of the molecular orientations and the extent of the LC-switching depend on the value of the applied voltage, the molecular anchoring conditions at the walls, the geometry of the structure, and the material properties of the LC and the surrounding isotropic materials. In the absence of an applied field, the alignment of the nematic material depends primarily on the anchoring conditions at the LC/material interfaces. As far as the LC/metal interface is concerned, silver is found to provide homogeneous alignment. In any case, none of the LC/metal interfaces involved in the proposed structure has been shown to promote homeotropic anchoring conditions. In our analysis, we assume strong homogeneous anchoring conditions, that is, the LC molecules are aligned with the *z*-axis at the channel's walls in the absence of any electric field. In the absence of the electric field, when the liquid crystal is at the rest state, all LC molecules lie in parallel to the *z*-axis and the tilt angle is equal to zero. The application via the silver layer of a voltage above a certain threshold value induces the switching of the LC molecules. As the applied voltage increases, the tilt angle of each molecule increases because the LC molecules tend to align with the electric field. For a sufficiently high voltage, the LC is considered to be fully switched, when the nematic director of the material tends to align in parallel to the *x*-axis in the bus waveguide and in the horizontal branches of the ring resonator so that the tilt angles of the molecules in these areas all approximate 90°. However, in the vertical branches, the nematic director of the material tends to align in parallel to the *z*-axis and the tilt angles in these areas approximate 0°. The profiles of the LC tilt angle and the electric potential, for an applied voltage just above the threshold value, are shown in Figs. 5 (a) and (b), respectively. The structural parameters of this structure are set as $w_{bus} = w_r =$ 100 nm, w_c = 300 nm, h_c = 250 nm, and s = 20 nm. The electric field is everywhere perpendicular to the boundaries of the silver layers. The electrostatic analysis yields the profile of the relative optical permittivity tensor $\overline{\overline{\varepsilon_r}}$ in the LC-infiltrated channel, which along with the other material parameters is imported to a fully anisotropic finite element eigenmode solver.

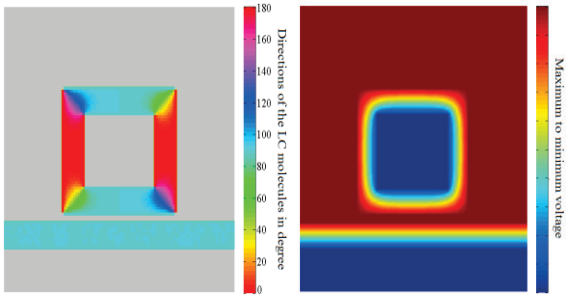

(a) (b)

Fig. 5. Profiles of: (a) the LC tilt angle in degrees, and (b) the electric potential, for an applied voltage above the threshold value.

A quantified evaluation of the structure's performance is provided by calculating the transmission responses. An adequately broadband Gaussian pulse with TM polarization, which is generated by a line source, is launched into port A. The plane 'T' (shown in Fig. 4) detects the power of internal fields that reach the output port (port B). The transmitted power is $P_{out} = P_T$. This transmitted power is computed by taking a fast Fourier transform (FFT) of the fields that are calculated by FDTD and integrating the Poynting vector over the cells of plane 'T'. A reference straight waveguide simulation is used to calculate the incident power P_{in}. The normalized transmittance is defined as 'normalized transmittance = P_{out}/P_{in}'. The transmission spectra are evaluated and depicted in Fig. 6 for two cases: with the LC in the rest state (in the absence of an applied voltage) and in the excited state (in the presence of an applied voltage above threshold). Comparison of these two spectra shows that changing the LC optical axis orientation alters the effective permittivity, and thus the resonance wavelengths of the ring resonator. As can be seen, the resonance wavelengths are blue-shifted by the applied voltage. The maximum tuning ranges of the first

and second modes by the applied voltage are about 109 nm and 91 nm, respectively.

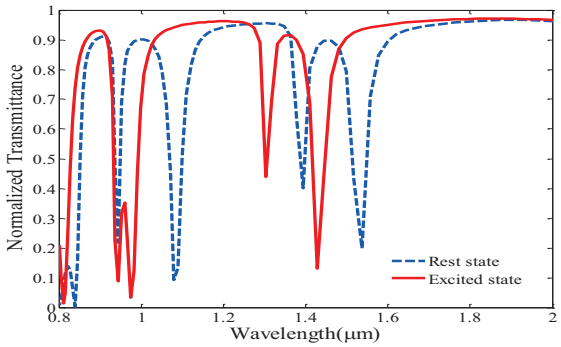

Fig. 6. Optical power transmission characteristics of the structure for LC in the rest state (blue dashed curve) and in the excited state (red solid curve).

When the tilt angle is fixed to be $\theta = 0°$ (rest state of the LC), the direction of the incident light is aligned with the optical axis of the LC molecules in the bus waveguide and also in the horizontal branches of the ring resonator. However, it is perpendicular to the optical axis of the LC molecules in the vertical branches of the ring resonator. Hence, the effective refractive index in the bus waveguide and horizontal branches has its maximum value, while that in the vertical branches of the structure has its minimum value (see Fig. 2). On the other hand, as voltage rises and switching is complete, the direction of the incident light becomes perpendicular to the optical axis of the LC molecules almost in the whole structure. Hence, the effective refractive index experienced by the light in the whole structure has its minimum value. Because the resonance wavelengths depend on the ring resonator properties, it is expected that the transmission spectrum blue-shifts to shorter wavelengths when the LC is switched to the excited state so that the effective refractive index in the ring resonator reaches its minimum.

IV. PLASMONIC OPTICAL SWITCH BASED ON A LIQUID CRYSTAL DIELECTRIC-LOADED RING RESONATOR

One typical configuration of add-drop coupler that consists of two parallel waveguides and a ring resonator is schematically shown in Fig. 7 where the incident port is labeled as A, and the exit ports are labeled as B, C and D. The gap waveguides, and the ring resonator, are M-LC-M structures.

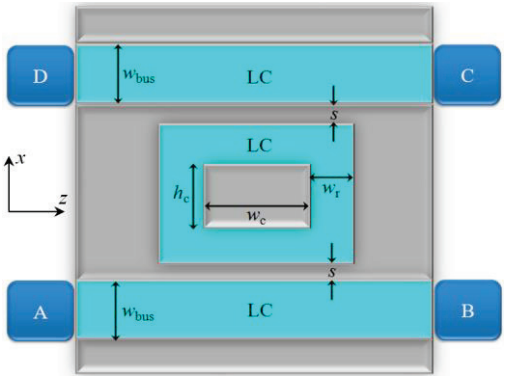

Fig. 7. Tunable plasmonic optical switch with liquid crystal in the bus waveguide and in the ring resonator.

At the resonance wavelength, the ring resonator couples the incident energy from the lower input branch into the resonator and drops it to the output branch. The LC layer width is set to be $w_{bus} = w_r = 50$ nm, which allows for lossless bending around the corners for wavelengths longer than 760 nm [45]. A low-frequency voltage of varying value is applied at the middle silver layer; the electrical path terminates at the upper and lower metal films and also at the metal core, which are all grounded. Shown in Figs. 8 (a) and (b) respectively, are the profile of the LC tilt angle and that of the electric potential, for an applied voltage just above the threshold value.

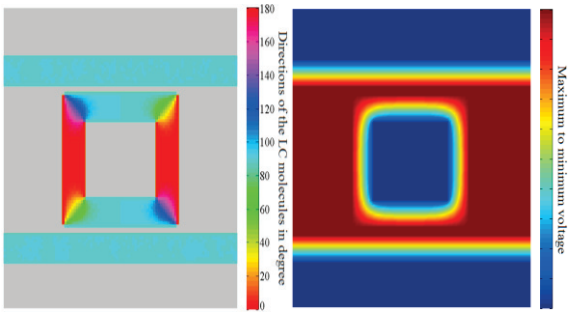

Fig. 8. Profiles of: (a) the LC tilt angle in degrees, and (b) the electric potential, for an applied voltage above the threshold value.

Shown in Fig. 9 are the corresponding transmission spectra for two cases: with the LC in the rest state (in the absence of the applied voltage) and in the excited state (in the presence of an applied voltage above threshold). As can be seen, there are two double dips in transmission spectra: at 1817 nm and 1763 nm in the spectrum for the excited state shown as the red solid curve and at 1394 nm and 1289 nm in the spectrum for the rest state shown as the blue dashed curve. This phenomenon was first reported in [13]. The resonant mode is split into two standing-wave modes due to the nonuniform distribution of n_{eff} round the ring resonator.

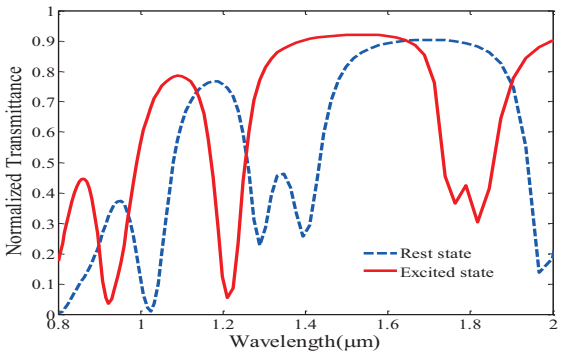

Fig. 9. Optical power transmission from port A to B characteristics of the structure for the rest-state (blue dashed curve), and the excited state (red solid curve).

Having fixed the values of the various parameters of the structure, the performance of the proposed device as an optical switch can be evaluated. Light of λ = 1025 nm wavelength is launched into Port A. When the device operates in the rest state, the power is coupled to the ring resonator and is dropped to the adjacent LC-filled output-branch waveguide. This case is also referred to as the off-state of the optical switch, in which the light is not able to reach the output port B. On the other hand, as voltage rises and switching intensifies, the power coupled to the ring resonator is reduced. Eventually when the voltage reaches above the threshold to fully switch the device to the excited state, most of the power is not coupled to the ring resonator but is transmitted to the output port B. This is the on-state of the optical switch. In order to gain better understanding of the physics behind the function of the optical switch, the structure is illuminated with a TM-polarized continuous-wave at the wavelength of λ = 1025 nm. Representative magnetic field distributions, H_y, calculated by FDTD simulations for off and on states are shown in Figs. 10 (a) and (b), respectively. As shown, when the structure is in the rest state, about 0.9% of the input power reaches the output port B. By applying a voltage above the threshold value over the structure, the orientation of the LC molecules changes, resulting in a discernable change in effective refractive index. Therefore, in the excited state, about 70% of the input power reaches the output port B.

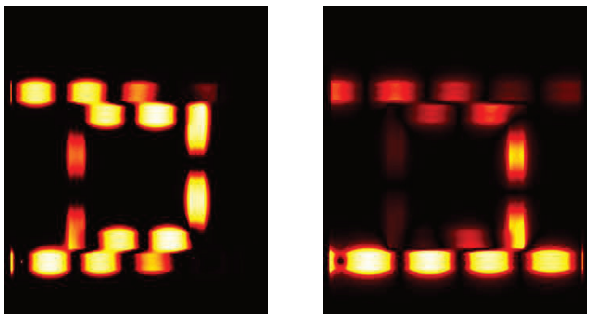

(a) (b)

Fig. 10. Magnetic field distribution patterns at the wavelength of λ = 1025 nm for: (a) the rest state (switch is off), and (b) the excited state (switch is on).

V. CONCLUSION

We propose a new tunable plasmonic ring resonator filter and optical switch based on the Metal-Liquid Crystal-Metal structure. Detailed characteristics of the device are studied by numerical simulations to demonstrate the feasibility of this concept. By applying an external voltage, the orientations of the LC molecules can be controlled, thus inducing a change of the LC refractive index seen by the guided SP mode field, which in turn leads to a change in SP mode characteristics. Through this change, the performance of the filter can be electrically tuned. The simulated results clearly show that the transmission response can be controlled easily without changing the geometrical parameters of the structure. Such electrically controlled dynamic plasmonic devices can provide a promising alternative in

terms of controlling and routing of optical signals in integrated plasmonics-based optical chips.

REFERENCES

[1] W. L. Barnes, A. Dereux, and T. W. Ebbesen, "Surface plasmon subwavelength optics," *Nature*, vol. 424, no. 6950, pp. 824-830, 2003.

[2] T. W. Ebbesen, H. J. Lezec, H. F. Ghaemi, T. Thio, and P. A. Wolff, "Extraordinary optical transmission through sub-wavelength hole arrays," *Nature*, vol. 391, no. 6668, pp. 667-669, 1998.

[3] E. N. Economou, "Surface plasmons in thin films," *Phys. Rev.*, vol. 182, no. 2, pp. 539-554, 1969.

[4] B. Prade, J. Y. Vinet, and A. Mysyrowicz, "Guided optical waves in planar heterostructures with negative dielectric constant," *Phys. Rev. B*, vol. 44, no. 24, pp. 13556-13572, 1991.

[5] J. J. Burke and G. I. Stegeman, "Surface-polariton-like waves guided by thin, lossy metal films," *Phys. Rev. B*, vol. 33, no. 8, pp. 5186-5201, 1986.

[6] G. Veronis and S. Fana, "Bends and splitters in metal-dielectric-metal subwavelength plasmonic waveguides," *Appl. Phys. Lett*., vol. 87, pp. (131102) 1-3, 2005.

[7] T. W. Lee and S. K. Gray, "Subwavelength light bending by metal slit structures," *Opt. Express*, vol. 13, no. 24, pp. 9652-9659, 2005.

[8] R. A. Wahsheh, Z. Lu, and M. A. G. Abushagur, "Nanoplasmonic couplers and splitters," *Opt. Express*, vol. 17, pp. 19033-19040, 2009.

[9] Z. Han, L. Liu, and Erik Forsberg, "Ultra-compact directional couplers and Mach–Zehnder interferometers employing surface plasmon polaritons," *Opt. Commun*., vol. 259, no. 2, pp. 690-695, 2006.

[10] H. Gao, H. Shi, C. Wang, C. Du, X. Luo, Q. Deng, Y. Lv, X. Lin, and H. Yao, "Surface plasmon polariton propagation and combination in Y-shaped metallic channels," *Opt. Express*, vol. 13, no. 26, pp. 10795-10800, 2005.

[11] Z. Kang and G. P. Wang, "Coupled metal gap waveguides as plasmonic wavelength sorters," *Opt. Express*, vol. 16, no. 11, pp. 7680-7685, 2008.

[12] S. Xiao, L. Liu, and M. Qiu, "Resonator channel drop filters in a plasmon-polaritons metal," *Opt. Express*, vol. 14, no. 7, pp. 2932-2937, 2006.

[13] A. Hosseini and Y. Massoud, "Nanoscale surface plasmon based resonator using rectangular geometry," *Appl. Phys. Lett*., vol. 90, no. 18, pp. (181102) 1-3, 2007.

[14] Z. Han, V. Van, W. N. Herman, and P.-T. Ho, "Aperture-coupled MIM plasmonic ring resonators with sub-diffraction modal volumes," *Opt. Express*, vol. 17, no. 15, pp. 12678-12684, 2009.

[15] T. B. Wang, X. W. Wen, C. P. Yin, and H. Z. Wang, "The transmission characteristics of surface plasmon polaritons in ring resonator," *Opt. Express*, vol. 17, no. 26, pp. 24096-24101, 2009.

[16] S. I. Bozhevolnyi, V. S. Volkov, E. Devaux, J. Y. Laluet, and T. W. Ebbesen, "Channel plasmon subwavelength waveguide components including interferometers and ring resonators," *Nature*, vol. 440, no. 7083, pp. 508-511, 2006.

[17] X. S. Lin and X. G. Huang, "Tooth-shaped plasmonic waveguide filters with nanometeric sizes," *Opt. Express*, vol. 33, no. 23, pp. 2874-2876, 2008.

[18] J. Tao, X. G. Huang, X. Lin, J. Chen, Q. Zhang, and X. Jin, "Systematical research on characteristics of double-sided teeth-shaped nanoplasmonic waveguide filters," *JOSA B*, vol. 27, no. 2, pp. 323-327, 2010.

[19] B. Wang and G. P. Wang, "Plasmon Bragg reflectors and nanocavities on flat metallic surfaces," *Appl. Phys. Lett*., vol. 87, no. 1, pp. (013107) 1-3, 2005.

[20] A. Hosseini and Y. Massoud, "A low-loss metal-insulator-metal plasmonic bragg reflector," *Opt. Express*, vol. 14, no. 23, pp. 11318-11323, 2006.

[21] J. Q. Liu, L. L. Wang, M. D. He, W. Q. Huang, D. Wang, B. S. Zou, and S. Wen, "A wide bandgap plasmonic Bragg reflector," *Opt. Express*, vol. 16, no. 7, pp. 4888-4894, 2008.

[22] Y. Gong, L. Wang, X. Hu, X. Li, and X. Liu, "Broad-bandgap and low-sidelobe surface plasmon polariton reflector with Bragg-grating-based MIM waveguide," *Opt. Express*, vol. 17, no. 16, pp. 13727-13736, 2009.

[23] B. Hu, Q. J. Wang, and Y. Zhang, "Broadly tunable one-way terahertz plasmonic waveguide based on nonreciprocal surface magneto plasmons," *Opt. Lett.*, vol. 37, no. 11, pp. 1895-1897, 2012.

[24] J. Wang, S. Liu, and A. Nahata, "Reconfigurable plasmonic devices using liquid metals," *Opt. Express*, vol. 20, no 11, pp. 12119-12126, 2012.

[25] J. Gu, R. Singh, A. K. Azad, J. Han, A. J. Taylor, J. F. O'Hara, and W. Zhang, "An active hybrid plasmonic metamaterial," *Opt. Mat. Express*, vol. 2, no. 1, pp. 31-37, 2012.

[26] R. A. Pala, K. T. Shimizu, N. A. Melosh, and M. L. Brongersma, "A nonvolatile plasmonic switch employing photochromic molecules," *Nano Lett.*, vol. 8, no. 5, pp. 1506-1510, 2008.

[27] L. Gao, L. Tang, F. Hu, R. Guo, X. Wang, and Z. Zhou, "Active metal strip hybrid plasmonic

waveguide with low critical material gain," *Opt. Express*, vol. 20, no. 10, pp. 11487-11495, 2012.
[28] C. Garcia, V. Coello, Z. Han, I. P. Radko, and S. I. Bozhevolnyi, "Partial loss compensation in dielectric-loaded plasmonic waveguides at near infra-red wavelengths," *Opt. Express*, vol. 20, no. 7, pp. 7771-7776, 2012.
[29] L. A. Sweatlock and K. Diest, "Vanadium dioxide based plasmonic modulators," *Opt. Express*, vol. 20, no. 8, pp. 8700-8709, 2012.
[30] M. K. Chen, Y. C. Chang, C. E. Yang, Y. Guo, J. Mazurowski, S. Yin, P. Ruffin, C. Brantley, E. Edwards, and C. Luo, "Tunable terahertz plasmonic lenses based on semiconductor microslits," *Micro. and Opt. Tech. Lett*., vol. 52, no. 4, pp. 979-981, 2010.
[31] M. A. Vincenti, A. D'Orazio, M. Buncick, N. Akozbek, M. J. Bloemer, and M. Scalora, "Beam steering from resonant subwavelength slits filled with a nonlinear material," *JOSA B*, vol. 26, no. 2, pp. 301-307, 2009.
[32] P. Li, T. Sasaki, L. F. Pan, and K. Hane, "Comb-drive tracking and focusing lens actuators integrated on a silicon-on-insulator wafer," *Opt. Express*, vol. 20, no. 1, pp. 627-634, 2012.
[33] X. Wang, B. Wang, P. J. Bos, P. F. McManamon, J. J. Pouch, F. A. Miranda, and J. E. Anderson, "Modeling and design of an optimized liquid-crystal optical phased array," *J. of Appl. Phys*., vol. 98, no. 7, pp. (073101) 1-8, 2005.
[34] E. Hendry, F. J. Garcia-Vidal, L. Martin-Moreno, J. Gomez Rivas, M. Bonn, A. P. Hibbins, and M. J. Lockyear, "Optical control over surface-plasmon-polariton-assisted THz transmission through a slit aperture," *Phys. Rev. Lett*., vol. 100, no. 12, pp. (123901) 1-8, 2008.
[35] A. V. Krasavin and N. I. Zheludev, "Active plasmonics: controlling signals in Au/Ga waveguide using nanoscale structural transformations," *Appl. Phys. Lett*., vol. 84, no. 8, pp. 1416-1418, 2004.
[36] D. E. Chang, A. S. Sorensen, E. A. Demler, and M. D. Lukin, "A singlephoton transistor using nanoscale surface plasmons," *Nat. Phys*., vol. 3, no. 11, pp. 807-812, 2007.
[37] J. G. Rivas, J. A. Sanchez-Gil, M. Kuttge, P. H. Bolivar, and H. Kurz, "Optically switchable mirrors for surface plasmon polaritons propagating on semiconductor surfaces," *Phys. Rev. B, Condens. Matter Mater. Phys*., vol. 74, no. 24, pp. 245324-6, 2006.
[38] I. I. Smolyaninov, "Quantum fluctuations of the refractive index near the interface between a metal and a nonlinear dielectric," *Phys. Rev. Lett*., vol. 94, no. 5, pp. 57401-57403, 2005.
[39] J. A. Porto, L. Martin-Moreno, and F. J. Garcia-Vidal, "Optical bistability in subwavelength slit apertures containing nonlinear media," *Phys. Rev. B*, vol. 70, no. 8, pp. 081402-1-081402-4, 2004.
[40] S. Yue, Z. Li, J. Chen, and Q. Gong, "Ultrasmall and ultrafast all-optical modulation based on a plasmonic lens," *Appl. Phys. Lett*., vol. 98, no. 16, 161108, 2011.
[41] P. A. Kossyrev, A. Yin, S. G. Cloutier, D. A. Cardimona, D. Huang, P. M. Alsing, and J. M. Xu, "Electric field tuning of plasmonic response of nanodot array in liquid crystal matrix," *Nano Lett.*, vol. 5, no. 10, pp. 1978-1981, 2005.
[42] M. BahramiPanah, S. A. Mirtaheri, and M. S. Abrishamian, "Electrical beam steering with metal-anisotropic-metal structure," *Opt. Lett.*, vol. 37, no. 4, pp. 1-3, 2012.
[43] A. C. Tasolamprou, D. C. Zografopoulos, and E. E. Kriezis, "Liquid crystal-based dielectric loaded surface plasmon polariton optical switches," *J. Appl. Phys*., vol. 110, no. 9, pp. 093102-1-093102-9, 2011.
[44] M. Dridi and A. Vial, "FDTD modeling of gold nanoparticles in a nematic liquid crystal: quantitative and qualitative analysis of the spectral tenability," *J. Phys. Chem. C*, vol. 114, no. 21, pp. 9541-9545, 2010.
[45] G. Veronis and S. Fan, "Bends and splitters in metal-dielectric-metal subwavelength plasmonic waveguides," *Appl. Phys. Lett*, vol. 87, 131102, 2005.

Seyed Mohammad Alavi has received his B.Sc. and M.Sc. degrees in Electronic. Eng. from Amir Kabir University of Technology (Polytechnic of Tehran), Iran, University of Tehran, Faculty of Engineering Tehran, Iran and Ph.D. degrees in Telecom. Eng. from Electrical and Computer Engineering of K. N. Toosi University of Technology, Tehran, Iran in 1987, 1991 and 2011 respectively. He had worked at Iran Telecom. Research Center (ITRC) Tehran, Iran between 1987 and 1989, at Iran Electronic Industry between 1991 and 1998 and at Laboratory of Electronic Instrumentation of Nancy (LIEN) France between 1998 and 2006. Now he works as an Assistant Professor in the Department of Electrical Engineering at Imam Hossein Comprehensive University in Tehran, Iran. His research interests are radar systems and high frequency microelectronic devices and circuits design.

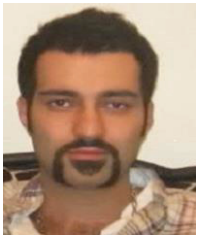

Hamed Armand has received his B.Sc. degree in Electronic. Eng. from Shiraz University of Technology, Shiraz, Iran in 2009 and M.Sc. degree in Telecom. Eng. from Electrical and Computer Engineering of K. N. Toosi University of Technology, Tehran, Iran in 2011. His research interests are Photonic Structures and Anisotropic Medias, high frequency microelectronic devices and Micowave circuits design.